An Experimental and Computational Study of Strain Sensitivity in Superconducting Nb_3Sn

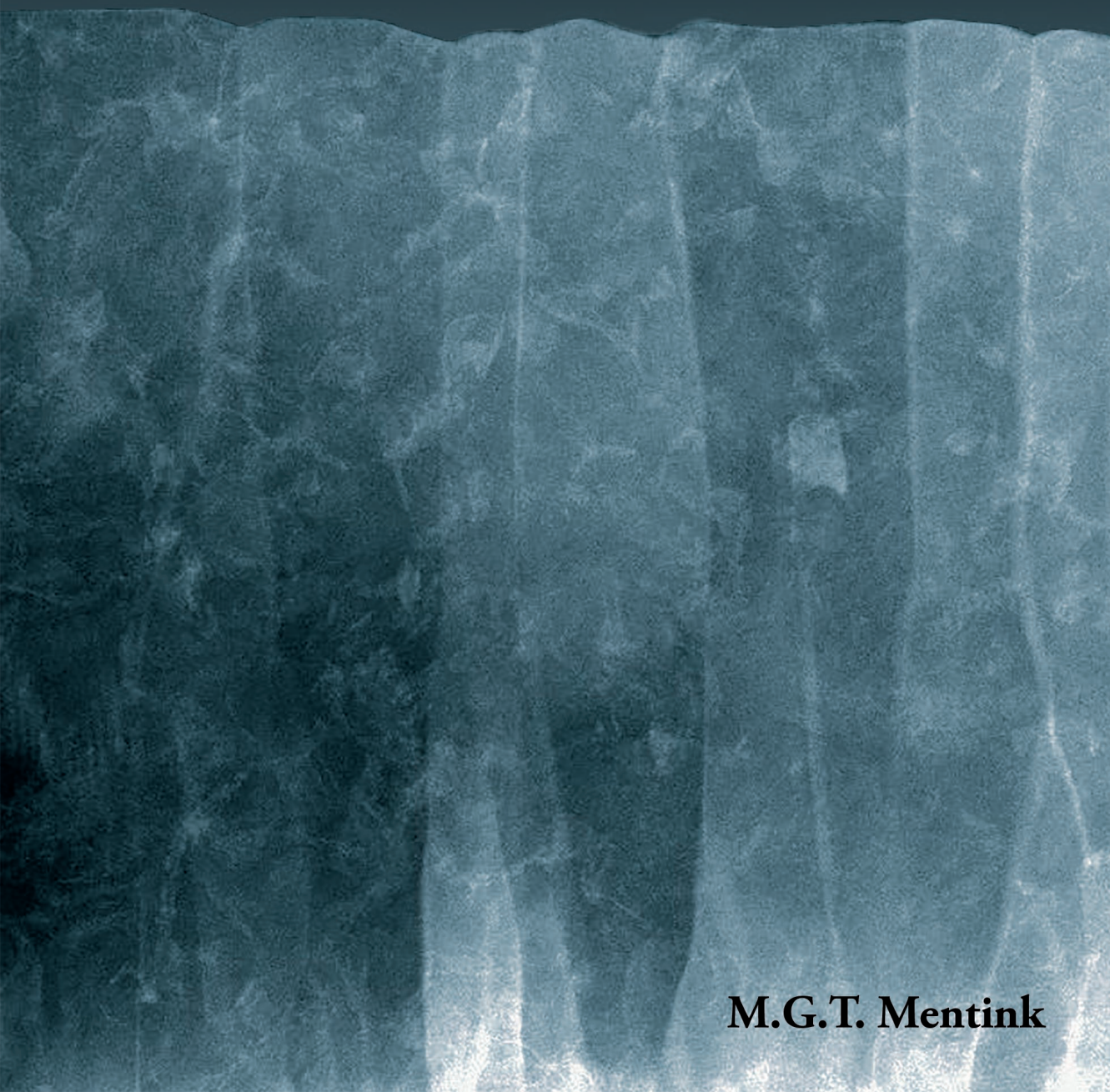

M.G.T. Mentink

AN EXPERIMENTAL AND COMPUTATIONAL STUDY OF STRAIN SENSITIVITY IN SUPERCONDUCTING Nb_3Sn

Dissertation graduation committee:

prof. dr. J. L. M. Cornelissen (Chairman and secretary)
prof. dr. ir. H. H. J. ten Kate (Supervisor)
prof. dr. F. Hellman (Supervisor)
dr. ing. A. Godeke (Assistant supervisor)
prof. dr. ir. H. J. M. ter Brake
dr. M. M. J. Dhallé
dr. W. Goldacker
dr. ir. ing. B. ten Haken
prof. dr. ir. J. W. M. Hilgenkamp
prof. dr. P. H. Kes
prof. dr. D. C. Larbalestier

This work was performed in a collaboration between the Energy, Materials and Systems group, chair for Industrial Application of Superconductivity at the University of Twente, the Netherlands, the Superconducting Magnet Program at Lawrence Berkeley National Laboratory, Berkeley, USA, and the Hellman Group at the University of California, Berkeley, USA.

This research was partially funded by the Director, Office of Science, US Department of Energy, under contract nr. DE-AC02-05CH11231.

M. G. T. Mentink
An experimental and computational study of strain sensitivity in superconducting Nb_3Sn
Ph.D. thesis, University of Twente, Enschede, the Netherlands.

ISBN: 978-90-365-3635-6

Cover: A STEM cross-section of a Nb-Sn thin film. Courtesy of J. Bonevich of NIST.

Printed by PrintPartners Ipskamp, Enschede

AN EXPERIMENTAL AND COMPUTATIONAL STUDY OF STRAIN SENSITIVITY IN SUPERCONDUCTING Nb_3Sn

PROEFSCHRIFT

ter verkrijging van
de graad van doctor aan de Universiteit Twente,
op gezag van de rector magnificus,
prof. dr. H. Brinksma
volgens besluit van het College voor Promoties
in het openbaar te verdedigen
op donderdag 13 maart 2014 om 16.45 uur

door

Matthias Gerhardus Theodorus Mentink

geboren op 19 maart 1984

te Lichtenvoorde

Dit proefschrift is goedgekeurd door de promotoren:

prof. dr. ir. H. H. J. ten Kate
prof. dr. F. Hellman

Assistent promotor:

dr. ing. A. Godeke

For my dad.

Preface

In this thesis several years of investigating how strain affects the superconducting properties of Nb_3Sn is summarized. Nb_3Sn is a superconductor that is used in important high-field applications, such as particle accelerators, experimental fusion reactors, high-field laboratory magnets, and nuclear magnetic resonance spectrometry. The high magnetic fields generated in these applications also result in large forces on the superconductor, which means that to some extent deformation of the conductor is unavoidable. The superconducting properties of Nb_3Sn are strongly affected by strain, and a clear understanding of how strain affects the superconducting properties is still lacking. This topic is of fundamental interest, as it is related to the underlying quantum-mechanical nature of superconductivity, but also has as practical implications, since the superconducting properties of Nb_3Sn affect the performance of high-field magnet applications. It is this combination that drew me to this topic.

While studying at the University of Twente, I first became acquainted with researchers at Lawrence Berkeley National Laboratory, including Arno Godeke and Dan Dietderich during an internship prior to the PhD. The PhD research was performed as a collaboration between researchers at the University of Twente, Lawrence Berkeley National Laboratory, and the University of California, Berkeley. Arno Godeke of LBNL had previously completed a PhD investigation at the University of Twente, which provided a detailed overview of how the superconducting properties of Nb_3Sn wires are affected by strain, composition and morphology. Professor Frances Hellman of UC Berkeley had investigated Nb_3Sn thin film deposition during her own PhD research. These two investigations were taken as starting points to this research.

A complication in investigating Nb_3Sn is that Nb_3Sn wires used in high magnetic field applications are inhomogeneous in both composition and morphology. The wires comprise Nb-Sn grains with various grain sizes and compositions in addition to other materials such as pure niobium and copper. As both composition and morphology strongly affect the superconducting properties, it is difficult to extract a detailed understanding from these samples. In light of this, a significant part of this research was spent fabricating homogeneous thin film samples, characterizing samples in terms of composition and morphology, and probing how strain affects the superconducting properties of the samples.

On the other hand, bits and pieces of understanding of what determines the superconducting properties of Nb_3Sn as a function of strain has been published, but an overarching whole was missing. We have combined microscopic theory with ab-initio calculations in an effort to determine in what manner strain affects the superconducting properties and why Nb_3Sn is so different from, for instance, niobium-titanium with regards to strain sensitivity. The results of this effort are validated through comparison with earlier published experimental observations as well as with new experimental observations collected as part of this research.

This thesis is the result of the combined efforts of people from a number of institutions in Europe and the United States. It would not have been possible to pursue this work without these people working together. I hope that, after six decades of research on superconducting Nb_3Sn, this thesis is a worthwhile contribution to our growing understanding of this superconductor.

Acknowledgments

This work is the result of efforts by many people, both in a professional and a personal sense. During my time in Berkeley I had the opportunity to work with friendly and supportive people who were pushing back scientific boundaries, regarding the limits of superconducting high field technology. It is an odd but good experience to read papers from various authors detailing one scientific breakthrough or another, and then to meet them in person. Being a multi-cultural hub, Berkeley also allowed me to meet and become friends with people from all corners of this planet.

Along the way, people have been instrumental in making this research happen. At LBNL, Jonathan Slack, Reuben Mendelsberg, and Andre Anders allowed me to use their lab for a rather extended period of time thus allowing for the fabrication of thin films, and have helped in various other ways along the years. The people at Ohio State University have helped by repeatedly performing heat capacity measurements on Nb_3Sn bulk samples which were kindly supplied by Wilfried Goldacker of the Karlsruhe Institute of Technology. In particular I would like to thank Mike Susner of the Ohio State University, who came to the lab in the weekends just to make sure my samples would get measured. John Bonevich of the National Institute of Science and Technology was kind enough to perform characterization work on some of the Nb-Sn thin films we made, which included the STEM image on the cover. A lot of the experimental work was made possible with software and hardware designed at the University of Twente (such as VI by Bennie ten Haken), and I have gotten useful recommendations and assistance along the way, such as the advice on thin film fabrication from Frank Roesthuis. Professors Marcel ter Brake, Herman ten Kate, David Larbalestier, and Frances Hellman were kind enough to write letters of recommendation which contributed to getting the CSC student fellowship award. Vladimir Kresin of LBNL was kind enough to answer various questions related to the microscopic properties of Nb_3Sn and comment on the description of microscopic theory in this thesis.

Shane Cybart and Stephen Wu have assisted Edwin Dollekamp and myself in attempting to do some very fancy experiments. Edwin, from the University of Twente, took on a complicated research topic and I was impressed with how far he managed to get in that work, and Shane and Stephen invested time in the evenings and weekends to make it happen. Professor Orlandos previous investigations of Nb_3Sn were an inspiration for some of the work described in this thesis, and he was kind enough to answer questions by email and over the phone. Derek Stewart of the Cornell NanoScale Science and Technology Facility helped me to get familiar with density functional theory calculations and computing clusters and made the suggestion of using Quantum Espresso ab-initio software. Robert Ryne and Steve Gourlay of LBNL helped me getting access to sizeable supercomputing resources at NERSC which were needed for this research.

My friends and family stuck together in difficult times. My parents and brother have always been warm, supportive, and encouraging in my pursuit of the PhD research, even in difficult times. It seems fitting that both my brother and I are completing our PhDs around the same time. Lynn Heimbucher was always in for a friendly chat, and gave up a weekend of free time to read through my thesis and correct for grammar. Tiina Salmi has been a good friend,

fellow PhD student, and office mate, and has on occasion helped out with research related things. Catherine Callaghan has been a vital support for a long time and has managed to be a source of motivation, thus allowing me to finish this work.

Last but not least, I would like to thank my supervisors. Marc Dhallé has invested time reading and correcting drafts of papers as well as this thesis and has left his mark on this work. Dan Dietderich has been a great support throughout the PhD research by introducing me to various people, instructing me on how to use equipment, making things happen when they needed to happen, and by offering advice and good spirits whenever the opportunity arose. Frances Hellman has been a patient and supportive teacher and supervisor, a walking library of scientific information, who has subtly but persistently pushed me and nudged me, thus saving me from wrong turns along the way. Herman ten Kate supported me in doing a PhD and has stepped on an airplane more than once so that we could meet in various places in Europe and the United States to discuss the PhD work. Throughout the years he has given lots of constructive advice and criticism and has also contributed by keeping one eye on the big picture and the other one on the lookout for errors in the details and grammar. Arno Godeke has been a constant source of encouragement, positive energy, ambition, and curiosity throughout this PhD research. Following on his own PhD work, his ideas and sense of direction got me started and has guided me on this research.

Contents

Chapter 1

Introduction

1.1 Introduction

Superconducting Nb_3Sn was discovered in 1954 by Matthias *et al.* [1] as the second A15 superconductor, after V_3Si was found by Hardy *et al.* [2]. Since then, Nb_3Sn has sparked a lot of scientific interest for a number of reasons. Before the discovery of the HTS superconductors, Nb_3Sn had one of the highest critical temperatures (18 K), it is relatively easy to form and is stable at low temperatures. Over time, it has become a 'workhorse' superconductor used for applications in superconducting magnets beyond 9 T, such as laboratory magnets for materials research, high field Nuclear Magnetic Resonance (NMR) systems, the International Thermonuclear Experimental Reactor (ITER) fusion research and engineering project, and more recently the High Luminosity Large Hadron Collider (HL-LHC). While a great deal of attention has been paid to the material in terms of processing and practical conductor development, there are still some scientific questions that have not yet been resolved. One question in particular is where the large degree of strain sensitivity in the superconducting properties originates from, the topic at the core of this thesis.

This chapter gives a brief description of the concepts of this thesis and an introduction to the history of superconductivity. Next, various types of Nb_3Sn samples and the application of microscopic theory are discussed. Finally, a number of key questions are formulated whose answers this thesis tries to find.

1.2 Some concepts

Throughout this thesis, a number of terms are used quite often. The following gives a brief description:

- Critical temperature T_c: the temperature at which a superconducting material exhibits a phase transition from the normal to the superconducting state.
- Upper critical (magnetic) field $\mu_0 H_{c2}$: the magnetic field at which a superconducting material reverts from superconducting state at $H < \mu_0 H_{c2}$, to the normal state at $H > \mu_0 H_{c2}$.
- Critical current density J_c: the maximum current density in a superconductor without dissipation. More specifically, the resistivity of the material is zero for current densities below the critical current density and non-zero for current densities above the critical current density.
- A15 crystal structure: the equilibrium crystal structure of Nb_3Sn (figure 1.1). The tin ions are arranged in a bcc crystal structure. The niobium ions form chains on the sides of the unit cell.
- Stoichiometry and off-stoichiometry: with regard to Nb_3Sn, stoichiometry means that there are exactly three niobium ions for every tin ion. Off-stoichiometry means that the ratio is different from three to one (typically due to excess niobium ions). According to Charlesworth *et al.* [3] the relevant A15 Nb-Sn phase occurs between 18 and 26 at.% Sn.
- Disorder: any deviation from the perfectly ordered (i.e. infinitely periodic) stoichiometric crystal structure. Examples of disorder are vacancies, where ions are missing

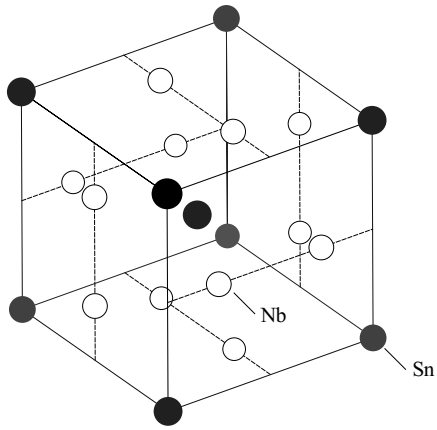

Figure 1.1: *The A15 crystal structure of stoichiometric Nb_3Sn. The Sn ions are arranged in a bcc crystal structure, while the niobium ions are arranged in chains along the sides of the unit cell.*

from the lattice, or anti-site disorder, where an ion of one species occupies the position that is ordinarily occupied by the other atomic species and vice versa.

- Martensitic transformation: highly ordered stoichiometric Nb_3Sn undergoes a cubic to tetragonal transformation when cooled below approximately 43 K. In this thesis, the phenomenon is also referred to as spontaneous tetragonal transformation and cubic instability.

1.3 Brief overview of superconductivity

Superconductivity, a phenomenon that occurs at low temperatures, was not discovered until after the successful liquefaction of helium by Onnes in 1908. Three years later, superconductivity was first observed in mercury by Onnes [4]. At about 4.2 K, the resistivity of the material was shown to disappear. Another important experimental discovery was in 1933, when Meissner *et al.* [5] found that the formation of the superconducting state results in the expulsion of the applied critical magnetic field, a phenomenon nowadays called the Meissner effect.

The first phenomenological model was presented in 1935 by the London brothers [6], describing a superconductor in terms of a two-fluid system and thereby explaining the Meissner effect. A large amount of progress was made in the 1950s. The Ginzburg-Landau theory [7], a phenomenological model that introduced the concept of a superconducting wave-function, was presented. Fröhlich [8] made the suggestion that the superconducting state is made possible by lattice vibrations, which is consistent with the observation of Maxwell [9] in the same year that the critical temperature T_c of conventional superconductors is related to the isotope mass. Pippard introduced the concept of a coherence length [10]. Abrikosov presented a description of type-II superconductors, in which the application of a magnetic

field above the lower critical magnetic field $\mu_0 H_{c1}$ results in the presence of normal zones, so-called fluxlines, in the superconducting bulk [11], until at the upper critical magnetic field $\mu_0 H_{c2}$ superconductivity is completely suppressed. In contrast, type-I superconductors are superconductors in which externally applied magnetic field is completely excluded up to a critical field $\mu_0 H_c$ and superconductivity is completely suppressed above $\mu_0 H_c$. Cooper showed that electrons can form bound pairs, so-called Cooper pairs, if a small net attraction is present. The BCS theory was presented by Bardeen, Cooper, and Schrieffer [12], which incorporates some of the experimental and theoretical progress of the decade into a convincing model of how superconductivity may work.

With the publication of the BCS theory, a qualitative picture of phonon-mediated superconductivity was formed. Electrons form Cooper pairs when a (weak) net attraction between the electrons is present. Under certain conditions (i.e. at low temperature, low magnetic field, and in certain materials), the superconducting state is energetically more favorable than the normal one. In order for electrons to form Cooper pairs, momentum needs to be transferred between them, which is where the phonons (i.e. lattice vibrations) come in. Momentum is transferred indirectly between electrons through virtual phonons (i.e. phonons that only exist temporarily). The lattice vibration temporarily holds the momentum, so that the first electron can already be elsewhere when the second electron picks up the momentum. This implies that the influence of the Coulomb repulsion is significantly reduced. A qualitative picture is one where an electron with negative charge distorts the lattice, resulting in a local positive charge. A second electron then comes in and is attracted to this positive charge, and thus momentum is exchanged between the electrons.

The formation of the superconducting state results in an energy gap in the electron density of states at the Fermi energy. At 0 K, the electron density of states between $E_F \pm \Delta$ is equal to zero, where E_F is the Fermi energy and Δ is the reduction in energy per electron achieved through the formation of the superconducting state. This gap is small relative to the Fermi energy (of the order of 3 meV for stoichiometric Nb_3Sn [13], i.e. about four orders of magnitude below the Fermi energy), but sufficiently large to prevent scattering of the Cooper pairs under most conditions. Excitation of the electron must exceed the binding energy of the Cooper pair in order to break the pair. Thus electrons can pass through the material without scattering, which means that the resistivity of the material is zero when excitations do not surpass this threshold.

After the series of discoveries culminating in the BCS description, the accuracy of the theory continued to improve. Eliashberg formulated a description relating the electron-phonon coupling constant to the phonon density of states [14]. This description is valid beyond the weak coupling limit of the BCS theory. Accurate calculations of T_c were developed by McMillan [15], Allen and Dynes [17], and Kresin [18]. After pointing out that the Ginzburg-Landau description is a limiting case of the BCS theory applicable near T_c in the absence of a magnetic field [19], Gor'kov combined the descriptions by Ginzburg and Landau with the description by Abrikosov to formulate a generalized theory which is known as the GLAG theory. The properties of Josephson junctions, two superconductors that are separated by a weak link, were predicted by Josephson in 1962 [20] and observed by Anderson *et al.* [21] in 1963. This lead to the development of extremely sensitive magnetometers, so-called superconducting quantum interference devices (SQUIDs).

A large number of superconductors were discovered after the initial finding of supercon-

ductivity in mercury, including the discovery of Nb_3Sn in 1954 by Matthias *et al.* [1]. A major breakthrough was the discovery by Bednorz and Müller [22] of high temperature superconductivity in LaBaCuO, a cuprate with a T_c of 35 K. Thereafter, superconductors were separated into 'conventional' superconductors like NbTi and Nb_3Sn and 'unconventional' superconductors like the cuprates. This discovery also triggered a search for more superconductivity in cuprates, leading to the discovery of superconductors with critical temperatures as high as 153 K ($HgBa_2Ca_2Cu_3O_{8+x}$ under high pressure, by Chu *et al.* [23]). More recently, superconductivity was observed in magnesium diboride by Nagamatsu *et al.*[24] and in ferropnictides by Kamihara *et al.* [25] in 2006.

1.4 Nb_3Sn samples

1.4.1 Nb_3Sn wires

Nb_3Sn is a phonon-mediated type-II superconductor. Slightly off-stoichiometric Nb-Sn has a critical temperature of approximately 18 K and an upper critical magnetic field of about 30 T. Comparing its critical temperature to other superconductors with T_c values as high as 165 K, it might seem unusual that this particular material is used as a workhorse superconductor for high field magnet applications. However, it has a combination of properties that makes it the most attractive choice for many high field applications at this time:

- Nb_3Sn wires feature a relatively high critical current density in the order of 3000 Amm^{-2} non-Cu at 12 T and 4.2 K [26].
- Nb_3Sn wires are relatively affordable and commercially readily available.
- The production of Nb_3Sn wires is reliable, with little inhomogeneity along the length, and long piece lengths can be manufactured reproducibly.
- The critical temperature and upper critical magnetic field are approximately two times higher in Nb_3Sn than in the significantly less expensive Nb-Ti, thus the accessible temperature and magnetic field range for applications in magnets is approximately doubled.
- Nb_3Sn can be produced as multi-filamentary wires, which can be bundled into transposed cables. Development of HTS cable and magnet technology is rigorously pursued (see for instance the work on Bi-2212 by Scanlan *et al.* [27], Dietderich *et al.* [28], and Godeke *et al.* [29, 30], and the work on ReBCO by Goldacker *et al.* [31] and Van der Laan *et al.* [32]), but this technology is not yet fully matured.

Nb_3Sn wires consist of filaments in a copper matrix. The Nb_3Sn filaments carry the current, while the highly conductive copper matrix allows for current exchange between the filaments and heat exchange to the environment.

Well-known Nb_3Sn wire production processes are the Bronze process, the Re-stacked Rod Process (RRP^{TM}), and the Powder-in-Tube (PIT) process (figure 1.2). While Nb_3Sn is a brittle material, its separate elements are not. For this reason, wires are formed in a process where the niobium and tin are separated. Once the wire has the desired final shape in a magnet, the Nb_3Sn phase is formed by heat treating the wire at a typical temperature of

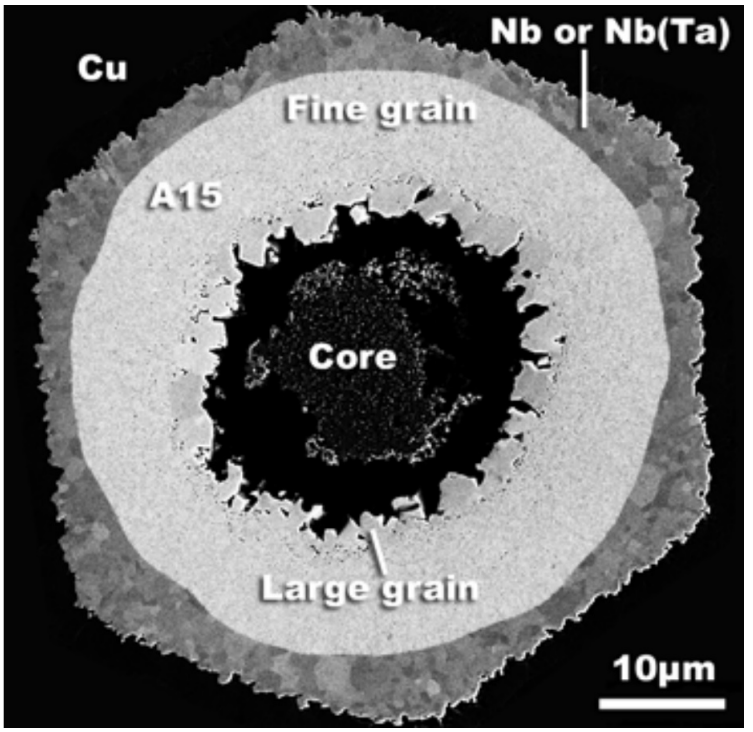

Figure 1.2: *High contrast field emission scanning electron microscopy (FESEM) backscatter micrograph of a typical Shape Metal Innovation Powder-in-tube (SMI-PIT) filaments, after Godeke [33]. The micrograph itself was taken by P. J. Lee.*

about 650 °C depending on the type of wire. During this heat treatment, tin diffuses into the niobium from a tin source, such as the core of the filament in the case of PIT strands or the subelement in the case of RRP strands (where a subelement is a bundle of filaments), or from the bronze surrounding the filaments in the case of the Bronze process.

The solid state diffusion reaction leads to an inhomogeneous composition, with large stoichiometric Nb_3Sn grains near the tin source and fine off-stoichiometric Nb-Sn grains (typically at 23.5 at.% Sn) further away from the tin source. Nb_3Sn also commonly contains additions such as copper, titanium, or tantalum, where copper is used to destabilize the tin-rich compounds Nb_6Sn_5 and $NbSn_2$ while titanium and tantalum additions improve the superconducting properties of Nb_3Sn, as shown by Suenaga *et al.* [34]. Furthermore, the Nb_3Sn filaments are surrounded by reaction barriers, such as pure niobium or tantalum, which prevent tin from diffusing into the copper matrix. Finally, the copper matrix shunts the Nb_3Sn, which means that the normal state resistivity of the wire is dominated by the copper when the material is not superconducting, decreasing the Ohmic heat production in the event that a part of the wire becomes non-superconducting.

In summary, one of the main reasons for investigating Nb_3Sn is its important technological, feasible, and affordable applications. A thorough understanding of the material is com-

plicated since composition and morphology of practical wires make them less suitable for scientific study. For this reason, model samples with carefully controlled compositions and morphologies are required.

1.4.2 Nb_3Sn bulk and thin films model samples

A significant part of this PhD research was spent on evaluating different types of model samples in terms of their suitability for determining the relation between composition and strain sensitivity. The samples considered are bulk samples and thin films. Bulk samples were provided by W. Goldacker of the Karlsruhe Institute of Technology, while thin films were fabricated as part of this research. The samples were characterized to determine their composition, morphology, and low temperature strain state. A technique was developed to evaluate the samples in terms of their strain dependence of the superconducting properties and the normal state properties. This work is mainly discussed in chapter 2, while the measurement results are spread throughout this thesis.

1.5 Microscopic theory

As will be shown, the amount by which strain affects the superconducting properties is dependent on the composition of the Nb-Sn, which means that any model that can describe the strain sensitivity of Nb-Sn should also consider how disorder affects the superconducting properties. To that end, chapter 4 includes a detailed review of microscopic theory, which is combined into a model that calculates how disorder affects the superconducting properties. The model combines verifiable hypotheses with ab-initio calculations. In chapter 5, this model is used to calculate the superconducting and normal state properties of Nb_3Sn, and the results of the calculation are compared to experimental observations.

1.6 Scope of this thesis

A number of key questions will be addressed in this dissertation:

How is critical current density affected by temperature, magnetic field, and strain in the case of stoichiometric and off-stoichiometric Nb-Sn?

The effect of temperature, magnetic field, and uni-axial strain (i.e. strain along the length of the conductor) on the superconducting properties of Nb_3Sn has been studied extensively in the past, with an emphasis on slightly off-stoichiometric Nb_3Sn conductors. In chapter 3, the descriptions in literature are reviewed and differences and similarities are discussed. Next, the effect of strain on the critical current density of stoichiometric and off-stoichiometric binary thin films is evaluated for both longitudinal and transverse strain. The observed strain dependence of J_c is compared to the strain dependence observed in resistivity measurements and to comparable data of Nb_3Sn wires.

How does disorder affect the critical temperature and the upper critical field of Nb-Sn?

The critical temperature and upper critical field of Nb-Sn are strongly affected by composition. Measurements were performed on Nb-Sn bulk samples and thin films with various compositions and the data are compared to literature results in chapters 2 and 3. In chapter 4, a model is presented which relates the critical temperature and the upper critical field to the amount of disorder in the material. This model combines ab-initio calculations with verifiable hypotheses, and the calculated results are compared to experimental observations.

How is the strain dependence of T_c and $\mu_0 H_{c2}$ affected by disorder?

In chapters 2 and 3, the strain dependence of the superconducting properties of bulk and thin film samples with various compositions is evaluated. The strain dependence is compared to the strain dependence observed in Nb_3Sn wires in chapter 3. In chapter 5, a model is presented which is used to calculate the strain dependence of the superconducting properties at various degrees of disorder. Once again, the model combines verifiable hypotheses with ab-initio calculations, and the calculated and measured strain dependencies are compared.

How does strain affect the normal state resistivity of Nb_3Sn?

It is observed that the application of strain results in an anisotropic change in the normal state resistivity, i.e. a change in the normal state resistivity that depends on the orientation of the current relative to the strain. Measurements of the effect of strain on the anisotropic normal state resistivity are presented in chapter 2. Ab-initio calculations are used to calculate the effect of strain on the anisotropic normal state resistivity in chapter 5. The calculated results are compared to experimental observations.

Does strain affect the superconducting properties of Nb_3Sn through changes in the electronic properties, the vibrational properties, or both?

There is a controversy in literature about whether strain affects the superconducting properties of Nb_3Sn through changes in the electronic properties, the vibrational properties, or a combination of the two. A review of the available literature is presented in chapter 5. The effect of strain on the electronic and vibrational properties of the crystal is determined through ab-initio calculations, and their relative influence on the superconducting properties is evaluated in chapter 5.

Why is the degree of strain sensitivity of the superconducting properties of A15 Nb_3Sn and Nb_3Al much larger than the strain sensitivity of the superconducting properties of bcc Nb and NbTi?

In chapter 2, the strain sensitivity of A15 Nb-Sn is shown to be large in comparison to that of bcc Nb. In chapter 5, the difference between these two materials, as well as Nb_3Al and NbTi is discussed to illustrate the underlying origin of the large strain sensitivity in Nb_3Sn.

Chapter 2

Experimental Aspects

2.1 Introduction

As part of this research, an extensive experimental investigation of well-characterized Nb-Sn samples was pursued. This experimental work involves fabrication and characterization of different types of samples as well as experiments for determining the strain sensitive superconducting and normal state properties. The effect of strain on the normal state resistivity, the critical temperature, and the upper critical field are investigated.

Two different types of samples are used: bulk samples and thin films. The bulk samples (provided by the Karlsruhe Institute of Technology) were fabricated with a hot isostatic pressure process, while the thin films were fabricated through simultaneous magnetron sputtering onto a heated substrate. While most of the samples consist of A15 Nb-Sn, a bcc niobium thin film sample was fabricated and investigated as well.

The samples were characterized using a variety of techniques, including Scanning Electron Microscopy - X-ray Energy Dispersive Spectroscopy (SEM-XEDS), Rutherford Backscattering Spectrometry (RBS), heat capacity measurements, Scanning Transmission Electron Microscopy (STEM), and X-Ray Diffraction (XRD). The various characterization techniques point to the conclusion that the bulk samples without copper additions which were investigated as part of this research contain nearly stoichiometric Nb_3Sn and Nb regardless of the nominal composition. Bulk samples with copper addition contain both a stoichiometric and an off-stoichiometric phase. Section 2.2 on Nb_3Sn bulk therefore largely focuses on characterizing the composition distribution of these samples.

The thin films, while not perfectly homogeneous, all have the desired single A15 phase (which can be either stoichiometric or off-stoichiometric), and are much more homogeneous than the bulk samples. Section 2.3 focuses on the three-dimensional strain state, morphology, and crystal orientation of these thin films.

The main experiment discussed here is the U-spring test rig (section 2.4), which allows for resistivity and critical current measurements as a function of temperature, magnetic field, and applied strain. From these measurements, various properties can be derived, including the effect of strain on the normal state resistivity ρ_n, the critical temperature T_c and the upper critical field $\mu_0 H_{c2}(0)$.

2.2 Bulk samples

In addition to the work that is presented here, the bulk samples were previously investigated by others, including X-ray diffraction measurements by Goldacker *et al.* [35] and Guritanu *et al.* [36], vibrating sample magnetometry by Goldacker *et al.* [35], and point-contact spectroscopy by Marz *et al.* [37].

2.2.1 Fabrication

A hot isostatic pressure technique was used to produce the bulk samples. In this process, powders are mixed, placed in a stainless steel container, and subsequently reacted at 1100 °C and 100 MPa for a duration of 24 hours. The end results are densely compacted blocks of Nb-Sn (figure 2.1, left).

In addition to binary samples with a variety of nominal composition ratios, a series of sam-

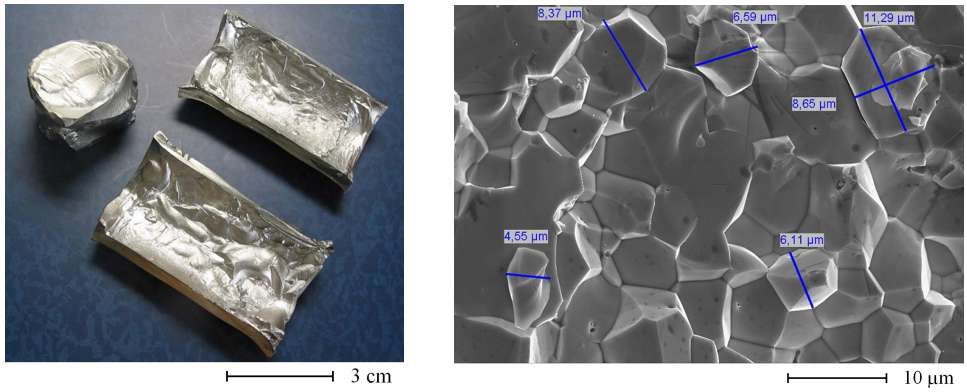

Figure 2.1: *Left: Nb-Sn bulk samples, provided by W. Goldacker at the Karlsruhe Institute of Technology. Right: SEM image of a binary bulk sample with 24.8 at.% Sn nominal composition, after Goldacker et al. [35].*

ples was made with copper, titanium and tantalum additions, as additions are also used in practical Nb_3Sn wires. Electrical discharge machining (EDM) was used to cut the bulk material into a shape that fits on the U-spring sample holder.

2.2.2 Morphology

The bulk samples are polycrystalline, with densely packed grains (figure 2.1, right). The typical grain diameter is 3 to 20 μm and the crystal orientation is random [35].

2.2.3 Critical temperature distribution from heat capacity measurements

Heat capacity measurements as a function of temperature and magnetic field were performed in order to determine the critical temperature distribution of the bulk samples, an effort which was undertaken by M. Susner of the Ohio State University.

In this technique, which is based on a method developed by Wang *et al.* [38], the critical temperature distribution is obtained by comparing the heat capacities in superconducting and normal state, where the normal state is enforced through the application of a magnetic field. A detailed discussion on the measurement technique and the derivation of the critical temperature distribution is found elsewhere [39].

The observed T_c distributions indicate that the composition of the bulk samples is inhomogeneous. As shown in figure 2.2, top, all samples contain Nb-Sn with a T_c of about 17.5 K, regardless of the nominal content of the bulk sample. This critical temperature is indicative of the presence of slightly disordered nearly-stoichiometric Nb-Sn [41, 42], while excess niobium is concentrated in regions of pure (oxidized) niobium (figure 2.3). It is interesting that no peak is observed around 9 K (the critical temperature of low-resistivity bcc niobium), which implies that either the niobium is strongly disordered so that T_c is suppressed (for instance through oxidation), or that it is in a different crystal symmetry with lower T_c such as

Nb_3Nb, also previously discussed by Flükiger [40].

The samples with copper addition contain two distinct T_c distributions, with a higher T_c fraction close to 17.5 K indicating the presence of stoichiometric Nb_3Sn and a lower T_c fraction corresponding to the presence of off-stoichiometric Nb-Sn. These observations are discussed in detail elsewhere [39].

2.2.4 Composition distribution from Scanning Electron Microscopy X-ray Energy Dispersive Spectroscopy (SEM-XEDS)

Uncalibrated SEM-XEDS was used to determine the composition of both the bulk and the thin film samples. The accuracy of this method is estimated from a comparison with literature results. Consistent with a previous observation by Rudman *et al.* [43], it was observed that a tin-rich region in a thin film deposited at 700 °C consists of Nb_6Sn_5 and of $Nb_{1-\beta}Sn_\beta$ with $\beta = 0.254$ (figure 2.4). Charlesworth *et al.* [3] estimated the maximum atomic tin content in Nb_3Sn to be $26\pm1\%$, while Rudman *et al.* [43] argued that it is $25\pm1\%$, based on microprobe and Rutherford Backscattering Spectrometry (RBS) measurements. An uncertainty of 1 at.% Sn is expected in the uncalibrated SEM-XEDS used here.

For a selected group of samples, the composition distributions were investigated with SEM-XEDS. The composition of 900 different spots within a 60×80 μm^2 area and the variation in the local Sn contents were measured. A detailed description of the method is found elsewhere [44].

All the bulk samples contain a nearly-stoichiometric Nb_3Sn phase that peaks at 25.5 at.% Sn (figure 2.2, bottom). The samples with copper additions contain both a nearly stoichiometric phase and an off-stoichiometric phase. Note that, although the SEM-XEDS data indicates that the (80 at.% Nb + 20 at.% Sn) + 5 wt.% Cu sample does not have a nearly stoichiometric phase, the onset of superconducting behavior at 18 K clearly illustrates that a nearly stoichiometric phase must be present, as Nb_3Sn with a T_c of 18 K is necessarily (very close to) stoichiometric, see Godeke *et al.* [41]. This is an example of macroscopic inhomogeneity: the sample is inhomogeneous on a length scale larger than the single probe region of 80×60 μm^2. In a similar fashion, regions of pure niobium-oxide were observed in all samples, but not in every investigated region of 80×60 μm^2.

As shown in figure 2.3, the samples with tantalum and titanium additions consist of Nb_3Sn but includes regions with pure tantalum, titanium oxide and niobium oxide, with a typical size of 100 - 200 μm^2. Oxygen is observed in all SEM-XEDS investigations, but it is unclear to what extent oxygen is present in the bulk of the samples. After heat treatment, the samples are cut with an Electrical Discharge Machining (EDM) process and polished, which may well introduce oxygen in the surface of samples. For this reason, the 'intrinsic' oxygen content immediately after reaction is not known and the observed oxygen content is omitted from figure 2.2, bottom, and figure 2.3.

One could speculate that the peculiar two-phase T_c distribution in the samples with copper addition is a result of the preferential formation of off-stoichiometric Nb-Sn in the presence of copper and stoichiometric Nb_3Sn in its absence. The addition of copper to the bulk samples results in the presence of the off-stoichiometric phases as evidenced by the presence and absence of off-stoichiometric Nb-Sn in the samples with and without copper respectively (figure 2.2). Furthermore, it is not a great leap to assume that binary regions, i.e. regions

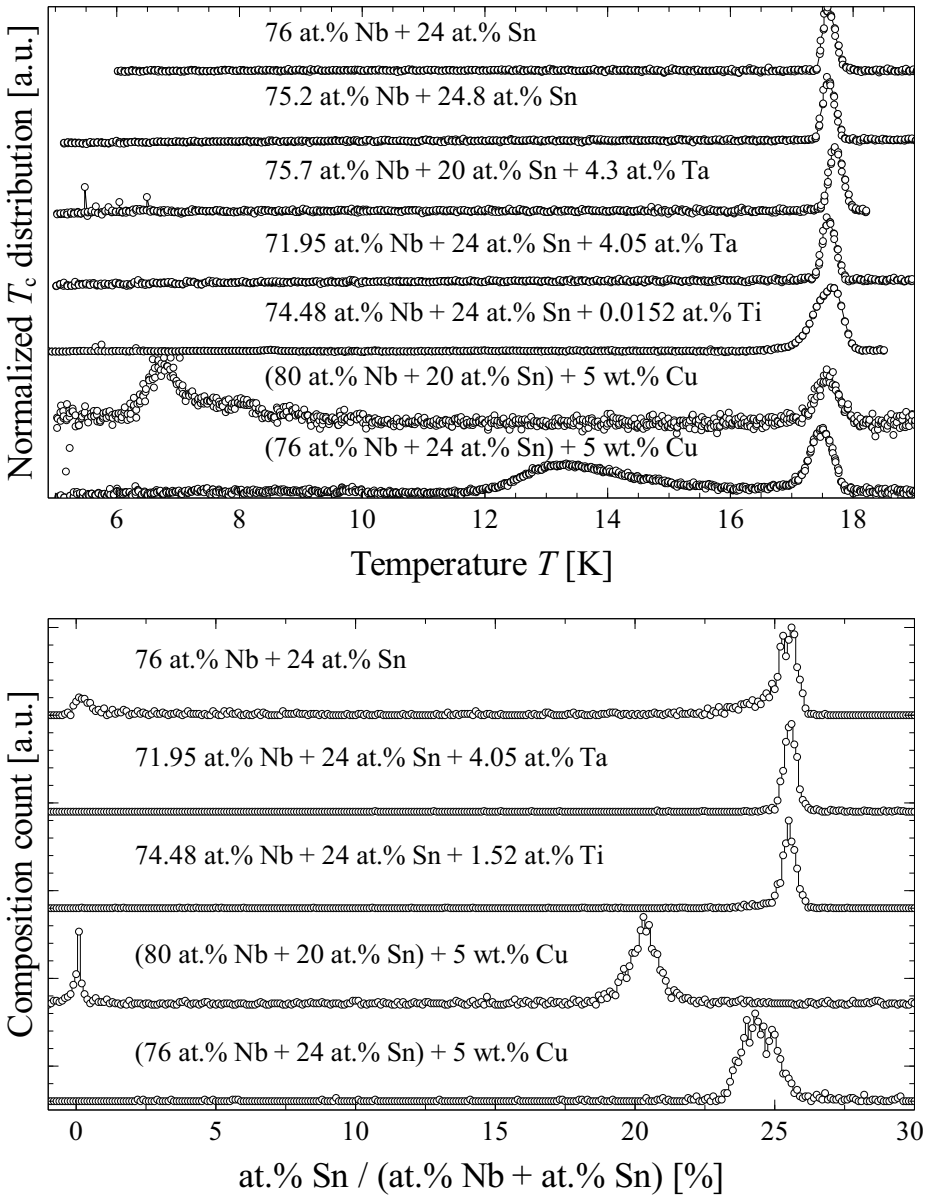

Figure 2.2: *Critical temperature distributions of bulk Nb-Sn samples derived from heat capacity measurements (top) and composition distributions derived from SEM-XEDS measurements (bottom). The nominal compositions of the bulk samples are indicated above each measurement.*

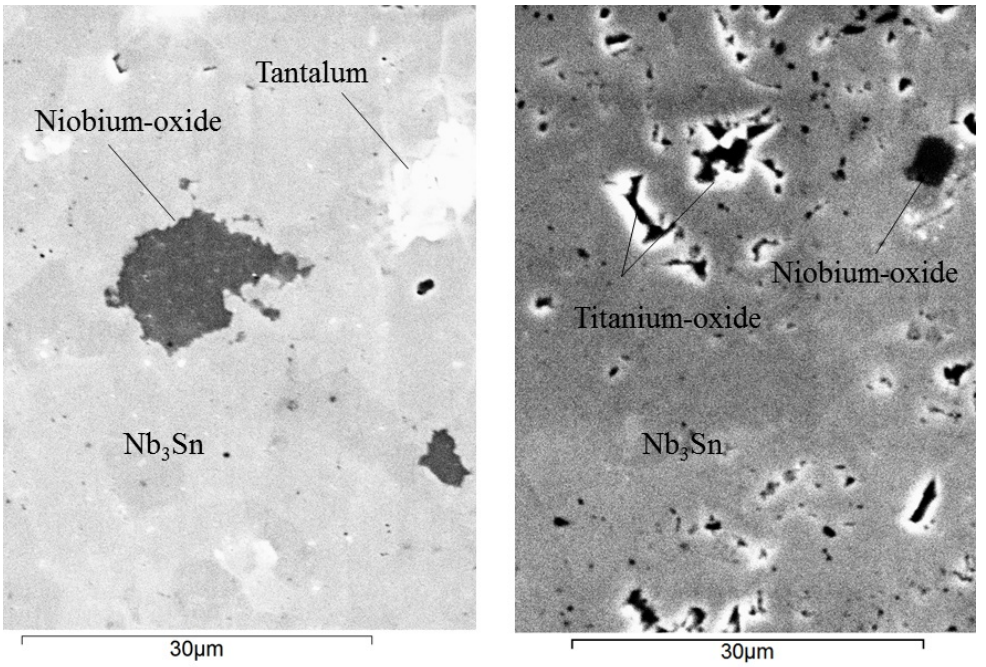

Figure 2.3: *SEM images of bulk samples with nominal compositions: 71.95 at.% Nb + 24 at.% Sn + 4.05 at.% Ta (left) and 74.48 at.% Nb + 24 at.% Sn + 1.52 at.% Ti (right).*

without copper additions, contain the same composition distribution as binary samples, i.e. they contain stoichiometric Nb_3Sn but no off-stoichiometric Nb-Sn.

Extending the speculation even further, two possible arguments could explain how the presence of copper results in the formation of off-stoichiometric Nb-Sn. Firstly, during the reaction the tin reacts with the copper to form bronze, and the bronze may react with niobium to form off-stoichiometric Nb-Sn, while the pure tin reacts with niobium to form stoichiometric Nb_3Sn. The path by which the Nb-Sn is formed matters if the formation of off-stoichiometric and stoichiometric Nb-Sn is energetically equally favorable, or if the reaction temperature is too low to achieve the energetically most favorable composition. Secondly, it is possible that copper reacts with oxygen which would otherwise react with niobium and form Nb-O. It is argued elsewhere [45] that in Nb-Sn thin film depositions it is energetically favorable to form Nb-O and stoichiometric Nb_3Sn rather than off-stoichiometric Nb-Sn, so that the oxygen content needs to be kept at a minimum to form off-stoichiometric Nb-Sn. While the first explanation is more likely to be the correct one, both mechanisms may explain how the presence of copper results in the formation of off-stoichiometric Nb-Sn, but proving the validity of either of these mechanisms is outside the scope of this thesis.

Note that a similar two-phase T_c distribution was also observed in Powder-In-Tube Nb_3Sn wires by Senatore *et al.* [46], where the two-phase distribution was attributed to the different properties of large grains near the core of the filaments and fine grains further away from the

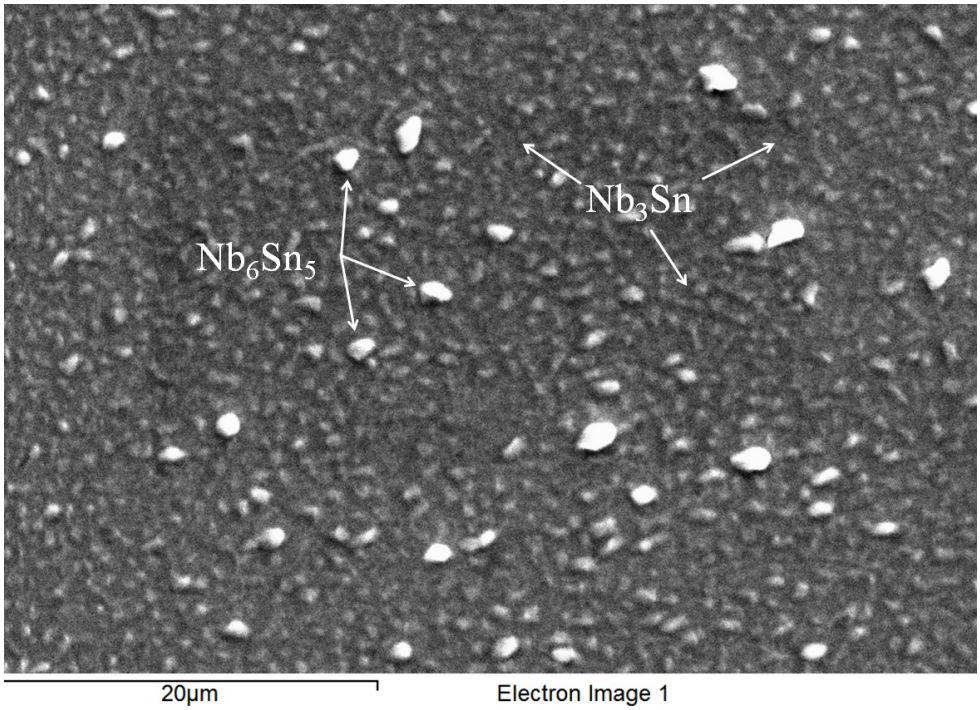

Figure 2.4: *A two-phase separation into Nb_6Sn_5 and $Nb_{1-\beta}Sn_\beta$ with β = 0.254±0.002 is observed in tin-rich regions, which is consistent with previous observations by Rudman et al. [43]. Image taken from deposition 2-14-11, which was deposited at 700 °C.*

core.

Based on the relation between local titanium, tantalum, niobium, and tin concentration, it was concluded that titanium preferentially replaces tin and tantalum preferentially replaces niobium in the A15 crystal structure. A detailed description of the experimental method leading to this conclusion can be found elsewhere [44].

2.2.5 Variable magnetic field T_c distribution measurement

In order to determine the range of $\mu_0 H_{c2}(0)$ values present in the binary bulk sample with 24 at.% Sn, T_c distributions were obtained from variable magnetic field heat capacity measurements. Figure 2.5, top, shows the critical temperature distribution normalized to the peak value. It is clear that the T_c range becomes increasingly wide with increasing magnetic field, a clear indication that the sample contains a continuous $\mu_0 H_{c2}$ range rather than a single upper critical field $\mu_0 H_{c2}$. An approximate magnetic field dependent T_c range is determined through a 10 % criterion (figure 2.5, top). At every magnetic field, a low and high critical temperature limit $T_{c,low}$ and $T_{c,high}$ are determined. In figure 2.5, bottom, the $\mu_0 H_{c2}$ range is plotted as a function of temperature.

The magnetic field dependence of the upper and lower limit of the T_c range of Nb-Sn is

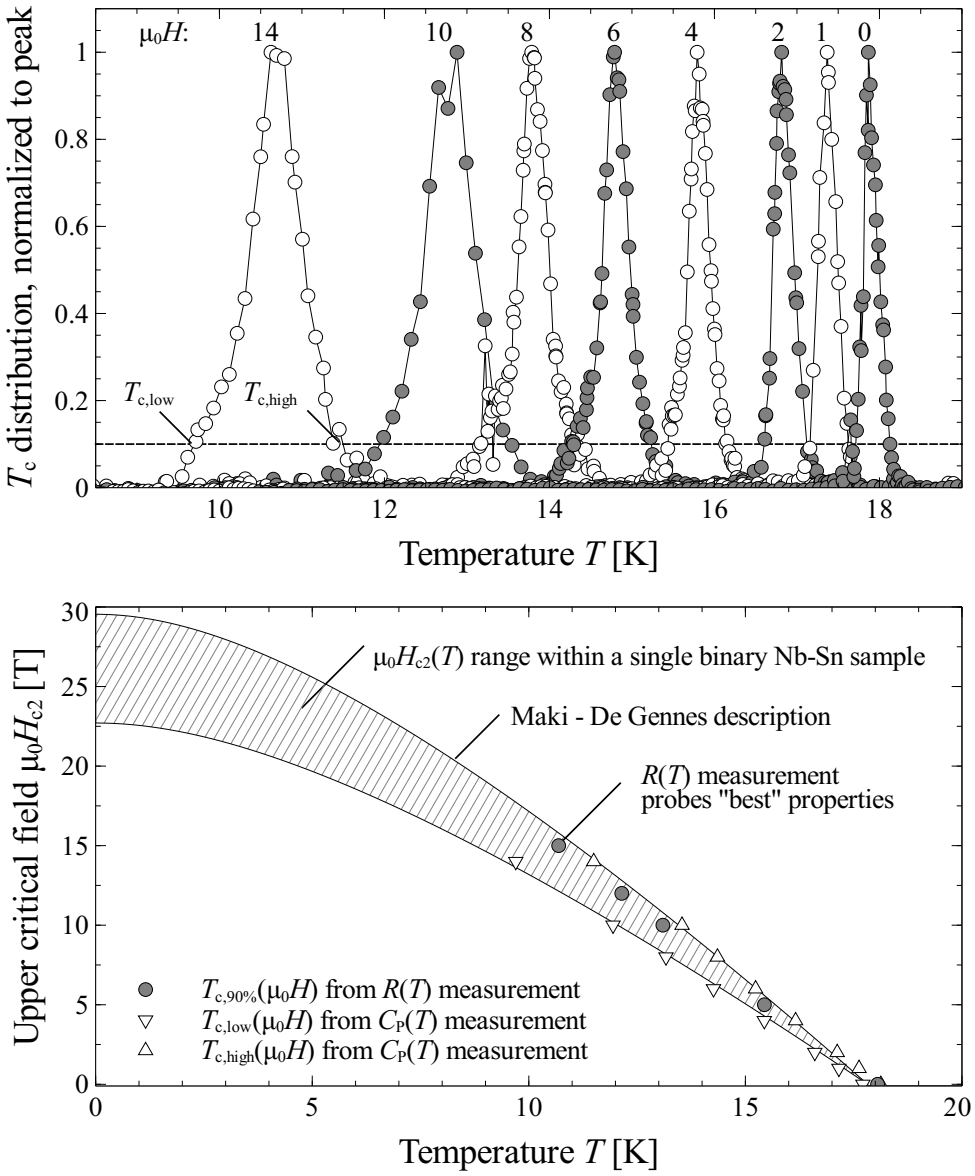

Figure 2.5: *Magnetic field dependent T_c distribution (top) and the corresponding $\mu_0 H_{c2}$ range as a function of temperature (bottom) of the (nominally 24 at.% Sn + 76 at.% Nb) binary bulk sample. The bottom figure gives a comparison between heat capacity (C_P) measurements which illustrate the $\mu_0 H_{c2}$ range of the sample, and resistivity measurements, which only probe the 'best' properties of the sample.*

described with the Maki-DeGennes (MDG) relation [47, 48]:

$$\ln\left(\frac{T}{T_{\mathrm{c}}(0)}\right) = \psi\left(\frac{1}{2}\right) - \psi\left(\frac{1}{2} + \left[\frac{1.764}{4\pi}\right]\frac{T_{\mathrm{c}}(0)}{T}\frac{H_{\mathrm{c2}}(T)}{H_{\mathrm{c2}}(0)}\right), \tag{2.1}$$

where ψ is the digamma function, T is the temperature in [K], T_{c} is the critical temperature at 0 T in [K], $\mu_0 H_{\mathrm{c2}}(T)$ is the upper critical field at temperature T, and $\mu_0 H_{\mathrm{c2}}(0)$ is the upper critical field at 0 K. It was shown by Godeke *et al.* [48] that this relation accurately describes the temperature dependence of $\mu_0 H_{\mathrm{c2}}$ of Nb-Sn with various compositions, and the underlying assumptions of this description will be discussed further in section 4.8.

Applying the MDG relation to the magnetic field dependent critical temperature, it follows that $\mu_0 H_{\mathrm{c2}}(0)$ ranges from 22.7 to 29.4 T within the single binary bulk sample. Near stoichiometry, T_{c} is weakly dependent on composition, while the upper critical field $\mu_0 H_{\mathrm{c2}}(0)$ varies strongly with composition. If we assume that the composition range of the sample is 24.5 to 25 at.%, then one would expect a T_{c} range of 17.5 to 18 K and a $\mu_0 H_{\mathrm{c2}}(0)$ range of 20 to 31 T, which is roughly consistent with the resistively determined $T_{\mathrm{c}}(\mu_0 \mathrm{H})$ dependence (see [49]) and the results of the heat capacity analysis (figure 2.5, bottom).

2.2.6 Conclusion

An investigation was performed of binary Nb-Sn bulk samples and bulk samples with titanium, tantalum, and copper additions which were manufactured with a hot isostatic pressure technique.

Using SEM-XEDS and heat capacity measurements, it was determined that the investigated binary samples consist of regions of (nearly) stoichiometric Nb_3Sn and regions of niobium (-oxide), regardless of the total niobium to tin atomic ratio of the sample. Based on magnetic field dependent T_{c} distribution measurements, the binary samples consist of a sharp T_{c} distribution within a temperature range of 17.4 to 18.0 K and an upper critical field range of 22.7 to 29.4 T.

Similar to the binary samples, the samples with titanium and tantalum additions consist of mainly stoichiometric Nb_3Sn, but also comprise regions of pure niobium, tantalum and titanium. The samples with copper additions are found to contain both stoichiometric and off-stoichiometric Nb-Sn.

2.3 Thin films

Once it became clear that achieving compositional control through the bulk sample route is problematic, an alternative sample fabrication route was pursued. Binary thin film samples were fabricated by simultaneously magnetron sputtering niobium and tin onto a heated sapphire substrate. In this section the fabrication process, the composition analysis, the morphology, the crystal orientation, and the room temperature strain state of the films are discussed, as well as a patterning process.

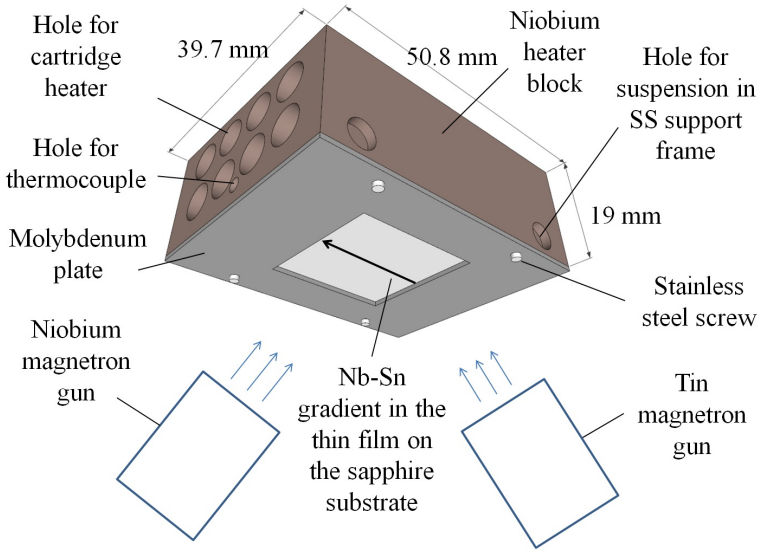

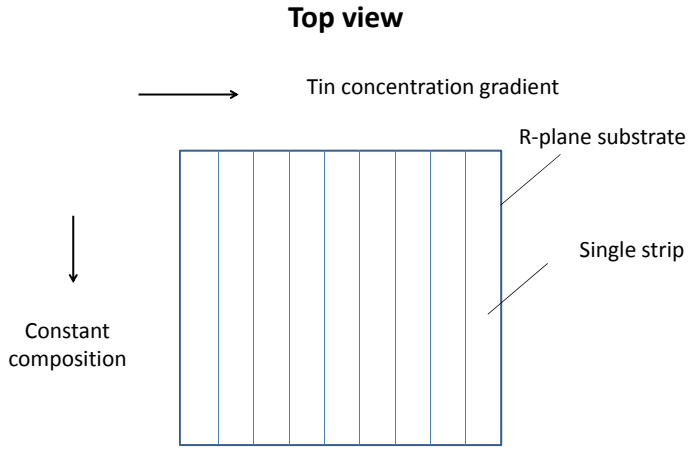

Figure 2.6: *Top: schematic view of the simultaneous niobium and tin magnetron deposition onto a heated sapphire substrate, resulting in a Nb-Sn gradient in the thin film that is deposited onto the sapphire substrate. Bottom: The R-plane substrate is cut into strips, so that each strip has a different composition but the composition is close to constant along the length of the strip, as demonstrated in figure 2.7.*

2.3.1 Fabrication

To heat sapphire substrates, a heater assembly was designed and used, see figure 2.6, top. The assembly consists of cartridge heaters inserted into the niobium block. A K-type thermocouple was inserted in a small hole in the niobium block, and a PID controller was used in combination with a power supply to regulate the temperature of the niobium block (figure 2.6, top).

25.4 mm $\times$ 25.4 mm $\times$ 0.075 mm sapphire substrates with $(1\bar{1}02)$ orientation (i.e. R-plane) were used. The substrates were cleaned in a three-step process, using an ultrasonic bath. The substrate was cleaned using acetone, iso-propanol, and electronic grade iso-propanol, respectively. After each step, the solvent was blown off with nitrogen gas.

Silver paint was applied to improve thermal contact between the substrate and the heater during growth. A molybdenum plate helps to fix the substrate to the heater, while the molybdenum plate was held in place with stainless steel screws. The heater assembly was supported by a stainless steel frame. Heat shields were added to reduce power consumption. This heater assembly is comparatively cheap to construct, easy to service, and durable. Temperatures up to 1000 °C were repeatedly maintained in periods up to a week using 300 W heater power. A cryo-pump maintained the vacuum, resulting in a typical base pressure of 1×10^{-6} Pa when the heater assembly is at room temperature. The base pressure was typically about 2×10^{-5} Pa when the heater assembly is heated to 1000 °C. During the deposition, 99.9998% pure argon gas continuously flowed through the chamber at a regulated pressure of 0.27 Pa and a typical flow rate of 80 cm^3min^{-1}. The niobium and tin targets were typically powered at 250 W (355 V) and 40 W (570 V), respectively, resulting in a combined deposition rate of 0.32 nm/s upon the substrate.

The placement of niobium and tin targets relative to the substrate was chosen such that the tin concentration as a function of position varies along one direction of the substrate, while it is approximately constant along the other direction (figure 2.6, bottom). The correct placement of the targets was confirmed with SEM-XEDS measurements (figure 2.7). By cutting strips perpendicular to the tin concentration gradient, 10 to 20 strips with different compositions could be produced in a single deposition.

2.3.2 Deposition parameters

Table 2.1 shows the key parameters of five selected depositions. The depositions were performed at 700 and 900 °C. The thermal contact between the heater and the substrate was verified by visually comparing the heater and substrate color during the deposition. In some depositions it was observed that the substrate had a darker color than the heater during the deposition. For these depositions, the substrate temperature is estimated by the color of the substrate, using the heater color as a calibration. The uncertainty in the substrate temperature is estimated at 50 °C.

The thickness of the thin films, detailed in table 2.1 was determined through a variety of methods. The thickness of depositions 9-14-10 and 2-14-11 were determined through profilometry on a thin film where material was selectively removed with an etching process. The thickness of deposition 3-17-11 was determined with a Scanning Transmission Electron Microscope (STEM) (figure 2.9). The thickness of depositions 2-17-11 and 8-22-11 were determined by observing the side of a fractured sample with a SEM microscope at lo-

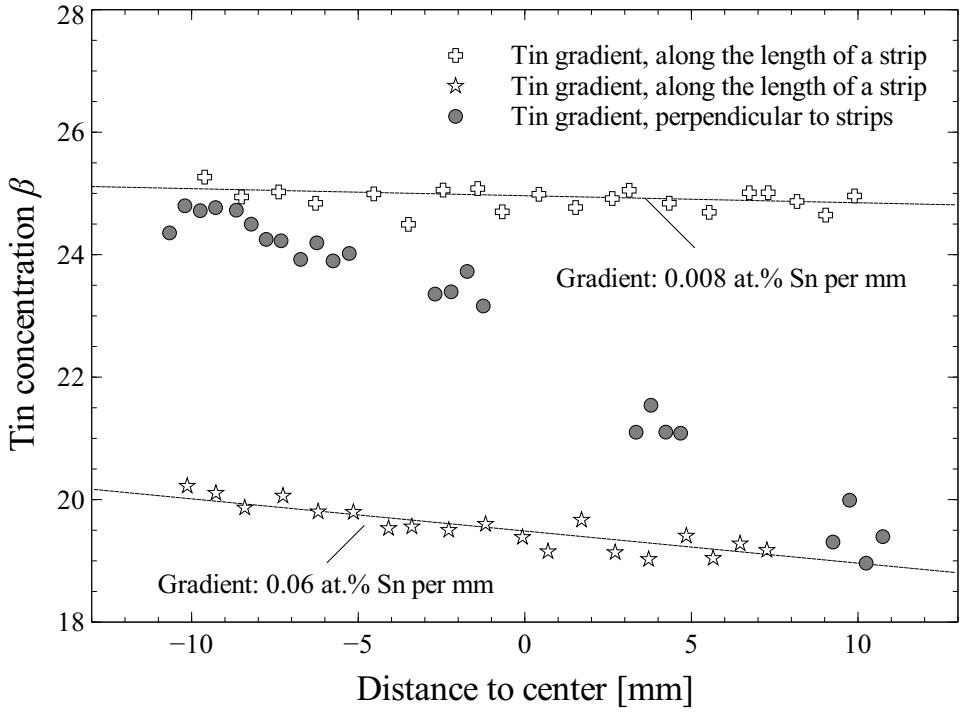

Figure 2.7: *Local tin content β (at.% Sn / [at.% Nb + at.% Sn]) as a function of position on deposition 8-22-11, measured with SEM-XEDS. The grey data points are measurements along the direction that is transverse to the direction in which the strips were cut, while the open data points are measurements along the length of the strips.*

cations corresponding to stoichiometric and off-stoichiometric compositions. The thickness of depositions 3-17-11 and 8-22-11 were also determined by a method by which material is selectively removed with a focused ion beam and the substrate is observed at an angle. The results of the various techniques are consistent within an uncertainty of 2% and within this uncertainty, the thickness is determined to be independent on composition. The STEM and some of the SEM micrographs were taken by J. Bonevich of the National Institute of Standards and Technology (NIST).

2.3.3 Morphology

The morphology of the samples was investigated with SEM and STEM. Figure 2.8, top, shows a surface image of deposition 3-17-11. From the image, it is clear that the films are polycrystalline with an average grain surface area of 0.10 μm^2, corresponding to a grain diameter of 0.31 μm. Grains with sizes ranging from 0.1 to 0.7 μm are observed. Figure 2.8, bottom, shows a surface image of deposition 8-22-11. Similar to deposition 3-17-11, the film is polycrystalline. However, the average grain surface area is 0.046 μm^2, corresponding to a grain diameter of 0.22 μm, and the observed grain diameters range between 0.1 and 0.4

Table 2.1: *Deposition parameters and geometry.*

Deposition date	Temperature [°C]	Deposition duration [min]	Thickness [μm]	Base pressure [10^{-5}Pa]
9-14-10	900	60	0.23	4.5
2-14-11	700	120	1.68	0.5
2-17-11	700	120	1.89	1.3
3-17-11	900	120	2.33	1.6
8-22-11	700	120	2.28	1.0

μm, i.e. notably smaller than the grains of deposition 3-17-11.

The grain diameter of the binary thin films is significantly smaller than the grain diameter observed in the bulk samples, but is comparable to the grain diameters found in some Nb_3Sn conductors. In an evaluation of Bronze process Nb_3Sn conductors and a powder-in-tube Nb_3Sn conductor that were reacted at varying temperatures by Godeke *et al.* [26], it was observed that the grain diameters vary between 0.18 and 1.5 μm at 700 °C and increase by a factor 2 to 4 between 700 °C and 900 °C. As with these conductors, a likely cause of the difference in grain diameters between depositions 3-17-11 and 8-22-11 is the different deposition temperatures of 900 and 700 °C, respectively (table 2.1).

Figure 2.9 shows a cross-sectional image of deposition 3-17-11 made with a STEM with a high angle annular dark field (HAADF) detector. From the figure, it is clear that the film consists of dense columnar grains. The thickness of the film is 2.31 μm with a surface roughness of 0.04 μm.

2.3.4 Composition determination from SEM-XEDS

As with the bulk samples, SEM-XEDS was used to determine the compositions of the thin films. During the deposition, the substrates were aligned in such a way that the composition gradient is oriented perpendicular to the direction in which the strips were cut, resulting in a homogeneous composition along the length of the strips (figure 2.6).

An evaluation of the composition gradient along the lengths of the strips shows that this approach is successful: the composition gradient along a stoichiometric strip was found to be 0.008 at.% Sn per mm, while the composition gradient along an off-stoichiometric strip was 0.06 at.% Sn per mm. The difference in gradient is likely a result of slightly different alignment of the strips relative to the niobium and tin targets. The voltage taps are typically spaced 5 mm apart, so that this worst-case gradient leads to a composition variation of 0.3 at.% between the voltage taps.

2.3.5 Rutherford Backscattering spectrometry (RBS)

Rutherford Backscattering Spectrometry (RBS) measurements were performed on two samples. In an evaluation of a strip from deposition 3-17-11, the composition was determined to be 22 ± 1 at.% Sn with RBS, while the SEM-XEDS investigation of the same strip indicated

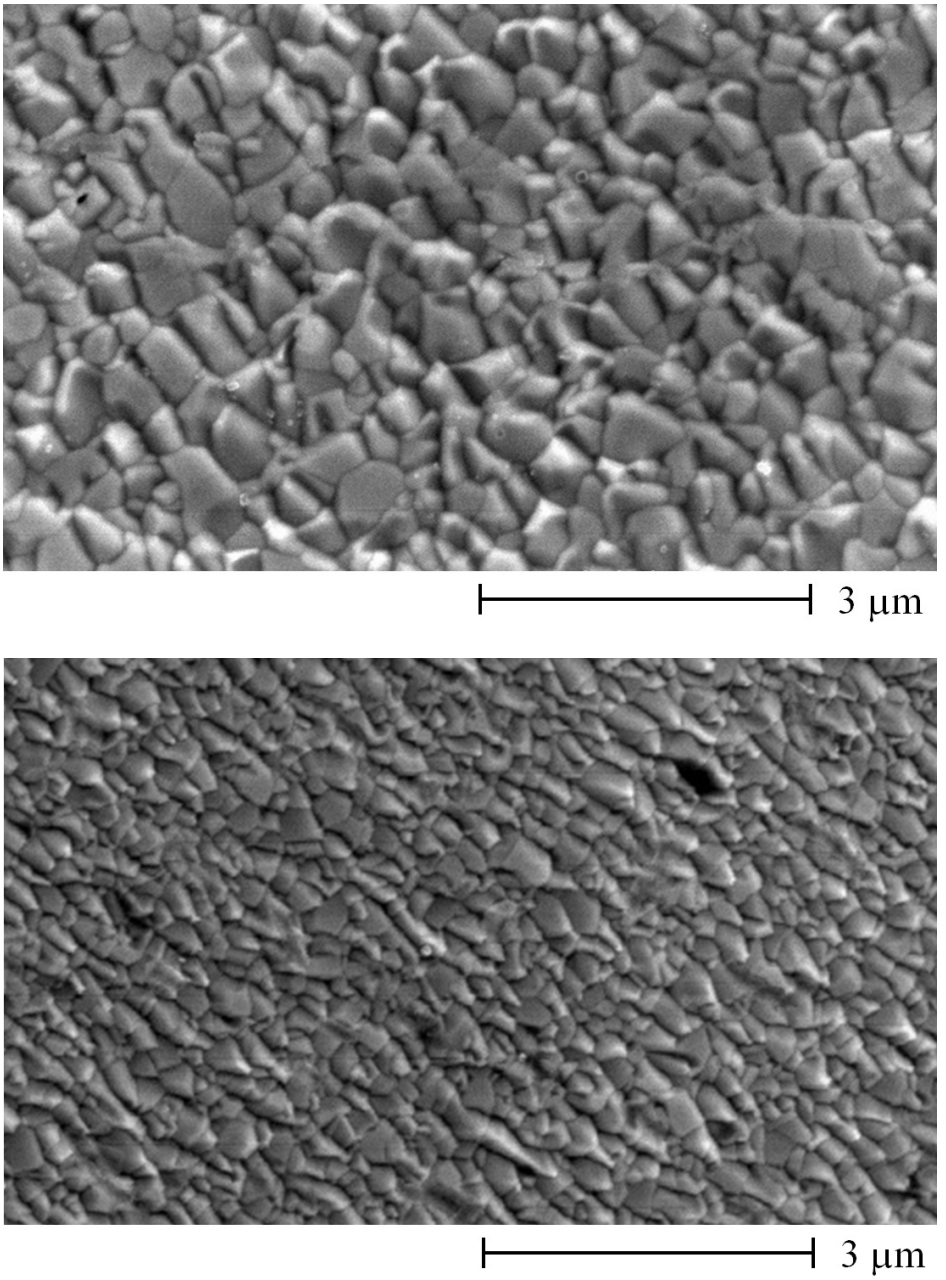

Figure 2.8: *Surface image of depositions 3-17-11 (top) and 8-22-11 (bottom), taken with Scanning Electron Microscope. Courtesy of J. Bonevich of the National Institute of Standards and Technology (NIST).*

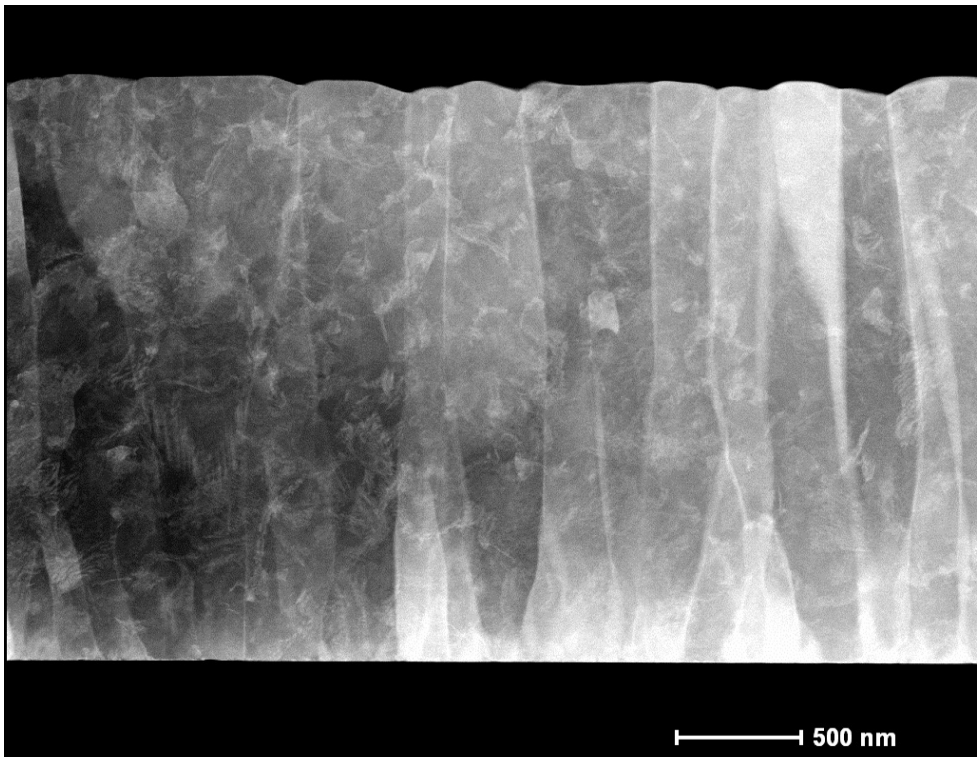

Figure 2.9: *Cross-sectional Scanning Transmission Electron Microscopy (STEM) image of deposition 3-17-11. Courtesy of J. Bonevich of NIST.*

a composition of 21.6 $\pm$ 0.5 at.% Sn. The results are thus consistent. Furthermore, the RBS analysis showed that the top 20 $\pm$ 10 nm of the thin film was oxidized while no oxygen was detected underneath this top layer.

An RBS measurement was also performed of deposition 9-14-10 (table 2.1). Here it should be noted that the limited thickness of this particular deposition (about 230 nm) makes the SEM-XEDS probing method difficult, so that the RBS measurement is the main composition probe. As in deposition 3-17-11, oxygen was detected in the top surface but not underneath. The thickness of the oxidized surface layer is 13 $\pm$ 3 nm.

2.3.6 In-plane and out-of-plane crystal orientations

For each of the depositions, the out-of-plane crystal orientation was determined with a 2-theta X-ray diffractometer, and the in-plane orientation of deposition 8-22-11 was determined with a 4-circle X-ray diffractometer.

In all thin films, the dominant peak in the out-of-plane orientation is the (200) peak, which indicates that the thin films are mainly oriented (100) out-of-plane. In addition to the (200) peak, weaker (210) and (211) reflections are observed in the spectra (figure 2.10). The ratio

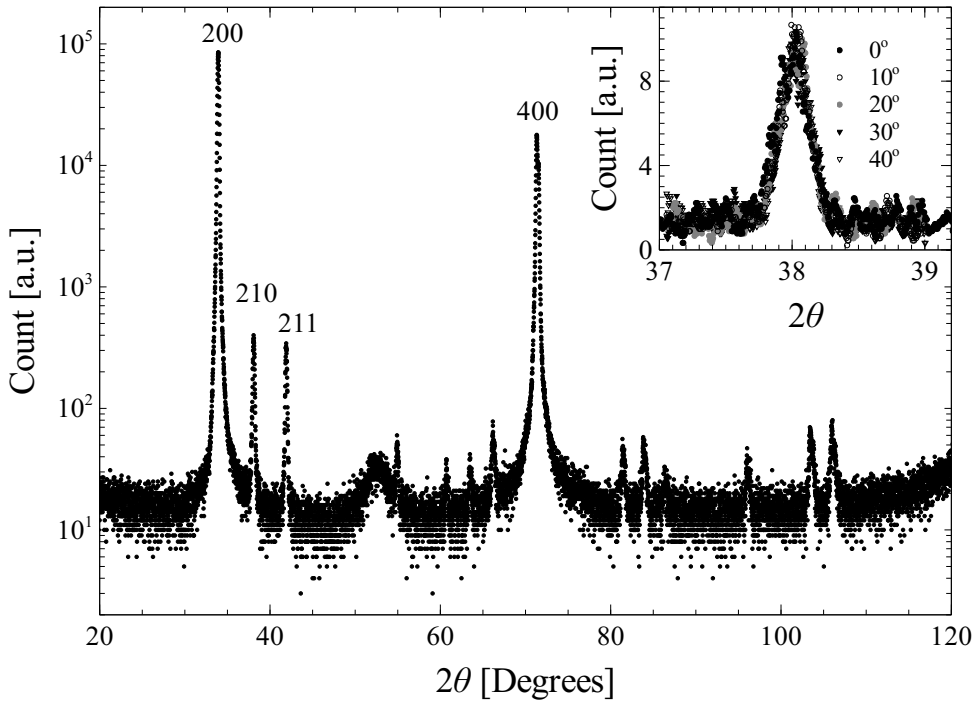

Figure 2.10: *θ-2θ scan of deposition 8-22-11. The large peak at 33.9 degree indicates that the dominant out-of-plane orientation is (200). Inset: The (210) off-axis peak was taken at an angle to the plan, and therefore indicates grains with (100) out-of-plane orientation. The angles in the inset indicate the various investigated substrate rotation angles φ.*

between the amplitude of the (200) and the (210) peak varies between the depositions and can be considered as a measure for the degree of texturing. The ratio between the (200) and the (210) is 0.61 for deposition 9-14-10, 19.8 for deposition 2-14-11, 27.6 for deposition 2-14-11, 13.0 for deposition 3-17-11, and 213 for deposition 8-22-11. Deposition 9-14-10 is deposited at a slower rate and a higher background pressure than the other samples, and the degree of contamination is likely to be higher in this sample than the other samples, which could explain the lower degree of texturing. The background pressures, deposition rates and thicknesses of the other samples are all comparable (table 2.1). The cause of the significantly higher degree of texturing in deposition 8-22-11 is not obvious, but it is plausible that this is due to an improvement in substrate cleanliness. In a bulk sample with randomly oriented grains, the ratio between the (200) and the (210) peak is 0.45 [35], i.e. lower than the lowest observed ratio in these thin film samples. This means that the dominant out-of-plane orientation is (100) in all investigated thin film samples.

Using a 4-circle diffractometer, the in-plane orientation of deposition 8-22-11 was investigated. In order to probe the off-axis (210) peak of grains which have (100) orientation normal to the plane, the off-axis rotation angle ψ is set to 26.6 degree (figure 2.11). By

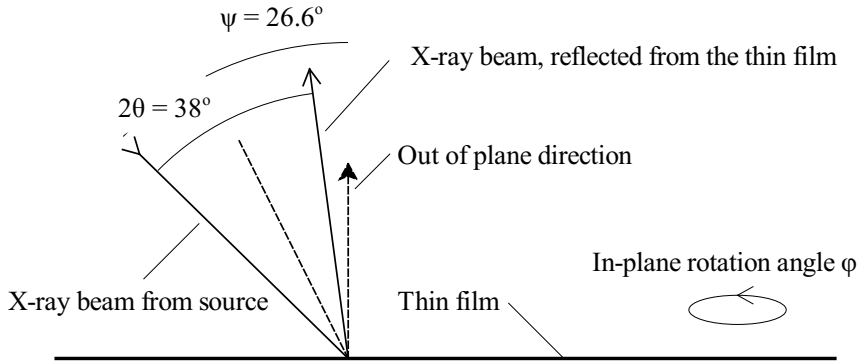

Figure 2.11: *Schematic representation of an XRD measurement of an off-axis (210) peak. Indicated are the 2θ angle between the incoming and reflected X-ray beams, the off-axis rotation angle ψ and the in-plane rotation angle φ.*

determining the intensity of the (210) peak (of $2\theta = 38°$) at various in-plane substrate rotation angles φ, the in-plane crystal orientation (if any) is determined. Only those crystallites for which the (210) direction is aligned along the substrate rotation angle φ contribute to the measured reflection. In an epitaxial film, peaks will be observed at particular substrate orientation angles and not at others. If, however, the in-plane crystal orientation is random, like in a polycrystalline film with out-of-plane texturing but no preferred in-plane orientation φ, then the intensity of the (210) reflection is independent of the substrate orientation angle as there is always some small fraction of the sample that is aligned parallel to the X-ray beam. As shown in figure 2.10, the latter case is precisely what is observed. Deposition 8-22-11 is the deposition with the highest degree of texturing and is found to be randomly oriented in the in-plane direction, so it is reasonable to assume that all other depositions are randomly oriented in the in-plane direction as well.

In summary, the out-of-plane orientation of various thin film depositions was investigated. In all investigated samples, the dominant out-of-plane orientation is (100), but the degree of texturing varies between samples. The in-plane orientation was determined to be random.

2.3.7 Room temperature strain state

In order to understand the effect of strain on the superconducting properties of Nb-Sn, it is important to fully understand the three-dimensional strain state. Since the Nb-Sn crystals are randomly oriented in-plane, they cannot be epitaxial with the substrate. This means that the mismatch with the substrate lattice parameter does not need to be considered as a possible contribution to the strain state of the thin film. The strain state at room temperature is then determined by the strain state of the thin film during the deposition and thermal strain due the differential thermal contraction between substrate and film, produced by the cool down

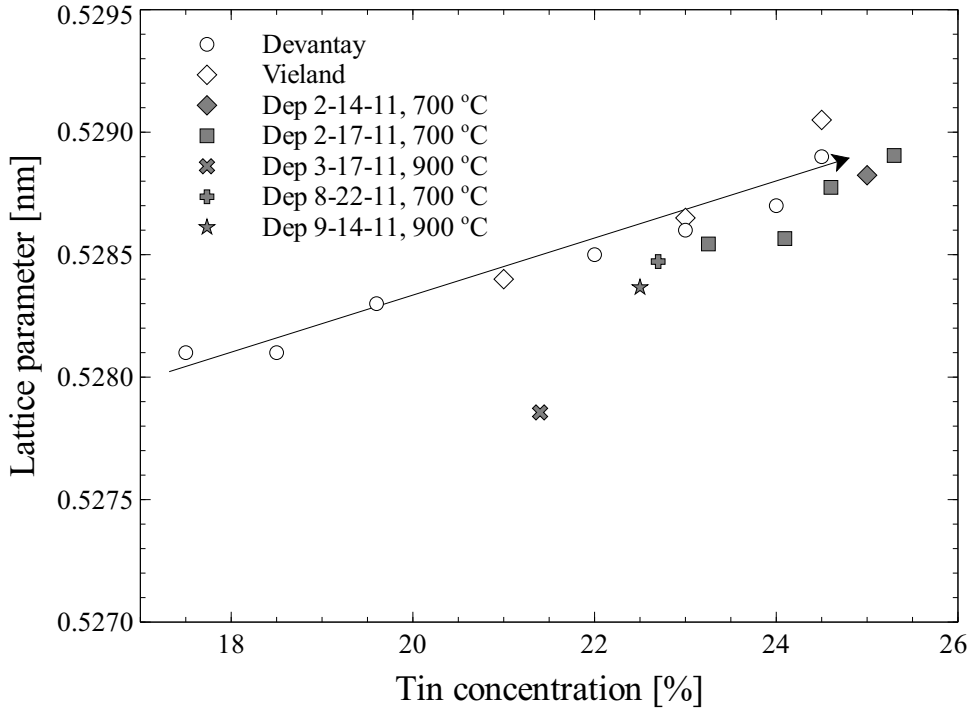

Figure 2.12: *Comparison of measured composition dependent out-of-plane lattice parameters of the thin film samples and the lattice parameters of previously measured bulk samples, after Devantay et al. [52], and Vieland et al. [53]. The arrow is a guide to the eye.*

from elevated temperature to room temperature.

In a magnetron deposition, ions are accelerated with a typical voltage of several hundred volt before impinging onto the substrate. This energy magnitude typically results in a compressively strained film. To some extent, the strain state of the thin film can be tuned by controlling the argon gas pressure, as ions travelling from the targets to the substrate collide with the argon gas and lose energy along the way. Furthermore, the strain state of the thin film is also related to a variety of other factors, such as ion species, the distance between the targets and the substrate, and substrate biasing, making it difficult to predict. This topic has been discussed in detail by Bilek *et al.* [54, 55], and McKenzie *et al.* [56].

Once the deposition is complete, the thin film cools down from elevated temperature (table 2.1) to room temperature. Differences in thermal contraction between the films and their surroundings, which are the R-plane oriented sapphire substrate, the niobium heater, and the molybdenum plate that holds the substrate in place, affect the strain state of the Nb-Sn thin film at room temperature. As shown in table 2.2, the thermal expansion of stoichiometric Nb_3Sn exceeds that of the other materials. Assuming that the thermal expansion of off-stoichiometric Nb-Sn is approximately the same as the one of stoichiometric Nb_3Sn, the cool down from elevated temperature to room temperature exerts tensile strain on the Nb-

Table 2.2: *Thermal expansion of various materials, defined as $a_0(T)$ / $a_0(293\ K)$, after Yim et al. [60], Edwards et al. [61], Tottle [62], and Schadler et al. [63].*

T [°C]	R-plane sapphire	bcc niobium	Nb_3Sn	Molybdenum
700	1.0052	1.0051	1.0059	1.0038
900	1.0066	1.0060	1.0077	1.0048

Sn. For example, if the strain is dominated by the R-plane sapphire, then the cool down from 700 °C exerts 0.07% tensile in-plane strain and the cool down from 900 °C exerts 0.10% tensile in-plane strain on the Nb-Sn.

The strain state of the material at room temperature was determined by measuring the out-of-plane lattice parameter and then calculating the out-of-plane strain by comparing the lattice parameter to the lattice parameter measured in bulk samples. The in-plane strain can then be determined using a known Poisson's ratio. The out-of-plane lattice parameter was determined by fitting the (200) peak in a θ-2θ spectra and is compared to previously measured composition-dependent bulk lattice parameters that were reported by Devantay *et al.* [52] and Vieland *et al.* [53]. Based on the comparison between the literature bulk data and the measured out-of-plane lattice constants, a difference between 0.05 and 0.5 pm is observed, which implies that the out-of-plane strain state at room temperature is -0.01% to -0.1% compressive.

Based on investigations by Ten Haken *et al.* [57], Muzzi *et al.* [58], and Watanabe *et al.* [59], the Poisson's ratio of Nb_3Sn is 0.38 ± 0.08. The in-plane strain can then be determined by applying Hooke's law with the added condition that the film is free to expand in the out-of-plane direction:

$$\varepsilon_{ip} = \left(\frac{\nu - 1}{2\nu}\right)\varepsilon_{op}, \tag{2.2}$$

where ν is the Poisson's ratio of Nb_3Sn, ε_{ip} is the in-plane strain, and ε_{op} is the out-of-plane strain. Using equation 2.2, the average in-plane strain is $0.04\pm0.04\%$ tensile at room temperature which implies that the strain state at the deposition temperatures is slightly compressive, in the order of $-0.04 \pm 0.06\%$.

2.3.8 Niobium on sapphire deposition

In addition to the Nb-Sn on sapphire depositions, a pure niobium film was deposited onto R-plane sapphire with a High Power Impulse Magnetron Sputtering Process (HiPIMS) by A. Anders at Lawrence Berkeley National Laboratory. The film was deposited at 410 °C, with a background pressure of 6×10^{-5} Pa. From XRD measurements, this film was found to be entirely (110) oriented out-of-plane (figure 2.13).

The out-of-plane lattice constant is 0.33529 nm, which is 1.6% larger than the literature value of 0.3300 nm by Barns [64]. As a caveat, note that the literature result is of high purity bcc niobium, while the relatively high $\mu_0 H_{c2}$ of the investigated thin film indicates that it contains at least some strongly disordered niobium (figure 2.28), which means the

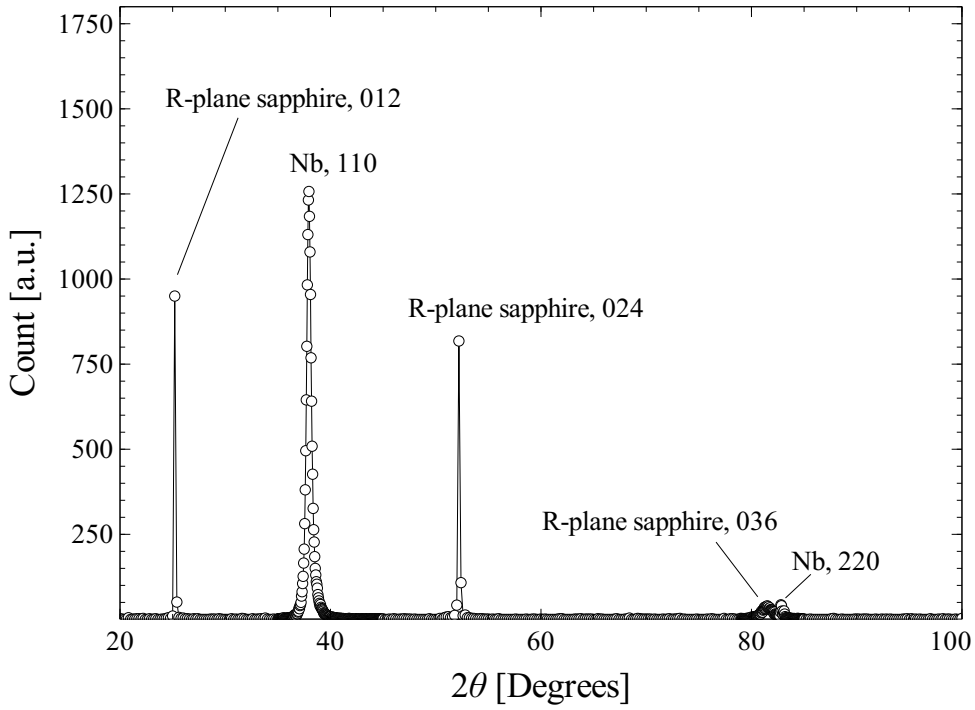

Figure 2.13: *θ-2θ scan of a pure niobium deposition. Besides the peaks of the sapphire substrate, only 110 and 220 niobium peaks are observed.*

disorder is another potential explanation of the relatively large observed lattice parameter. Using a Poisson's ratio of 0.38 [65], a compressive in-plane strain of 1.3% is found. In comparison to the Nb-Sn thin film, this strain state is significantly more compressive, which is likely a result of different deposition conditions. Unlike the Nb-Sn thin films, no argon was present during this deposition, leading to a higher energy of the impinging ions and therefore a more compressive strain state.

2.3.9 Thin film patterning

A number of depositions were etched in a specific pattern (figure 2.14). The patterning enables a number of measurements, including the determination of the normal state resistivity and critical current density parallel and perpendicular to the applied strain direction, and a thickness determination of the thin films through profilometry.

Selective etching was achieved by spinning a layer of positive photo-resist onto a thin film, selectively exposing unmasked areas to ultraviolet light, removing the exposed photo-resist with a developer, and etching through the film regions that are not covered with photo-resist using a mixture of hydro-fluoric and nitric acid. Details on the etching process are found elsewhere [45]. Etched thin film samples were fabricated from Nb-Sn depositions 9-14-10

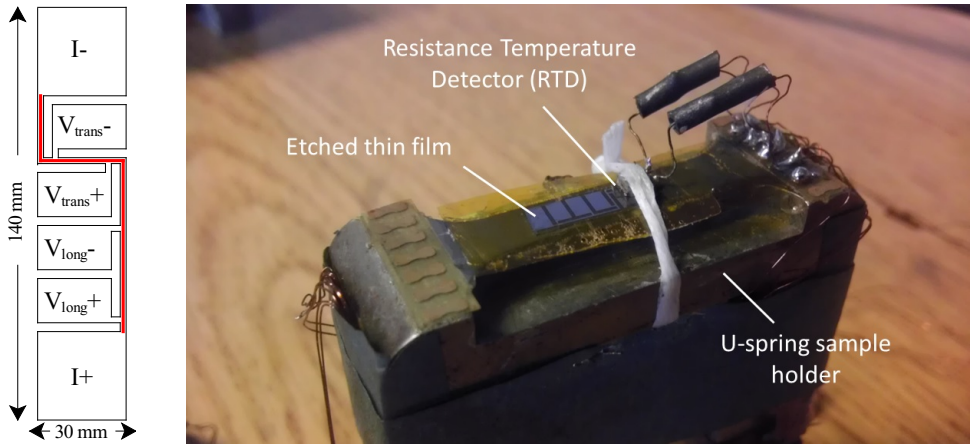

Figure 2.14: *Left: schematic representation of the etched pattern in the thin film samples. Current flows between the current taps (I+, I-), and the voltage drop is measured between the voltage tap pairs (V_{long}+,V_{long}-,V_{trans}+,V_{trans}-). Strain is applied along the length of the samples, so that current flows parallel to the applied strain direction in the longitudinal direction and perpendicular to the applied strain direction in the transverse direction. Right: picture of an etched sample glued onto the U-spring test rig, where the leads are not yet attached to the sample. A thermometer is fixed on the sample with wax string.*

and 2-14-11, and from niobium deposition 2-13-12.

2.3.10 Conclusion

Nb-Sn thin films were fabricated using a magnetron sputtering technique, by which niobium and tin were simultaneously deposited onto a heated R-plane sapphire substrate. Cutting depositions into strips resulted in samples with various compositions between 19.5 and 25 at.% Sn.

The thin films were investigated using a scanning electron microscope (SEM), equipped with an X-ray energy dispersive spectroscope (XEDS), scanning transmission electron microscopy (STEM), X-ray diffraction (XRD), and Rutherford Backscattering Spectrometry (RBS). The thin films show a dense columnar polycrystalline microstructure and are highly textured. They are predominantly (100) oriented in the out-of-plane direction and randomly oriented in the in-plane direction. The films were determined to be in a 0.04 ± 0.04% tensile strain state at room temperature in the in-plane direction.

A pure niobium film was fabricated using a high power impulse magnetron sputtering technique. This film was found to be (110) oriented out-of-plane. The room temperature in-plane strain state is 1.3% compressive.

Patterning was applied to some of the Nb-Sn films and to the Nb film, allowing for the measurement of normal state resistivity parallel and transverse to the uni-axial applied strain direction, as well as critical current density measurements in these directions.

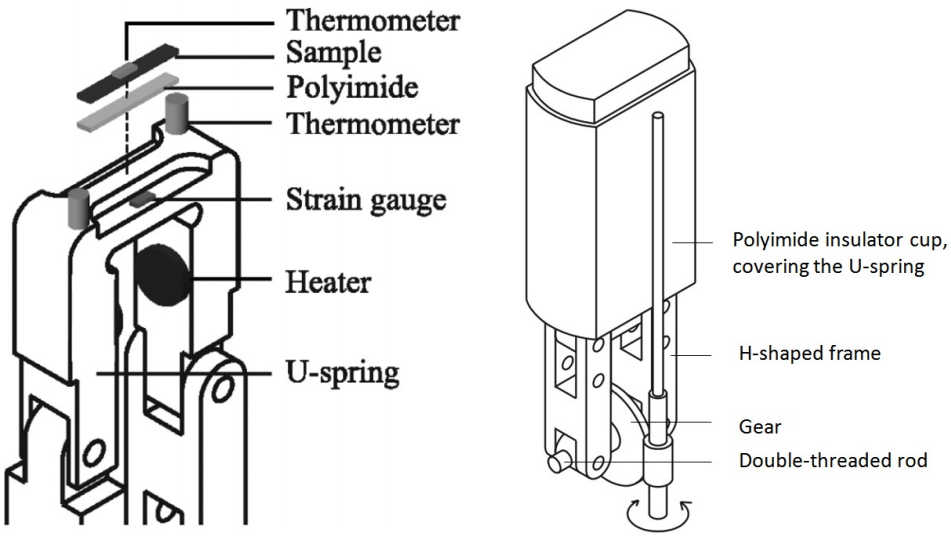

Figure 2.15: *Left: Schematic representation of the U-spring test rig. Right: Illustration of thermal insulation with an 'inverted cup' system and strain application through a gear box, after PhD thesis Godeke [33].*

2.4 Cryogenic measurements with the U-spring

A U-spring test rig was constructed and optimized for the purpose of measuring the superconducting properties of Nb_3Sn bulk samples and thin films. With this test rig, cryogenic measurements were performed by which the voltage drop over a sample was measured as a function of temperature, magnetic field, applied strain and current density. In this way, the normal state resistivity, critical temperature, upper critical field and critical current density under various conditions were determined. These measurements are discussed further in the next chapters: chapter 3 focuses on the critical current density, chapter 4 on the relation between composition, critical temperature and upper critical field, and chapter 5 on the effect of strain on both the superconducting properties T_c and $\mu_0 H_{c2}$ as well as the normal state resistivity ρ_n.

2.4.1 U-spring test rig

The U-spring test rig (figure 2.15) was originally developed by Ten Haken *et al.* [33, 71, 72] for the purpose of measuring the critical current of Nb_3Sn tapes as a function of temperature, magnetic field and strain, but also allows for the measurement of samples with various geometries such as wires [33], thin films [45], and bulk samples [73, 74]. Detailed descriptions of the operation of the U-spring for the purpose of measuring wires, bulk samples and thin films are available elsewhere [33, 39, 45, 74].

The U-spring is made of Ti-6Al-4V, a type of titanium alloy that maintains elastic behavior up to a strain limit of $\pm 1.3\%$, i.e. both high levels of compressive and tensile strain can be

achieved. Strain is applied through a gear box. The gear drives a double-threaded rod which results in the movement of the legs of an H-shaped frame. The movement of the top of the H-shaped frame is transferred to the legs of the U-spring, such that the top of the U-spring is bent, resulting in the application of strain onto the sample (figure 2.15). Since the spring remains elastic, the relation between the strain on top of the sample and the strain gauge is linear and reproducible, so that the strain of the sample can be determined in-situ.

The temperature of the sample is controlled with a combination of a thermally insulating polyimide cup, heaters and temperature sensors. The U-spring is placed inside the inverted insulating polyimide cup. When heat is applied to the U-spring, the liquid helium inside the cup evaporates, thus filling it with helium gas, and the temperature of the U-spring increases. The sample temperature is measured with a temperature sensor that is pressed onto the sample (figure 2.14, right). A PID controller measures the temperature and controls the heaters, thus allowing for a regulation of the temperature to a desired set-point temperature.

Both bulk samples and thin films can be glued on the U-spring. A thin polyimide foil is glued in between the bulk sample and the U-spring, so that the sample is electrically insulated from the spring. Voltage and current tap wires are attached with conducting silver paint. Resistivity and critical current measurements are performed in a 4-point measurement setup. The current taps are electrically connected to the ends of the sample and the voltage taps are connected several millimeters away from the current taps, so that the current is sufficiently uniform in the region between the voltage taps and the contact resistance is not included in the measured signal.

The U-spring is placed in the bore of a 15 T solenoid, thus allowing for the application of magnetic field. The magnetic field value was verified with a Hall-probe measurement and is accurate within the 1% uncertainty of the hall-probe calibration. The magnetic field affects the resistive temperature sensors, a phenomenon investigated in detail by Brandt *et al.* [75], and this effect is accounted for.

The thermal setup was verified for bulk samples by comparing the measured data to measurements performed with different cryogenic instruments [49], such as heat capacity measurements [39], vibrating scanning magnetometer (VSM) measurements [74], and an alternative variable temperature resistance measurement setup [74]. With regards to the thin films, the $R(T)$ measurement of a number of samples is verified by performing slow warm-up measurements of the entire cryostat. The U-spring is placed in the center of a solenoid that is slowly warming up, resulting in a small temperature gradient and nearly ideal isothermal behavior. Based on the validations, the absolute accuracy in temperature readout is estimated at 0.1 K.

2.4.2 Thermal pre-compression

Samples are glued to the U-spring and consequently the difference in thermal contraction between Nb-Sn and Ti-6Al-4V affects the low temperature strain state of the Nb-Sn. The gluing involves applying M-bond 610 [76] between the sample holder, polyimide layer and sample. Sample and sample holder are heated up to 150 °C and kept at this temperature for a two-hour period to allow the glue to set. Once the test rig is at cryogenic temperature, the amount of strain exerted on the sample by the sample holder due to thermal pre-compression is equal to the difference in thermal contraction between the sample holder and the sample between 423 K and 4.2 K, where it may be assumed that the much larger sample holder

dominates the strain state of the sample.

To estimate the thermal contraction of the Nb-Sn, it is assumed that the thermal expansion is the same as for stoichiometric Nb_3Sn. The lattice parameter of stoichiometric Nb_3Sn decreases from 0.52974 nm at 423 K [63], to 0.52915 $\pm$ 0.00001 nm at 297 K [63, 77], and further to 0.52807 nm at 50 K. Below 50 K, stoichiometric Nb_3Sn undergoes a martensitic transformation as discussed by Mailfert *et al.* [77], which does not occur in off-stoichiometric samples as shown by Devantay *et al.* [52]. Since most of the investigated samples are off-stoichiometric, it is assumed that (like for most cryogenic materials [78]) the change in lattice parameter below 50 K is negligible, which means that the amount of thermal contraction between 423 K and 4.2 K is -0.32%. Ti-6Al-4V contracts 0.12% between 423 K and 293 K [79] and 0.17% between 293 and 4.2 K, according to Marquardt *et al.* [80], totaling 0.29%. A complicating factor in the case of thin films is that during the warm-up between 297 K and 423 K, i.e. before the glue sets, the strain state of the Nb-Sn is determined by the R-plane sapphire. The R-plane sapphire expands by 0.096% between 293 and 423 K [60], while Nb_3Sn expands by 0.095% in the sample temperature range [63]. Thus for all intents and purposes, the difference in thermal expansion between the Nb_3Sn and the R-plane sapphire can be considered negligible between 293 and 423 K.

Gluing the Nb-Sn samples to the U-spring and cooling down to 4.2 K thus results in the application of 0.03% additional tensile in-plane strain on the Nb-Sn. As was discussed in section 2.3.7, the thin films are already strained $0.04\pm0.04\%$ in the in-plane direction at room temperature, so that the cool down to 4.2 K results in a $0.07\pm0.04\%$ in-plane tensile strain state. The niobium thin film on R-plane sapphire can be evaluated following the same argument. Niobium expands by 0.090% between 297 K and 423 K and contracts by 0.13% between 297 and 50 K [63]. Thus the gluing process and subsequent cool down results in an extra 0.07% compressive in-plane strain in the niobium. At room temperature, the niobium thin film is already strained by -1.3% in the in-plane direction, so that the cool down results in -1.37% strain. The Nb_3Sn bulk samples are assumed to be strain-free at room temperature, leading to a 0.03% tensile strain state at 4.2 K.

2.4.3 Three-dimensional sample strain state as a function of applied strain

Under the assumption that the deformation of the sample holder dominates the strain state of the sample in the plane directions, the sample strain state as a function of applied strain depends on thermal pre-strain, and the longitudinally applied strain. In the case of the U-spring, longitudinal strain is applied by bending the U-spring. The resulting transverse applied strain is determined by the Poisson's ratio of Ti-6Al-4V, with:

$$\varepsilon_{\mathrm{ip,tr,a}} = -\nu_{\mathrm{sh}}\varepsilon_{\mathrm{ip,long,a}}, \tag{2.3}$$

where $\varepsilon_{\mathrm{ip,long,a}}$ is the amount of longitudinally applied uni-axial in-plane strain and is typically shortened to ε_{a}, $\varepsilon_{\mathrm{ip,tr,a}}$ is the amount of transversely applied in-plane strain, and ν_{sh} is the Poisson's ratio of the Ti-6Al-4V sample holder, which is equal to 0.342 [79]. The relation between longitudinal strain on top of the sample and the strain on the bottom of the U-spring is linear and reversible [33], so that the longitudinal and transverse strain on top of the sample can be determined from a strain measurement on the bottom of the U-spring.

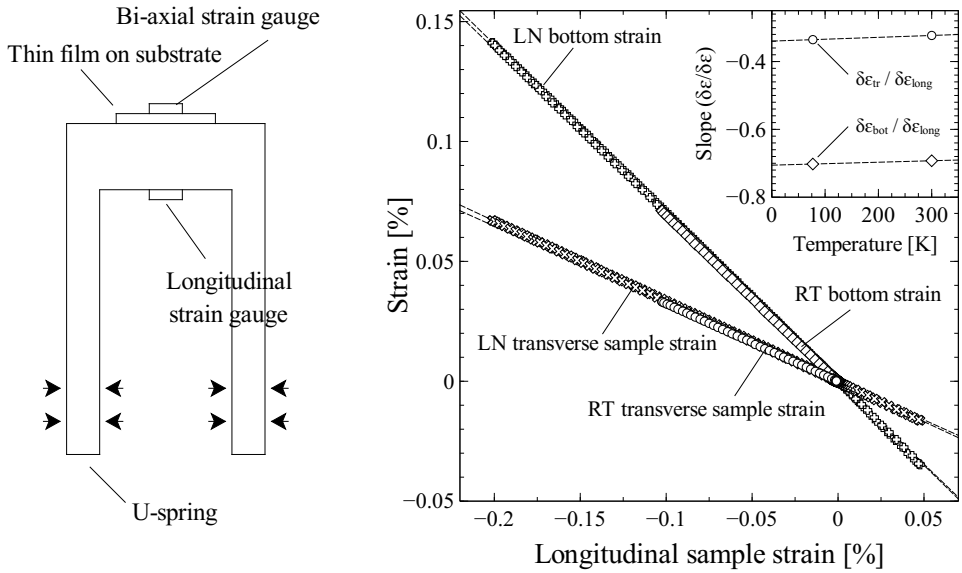

Figure 2.16: *Left: Schematic representation of bi-axial strain experiment. The applied strain is measured with the longitudinal strain gauge at the bottom of the U-spring and the bi-axial strain gauge on top of the sample. Right: Strain gauge measurements at room temperature (RT) and 77 K (LN).*

The validity of these arguments was verified by performing a measurement in which the longitudinal and transverse sample strain, as well as the strain on the bottom of the U-spring were measured simultaneously (figure 2.16). The experiment confirms the linearity of the relationships between the strain of the bottom of the U-spring, the longitudinal strain on top of the sample and the transverse strain on top of the sample (figure 2.16, right). The proportionality constants at 4.2 K were determined through extrapolation. Consistent with expectations, the Poisson's ratio at 4.2 K was determined to be 0.340 ± 0.007, while the proportionality constant between the longitudinal sample strain and the bottom strain was determined to be -0.706 ± 0.014. Here, the uncertainty is due to the measurement uncertainty of the strain gauges. In summary, the three-dimensional strain state of the sample is known: the longitudinal and transverse in-plane strain state are dominated by the sample holder while the out-of-plane strain is determined by the Poisson's ratio of the Nb-Sn itself.

2.4.4 Resistivity measurement as a function of temperature, magnetic field and applied strain

For each sample, the resistivity was determined at various temperatures, magnetic fields, and strain, by keeping constant the magnetic field and strain while slowly sweeping the temperature and then measuring the resistivity. A four terminal measurement technique was

used to inject current and measure the voltage drop. The distance between the voltage taps and the current injection points was in all cases more than 2 mm to avoid voltage measurement anomalies that are related to inhomogeneous current injection. A DC current was used that is sufficiently small not to affect the superconducting properties of the sample. This was verified by measuring at various current amplitudes and confirming that the resistivity is independent of current. Normally, a current of 1 mA was applied for the bulk samples and 10 μA for the thin film samples. To avoid voltage offsets related to thermo-electric effects, a bipolar measurement technique was used.

The resistivity was measured while the temperature was varied at a rate of -25 mK/s, while the strain and magnetic field were fixed. It was observed that after changing the magnetic field and the strain and returning to a previously investigated combination of magnetic field and strain, the $R(T)$ measurement is reproduced within a typical temperature uncertainty of 25 mK after the temperature.

A typical dataset consists of 50 temperature-dependent resistivity measurements per magnetic field and strain, 5 different magnetic fields per strain and 10 different strain states, for a total of 2500 measurements. A subset of such a dataset is shown in figure 2.17, consisting of resistivity versus temperature measurements at various magnetic fields, and two different strains. The strain $\varepsilon_a = 0\%$ refers to the strain state that the sample is in immediately after cool down (i.e. no applied strain), while the strain -0.3% refers to a strain state where the sample is compressed by 0.3% along its length.

2.4.5 Critical current density measurements as a function of temperature, applied strain, and magnetic field

Critical current density measurements were also performed by measuring the electric field at various combinations of current, temperature, magnetic field, and strain (figure 2.18). J_c is defined as the current density at which the electric field crosses the electrical field criterion E_c, which was set to 0.5 Vm^{-1}.

The main difference between resistivity and critical current density measurements is that unlike in critical current density measurements, the current density in resistivity measurements is sufficiently small not to affect the superconducting properties. The critical current density measurements were performed on the etched samples, which brings two distinct advantages. The geometry is more carefully controlled, which reduces the uncertainty in the critical current density from the cross-section dimensions to about 10%, and the current carrying cross-section is significantly smaller, which allows for a higher achievable current density at the same level of dissipation. The $J_c(T, \mu_0 H, \varepsilon_a)$ measurements are discussed in section 3.7.

2.4.6 Strain dependent normal state resistivity

As shown in figure 2.19, strain affects the normal state resistivity ρ_n, i.e. the resistivity just above the normal to superconducting transition. The effect of strain on the normal state resistivity was investigated in more detail using the patterned samples (figure 2.14), where current flows either parallel or perpendicular to the direction in which the strain is applied.

In order to determine the resistivity as a function of strain, the change in resistance due to the change in the sample geometry has to be accounted for. The in-plane longitudinal

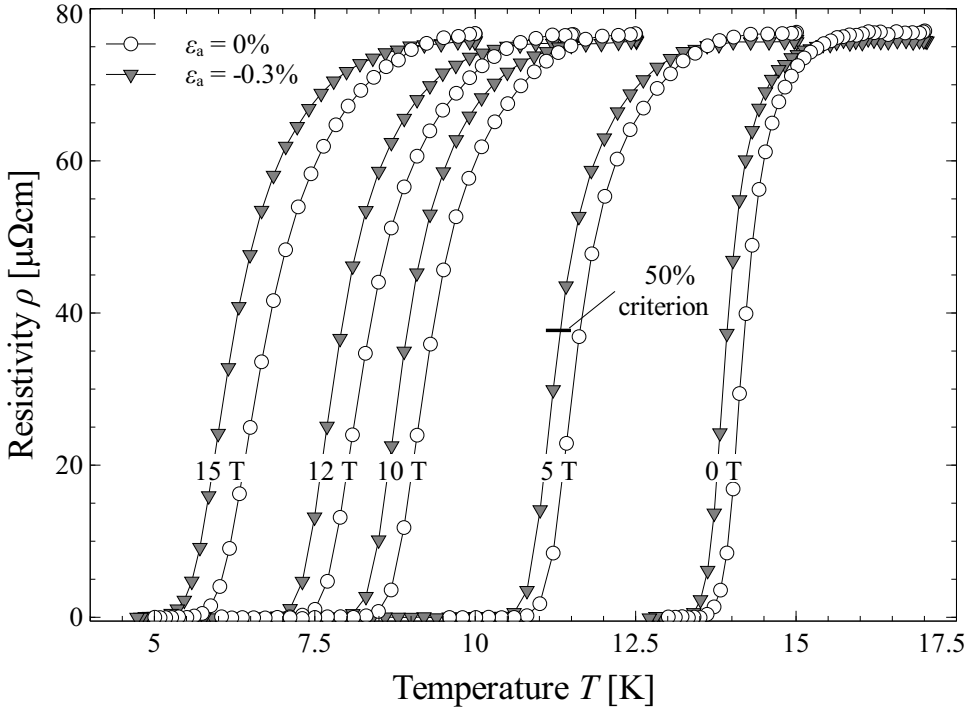

Figure 2.17: *Subset of the ρ(T) measurements performed on deposition 8-22-11, with 22.1 at.% Sn. The resistivity was determined as a function of temperature at various magnetic fields $\mu_0 H$ and applied strains ε_a. The measurements at $\varepsilon_a = -0.3\%$ and 0% are represented with grey and open symbols respectively.*

and transverse strains $\varepsilon_{ip,long,a}$ and $\varepsilon_{ip,tr,a}$ are known, while the out-of-plane strain can be determined from Hooke's law, with:

$$\varepsilon_{op} = \frac{-\nu_{sample}}{1-\nu_{sample}} \left(\varepsilon_{ip,long,a} + \varepsilon_{ip,tr,a}\right), \tag{2.4}$$

where ν_{sample} is the Poisson's ratio of the sample and ε_{op} is the out-of-plane strain resulting from in-plane longitudinal and transverse strain. The resistivity ρ is related to the resistance R, length l, width w, and thickness th as:

$$\rho = \frac{R \cdot w \cdot t}{l}. \tag{2.5}$$

The relations between the dimensions l, w, and t on the one hand and the strains $\varepsilon_{ip,long,a}$, $\varepsilon_{ip,tr,a}$ and ε_{op} on the other depend on the direction of the current relative to the strain direction. In the case of the patterned samples, the resistivity is expressed with:

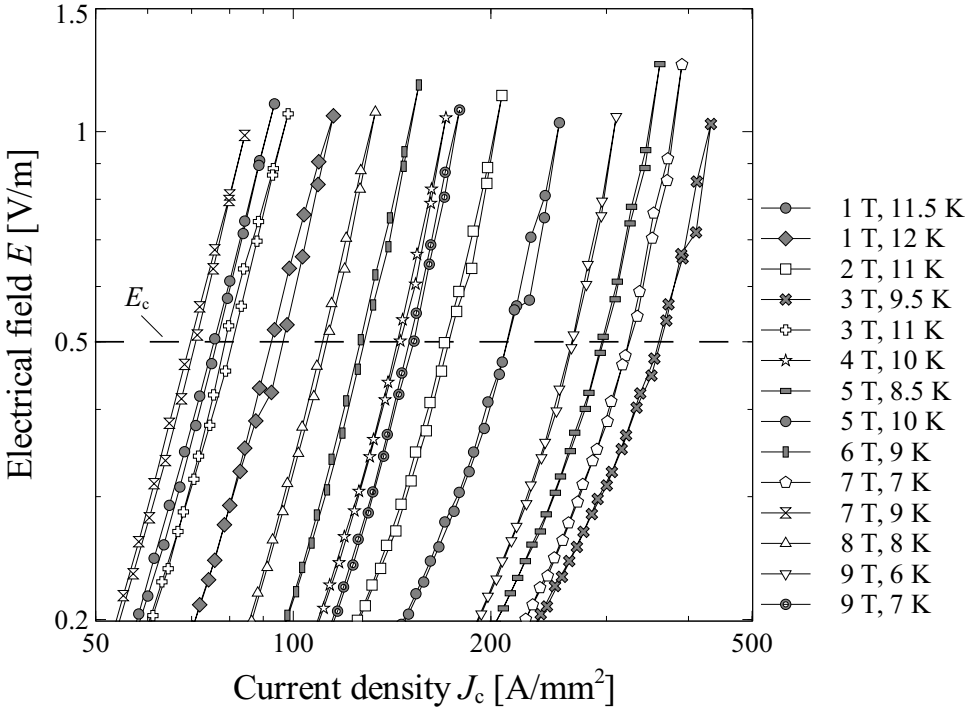

Figure 2.18: *Electric field versus current density measurements at various temperatures and magnetic fields. The measurements shown are from deposition 9-14-10 and were all taken at* ε_a *= 0%.*

$$\rho_{\text{long}}\left(\varepsilon_{\text{ip,long,a}}\right) = R\left(\varepsilon_{\text{ip,long,a}}\right)\left(\frac{w_0 \cdot t_0}{l_0}\right)\frac{\left(1+\varepsilon_{\text{ip,tr,a}}\right)\left(1+\varepsilon_{\text{op}}\right)}{1+\varepsilon_{\text{ip,long,a}}}, \tag{2.6}$$

$$\rho_{\text{tr}}\left(\varepsilon_{\text{ip,long,a}}\right) = R\left(\varepsilon_{\text{ip,long,a}}\right)\left(\frac{w_0 \cdot t_0}{l_0}\right)\frac{\left(1+\varepsilon_{\text{ip,long,a}}\right)\left(1+\varepsilon_{\text{op}}\right)}{1+\varepsilon_{\text{ip,tr,a}}}, \tag{2.7}$$

where l_0, w_0, and t_0 are the original dimensions of the sample with respect to the current directions, ρ_{long} is the resistivity of a sample where the current flow is parallel to the uni-axial strain direction, and ρ_{tr} is the resistivity of a sample where the current flow is perpendicular to the applied strain direction. With $\nu_{\text{sample}} \approx 0.38$, the resistance change due to geometry change is 1.74% per % elongation in the longitudinal strain direction and -0.94% per % elongation in the transverse strain direction.

The change in normal state resistivity with applied strain was determined for different samples at various temperatures, including longitudinal and transverse resistivity measurements of low-resistivity Nb-Sn samples, high-resistivity Nb-Sn samples and a niobium sample. A subset of the measurements is shown in figure 2.19, which shows that the effect of compres-

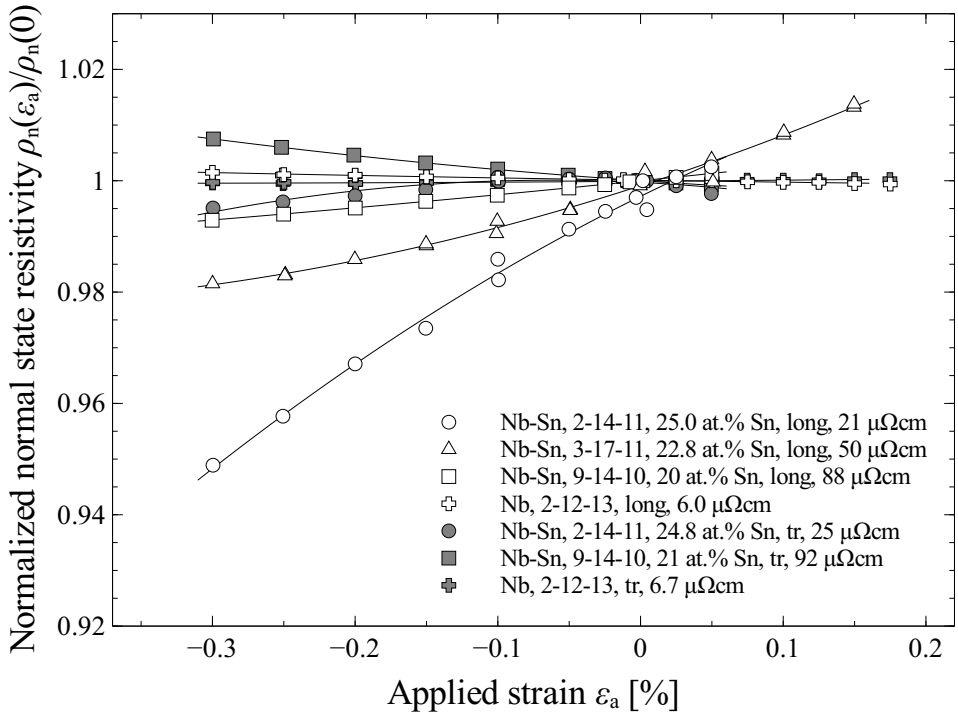

Figure 2.19: *Normal state resistivity ρ_n as a function of applied strain ε_a. In the 'longitudinal' data, the strain is applied parallel to the current flow direction, while in the 'transverse' data the strain is applied perpendicular to the current direction. Longitudinal and transverse measurements of Nb-Sn with various tin concentrations and bcc Nb are shown. The lines are guides to the eye.*

sive strain on the normal state resistivity varies between the samples. Under the influence of compressive strain, the longitudinal resistivity is strongly reduced in the case of samples with lower resistivity ($\rho \approx 20\ \mu\Omega$cm) but only weakly reduced in the case of samples with higher resistivity ($\rho \approx 90\ \mu\Omega$cm), while the longitudinal and transverse normal state resistivities of the niobium sample are nearly independent of strain. Compressive strain weakly reduces the transverse resistivity of the lower resistivity Nb-Sn sample and weakly increases that of the higher resistivity Nb-Sn sample, while the transverse resistivity of the bcc niobium is once again nearly independent of strain.

For each of the samples, the effect of strain on the normal state resistivity was determined at various temperatures, also in measurements where the critical temperature was suppressed by an applied magnetic field of up to 15 T. It should be noted that the normal state resistivity is nearly independent of applied magnetic field in the investigated temperature regime. In a sample with a normal state resistivity of 70 $\mu\Omega$cm, the application of 15 T at T = 16 K and $\varepsilon_a = 0\%$ resulted in an increase in normal state resistivity of 0.04% in comparison to the normal state resistivity at 0 T.

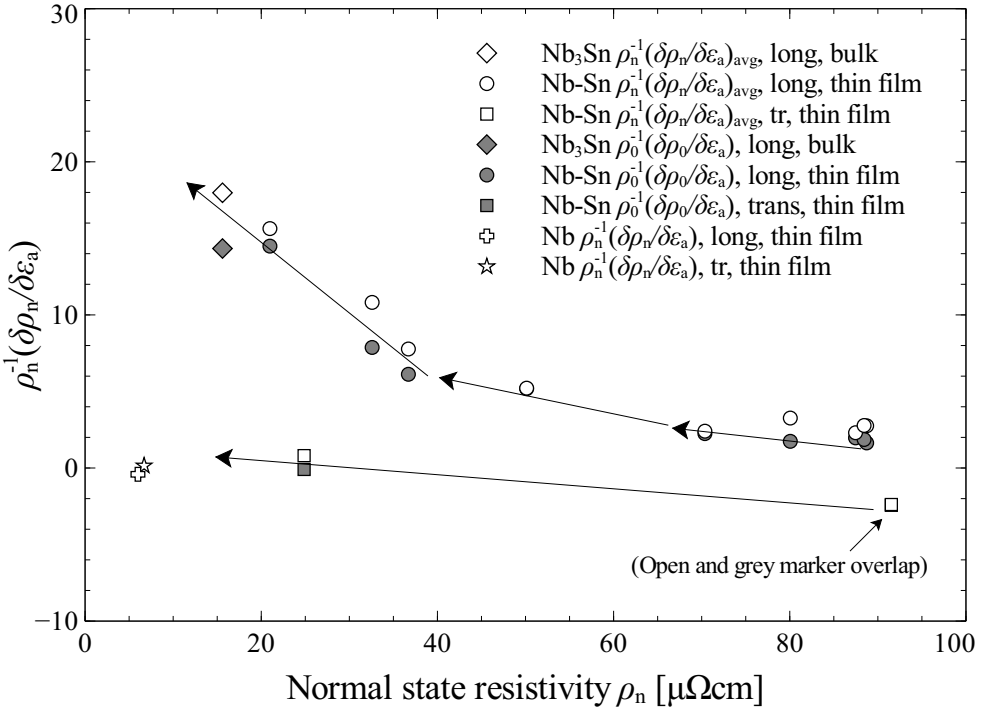

Figure 2.20: *Normalized strain sensitivity of ρ_n of Nb-Sn and Nb binary bulk and thin film samples versus normal state resistivity. 'long' and 'trans' indicate measurements where the resistivity is measured parallel and perpendicular to the strain direction, respectively. The average $\rho_n^{-1}(\delta\rho_n/\varepsilon_a)_{avg}$ and the extrapolated $\rho_0^{-1}(\delta\rho_0/\varepsilon_a)$ of Nb-Sn are shown with open and grey symbols respectively. Also shown is $\rho_n^{-1}(\delta\rho_n/\varepsilon_a)_{avg}$ of the niobium samples. The arrows are guides to the eye.*

The normalized slope $(\rho_n^{-1}\delta\rho_n/\delta\varepsilon_a)_T$ was determined at various temperatures. A small temperature dependence was found in the normalized slope: The slope $\rho_n^{-1}\delta\rho_n/\delta\varepsilon_a$ increases with increasing temperature. It was shown elsewhere by Devantay *et al.* [52] and Gurvitch *et al.* [187], that ρ_n scales with T^2 at lower temperatures, with:

$$\rho_n(T) = \rho_0 + \rho_1 T^2. \tag{2.8}$$

To distinguish between the strain dependence of the residual resistivity ρ_0 and the parameter describing temperature dependence ρ_1, the temperature dependence of $\rho_n^{-1}\delta\rho_n/\delta\varepsilon_a$ is described with:

$$\left[\rho_n^{-1}\left(\delta\rho_n/\delta\varepsilon_a\right)\right](T) \approx \rho_0^{-1}\left(\left(\delta\rho_0/\delta\varepsilon_a\right) + T^2\left(\delta\rho_1/\delta\varepsilon_a\right)\right), \tag{2.9}$$

where $[\rho_n^{-1}(\delta\rho_n/\delta\varepsilon_a)]T$ and $\rho_0^{-1}(\delta\rho_0/\delta\varepsilon_a)$ are dimensionless parameters and

$\rho_0^{-1}(\delta\rho_1/\delta\varepsilon_a)$ is in [K^{-2}]. In figure 2.20, the average slope $(\rho_n^{-1}\delta\rho_n/\delta\varepsilon_a)_{avg}$ and the extrapolated slope $\rho_0^{-1}(\delta\rho_0/\delta\varepsilon_a)$ are shown for the Nb-Sn thin films and Nb_3Sn binary bulk sample, also see [49]. The parameter $\rho_0^{-1}(\delta\rho_1/\delta\varepsilon_a)$, which is barely distinguishable above the noise level of the measurement, is within 0 and 0.017 K^{-2} for all measurements and on average equal to 0.006 K^{-2}. In figure 2.20, the average $\rho_n^{-1}(\delta\rho_n/\varepsilon_a)_{avg}$ and the extrapolated $\rho_0^{-1}(\delta\rho_0/\varepsilon_a)$ are compared, and it is clear that at the temperature below 20 K at which these measurements were taken, the strain sensitivity of ρ_n is dominated by the strain sensitivity of ρ_0. Also shown is $\rho_n^{-1}(\delta\rho_n/\delta\varepsilon_a)$ of the Nb film, which was only measured at 9.5 K.

In summary, the normal state resistivity of Nb-Sn depends on the direction in which strain is applied. This effect is not due to a geometry change, since the degree of change in normal state resistivity with strain is much larger than can be explained by a mere geometry effect, and the measurements are corrected for geometry changes. It is highly unlikely that this is a measurement error, as three different measurement types were used: regular measurements on (thicker) bulk samples and (thinner) thin films, and measurements on patterned thin film samples. The latter measurement in particular uses a well-controlled geometry, resulting in a high degree of confidence that indeed the sample resistivity is changing. It is also noteworthy that the degree of normal state resistivity change in the binary bulk sample is very close to that of the thin films even though the typical grain diameter in the bulk samples is more than ten times larger. This implies that the strain dependence of ρ_n is not related to the grain boundaries.

$\rho_n^{-1}(\delta\rho_n/\delta\varepsilon_a)$ is larger for Nb-Sn samples with a lower normal state resistivity, smaller for Nb-Sn samples with higher normal state resistivity and negligible for the Nb thin films. The normal state resistivity is only weakly strain dependent in the direction perpendicular to the applied strain, which means that under the influence of strain, the normal state resistivity becomes anisotropic. A weak temperature dependence was observed in $\rho_n^{-1}(\delta\rho_n/\delta\varepsilon_a)$, but this effect is insufficient to explain the strain dependence of ρ_n. Thus, the residual resistivity (i.e. ρ_n at 0 K) changes as a function of strain, which implies that strain affects the electrical properties of the crystal, a phenomenon that is explained in section 5.5.2.

2.4.7 Determination of the T_c of Nb-Sn samples from resistivity measurements

At a given magnetic field and strain, the critical temperature is determined from resistivity measurements through the use of a resistivity criterion. For instance, using a resistivity criterion of 50% means that T_c is the temperature at which the resistivity is at 50% of the normal state resistivity, where the normal state resistivity is the resistivity at a temperature slightly above T_c (figure 2.17).

The choice of resistivity criterion is somewhat arbitrary and different arguments can be presented for different criteria. Using a high resistivity criterion (90%) results in a T_c value that is indicative of the highest T_c present in the sample. Using a low resistivity criterion (10%) results in a T_c that is indicative for the highest temperature at which a superconducting path is formed in the sample, which allows for a more consistent comparison with other experiments such as critical current measurements. Finally, a 50% criterion is useful, because $\delta\rho_n/\delta T$ is the largest at 50% of the normal state resistivity, resulting in the greatest degree of sensitivity to changes in T_c. Strain typically causes small changes in the critical

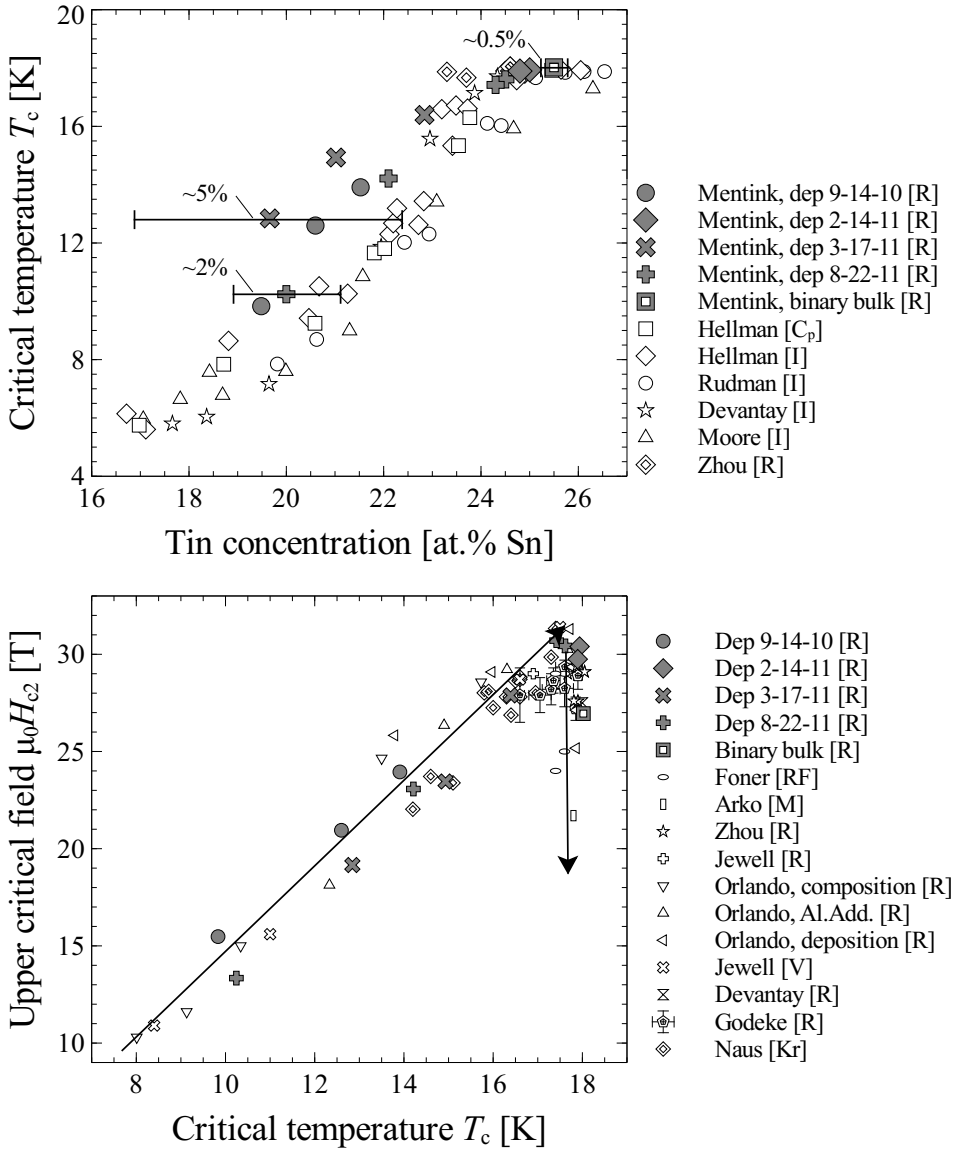

Figure 2.21: *Critical temperature T_c as a function of tin content (top), and upper critical field $\mu_0 H_{c2}(0)$ as a function of T_c for the various investigated samples (grey symbols), compared to literature data (open symbols) (section 4.8.5). The composition distribution width near stoichiometry is about 0.5 at.% Sn, while the composition distributions of the off-stoichiometric samples ranges between 2 at 5 at.% Sn. The arrows are guides to the eye.*

temperature, so that sensitivity is paramount, and this last criterion is selected as standard criterion throughout this thesis.

The T_c is extracted for every sample and compared to literature data (figure 2.21, top). The referenced authors, which are Moore *et al.* [13], Hellman *et al.* [51], Devantay *et al.* [52], and Rudman *et al.* [82] used either inductive or heat capacity measurements. While interpreting inductive measurements is not trivial due to complicating effects such as the undefined paths of shielding currents, the heat capacity measurement in particular is a truly volumetric measurement and is therefore considered as a highly reliable indication of the T_c distribution of the sample.

As seen in figure 2.21, top, the T_c derived from resisitivity measurements is equal to or above any average T_c at a given composition. This is to be expected since only a small percolating path needs to be superconducting to short out the sample. As a result, the best rather than the average superconducting properties of a sample are determined through resistivity measurements (also see figure 2.5, bottom). T_c increases with increasing tin concentration, so that composition distribution width is approximately equal to twice the difference between the highest composition in a sample (which is determined from the resistively determined T_c) and the average composition of the sample (which is determined through SEM-XEDS or RBS). This rough estimate shows that the samples near stoichiometry are very homogeneous with a composition distribution width in the order of 0.5 at.% Sn, while the off-stoichiometric samples are less homogeneous with composition distribution widths that range from 2 to 5 at.% Sn.

While the most inhomogeneous off-stoichiometric thin film samples likely have broad T_c distributions in the order of several kelvin wide [50], this does not fully explain the observed behavior. The average T_c transition width (as defined by the difference in T_c that is determined with a 10% and a 90% criterion) is 0.5 K while the broadest T_c transition is 1.1 K wide. Partly, this is due to the percolating path argument discussed above. In addition, it is not inconceivable that this effect may be due to oxidation resulting in local regions of niobium-oxide. As this effectively traps some of the excess niobium, the niobium to tin ratio in the A15 Nb-Sn is lower, resulting in the observed behavior. This argument is consistent with the experimental observations by Hellman *et al.* [51] as well as with the deposition conditions of the investigated samples [45].

2.4.8 Determination of $\mu_0 H_{c2}$ of Nb-Sn samples from resistivity measurements

The T_c value is determined at a number of discrete magnetic fields, which allows for an extrapolation to $\mu_0 H_{c2}(0)$, as illustrated in figure 2.22. Similarly to the magnetic field dependent heat capacity measurements (section 2.2.5), the Maki-DeGennes description is applied to the experimental data to determine the upper critical field at each strain, see equation 2.1.

Consistent with previous observations by Orlando *et al.* [81] and by Devantay *et al.* [52], it is observed that the $\delta T_c / \delta \mu_0 \mathrm{H}$ decreases between 0 and 5 T (figure 2.22), leading to minor deviations from the Maki-DeGennes description (the measured T_c values at 0 T are approximately 0.5 K higher than the fitted ones). This phenomenon is investigated in more detail elsewhere [45]. While the precise cause of this deviation in unclear, it is noted that the underlying assumptions of Maki-DeGennes description, (dirty limit, weak coupling, no

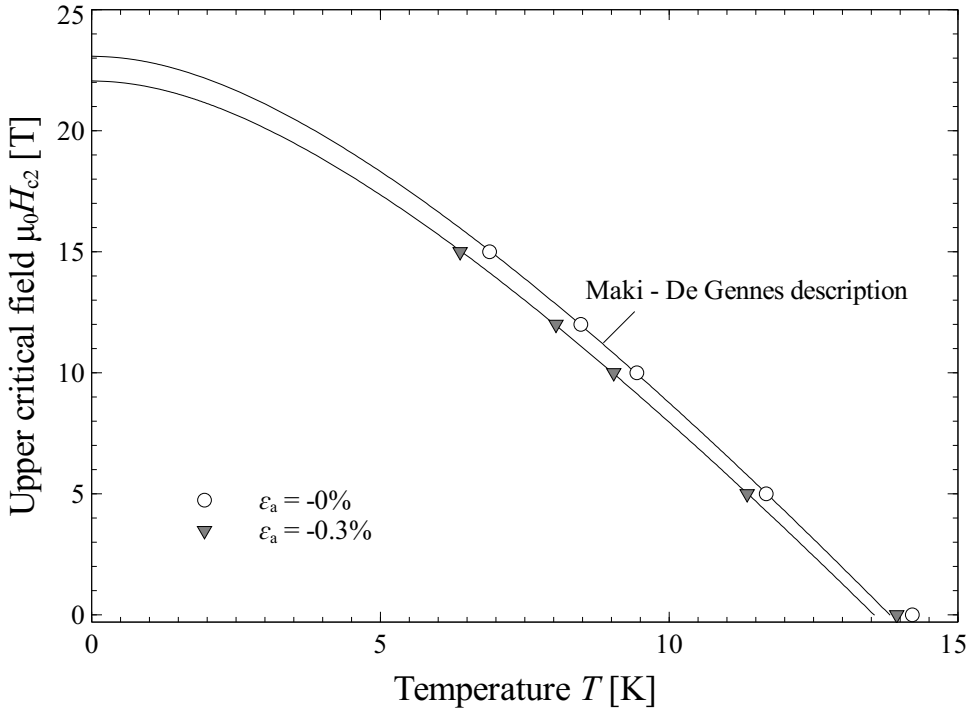

Figure 2.22: *$\mu_0 H_{c2}$ as a function of temperature. T_c was determined at various magnetic fields and two different strains. The Maki-DeGennes description was fitted to the data using fit parameters T_c and $\mu_0 H_{c2}(0)$.*

Pauli paramagnetic limiting, no spit-orbit coupling, and a spherical Fermi surface) are somewhat inaccurate or debatable, a subject discussed in more detail in section 4.8. As the description does not fully account for the details of the microscopic properties of Nb_3Sn, the observation of minor deviations is not unexpected.

With these considerations in mind, $\mu_0 H_{c2}$ is determined by performing a least-squares fit to the Maki-DeGennes description, where the T_c measurement at 0 T is not included. This results in a fit that matches the observed behavior in the intermediate to high magnetic field range, i.e. $\mu_0 H > 5$ T, but is up to 0.5 K below the actually observed T_c in the low magnetic field range, i.e. $\mu_0 H < 5$ T (figure 2.22).

For each of the investigated samples $\mu_0 H_{c2}(0)$ is determined and the result is compared to literature values (figure 2.21), bottom. Only literature values are included in which T_c and $\mu_0 H_{c2}(0)$ are reported simultaneously. The literature values reflect a variety of measurement techniques and a variety of measurement criteria, including resistivity measurements [R], vibrating sample magnetometer measurements [V], magnetic measurements [M], and radio frequency measurements [RF] of bulk samples, thin films, and wires. Of particular interest are the resistivity measurements by Godeke *et al.* [48], Zhou *et al.* [66], Jewell *et al.* [68], the radio frequency measurements by Foner *et al.* [67], and the magnetic measurement

by Arko [70]. All these extend over a range down to temperatures close to 0 K and up to magnetic fields close to $\mu_0 H_{c2}(0)$. Other literature data by Orlando *et al.* [42], Devantay *et al.* [52], and Jewell *et al.* [68] reflect extrapolations from lower magnetic field ranges, making the uncertainty of these values higher. The values by Naus [69] are based on magnetic measurements. These various literature results are discussed in detail in section 4.8.5.

It is clear that the measured $\mu_0 H_{c2}(0)$ values are consistent with literature values. This might seem confusing as the critical temperature versus composition data indicates the presence of compositional inhomogeneity or compositional uncertainty due to niobium oxidation. However, in off-stoichiometric Nb-Sn samples the fraction that is probed resistively has both the highest T_c and the highest $\mu_0 H_{c2}(0)$ values, which is why inhomogeneity does not affect the $\mu_0 H_{c2}(0)$ as a function of T_c curve of off-stoichiometric samples.

Consistent with the literature data, the experimentally observed $\mu_0 H_{c2}(0)$ increases with increasing T_c up to $T_c \approx 17.5$ K, and then sharply decreases. Due to inhomogeneity, the thin films do not display the characteristic drop near stoichiometry, because the resistivity measurement probes the best rather than the average properties of the samples. The underlying cause of the drop in $\mu_0 H_{c2}(0)$ near stoichiometry is discussed in section 4.8.7.

2.4.9 Strain dependence of T_c and $\mu_0 H_{c2}$ of Nb-Sn samples

T_c and $\mu_0 H_{c2}$ were determined as a function of applied strain for bulk samples and thin films (figure 2.23). Bulk samples can be reversibly compressed down to 0.7% compressive strain while thin films can be reversibly compressed by 0.35%. The tensile strain limit is somewhere between 0.05% and 0.15%, so typically a 'safe' experimental limit of 0.05% was used.

The deviatoric strain model [71] was used as a data reduction tool for describing both $T_c(\varepsilon_a)$ and $\mu_0 H_{c2}(\varepsilon_a)$. While the deviatoric strain model is no longer applicable at high compressive strains and a combination of compressive and tensile data, the description is accurate in the strain range in which the bulk samples and thin films are measured and is therefore useful as a parameterization tool. T_c and $\mu_0 H_{c2}$ as a function of applied strain are described with:

$$T_c(\varepsilon_a) = \frac{T_{cm}\left(1 - C_{a,Tc}\sqrt{(\varepsilon_a - \varepsilon_m)^2 + \varepsilon_{0,a}^2}\right)}{1 - C_{a,Tc}\varepsilon_{0,a}}, \tag{2.10}$$

$$\mu_0 H_{c2}(\varepsilon_a) = \frac{\mu_0 H_{c2,m}\left(1 - C_{a,Hc2}\sqrt{(\varepsilon_a - \varepsilon_m)^2 + \varepsilon_{0,a}^2}\right)}{1 - C_{a,Hc2}\varepsilon_{0,a}}, \tag{2.11}$$

where T_{cm} and $\mu_0 H_{c2m}$ indicate the maximum T_c and $\mu_0 H_{c2}$ values, $C_{a,Tc}$ and $C_{a,Hc2}$ indicate the degree of strain sensitivity (with a higher value indicating more strain sensitivity), $\varepsilon_{0,a}$ represents the amount of rounding of the curve, and ε_m the position of the maximum T_c and $\mu_0 H_{c2}$ relative to the strain ε_a immediately after cool down. The optimal value of $\varepsilon_{0,a}$ of the thin films was determined to be $0.3 \pm 0.1\%$, so for data reduction this parameter is fixed to 0.3%. Likewise, $\varepsilon_{0,a}$ is fixed to 0.44% for the bulk samples. A single ε_m value is determined per sample.

Figure 2.24 shows the strain sensitivity parameter $C_{a,Tc}$ as a function of T_c and the strain

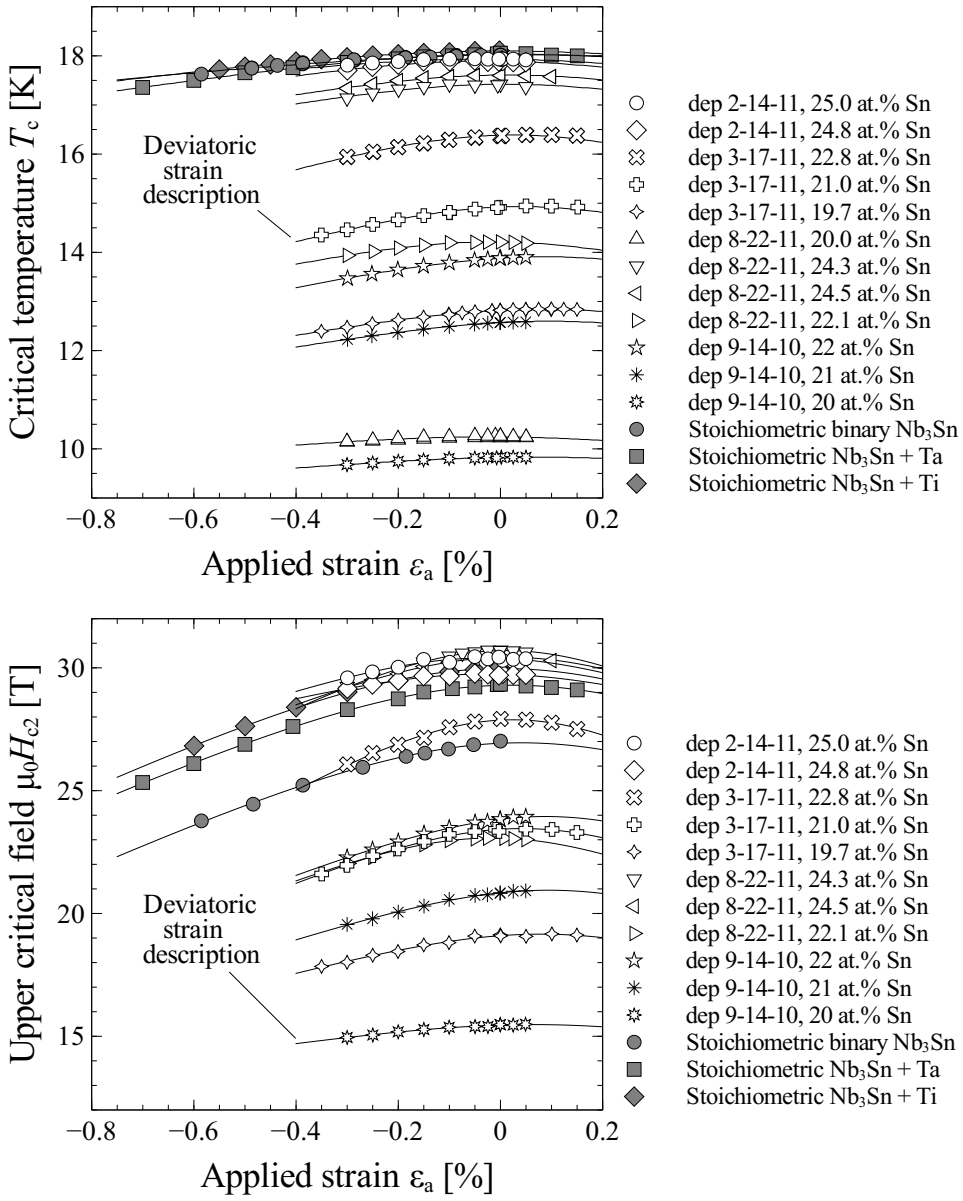

Figure 2.23: *Strain dependent T_c (top) and $\mu_0 H_{c2}(0)$ (bottom) determined from resistivity measurements. The solid lines show individual fits of the measurement data with the deviatoric strain description. The open and grey symbols represent measurements on thin films and on bulk samples, respectively.*

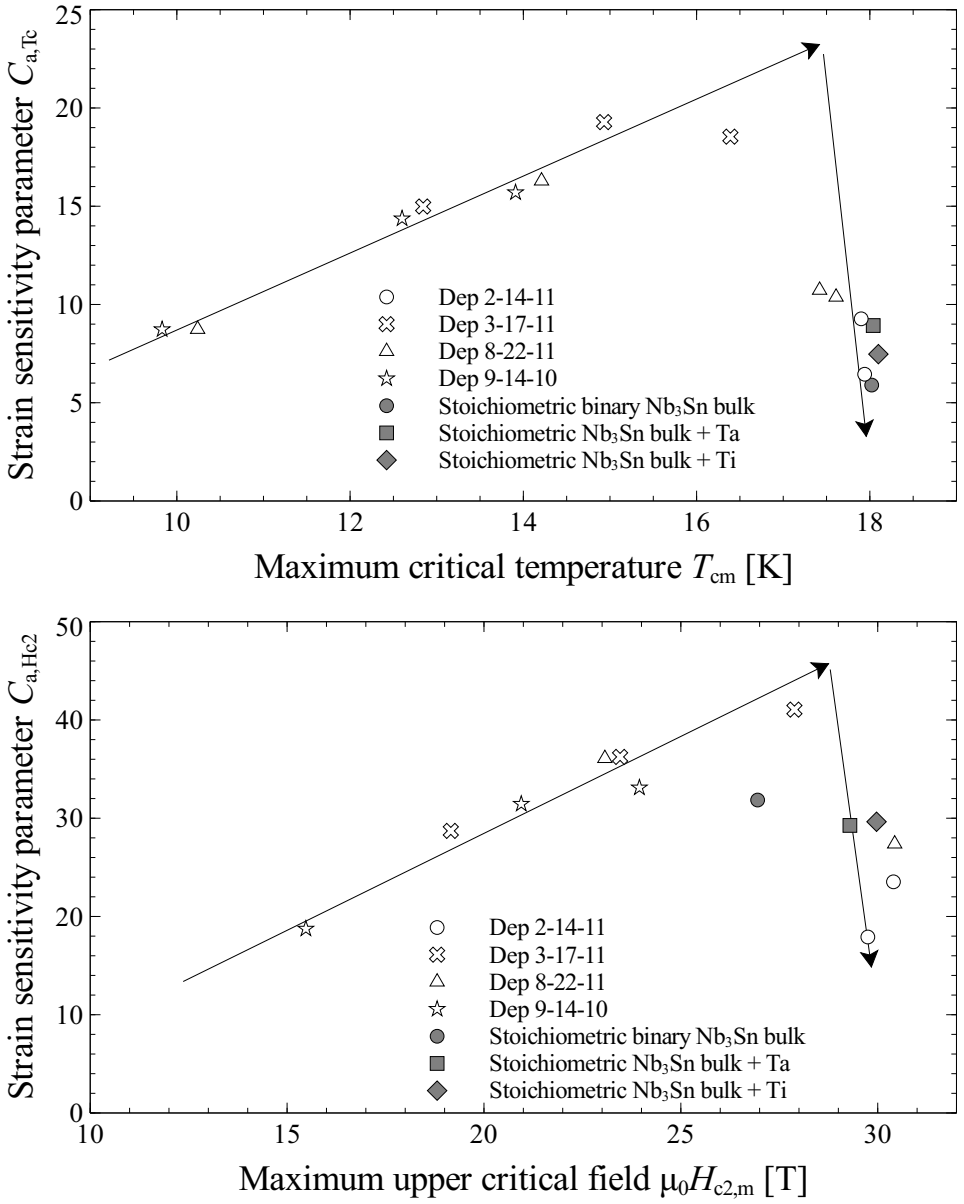

Figure 2.24: *Strain sensitivity parameters $C_{a,Tc}$ as a function of T_{cm} (top) and $C_{a,Hc2}$ as a function of $\mu_0 H_{c2m}$ (bottom). The open and grey symbols represent measurements on thin films and on bulk samples, respectively. The arrows are guides to the eye.*

sensitivity parameter $C_{a,Hc2}$ as a function of $\mu_0 H_{c2}$. The two figures look very similar, with a general increase in strain sensitivity with increasing T_c or $\mu_0 H_{c2}$, and a decrease near the

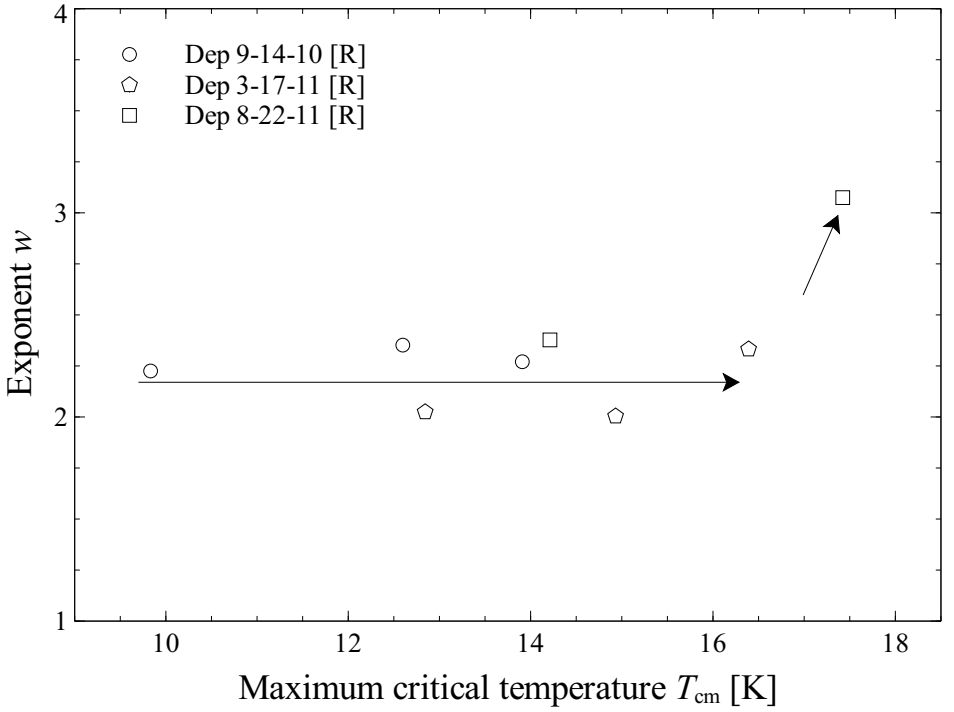

Figure 2.25: *Power-law exponent w reflecting the larger degree of strain sensitivity in $\mu_0 H_{c2}(0)$ in comparison to T_c (equation 2.12). The arrows are guides to the eye.*

stoichiometric composition, with $T_c \approx 18$ K and $\mu_0 H_{c2} \approx 30$ T. It is thus interesting to note that the main factor determining the strain sensitivity seems to be the superconducting properties (and, by extension, the tin content), rather than fabrication method, i.e. the microstructure. More specifically, the strain sensitivity observed in the bulk samples and the thin films is consistent, even though the grain diameters in the bulk samples are more than ten times larger, which points to the conclusion that the strain sensitivity is rather insensitive to the grain diameters for grain diameters on the order of several hundred nanometers and higher. Also, the strain sensitivity of T_c and $\mu_0 H_{c2}$ in deposition 3-17-11, which was deposited at 900 °C and contains larger grains, is nearly the same as for deposition 8-22-11, which was deposited at 700 °C and contains smaller grains (figure 2.8).

The degree of strain sensitivity in $\mu_0 H_{c2}(0)$ in comparison to T_c is often described with a power law description:

$$\mu_0 H_{c2}(0, \varepsilon_a) \propto T_c(\varepsilon_a)^w, \tag{2.12}$$

where w normally lies between 2 and 3 (see Ekin [83] and Taylor *et al.* [84]). The optimal value of w is determined for each of the samples and shown in figure 2.25. In the off-stoichiometric limit, w is around 2, while near stoichiometry $w \approx 3$. The arrows in the figure

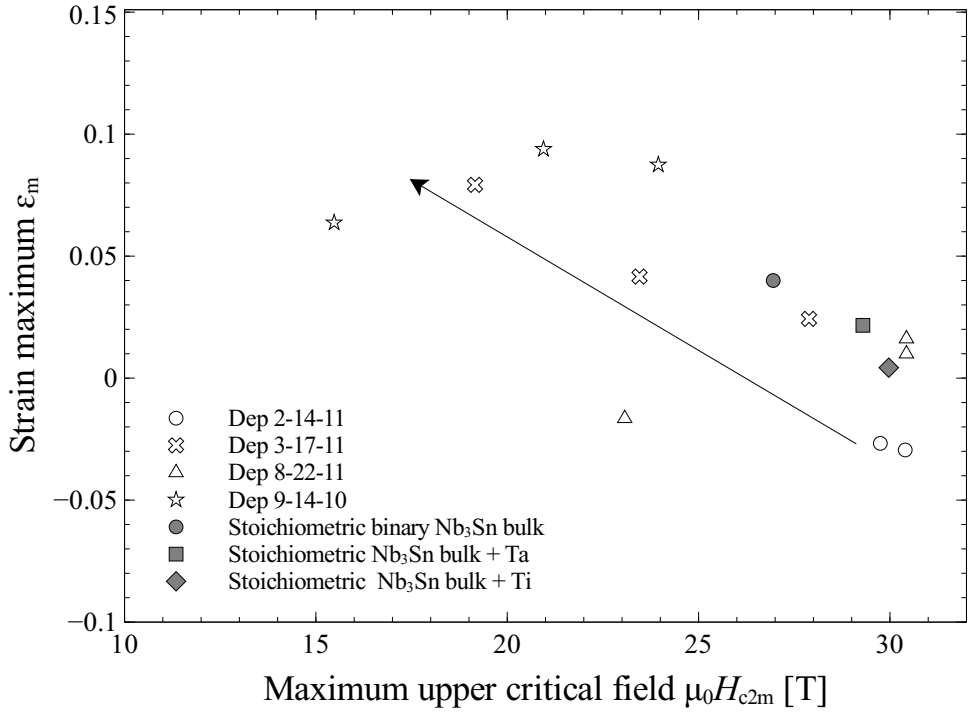

Figure 2.26: *Strain maximum ε_m (i.e. the applied strain ε_a at which $\mu_0 H_{c2}$ is maximum) as a function of $\mu_0 H_{c2m}$. The open and grey symbols represent measurements on thin films and on bulk samples respectively. The arrow is a guide to the eye.*

serve as guides to the eye. Note that the stoichiometric samples are omitted from this figure: Near stoichiometry, $\mu_0 H_{c2}(0)$ decreases with increasing T_c, which means that in a somewhat inhomogeneous sample, the resistively determined T_c reflects a different composition than the resistively determined $\mu_0 H_{c2}(0)$, which makes a comparison of the strain sensitivity of T_c and $\mu_0 H_{c2}(0)$ less useful. While one might wonder if the outlier at a critical temperature of 17.4 K is a measurement anomaly, further evidence of the accuracy of this data point is given in section 3.7.3.

Figure 2.26 indicates the strain at which $\mu_0 H_{c2}$ reaches a maximum. While ε_m does seem to be affected by composition, there is substantial variation between the samples, which is indicative for varying thermal pre-strains on the samples. Based on the strain state of the thin films at room temperature and the difference in thermal contraction between room temperature and 4 K, it was argued that the thin films are $0.07 \pm 0.04\%$ in tension (section 2.4.2). If the maxima in T_c and $\mu_0 H_{c2}$ are found when the samples are strain free, then ε_m is expected to be -0.07±0.04%, i.e. compression counters the tensile strain state of the thin film after cool down and thus can cause an increase in T_c and $\mu_0 H_{c2}$. While this is indeed the case for samples near stoichiometry, it does not apply for off-stoichiometric samples. A possible explanation is that the thermal expansion of off-stoichiometric Nb-Sn is somewhat

different from stoichiometric Nb_3Sn, leading to the observed (small) deviation.

2.4.10 Determination of $\mu_0 H_{c2}$ of niobium

As with the Nb-Sn samples, $\mu_0 H_{c2}$ of the niobium can be derived from the magnetic field dependence of T_c. According to Rosenblum *et al.* [85], the relation between critical temperature and magnetic field is described with:

$$\mu_0 H_{c2}(T) / \mu_0 H_{c2}(0) = 1 - \left(T/T_c\right)^2. \tag{2.13}$$

Figure 2.27 shows $\mu_0 H_{c2}$ as a function of temperature. As with the Nb-Sn samples, it is observed that T_c curves upwards near $\mu_0 H = 0$ T. It was previously shown by Rosenblum *et al.* [85] that in bcc Nb with $T_c > 7.7$ K $\mu_0 H_{c2}(0)$ increases with decreasing T_c. At lower magnetic field (i.e. $\mu_0 H < 1$ T), the resistively determined T_c reflects the less disordered niobium (i.e. lower ρ_n) with higher T_c and lower $\mu_0 H_{c2}(0)$, while at higher magnetic field it reflects the more disordered niobium (i.e. lower ρ_n) with lower T_c and $\mu_0 H_{c2}(0)$. Thus, the deviation of the empirical curve (equation 2.13) in figure 2.28 is a strong indication that the samples comprise Nb with varying degrees of disorder. Equation 2.13 is applied only to the measurements at elevated magnetic fields, with $\mu_0 H \geq 1$ T. The thus determined upper critical field $\mu_0 H_{c2}$ at $\varepsilon_a = 0\%$ is 2.6 T.

2.4.11 Strain dependence of T_c and $\mu_0 H_{c2}$ of the niobium samples

The T_c as a function of strain of a sample of bcc niobium was measured on a patterned and a regular niobium thin film sample (figure 2.14). As seen in figure 2.28, top, the critical temperatures of the longitudinal and transverse sections are nearly identical, with an average difference of 8 mK between the two sections, while the T_c value of the unpatterned sample is about 50 mK lower than the patterned sample. This difference could be due to either an error in the temperature measurement (which is estimated at 0.1 K absolute) or due to a slight difference in composition and morphology between the two samples. In comparison to the Nb-Sn, the strain sensitivity of the superconducting properties of bcc niobium is weak, a phenomenon that is explained in section 5.4.3.

The upper critical field $\mu_0 H_{c2}$ was determined as a function of applied strain for the unpatterned sample (figure 2.28, bottom). Consistent with the T_c measurement, the application of strain results in a weak increase in $\mu_0 H_{c2}$. Unfortunately, the upper critical field of the patterned sample could not be measured.

2.4.12 Conclusion

The U-spring test rig is discussed in terms of experimental aspects and characteristic results. The test rig allows for the measurement of the resistivity and critical current density as a function of temperature, magnetic field, and applied strain.

The longitudinal and transverse strain states of a thin film sample on the sample holder were determined through the use of a bi-axial strain gauge. The thermal pre-compression of the Nb-Sn and Nb samples was determined from XRD-measurements.

Strain was shown to affect the normal state resistivity of the Nb-Sn samples in an unusual

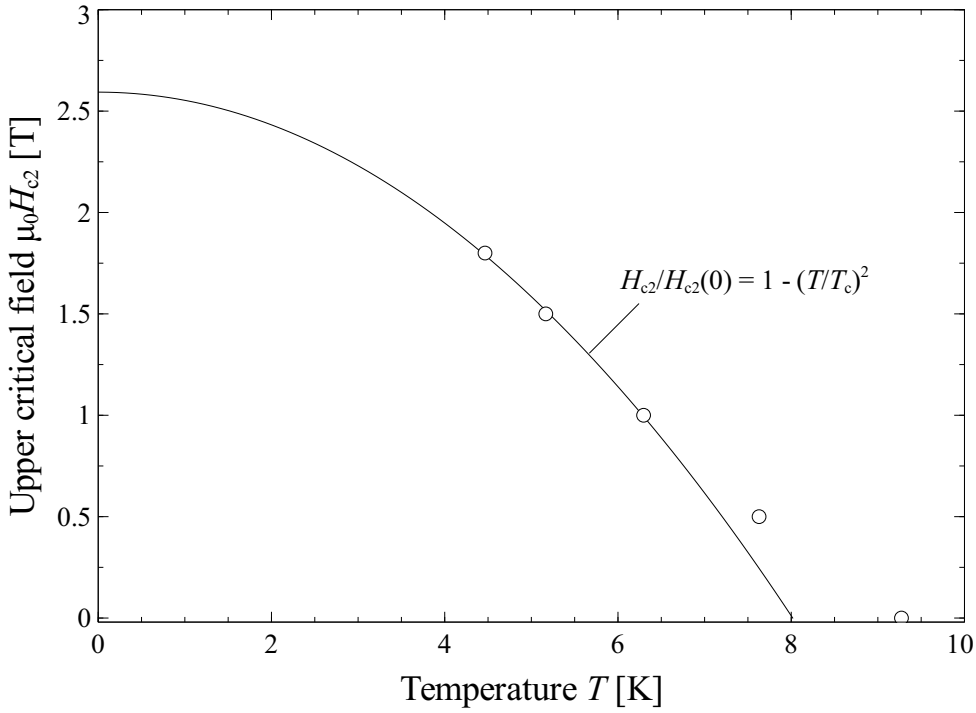

Figure 2.27: *$\mu_0 H_{c2}$ as a function of temperature of the niobium thin film dep2-12-13. Near $\mu_0 \mathrm{H} \approx 0$ T, T_c deviates from the behavior expected for a homogeneous sample [85].*

way resulting in a strong and anisotropic change in the normal state resistivity for the lower resistivity samples and a significantly weaker change for the higher resistivity samples. In contrast, it was shown that the effect of strain on the normal state resistivity of niobium is negligible.

Several mechanisms are considered that would explain the experimentally observed change in normal state resistivity. Geometrical effects are ruled out as a possible explanation as they would lead to a much smaller change in the normal state resistance. The strain dependence of ρ_n is consistently observed in different sample geometries, including regular Nb_3Sn bulk samples, regular Nb-Sn thin films, and patterned Nb-Sn thin films. The high degree of consistency between the measurement types indicates that the observed phenomenon is not a measurement anomaly. The behavior observed in a Nb_3Sn bulk sample overlaps with the behavior of Nb-Sn thin films, in spite of the fact that the typical grain diameter in the bulk sample is over ten times larger than the typical grain diameter in the thin films. This implies that the change in normal state resistivity is not related to the grain boundaries. Finally, the change in normal state resistivity with strain is weakly related to the temperature, but this effect is not large enough to explain the complete effect. The normal state resistivity changes because the residual resistivity (i.e. ρ_n at 0 K) changes, and the temperature dependent behavior is a smaller second-order effect. The relevance of these experimental observations

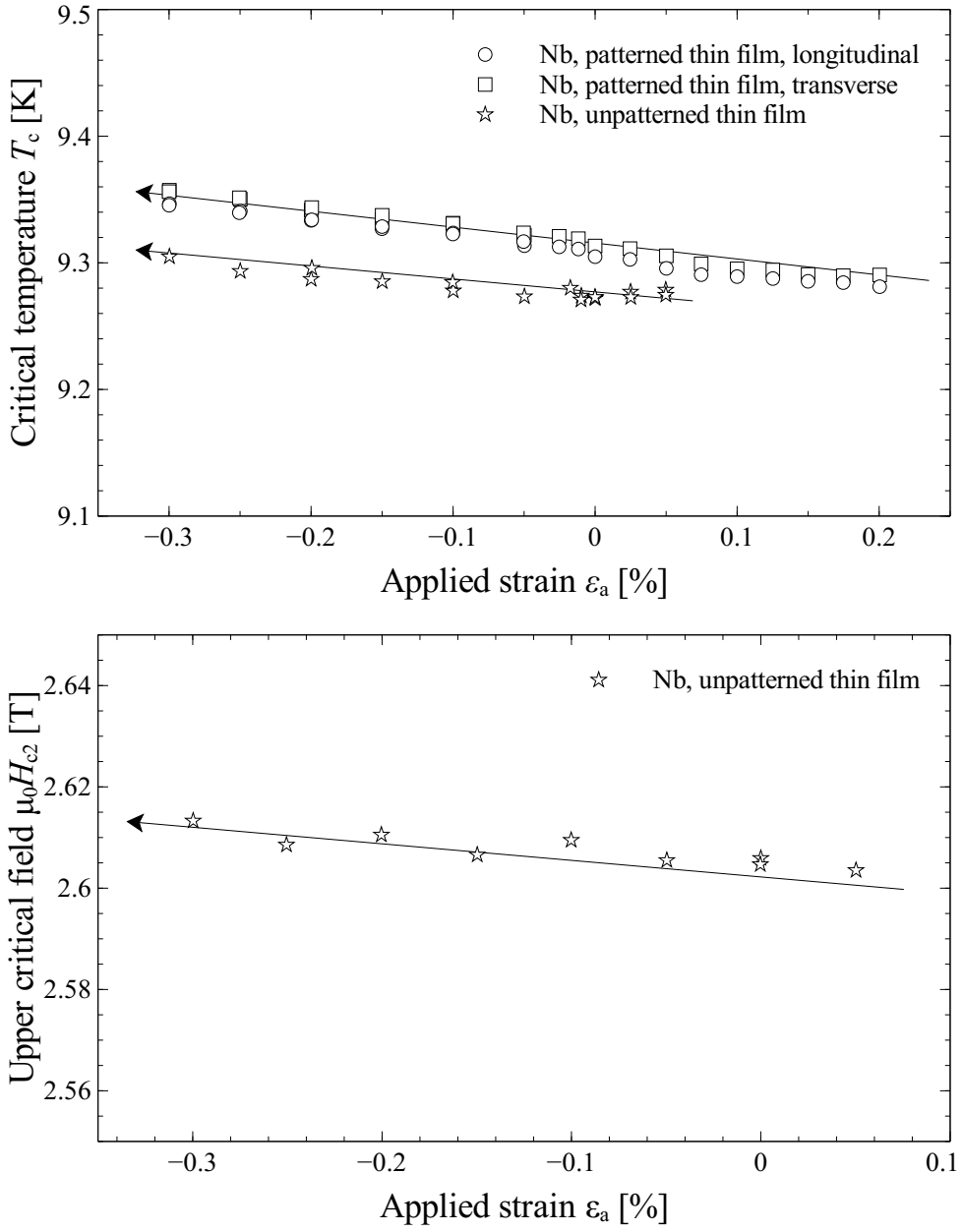

Figure 2.28: *T_c as a function of applied strain for a patterned and an unpatterned niobium sample (top) and $\mu_0 H_{c2}$ as a function of applied strain for the unpatterned niobium sample (bottom). The arrows are guides for the eye.*

is presented in section 5.4. It will be demonstrated that the underlying cause of the strain dependence of ρ_n can also explain the strain sensitivity of the superconducting properties.

The Nb-Sn thin film and bulk samples have a range of superconducting properties, with T_c varying between 9.8 and 18.1 K, and $\mu_0 H_{c2}$ between 15.5 and 30.4 T. The composition dependent critical temperature indicates that the off-stoichiometric thin film samples (with a composition distribution width ranging between 2 and 5 at.% Sn) are less homogeneous than the stoichiometric thin films (with a composition distribution width of the order of 0.5 at.% Sn). The $\mu_0 H_{c2}(0)$ versus T_c relation is consistent with literature values. The niobium sample has a T_c of 9.3 K and a $\mu_0 H_{c2}$ value of 2.6 T. The observed temperature dependence of $\mu_0 H_{c2}$ is consistent with a bcc niobium sample that contains both weakly disordered niobium (evident from the high T_c) and strongly disordered niobium (evident from the high $\mu_0 H_{c2}(0)$).

The strain sensitivity of T_c and $\mu_0 H_{c2}$ of the Nb-Sn samples increase with increasing T_c and $\mu_0 H_{c2}$, which indicates that samples with higher tin concentration are more strain sensitive. However, near stoichiometry (i.e. $T_c > 17$ K and $\mu_0 H_{c2}(0) \approx 29$ T) the observed strain sensitivity decreases strongly. As discussed in section 5.5.4, this can be related to the martensitic transformation that occurs in low-resistivity Nb_3Sn. In contrast, T_c and $\mu_0 H_{c2}$ of the niobium thin films weakly increase with applied compressive strain, a phenomenon that is further explained in section 5.4.3.

2.5 Conclusion

This chapter gave a general overview of sample fabrication, characterization, and determination of the superconducting properties and normal state properties, while the detailed analysis of these properties is discussed in the following chapters.

Bulk samples were investigated in terms of their composition and morphology. In spite of nominal off-stoichiometry in the starting powder ratios, the binary samples and the samples with titanium and tantalum additions were shown to consist of stoichiometric Nb_3Sn, niobium, and regions of tantalum or titanium. In contrast, the samples with copper addition comprise both stoichiometric and off-stoichiometric Nb-Sn.

A binary bulk sample was investigated in terms of $\mu_0 H_{c2}$ through heat capacity measurements, and it was found that while the binary sample exhibits a narrow T_c distribution near 17.5 K, the $\mu_0 H_{c2}(0)$ ranges between 22.4 and 29.4 T.

Thin film samples were fabricated as an alternative to the bulk samples, allowing for improved control of composition and its distribution. The fabrication process involved simultaneous magnetron sputtering of niobium and tin onto a heated R-plane sapphire substrate. This results in dense, highly textured, polycrystalline Nb-Sn films with various compositions. Unlike the bulk samples, both stoichiometric and off-stoichiometric single phase films were produced.

The films were determined to be predominantly (100) oriented in the out-of-plane direction and randomly oriented in the in-plane direction. A niobium film was also produced in a high power impulse magnetron sputtering process (HiPIMS), resulting in a dense, highly textured niobium film. Patterning was applied to some of the thin films in order to measure the orientation-dependent normal state resistivity and the critical current density.

The U-spring test rig was used for resistivity and critical current density measurements as a function of temperature, magnetic field, and applied strain. The critical current is discussed in detail in the next chapter. Uni-axial strain affects the normal state resistivity in an anistropic manner. The degree of strain sensitivity correlates to the magnitude of the normal state resistivity. In contrast, the normal state resistivity of the niobium is nearly independent of applied strain. The results and implications of a strain sensitive ρ_n are discussed in detail in chapter 5.

The strain sensitivity, i.e. the amount of reduction of T_c and $\mu_0 H_{c2}(0)$ with applied strain correlate with the overall magnitude of the superconducting properties and by extension with the composition. In general, the observed strain sensitivity increases with increasing T_c and $\mu_0 H_{c2}$, only to drop near $T_c \approx 18$ K and $\mu_0 H_{c2} \approx 30$ T, i.e. when approaching the stoichiometric composition. In contrast, T_c and $\mu_0 H_{c2}$ of the niobium thin film only weakly increases with compressive strain, which will be discussed further in chapter 5.

Chapter 3

Strain Dependent Critical Current Density of Nb_3Sn and Nb-Ti

3.1 Introduction

The effect of temperature, magnetic field and strain on the critical current density of Nb-Ti and Nb_3Sn is introduced. The three most commonly used Nb_3Sn critical current density scaling relations and a commonly used Nb-Ti critical current density scaling relation are evaluated. The scaling relations are shown to be largely indistinguishable except for some subtle differences.

The scaling descriptions for Nb_3Sn are the Mentink-Arbelaez-Godeke (MAG) scaling relation [86], as used by the nuclear fusion [87] and high energy physics communities [88], the Ekin scaling relation [83, 89], and the Durham scaling relation [84, 90]. Seven different descriptions that describe the normalized upper critical field of Nb_3Sn as a function of uni-axial strain are discussed. The difference between these descriptions is that they were formulated by various authors, that the strain range in which they are valid varies between the descriptions, and the mechanism which explains the strain sensitivity in Nb_3Sn varies between the descriptions as well.

Also presented is the scaling relation by Bottura *et al.* [91] which describes the critical current density of Nb-Ti. Even more scaling relations were developed, and comprehensive overviews of these scaling relations are published elsewhere [89, 92, 41].

An experiment is presented for measuring the critical current density of stoichiometric and off-stoichiometric Nb-Sn as a function of temperature and magnetic field, as well as strain, applied either longitudinally or transversely to the current direction. The MAG relation relates the strain sensitivity of the critical current density to strain sensitivity of the superconducting properties T_c and $\mu_0 H_{c2}(0)$. T_c is isotropic while $\mu_0 H_{c2}(0)$ is close to isotropic (with a maximum observed direction dependent variation from the average of less than 3%, see Foner *et al.* [67]), which implies that the critical current density as a function of applied strain is independent of whether strain is applied parallel or perpendicular to the current flow direction, a hypothesis that is extensively discussed here.

3.2 Underlying physics of the critical current density

3.2.1 Lorentz force and bulk pinning force

The critical current for a given temperature, magnetic field and strain in a type II superconductor reflects a force balance between the bulk pinning force and the Lorentz force that is exerted on the fluxlines.

A type-II superconductor like Nb_3Sn is permeated with flux lines when a magnetic field is applied that is larger than $\mu_0 H_{c1}$ (approximately 50 mT for stoichiometric Nb_3Sn). The core of a flux line is in normal state, and this permeation with normal cores is energetically favorable, due to the negative surface energy of the boundaries between superconducting and normal states [93].

A Lorentz force F_l is exerted on the flux lines when current flows through the material in the presence of a non-zero magnetic field, with:

$$\overrightarrow{F_L} \equiv \overrightarrow{J_c} \times \overrightarrow{B}\,. \tag{3.1}$$

Movement of flux lines results in a non-zero electric field, following $\nabla \times E = -\delta B/\delta t$, and thus dissipation. However, flux lines can be held in place by so-called pinning sites, which are imperfections in the material such as grain boundaries in the case of Nb_3Sn [94, 95] or α-Ti precipitates in the case of NbTi [117]. It is energetically favorable for the normal cores of flux lines to overlap with the pinning cites and energetically unfavorable for the flux lines to move away from this configuration. Moreover, flux lines exert a repelling force on each other, which results in collective pinning. In Nb_3Sn where the pinning site density is insufficient to pin each individual flux line, through collective behavior the pinned flux lines also hold the other flux lines in place (figure 3.6).

Provided the bulk pinning force is larger than the Lorentz force exerted on the flux-line lattice, the flux lines are prevented from macroscopic movement, and the electric field along the superconductor remains zero. The critical current density is the current density at which the Lorentz force and the bulk pinning force are equally strong. Exceeding the critical current density results in collective movement of the flux lines and a non-zero macroscopic electric field.

The critical current density is not to be confused with the significantly larger depairing current density, which is the current density at which the kinetic energy of the moving electrons exceeds the pairing energy.

3.2.2 Experimental critical current density

The macroscopic electric field in a superconductor as a function of current density, see for instance figure 2.18, can be empirically described rather well with a power law:

$$E = E_c \left(\frac{J}{J_c} \right)^n, \tag{3.2}$$

where J_c is the critical current density, and n is determined by various factors like the homogeneity of the conductor [33] and the effect of temperature on the movement of flux lines [100], and E_c is an arbitrary electric field criterion such as 10 μVm^{-1}.

3.3 Tools for measuring temperature, magnetic field, and uni-axial strain dependent critical current density

Besides the U-spring test rig, which was developed by Godeke *et al.* [33, 71, 72], various other experimental tools were developed to measure the critical current of Nb_3Sn conductors as a function of temperature, magnetic field, and uni-axial strain. Well-known tools are the PACMAN, developed by Godeke *et al.* [107] and the Walters spring, developed by Walters *et al.* [108]. The main difference of these tools with the U-spring test rig is the larger length of the homogeneously strained region, which allows for a more homogeneously distributed current inside the conductor as well as a higher voltage resolution, which sometimes is an advantage.

3.4 Nb_3Sn scaling relations

3.4.1 Nb_3Sn critical current density following the MAG relation

The MAG relation is derived from Ekin's originally proposed parameterization model [83]. It was refined by Godeke *et al.* [33, 103, 106] and accepted as the standard scaling relation by the HEP [86] and ITER [92] communities.

Subsequently, the MAG relation was mathematically simplified for the purpose of making the description more accessible and to show a clear separation of temperature and magnetic field on one hand, and strain on the other hand [104, 105]. The critical current density is expressed as a function of temperature, magnetic field, and strain with:

$$J_c(T,\mu_0 H,\varepsilon) = C_I \left(1-t^2\right)^{\mu} h^{p-1}(1-h)^q, \tag{3.3}$$

$$C_I = \sqrt{2} C^* \mu_0 H_c^*(0), \tag{3.4}$$

$$t \equiv \frac{T}{T_c(0,\varepsilon)}, \tag{3.5}$$

$$h \equiv \frac{H}{H_{c2}(T,\varepsilon)}, \tag{3.6}$$

where C^* is a normalization constant related to the maximum bulk pinning force, p and q are free parameters describing the magnetic field dependence of the pinning force, $T_c(0, \varepsilon)$ is the critical temperature in the absence of applied magnetic field for a given strain, $\mu_0 H_{c2}(T, \varepsilon)$ is the upper critical field at a given temperature and strain, and ε represents the three-dimensional strain state of the Nb_3Sn.

μ is a scaling parameter that describes the temperature dependence of the critical current density and is typically set to 1. However, as pointed out by a few authors [104, 105, 92] and also demonstrated here, the temperature dependence of Nb_3Sn conductors varies, which means that this parameter is in fact conductor dependent. A possible explanation is that practical Nb_3Sn conductors are inhomogeneous in composition.

This can be illustrated with a mental exercise. Assume that the temperature dependence of a perfectly homogeneous conductor scales as $(1-t^2)$. Then one can imagine an inhomogeneous conductor that consists of two perfectly homogeneous Nb_3Sn regions with different critical temperatures (for example 15 K and 18 K) but otherwise having identical microscopic properties. The current density of this conductor is then described with:

$$I_{c1}(T,\mu_0 H,\varepsilon) = \left(1-(T/15)^2\right) f(\mu_0 H,\varepsilon) \text{ for } T \le 15K, \tag{3.7}$$

$$I_{c2}(T,\mu_0 H,\varepsilon) = \left(1-(T/18)^2\right) f(\mu_0 H,\varepsilon) \text{ for } T \le 18K, \tag{3.8}$$

$$I_{c,tot} = I_{c1} + I_{c2}, \tag{3.9}$$

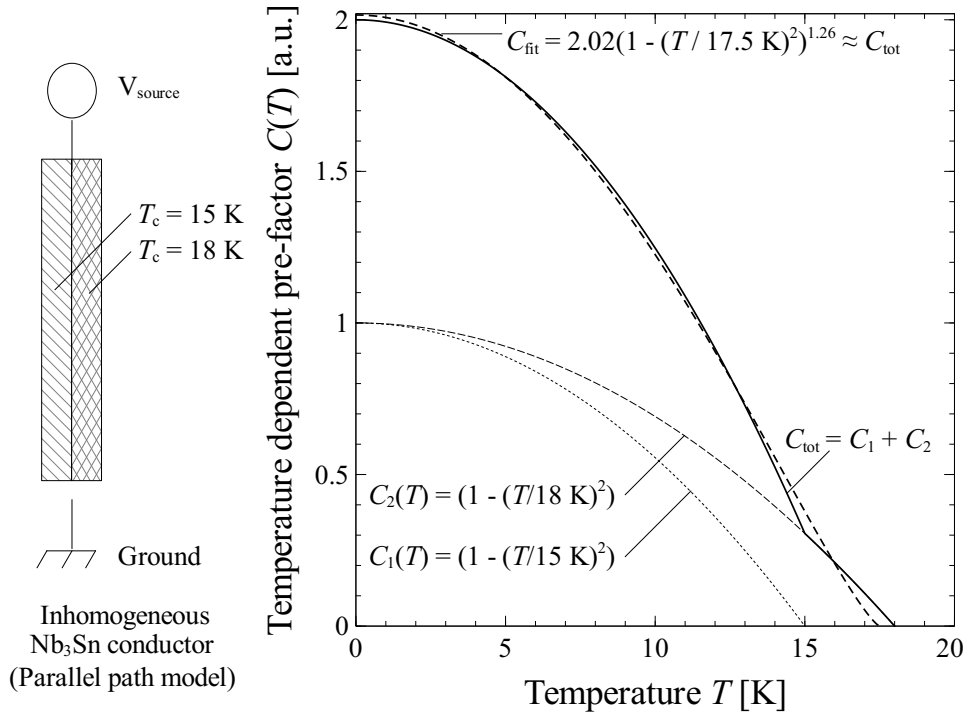

Figure 3.1: *Critical current density pre-factor $C(T)$ as a function of temperature. Illustration of compositional inhomogeneity resulting in $\mu > 1$.*

where $f(\mu_0 H, \varepsilon)$ describes the magnetic field and strain dependence of the critical current, and I_{c1} and I_{c2} describe the two parallel sections with different critical temperatures. As the two sections are parallel, the total critical current of this imaginary wire is simply the sum of the two sections. As shown in figure 3.1, the summation of the two sections results in a 'tail' in the temperature dependent critical current density that is similar to the 'tail' that is observed when sections with different upper critical fields are shunted in a parallel fashion as described by Cooley *et al.* [96]. As is also illustrated in figure 3.1, this tail can be approximated by using a description of the temperature dependence with a free parameter μ:

$$I_{c,tot} \approx 2.02\left(1-(T/17.5)^2\right)^{\mu} f(\mu_0 H, \varepsilon) \text{ for } T \leq 17.5K, \tag{3.10}$$

where μ is equal to 1.26 for this imaginary conductor.

In summary, if the temperature dependence of a perfectly homogeneous conductor is accurately described with $\mu = 1$, then it follows that a somewhat inhomogeneous conductor is more accurately described with $\mu \neq 1$.

In the MAG relation, the temperature dependence of the upper critical field is described with

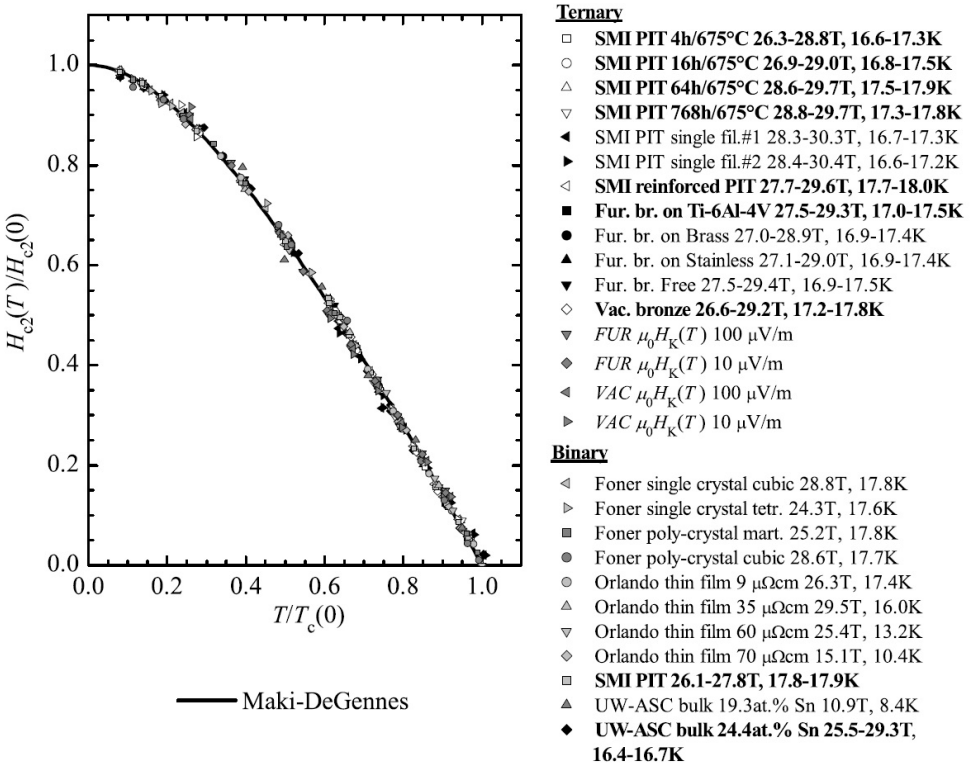

Figure 3.2: *Reduced upper critical field as a function of reduced temperature. The applicability of the Maki-DeGennes description of $\mu_0 H_{c2}$ is demonstrated on a wide range of compositions for various types of Nb_3Sn superconductors, after Godeke et al. [48].*

the Maki-DeGennes description (section 2.2.5). It has been convincingly demonstrated that this description accurately describes the temperature dependence of the upper critical field $\mu_0 H_{c2}$ of various Nb_3Sn conductors over a wide range of compositions and strain states [33, 48] (figure 3.2). The temperature dependence of $\mu_0 H_{c2}$ can be approximated by [103]:

$$h_{c2} \approx \left(1 - t^{1.52}\right), \tag{3.11}$$

which provides an accurate approximation over the full temperature range with an average error of 0.7% and a standard deviation of 0.4%. The strain sensitivity of the upper critical field is captured in a parameter $s(\varepsilon) \leq 1$, following:

$$\mu_0 H_{c2}(0,\varepsilon) = \mu_0 H_{c2m}(0) s(\varepsilon), \tag{3.12}$$

where $\mu_0 H_{c2}(0, \varepsilon)$ is the upper critical field as a function of strain and $\mu_0 H_{c2m}(0)$ is the maximum upper critical field of the material.

Similar to the upper critical field, the critical temperature is also affected by strain. The relation between the strain sensitivity of the upper critical field and that of the critical temperature is described by a power law [83], with:

$$T_c(0,\varepsilon) = T_c(0,\varepsilon_m)s(\varepsilon)^{1/w}, \tag{3.13}$$

where $T_c(0, \varepsilon)$ is the critical temperature as a function of strain, $T_{cm}(0)$ is the maximum critical temperature and w is a composition dependent parameter, which for nearly stoichiometric Nb_3Sn is approximately equal to 3.

The strain dependence of $s(\varepsilon)$ is described by a relation by Arbelaez *et al.* [106], which is discussed in the next section.

3.4.2 Nb_3Sn critical current density following Ekin

Ekin, in an updated version [89] of his original scaling relation [83] proposed to describe the critical current density for Nb_3Sn, with:

$$J_c(T,\mu_0 H,\varepsilon) = \frac{C_e}{\mu_0 H} s(\varepsilon)^{\gamma} f(t) f(h), \tag{3.14}$$

$$f(t) = \left(1-t^2\right)^{\mu}\left(1-t^{1.52}\right)^{\eta-\mu}, \tag{3.15}$$

$$f(h) = h^p(1-h)^q, \tag{3.16}$$

where p, q, and C_e are free parameters. The approximation to the Maki-DeGennes relation (equation 3.11) is used to find:

$$\mu_0 H_{c2}(T,\varepsilon) = \mu_0 H_{c2m}(0) s(\varepsilon)\left(1-t^{1.52}\right), \tag{3.17}$$

and the normalized magnetic field is defined as:

$$h = \frac{H}{H_{c2}(T,\varepsilon)} = \frac{H}{H_{c2m}(0)}\left(1-t^{1.52}\right)^{-1} s(\varepsilon)^{-1}. \tag{3.18}$$

Using equation 3.18, equation 3.14 is reformulated as:

$$J_c(T,\mu_0 H,\varepsilon) = C_I s(\varepsilon)^{\gamma-1}\left(1-t^2\right)^{\mu}\left(1-t^{1.52}\right)^{\eta-\mu-1} h^{p-1}(1-h)^q, \tag{3.19}$$

$$C_I = \frac{C_e}{\mu_0 H_{c2m}(0)}. \tag{3.20}$$

Ekin observed that $\gamma \approx 1$ [83, 109, 110] and that in order to accurately describe the temperature dependence of various Nb_3Sn samples, only one of the two parameters μ and η is required as a free parameter [89]. With $\gamma = 1$ and setting $\eta = \mu + 1$, equation 3.19 is

reduced to:

$$J_c(T,\mu_0 H,\varepsilon) = C_1\left(1-t^2\right)^{\mu} h^{p-1}(1-h)^q, \tag{3.21}$$

which is identical to equation 3.3. Thus, even though the starting equations seem very different, the two descriptions are in fact identical.

3.4.3 Nb_3Sn critical current density following the Durham group

The Durham group proposed for J_c as described by Taylor *et al.* [84]:

$$J_c\left(T,\mu_0 H,\varepsilon_I\right) = A\left(\varepsilon_I\right)\left(T_c\left(\varepsilon_I\right)\left(1-t^2\right)\right)^2\left(\mu_0 H_{c2}\left(T,\varepsilon_I\right)\right)^{n-3} h^{p-1}(1-h)^q, \tag{3.22}$$

$$\mu_0 H_{c2}\left(T,\varepsilon_I\right) = \mu_0 H_{c2}\left(0,\varepsilon_I\right)\left(1-t^{\nu}\right), \tag{3.23}$$

$$\left(\frac{A\left(\varepsilon_I\right)}{A\left(0\right)}\right)^{1/u} = \left(\frac{H_{c2}\left(0,\varepsilon_I\right)}{H_{c2}\left(0,0\right)}\right)^{1/w} = \frac{T_c\left(\varepsilon_I\right)}{T_c\left(0\right)}. \tag{3.24}$$

In a detailed overview of scaling of various high J_c Nb_3Sn conductors by Lu *et al.* [90], it was shown that optimal values for n, ν, w, and u are 2.5, 1.5, 2.2, and 0, respectively, while the remaining parameters are free parameters. Equation 3.23 is approximately the same as equation 3.11 (because $1.50 \approx 1.52$). Using the fixed values of n, ν, w and u, equations 3.22, 3.23, and 3.24 can be reformulated into a mathematically equivalent form:

$$J_c\left(T,\mu_0 H,\varepsilon_I\right) = C_1 s(\varepsilon_I)^{9/22} f\left(T\right) h^{p-1}(1-h)^q, \tag{3.25}$$

$$f\left(T\right) = \left(1-t^2\right)^2\left(1-t^{1.5}\right)^{-0.5}, \tag{3.26}$$

$$C_1 = A\left(0\right) T_{cm}^2(\mu_0 H_{c2m}(0))^{-0.5}, \tag{3.27}$$

$$s\left(\varepsilon_I\right) = \frac{H_{c2}\left(0,\varepsilon_I\right)}{H_{c2m}\left(0\right)}. \tag{3.28}$$

For $0.1 < t < 1$, the temperature dependent part is approximated by:

$$f\left(T\right) = \left(1-t^2\right)^2\left(1-t^{1.5}\right)^{-0.5} \approx 1.03\left(1-t^2\right)^{\mu}, \tag{3.29}$$

with μ = 1.38 (figure 3.3). Including this approximation, the general form is:

$$J_c\left(T,\mu_0 H,\varepsilon_I\right) = C_D s(\varepsilon_I)^{9/22}\left(1-t^2\right)^{1.38} h^{p-1}(1-h)^q. \tag{3.30}$$

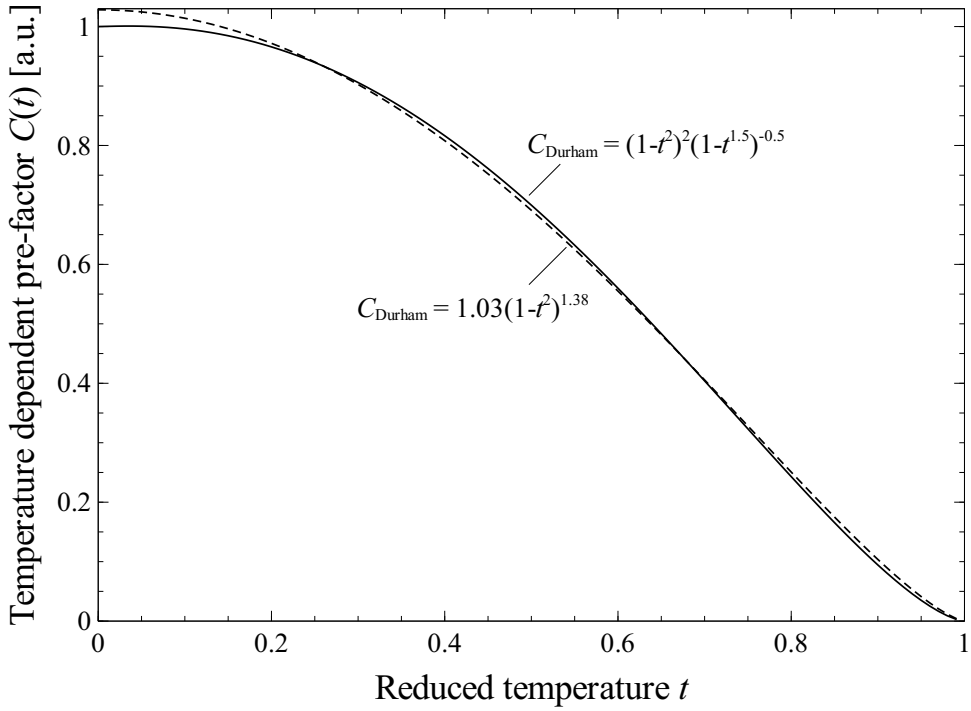

Figure 3.3: *Critical current density pre-factor as a function of temperature of the Durham scaling relation and a simpler approximation.*

$$C_{\mathrm{D}} = 1.03A\,(0)\,{T_{\mathrm{cm}}}^2(\mu_0 H_{\mathrm{c2m}}(0))^{-0.5}. \tag{3.31}$$

At constant temperature and magnetic field, the change in critical current due to a strain induced change in h and t dominate the strain dependence of J_{c} , i.e. :

$$s(\varepsilon_{\mathrm{I}})^{9/22} \approx 1. \tag{3.32}$$

Inserting this approximation into equation 3.30, the Durham description reduces to:

$$J_{\mathrm{c}}\,(T, \mu_0 H, \varepsilon_{\mathrm{I}}) = C_{\mathrm{D}}\left(1 - t^2\right)^{1.38} h^{p-1}(1-h)^q. \tag{3.33}$$

Thus, the Durham scaling relation is nearly identical to the MAG relation (equation 3.3) and Ekin's scaling description (equation 3.21), with the main difference being a fixed value of μ equal to 1.38. Thus, a striking conclusion is reached: the scaling following MAG, Ekin, and Durham are nearly indistinguishable. This is a powerful testament to the validity of the MAG relation, as competing groups of scientists developed different scaling relations that converge onto the same result.

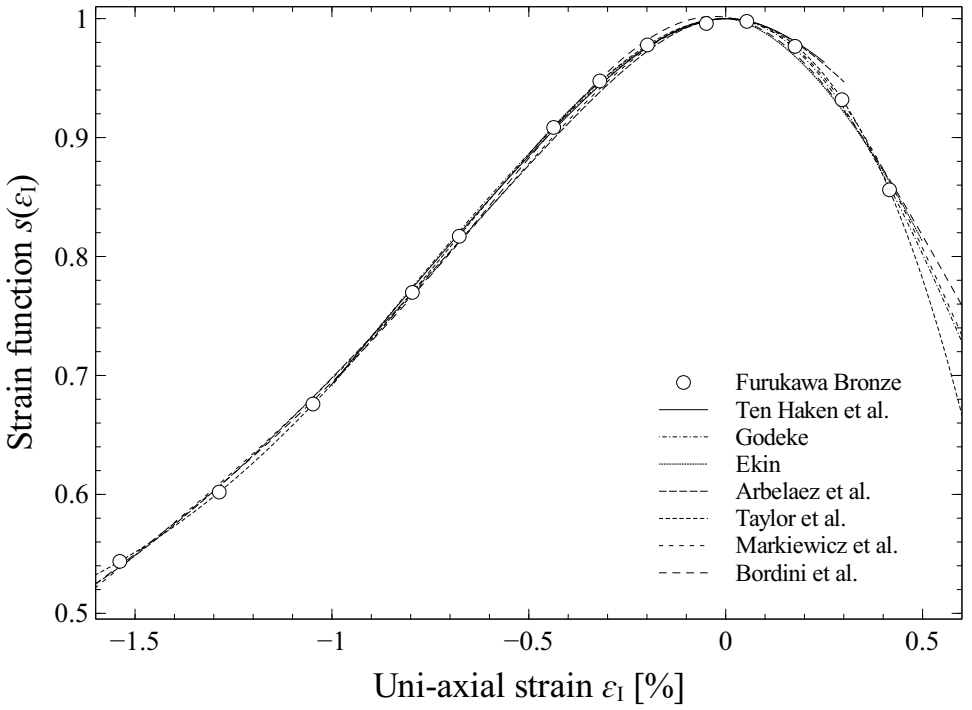

Figure 3.4: *Strain function s as a function of uni-axial strain. A variety of strain function descriptions are compared to experimental data, after Lu et al. [90]. An additional normalization factor was added to the strain function description by Bordini et al. [99].*

3.5 Strain function $s(\varepsilon_I)$

3.5.1 Introduction

A number of different descriptions were developed describing the strain dependence of $\mu_0 H_{c2}(0)$ through the strain function $s(\varepsilon_I)$, defined as:

$$s(\varepsilon_I) \equiv \frac{\mu_0 H_{c2}(0, \varepsilon_I)}{\mu_0 H_{c2}(0,0)}. \tag{3.34}$$

The parameter ε_I is related to the applied uni-axial strain ε_a and a term ε_m that is equal to ε_a at which the superconducting properties are at a maximum:

$$\varepsilon_I = \varepsilon_a - \varepsilon_m. \tag{3.35}$$

In this section, some of the most commonly used strain function descriptions are discussed, and their applicability is illustrated in figure 3.4.

3.5.2 Strain function description by Ten Haken *et al.*

The deviatoric strain description by Ten Haken *et al.* [101] is based on the idea that a change in $\mu_0 H_{c2}(0)$ is proportional to the second strain invariant in addition to rounding near the maximum $\mu_0 H_{c2}(0)$, which is described with a remaining strain term $\varepsilon_{0,a}$. It is the first description that accounts for the three-dimensional strain state. This description was used to parameterize the observed strain sensitivity in the superconducting properties of the Nb-Sn bulk samples and thin films:

$$s(\varepsilon_I) = \frac{1 - C_{a,Hc2}\sqrt{(\varepsilon_I)^2 + (\varepsilon_{0,a})^2}}{1 - C_{a,Hc2}\varepsilon_{0,a}}. \tag{3.36}$$

The value of this description is in its simplicity, as well as making a verifiable prediction for any strain state rather than just the strain state that is found in uni-axial strain experiments. The drawback of this description is that it does not account for a slight asymmetry near the maximum of $s(\varepsilon_I)$, nor the upward curvature in the observed strain function at high compressive strain.

3.5.3 Strain function description by Godeke *et al.*

The strain function by Godeke *et al.* [33] is an extension of the deviatoric strain model with an empirical correction for the asymmetry of the strain function near the maximum $\mu_0 H_{c2}(0)$, with:

$$s(\varepsilon_I) = \frac{C_{a,1}\left(\sqrt{(\varepsilon_{sh})^2 + (\varepsilon_{0,a})^2} - \sqrt{(\varepsilon_I - \varepsilon_{sh})^2 + (\varepsilon_{0,a})^2}\right) - C_{a2}\varepsilon_I}{1 - C_{a,1}\varepsilon_{0,a}} + 1, \tag{3.37}$$

$$\varepsilon_{sh} = \frac{C_{a,2}\varepsilon_{0,a}}{\sqrt{C_{a,1} + C_{a,2}}}. \tag{3.38}$$

The application of this correction increases the strain range in which the Deviatoric strain model is applicable, although this description does not account for the upward curvature at high compressive strains. Note that equation 3.37 is identical to equation 3.36 when $C_{a,2}$ is set to 0.

3.5.4 Strain function description by Arbelaez *et al.*

The strain description by Arbelaez *et al.* [106] is also an extension of the Deviatoric strain description. It relates the strain function to the third invariant as well as the second, and thus accounts for the upward curvature at high compressive strain:

$$s(\varepsilon_I) = \frac{1 - C_{a,1}\sqrt{(\varepsilon_I)^2 + (\varepsilon_{0,a})^2} - C_{a,2}\left((\varepsilon_I)^3 - 3(\varepsilon_{0,a})^2\varepsilon_I\right)}{1 - C_{a,1}\varepsilon_{0,a}}. \tag{3.39}$$

The benefit of this description is, similar to the Deviatoric strain model, that a general pre-

diction is made which relates the strain function to the three-dimensional strain state of the material. Note that equation 3.39 is identical to equation 3.36 when $C_{a,2}$ is set to 0.

3.5.5 Strain function description by Ekin

The description by Ekin [83] relates the strain function to ε_I in the case of uni-axial strain:

$$s(\varepsilon_I) = \left(1 - a|\varepsilon_I|^{1.7}\right). \tag{3.40}$$

This description is very simple, and still accounts for the asymmetry in the strain function by using different values for a depending on whether ε_I is positive or negative. The drawback is that it is only applicable at moderate strains.

3.5.6 Strain function description by Taylor *et al.*

The strain function by Taylor *et al.* [84] uses a polynomial form:

$$s(\varepsilon_I) = 1 + c_2(\varepsilon_I)^2 + c_3(\varepsilon_I)^3 + c_4(\varepsilon_I)^4. \tag{3.41}$$

This simple and compact description very accurately describes the strain function in the case of uni-axial strain without addressing the underlying physics.

3.5.7 Strain function description by Markiewicz

The strain function by Markiewicz [97] is very similar to the strain function by Taylor *et al.*, and describes the strain function in the case of uni-axial strain, with:

$$s(\varepsilon_I) = \frac{1}{1 + c_2(\varepsilon_I)^2 + c_3(\varepsilon_I)^3 + c_4(\varepsilon_I)^4}. \tag{3.42}$$

By the author's own account, this description is empirical, although the author did present a model of the underlying physics elsewhere [98], relating the strain function to changes in the vibrational properties of the Nb_3Sn. This model is discussed further in section 5.4.2.

3.5.8 Strain function by Bordini *et al.*

The most recent addition is the strain function by Bordini *et al.* [99], which describes the strain function as a function of uni-axial strain, with:

$$s(\varepsilon_I) = \frac{\exp\left(-C_1\left(\frac{J_2+3}{J_2+1}\right)J_2\right) + \exp\left(-C_1\left(\frac{I_1^2+3}{I_1^2+1}\right)I_1^2\right)}{2}, \tag{3.43}$$

$$I_1 = (1-2\nu)\,\varepsilon_a + \varepsilon_{10} + 2\varepsilon_{t0}, \tag{3.44}$$

$$J_2 = \left(\frac{1}{3}\right)(\varepsilon_{10} - \varepsilon_{t0} + (1+\nu)\,\varepsilon_a)^2, \tag{3.45}$$

$$\varepsilon_{t0} = -\nu\varepsilon_{10} + K. \tag{3.46}$$

The various parameters are optimized to match the experimental observations of high-J_c Nb_3Sn wires. According to the authors, this approach makes this description highly predictive (i.e. only a limited strain range needs to be measured in order to accurately predict the full strain range). An unusual feature is that this strain function is not normalized.

3.5.9 Conclusion

A variety of descriptions of the strain function are discussed. Some are applicable over a rather limited range while others are applicable over the entire range of practical strain.

While the descriptions match the observed behavior well, they rely on free parameters to relate the change in superconducting properties to a strain related property (applied strain, strain energy, or pressure) in an empirical fashion. In order to fully understand the underlying physics of strain sensitivity of the superconducting properties, it is important to calculate the strain sensitivity of the superconducting properties without the use of free parameters. Such a calculation is presented in chapter 5.

3.6 Nb-Ti critical current density description by Bottura *et al.*

3.6.1 Similarities between the critical current density descriptions for Nb-Ti and Nb_3Sn

A critical current density relation was formulated by Bottura *et al.* [91], with:

$$J_c(T,\mu_0 H) = \frac{C_B}{\mu_0 H} h^p (1-h)^q \left(1 - t^{1.7}\right)^\gamma, \tag{3.47}$$

$$t = \frac{T}{T_c(0)}, \tag{3.48}$$

$$h = \frac{H}{H_{c2}(T)}, \tag{3.49}$$

where C_B, p, q and γ are free parameters and the effect of strain is considered negligible. The temperature dependence of the upper critical field is described following [111, 112]:

$$\mu_0 H_{c2}(T) = \mu_0 H_{c2}(0)\left(1 - t^{1.7}\right). \tag{3.50}$$

When combining equations 3.47, 3.49 and 3.50, the critical current density can be reformulated:

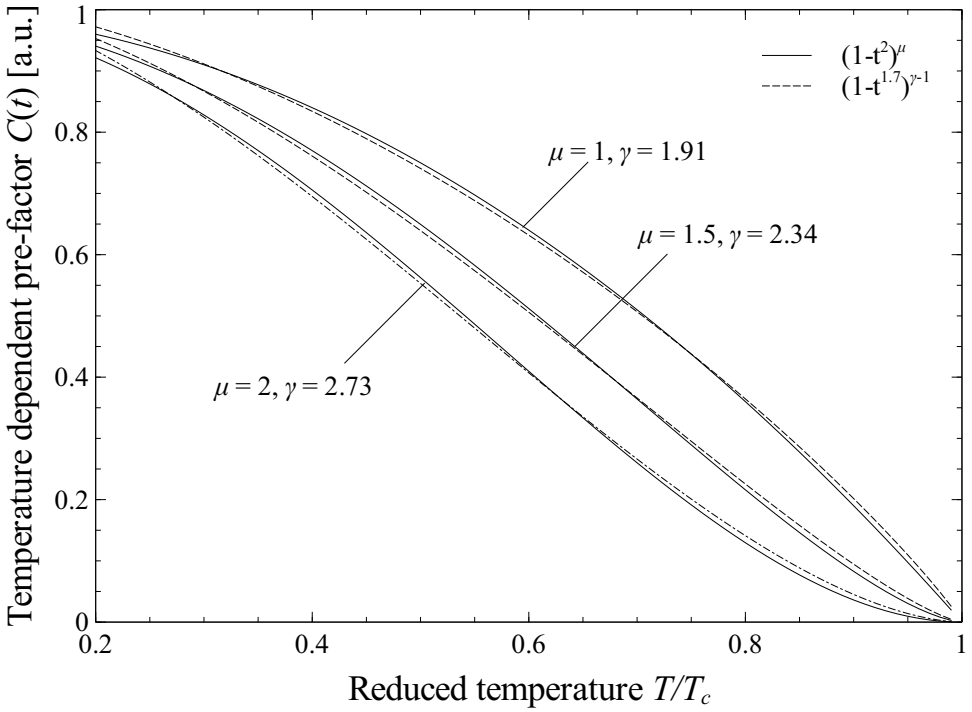

Figure 3.5: *Critical current density pre-factor as a function of temperature. The temperature dependent parts of equations 3.21 and 3.51 are shown to be approximately equal for various values of γ.*

$$J_c(T, \mu_0 H) = C_I \left(1 - t^{1.7}\right)^{\gamma-1} h^{p-1} (1-h)^q, \tag{3.51}$$

$$C_I = \frac{C_B}{\mu_0 H_{c2}(0)}. \tag{3.52}$$

Equation 3.51 is similar to equation 3.21, although the description of the temperature dependence is somewhat different. However, the temperature dependence is accurately approximated by the temperature dependence of the MAG relation (figure 3.5):

$$\left(1 - t^{1.7}\right)^{\gamma-1} \approx \left(1 - t^2\right)^{\mu}. \tag{3.53}$$

In the MAG relation, the recommended value of $\mu \approx 1$ corresponds to $\gamma \approx 1.91$, while for Nb-Ti a typical range of $\gamma = 1.76$ to 2.30 is observed [91]. In other words, the temperature dependencies of the Nb-Ti and Nb_3Sn are identical for all intents and purposes and also overlap in terms of parameter values.

Combining equations 3.51 with 3.53, the critical current density of NbTi is found to be accurately described by:

$$J_c(T,\mu_0 H) = C_1\left(1-t^2\right)^{\mu} h^{p-1}(1-h)^q, \tag{3.54}$$

which is identical to equation 3.3, i.e. the MAG relation which describes the critical current density of Nb_3Sn.

3.6.2 Differences between J_c parameterizations of Nb-Ti and Nb_3Sn

There are some distinct differences between Nb-Ti and Nb_3Sn in terms of the critical current density dependence on magnetic field, temperature, and strain.

The temperature dependence of the upper critical field $\mu_0 H_{c2}$ is different for Nb_3Sn and Nb-Ti, see equations 3.11 and 3.50. The difference in the temperature dependence of $\mu_0 H_{c2}$ between Nb_3Sn and Nb-Ti implies that the underlying physics mechanism is different. One likely explanation is that Pauli limiting plays a smaller role in the case of Nb_3Sn [81] (section 4.8.3), but a larger role in the case of Nb-Ti. A very detailed experimental investigation of the temperature dependence of $\mu_0 H_{c2}$ in Nb-Ti was performed by Muller [114], which also includes a discussion on the underlying physics.

Another difference is the magnetic field dependence of the critical current density. For Nb_3Sn, the parameters p and q are close to 0.5 and 2 respectively, while for Nb-Ti these parameters are both close to 1. This has been explained in terms of the difference in pinning site density by Godeke *et al.* [33, 115]. α-Titanium precipitates are introduced into Nb-Ti conductors, resulting in a nearly optimal pinning site density as shown by West *et al.* [117]. In Nb_3Sn, however, pinning occurs mainly at the grain boundaries and the grains have a typical diameter of about 150 nm for optimized commercial high-J_c wire. In order to achieve optimal pinning at 12 T, for example, the grain diameter would need to be reduced to 12 nm. This relative scarcity of pinning sites not only results in a reduced maximum achievable pinning force, but also a less desirable magnetic field dependence, with $p \approx 0.5$ and $q \approx 2$, as opposed to $p \approx 1$ and $q \approx 1$ found in Nb-Ti. In figure 3.6, it is illustrated that in NbTi the pinning force peaks at a higher reduced magnetic field, which is desirable for high field applications. It was previously demonstrated that pinning in Nb_3Sn can be improved substantially through ternary additions in thin films by Dietderich *et al.* [116] and Godeke *et al.* [115], which could lead to a future method for improving the pinning properties of Nb_3Sn wires.

A third distinct difference is the degree of strain sensitivity in the upper critical field $\mu_0 H_{c2}$. While equation 3.47 is motivated by the approximation that the strain sensitivity of J_c in Nb-Ti is negligible, some strain sensitivity is presented and has been observed by Ekin [118], though in particular at magnetic fields close to $\mu_0 H_{c2}$. Similarly to Nb_3Sn, Ekin concluded that the strain sensitivity of the critical current density of Nb-Ti is mainly related to a reduction of $\mu_0 H_{c2}$ under the influence of strain. However, the strain sensitivity is considerably weaker for Nb-Ti than for Nb_3Sn, which is explained in section 5.4.3.

It should be emphasized that equation 3.47 is based on the approximation that the strain sensitivity is negligible and that the subsequent derivation leading to equation 3.51 is valid under this approximation. For more details on how strain affects the critical current density

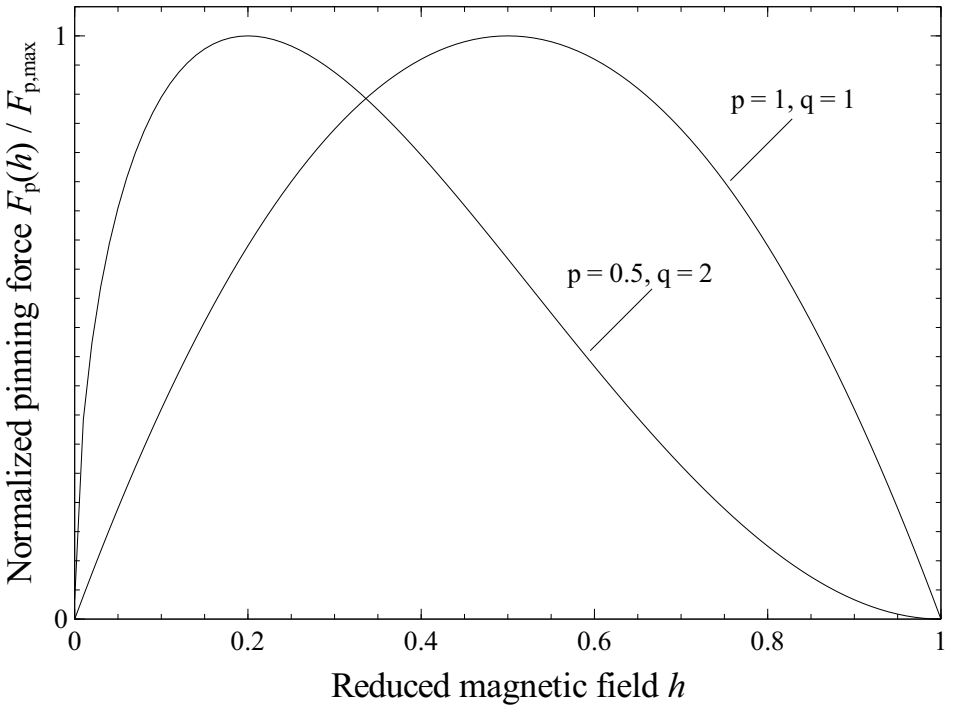

Figure 3.6: *Magnetic field dependence of the macroscopic pinning force $F_P = \mu_0 H \times J_c$, with p = 0.5 and q = 2, typical of Nb_3Sn, and p = 1 and q = 1, typical for Nb-Ti.*

of NbTi, the reader is referred to the investigation by Ekin [109].

3.7 Experimentally observed temperature, magnetic field, and longitudinal and transverse strain dependence of the critical current density of Nb_3Sn

3.7.1 Introduction

The critical current density of a stoichiometric Nb_3Sn in thin films was measured as a function of temperature, magnetic field, and both longitudinal and transverse strain.

Non-hydrostatically applied strain is anisotropic by definition. On the other hand, the MAG relation of the critical current density of Nb_3Sn relates the strain dependence of the critical current to the critical temperature T_c and upper critical field $\mu_0 H_{c2}$, which are both isotropic properties [70]. This implies two things:

- First, in the case of the thin films, uni-axial applied strain should affect the critical current density in the same way regardless of whether the critical current density is perpendicular or transverse to the direction in which the samples are strained.

Table 3.1: *MAG scaling parameters derived at constant strain of stoichiometric (dep 2-14-11) and off-stoichiometric (dep 9-14-10) samples, where current flows parallel ('long') and perpendicular ('tr') to the strain direction.*

	2-14-11, long	2-14-11, tr	9-14-10, long	9-14-10, tr
T_c [K]	17.6	17.4	13.6	12.4
$\mu_0 H_{c2}(0)$ [T]	29.4	29.9	22.4	20.8
p	0.50	0.50	0.61	0.66
q	1.33	1.37	2.07	2.75
C_I [kA/mm^2]	2.7	1.8	1.8	1.7
μ	1.47	1.63	1.83	2.28

- Second, the strain sensitivity of T_c and $\mu_0 H_{c2}$ which is extracted from critical current density measurements should be close to the observed strain sensitivity that was determined from resistivity measurements.

As presented in section 2.3.9, a selected number of samples were etched into a pattern that allows for the measurement of the critical current density parallel and perpendicular to the direction in which strain is applied. Each sample consists of a 'longitudinal' and a 'transverse' section, in which the critical current density is aligned parallel and perpendicular to the uni-axial strain direction, respectively. In both sections the strain and current directions are perpendicular to the magnetic field orientation.

3.7.2 Evaluation of the temperature and magnetic field dependence of the critical current density at constant strain

An extensive set of measurements was performed at constant strain to allow for a careful analysis of the effect of temperature and magnetic field on the critical current density. The critical current density was determined at magnetic fields above 60% of $\mu_0 H_{c2}(T, \varepsilon)$ in deposition 2-14-11 and 15% of $\mu_0 H_{c2}(T, \varepsilon)$ in deposition 9-14-10. In the case of deposition 2-14-11, p is set at 0.5, because the lack of data at magnetic fields that are low relative to $\mu_0 H_{c2}(T, \varepsilon)$ means that this parameter cannot reliably be extracted [33]. In contrast, p is a free parameter in deposition 9-14-10. q is a free parameter in both depositions.

A temperature dependent $C(T)$ and an extrapolated $\mu_0 H_{c2}$ are derived at each temperature (figure 3.7), using:

$$J_c(T,H) = C(T)\left(\frac{H}{H_{c2}(T)}\right)^{p-1}\left(1-\frac{H}{H_{c2}(T)}\right)^{q}, \tag{3.55}$$

where a unique temperature dependent $C(T)$ and $\mu_0 H_{c2}(T)$ are extracted for all critical current density measurements at a given temperature, and where p and q are global constants. The optimal values are determined by applying equation 3.55, and minimizing the mean square error.

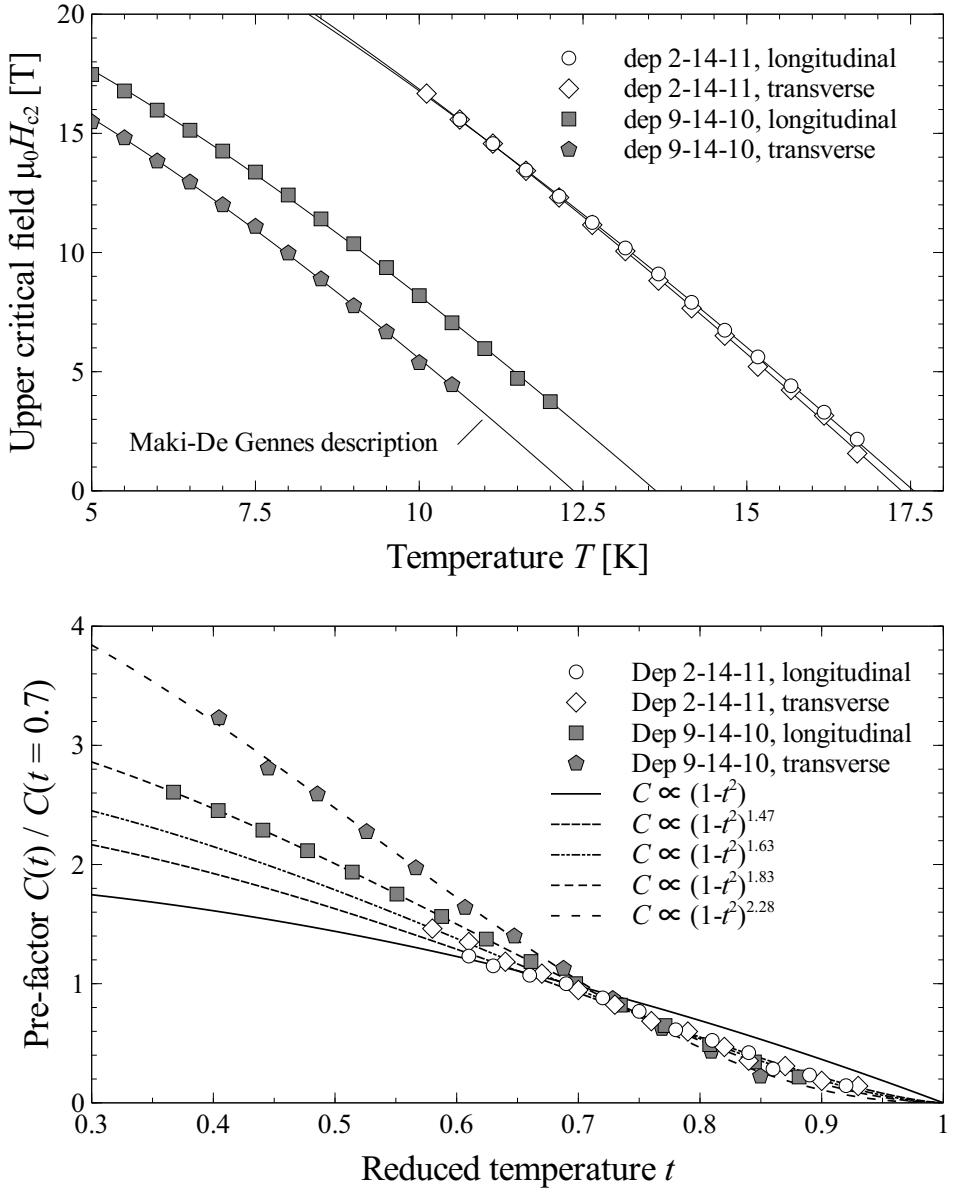

Figure 3.7: *Top: Maki-DeGennes fit of temperature dependence of the upper critical field $\mu_0 H_{c2}$. Bottom: Normalized temperature dependence of the critical current density pre-factor.*

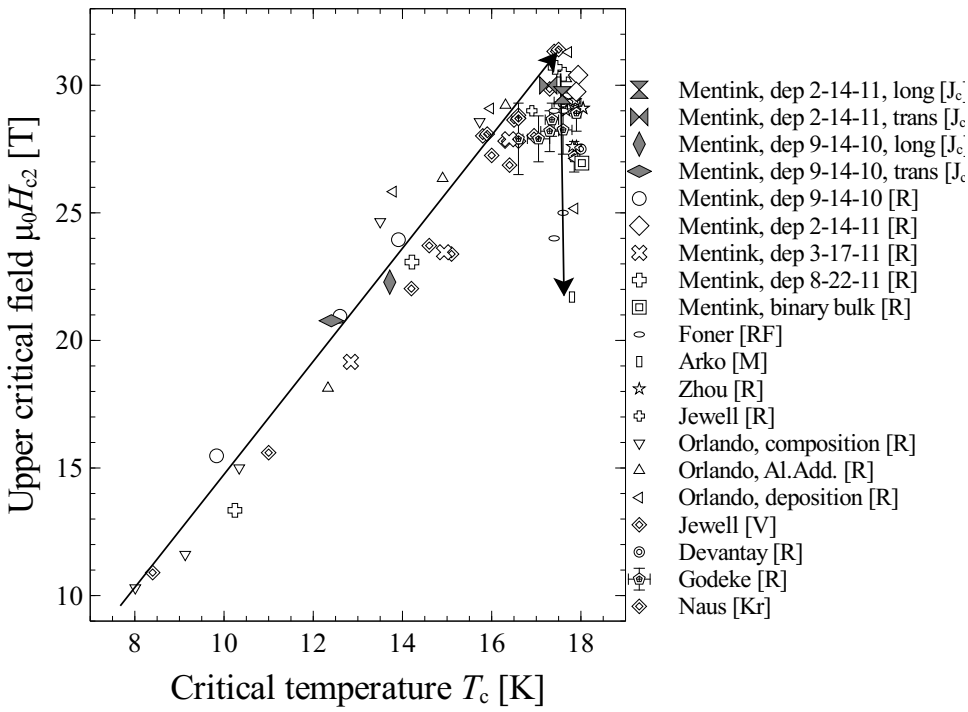

Figure 3.8: *Upper critical field $\mu_0 H_{c2}$ as a function of critical temperature T_c. The grey symbols indicate the properties extracted from the critical current density measurements, while the open symbols indicate the measurements and literature results as discussed in sections 2.4.8 and 4.8.5. The arrows are guides to the eye.*

The Maki-DeGennes relation is used to determine T_c and $\mu_0 H_{c2}(0)$. The accuracy of this relation is illustrated in figure 3.7, top. The extrapolated critical temperatures and upper critical fields (table 3.1) are closely consistent with the results from the resistivity measurements and the literature results, as is demonstrated in figure 3.8.

As discussed in the preceding sections, the temperature dependent pre-constant is described with:

$$C(T) = C_I\left(1 - \left(T/T_c\right)^2\right)^{\mu}, \tag{3.56}$$

where T_c is extracted by extrapolation with the Maki-DeGennes description, and μ is a free parameter (table 3.1). It is clear that a free parameter μ is indeed beneficial for improving accuracy and that equation 3.56 accurately describes the observed behavior, which is illustrated in figure 3.7, bottom.

As shown in table 3.1, the pre-constant C_I is nearly identical for the two sections in deposition 9-14-10, and the transverse section of 2-14-11, but noticeably deviates in the longitudi-

Table 3.2: *MAG scaling parameters describing the strain dependence of T_c and $\mu_0 H_{c2}$.*

	2-14-11, long	2-14-11, tr	9-14-10, long	9-14-10, tr
T_{cm} [K]	17.6	17.3	13.7	12.4
$\mu_0 H_{c2m}(0)$ [T]	29.6	30.0	22.3	20.8
w	3.30	3.29	1.77	1.70
ε_m [%]	−0.01	−0.01	0.08	0.10
$\varepsilon_{0,a}$ [%]	0.30	0.30	0.30	0.30
$C_{a,Hc2}$	43.7	53.3	26.4	20.7
$C_{a,Tc}$	15.2	19.7	15.6	12.6

nal section of deposition 2-14-11. This difference can be explained in two ways. Firstly, it should be noted that the longitudinal section of deposition 2-14-11 has an average tin concentration of 25.0 at.% Sn, while the transverse section of this sample and the longitudinal and transverse sections of deposition 9-14-10 contain 24.8, 23.2, and 22.2 at.% Sn, respectively. The measured normal state resistivities are 21, 25, 70 and 91 $\mu\Omega$cm, respectively. Below a normal state of 27 $\mu\Omega$cm, Nb_3Sn is preferentially tetragonal, while it is otherwise preferentially cubic (see section 4.4.5). Tweed modulation occurs when the material is preferentially tetragonal (section 4.4.6), and it is not inconceivable that the tweed pattern contributes to the pinning of flux-lines, thus increasing C_I. Secondly, a more mundane explanation is that this is a measurement anomaly related to sample inhomogeneity. The critical current density measurements of this particular sample were mainly performed at magnetic fields near $\mu_0 H_{c2}$ due to current limitation considerations (i.e. the current density in the sample was limited to avoid thermal runaway in the sample). As with the binary bulk samples that were discussed in section 2.2.5, this sample likely contains a $\mu_0 H_{c2}(0)$ range rather than a single $\mu_0 H_{c2}(0)$ (figure 3.8). Thus, as C_I is determined through extrapolation from measurements near $\mu_0 H_{c2}$, and $\mu_0 H_{c2}$ of this sample is poorly defined, this could explain the deviating value of C_I.

3.7.3 Evaluation of the strain dependence of the critical current density

Besides extensive measurements at constant strain, the critical current density was measured at various values of applied strain in the range −0.3 to 0.05%, where the negative sign indicates compressive strain. At each strain, the critical current density is measured at at least three different temperatures and at least three different magnetic fields per temperature. Equation 3.3 is applied to the entire dataset, where C_I, p, q and μ are as listed in table 3.1. $T_{cm}(0)$ and w are determined from a global fit (table 3.2), and $\mu_0 H_{c2}(0, \varepsilon_a)$ is determined per strain as shown in figure 3.9.

As in the procedure that was applied to the resistivity measurements (section 2.4.9), the strain dependent T_c and $\mu_0 H_{c2}(0)$ are fitted with the deviatoric strain description, where $\varepsilon_{0,a}$ is fixed to 0.3 %. The results are shown in table 3.2 and figure 3.9.

The strain sensitivity of T_c is shown to be closely consistent with the strain sensitivity as

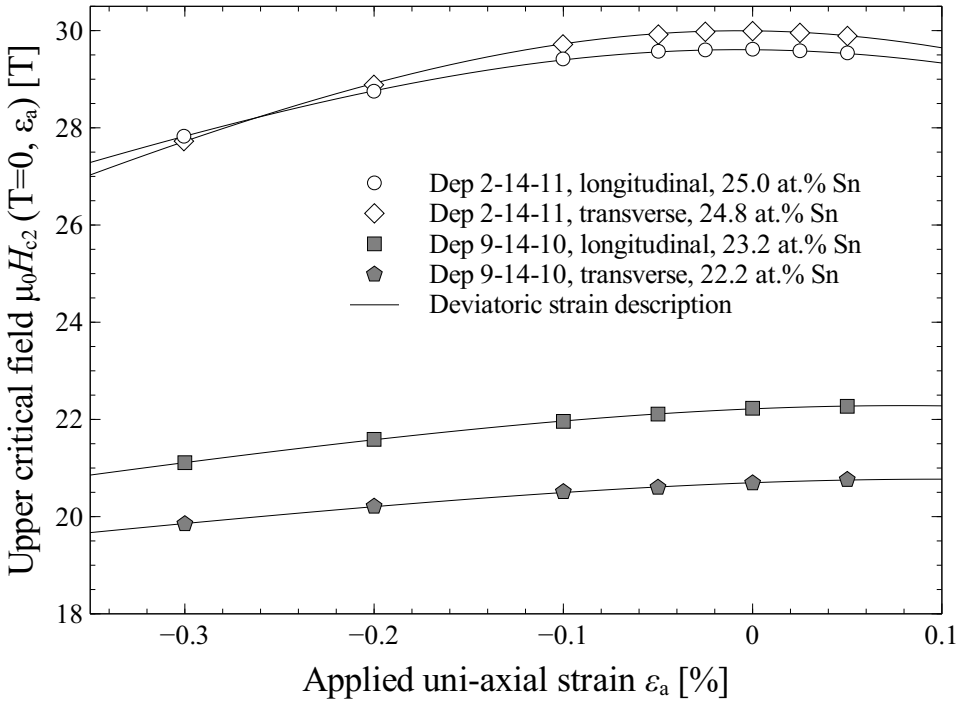

Figure 3.9: *Extrapolated strain dependent upper critical field $\mu_0 H_{c2}(0)$ as a function of strain, compared to the deviatoric strain description.*

extracted from resistivity measurements (figure 3.10, top). The observed strain sensitivity in $\mu_0 H_{c2}$ is also consistent, although the degree of scatter is larger (figure 3.10, bottom). Also shown are parameterization results of Nb_3Sn wires (after Lu *et al.* [90] and Arbelaez *et al.* [106]) which are consistent with the overall observations.

The optimal values of w shown in table 3.2 are consistent with the optimal parameters as determined from resistivity measurements, within an uncertainty of about 0.3 (figure 3.11). The increased value of w for the tin rich sample validates the rise in w when approaching stoichiometry in figure 2.25.

To illustrate the applicability of the scaling procedure, figure 3.12 shows a comparison of the measured J_c at various temperatures, magnetic fields, and strains, and a global description of the longitudinal and transverse sections of deposition 9-14-10 (which covers a much larger reduced magnetic field range in comparison to deposition 2-14-11), that combines the MAG relation (equation 3.3) with the Deviatoric strain description (equation 3.36). The fit parameters are shown in tables 3.1 and 3.2. The average error and the standard deviation are displayed in table 3.3, which are measures of both the experimental uncertainty and the applicability of the fit.

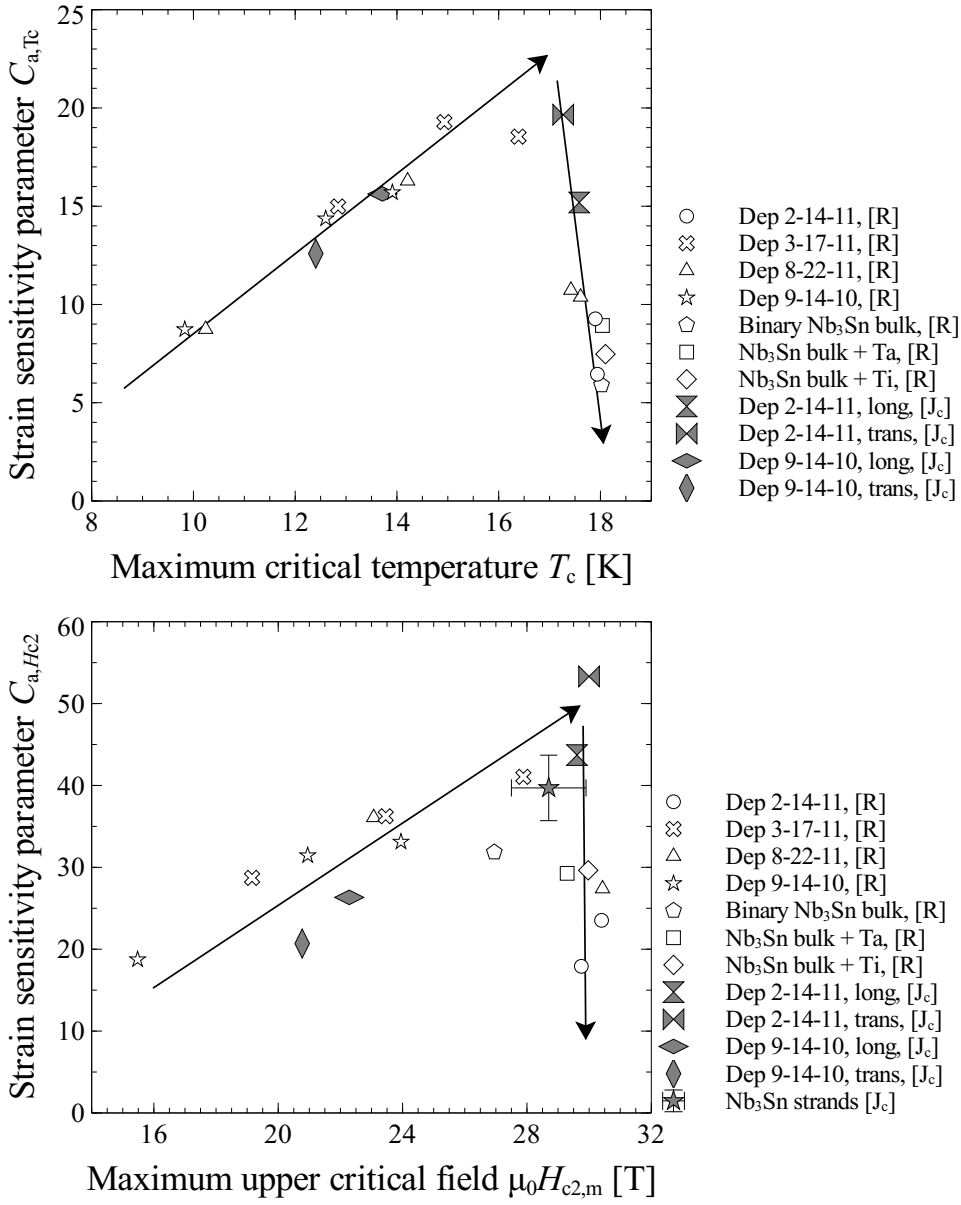

Figure 3.10: *Strain dependence parameter $C_{a,Tc}$ as a function of T_c and $C_{a,Hc2}$ as a function of $\mu_0 H_{c2}(0)$. The parameters are extracted from resistivity measurements (open symbols) and critical current density measurements (grey symbols). Also shown are results from strain sensitivity measurements on Nb_3Sn strands, after Lu et al. [90] and Arbelaez et al. [106]. The arrows are guides to the eye.*

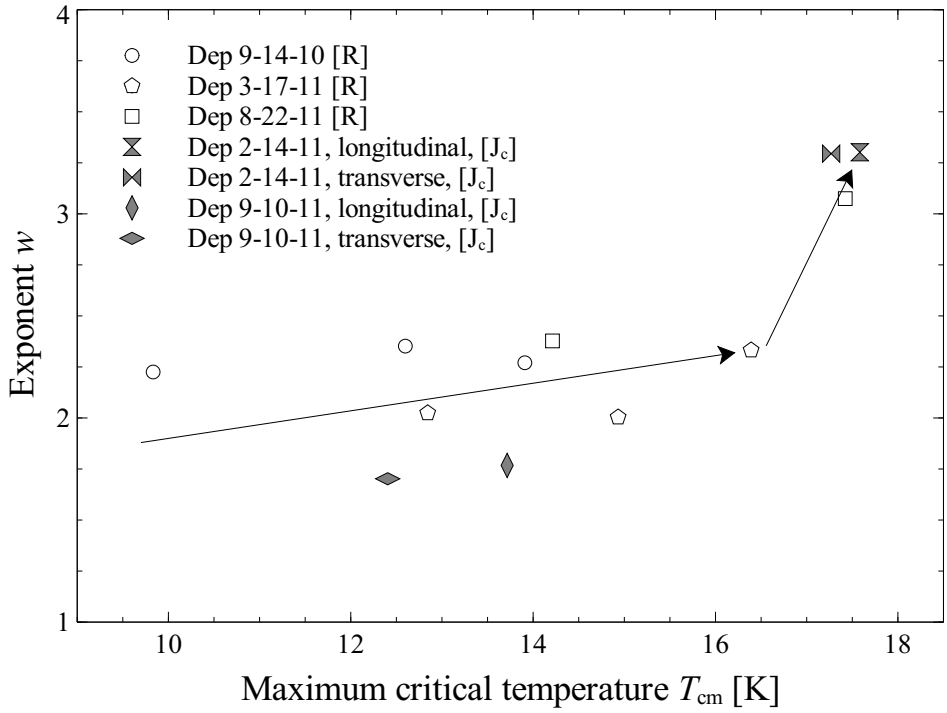

Figure 3.11: *Exponent w as a function of maximum critical temperature T_c, from resistivity measurements ([R], open symbols) and critical current measurements ([J_c], grey symbols). The arrows are guides to the eye.*

Table 3.3: *Average error and standard deviation of the global fits for 4 thin film samples.*

	2-14-11 long	2-14-11 tr	9-14-10 long	9-14-10 tr
$J_{c,max}$ [A/mm^2]	71	76	360	280
avg. error [A/mm^2]	1.2	1.5	1.1	1.8
st.dev [A/mm^2]	1.2	2.0	0.7	1.4
avg. error / $J_{c,avg}$ [%]	2.5	6.9	0.8	1.3

3.8 Conclusion

An extensive survey of the descriptions of the critical current density of Nb_3Sn and Nb-Ti as a function of temperature, magnetic field and strain was presented.

It is argued and demonstrated that indeed the general accuracy of the MAG relation can be improved through the addition of a free parameter that describes the temperature dependence

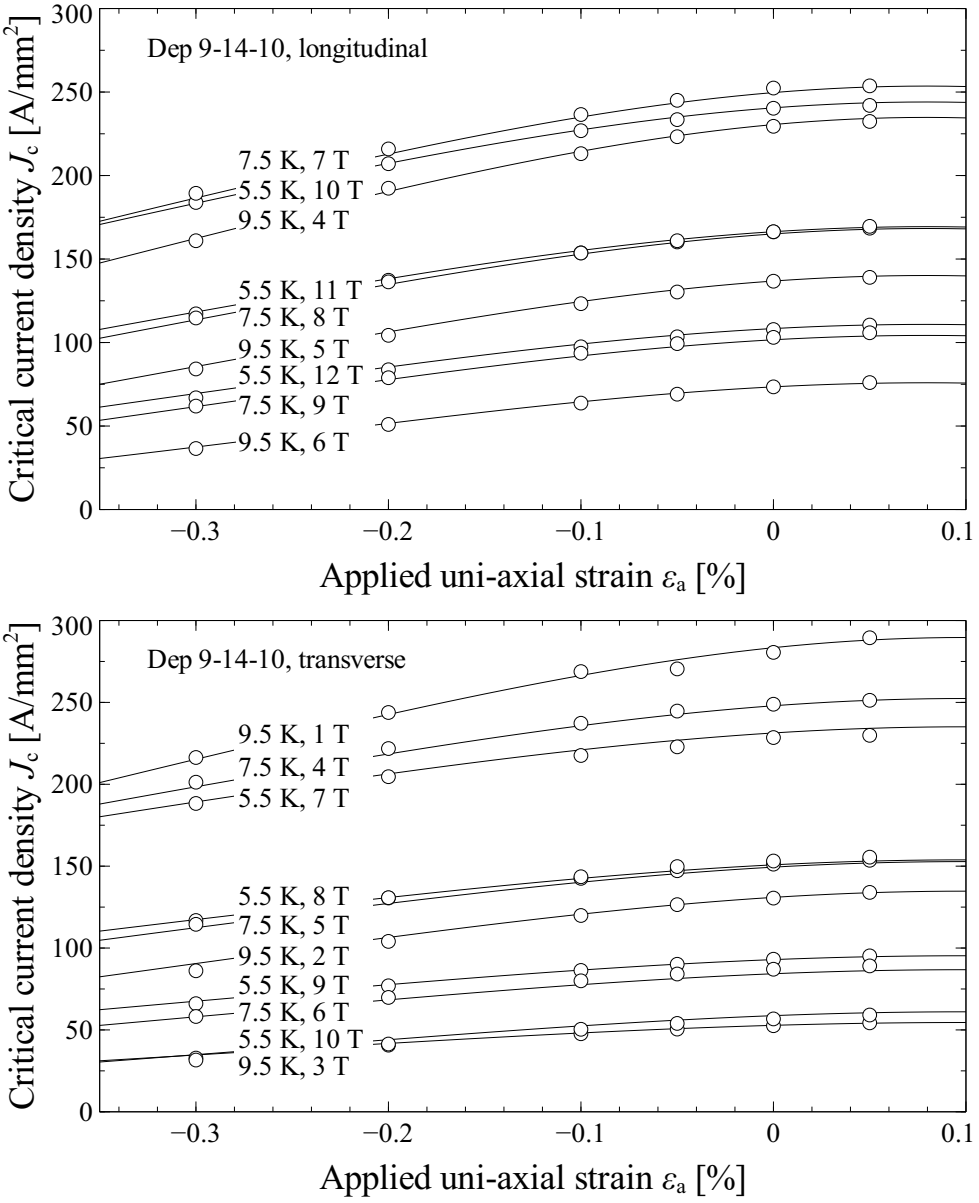

Figure 3.12: *Critical current density as a function of applied uni-axial strain, at various temperatures, and magnetic fields.*

of the critical current as was suggested earlier [104, 105, 92].

Two other commonly used scaling relations that describe the critical current density of Nb_3Sn are shown to be indistinguishable from the MAG relation. A commonly used description of the critical current density of Nb-Ti is shown to be identical as well, except for a different temperature dependence in $\mu_0 H_{c2}(T)$.

Results of an experiment are presented in which the critical current densities of nearly stoichiometric and off-stoichiometric Nb-Sn were measured as a function of temperature, magnetic field, and longitudinal and transverse strain. The MAG relation indicates that the strain dependence of the critical current density is a result of the strain dependence of the critical temperature T_c and the upper critical field $\mu_0 H_{c2}$, which are both (nearly) isotropic properties (also see [67]). This implies that transversely applied strain affects the critical current density in the same manner as perpendicularly applied strain, a hypothesis that is indeed shown to be correct.

The observed strain dependence in the critical current density measurements was shown to be consistent with the temperature, magnetic field, and strain dependent resistivity measurements as presented in chapter 2, as well as the strain dependence of various commercially available Nb_3Sn wires. This confirms the accuracy of the MAG relation, which relates the strain dependence of the critical current density to the strain dependence of the critical temperature and upper critical field.

In order to understand the origin of the strain sensitivity of the superconducting properties of Nb_3Sn, emphasis should be placed on the physics behind $T_c(\varepsilon)$ and $\mu_0 H_{c2}(0,\varepsilon)$, which will be discussed in detail in chapters 4 and 5.

Chapter 4

Calculation of the Microscopic Properties of Nb_3Sn

4.1 Introduction

In this chapter, microscopic theory and computational calculations of the effect of disorder on T_c and $\mu_0 H_{c2}(0)$ are discussed. A model is discussed for calculating the effect of disorder on T_c and $\mu_0 H_{c2}(0)$, and the results are compared to experimental observations.

Microscopic properties of Nb-Sn are calculated using density functional theory (DFT) and Density Functional Perturbation Theory (DFPT). Various starting models are evaluated for feasibility, including a free electron model, a single unit cell configuration, and two super-cell configurations. Disorder is introduced into these models through an electron lifetime broadening description.

To validate the modeling approach, the calculated properties of Nb-Sn are compared to experimental results. In particular, the disorder dependent martensitic transformation, the critical temperature T_c, and the upper critical field $\mu_0 H_{c2}(0)$ are considered.

4.2 Density Functional Theory and Density Functional Perturbation Theory

Density Functional Theory (DFT) is a tool used to calculate the most optimal distribution of charge density, i.e. the ground state, of a system consisting of ions and electrons. Inspired by the Thomas-Fermi model [120, 121], it was proven by Kohn and Hohenberg [122] that the non-degenerate ground state of a system is uniquely determined by the charge density of the system. Specifically, the two theorems formulated [123], are:

1. The external potential $V_{\text{ext}}(\overrightarrow{r})$ is (to within a constant) a unique functional of $\rho(\overrightarrow{r})$. Since, in turn $V_{\text{ext}}(\overrightarrow{r})$ fixes $\widehat{H}$ the full many particle ground state is a unique functional of $\rho(\overrightarrow{r})$.

2. $F_{\text{HK}}(\rho)$, the functional that delivers the ground state energy of the system, delivers the lowest energy if, and only if, the input density is the true ground state density.

After the formulation of the HK theorems, the self-consistent Kohn-Sham equations [124] were defined, which equate the total energy of a system of interacting particles to the sum of the total energy of a system of non-interacting particles and an exchange-correlation energy term E_{XC}. If the term E_{XC} is known precisely, then the optimal charge density distributions of the two systems are identical. The advantage of this approach is that finding the optimal charge density distribution of the system of non-interacting particles requires significantly less computational effort in comparison to calculating the optimal charge density distribution of the system with interacting particles.

Once the optimal charge density distribution is known, various electronic properties are readily derived, such as the electron density of states and the Fermi velocity. In addition, the vibrational properties can be calculated using Density Functional Perturbation Theory (DFPT) as shown by Baroni *et al.* [125, 126]. This involves introducing perturbations and evaluating the linear response of the system.

The main challenge in the development of DFT calculations is to find suitable approximations for E_{XC}. Since the original formulation of the HK theorems and the Kohn-Sham equations, significant progress has been made in the accuracy of these approximations. Well-known approximations for E_{XC} are the local density approximation (LDA) and the

generalized gradient approximation (GGA).

Both DFT and DFPT are powerful techniques that allow for accurate predictions of various material properties in a computationally efficient way.

4.2.1 Quantum Espresso

Quantum Espresso [127] software is used to perform both the DFT and the DFPT calculations. The source code is freely available online as well as manuals, tutorials, and a support group.

4.2.2 Pseudopotentials

The pseudopotential approximation, first introduced by Hellmann [128], is an approximation based on the assumption that the core electrons are tightly bound to the nuclei and exert a fixed potential on the electrons in the higher energy bands. As most of the properties of solids are related to interaction of electrons in the highest energy bands, approximating the core electrons by a fixed potential can dramatically reduce the amount of electrons that need to be considered in a DFT calculation without reducing the predictive power of the calculation.

Suitable ultra-soft pseudopotentials were used which are available on the quantum espresso website. The pseudopotentials use the Perdew-Wang 91 gradient corrected functional approximation by Perdew *et al.* [129], a variation on the generalized gradient approximation.

4.2.3 Computational details

All calculations used a kinetic energy cutoff of 40 Rydberg and a charge density cutoff of 320 Rydberg. Structural optimization and density of states calculations were performed with a k-point grid consisting of $16\times16\times16$ automatic Monkhorst-Pack divisions. Fermi velocity calculations were performed with a k-point grid of $40\times40\times40$ automatic Monkhorst-Pack divisions. The phonon calculations utilized a k-point grid consisting of $8\times8\times8$ Monkhorst-Pack divisions and a q-point grid consisting of $4\times4\times4$ Monkhorst-Pack divisions.

4.3 Computational modeling of disorder

Three different approaches are considered for understanding how off-stoichiometry affects the superconducting properties.

4.3.1 Free electron model

The Drude-Sommerfeld model, better known as the free electron model, is a relatively simple model for predicting the properties of a material that contains a free electron gas.

The model predicts the Fermi energy and the electron density of states under the assumption of a free electron gas, following:

$$E_{\mathrm{F}} = \frac{\hbar^2}{2m}\left(\frac{3\pi^2 N_{\mathrm{e}}}{a_0^3}\right)^{2/3}, \tag{4.1}$$

$$N(E_F) = \frac{3}{2}\frac{N_e}{E_F}, \tag{4.2}$$

where $\hbar$ is the Planck constant in [J×s], m is electron mass in [kg], N_e the amount of free electrons per unit cell, a_0 the lattice parameter of a unit cell, E_F the Fermi energy in [J], and $N(E_F)$ the electron density of states in [states / (J×unit cell)]. A stoichiometric Nb_3Sn unit cell contains six niobium ions and two tin ions. The valence of niobium is 5 (4 d-electrons and 1 s-electron) and the valence of tin is 2 (1 s-electron and 1 p-electron), which means there are 38 'free' electrons per unit cell. According to Devantay *et al.* [52], the lattice parameter of stoichiometric Nb_3Sn is about 0.529 nm. The free electron model (equation 4.1) predicts a Fermi energy E_F of 2.4×10^{-18} J, or 14.7 eV. The density of states $N(E_F)$ is 2.4×10^{19} states/(J×unit cell), which is equal to 3.87 states / (eV × unit cell). For comparison, Orlando *et al.* [81] determined that the electron density of states of stoichiometric Nb_3Sn is equal to $N(E_F)$ = 15±6 states / (eV × unit cell). This large deviation is to be expected, since the free electron model is poorly suited for systems that contain lots of d-electrons, meaning that this model is too simplistic to be useful.

4.3.2 Electron lifetime broadening in a stoichiometric unit cell

Testardi *et al.* [130] and Mattheiss *et al.* [131] argued that the effect of disorder on the band structure can be calculated with an electron lifetime broadening approximation. If the density of scattering centers in the material is increased, electrons scatter more often. This scattering results in a broadening of the band structure, with:

$$E_B = \frac{\hbar}{\tau}, \tag{4.3}$$

where E_B is the broadening energy in [eV], $\hbar$ the Planck constant in [eV×s], and τ the mean scattering time (i.e. the mean time between electron scattering events). This follows from the uncertainty principle: the energy of an electron that never scatters is well defined, while the energy of an electron that scatters often is poorly defined. An analogy is a Fourier transform of a sound wave: the frequency of a short sample is poorly defined. Furthermore, if the frequency spectrum of a sample is infinitely sharp then the sample is by definition infinitely long.

Consistent with Testardi's paper [130], Fermi-Dirac broadening is used and the broadening is applied to a single unit cell, which consists of six niobium ions and two tin ions arranged in an A15 crystal structure. After performing structural optimization, a variety of properties can be calculated, such as the electron density of states. Figure 4.1 shows two calculated results in which different mean scattering times were used as input. The calculated results illustrate the effect of broadening. At lower mean scattering time, the peak structure in the electron density of states is washed out and the electron density of states at the Fermi energy $N(E_F)$ is reduced.

As this model is used to calculate the effect of disorder on stoichiometric Nb_3Sn, one could argue about the usefulness of this model for understanding the properties of off-stoichiometric Nb-Sn. However, it was argued by Orlando *et al.* [42] that in samples in which the influence of strain is not considered, the degree of disorder, as measured by the normal state

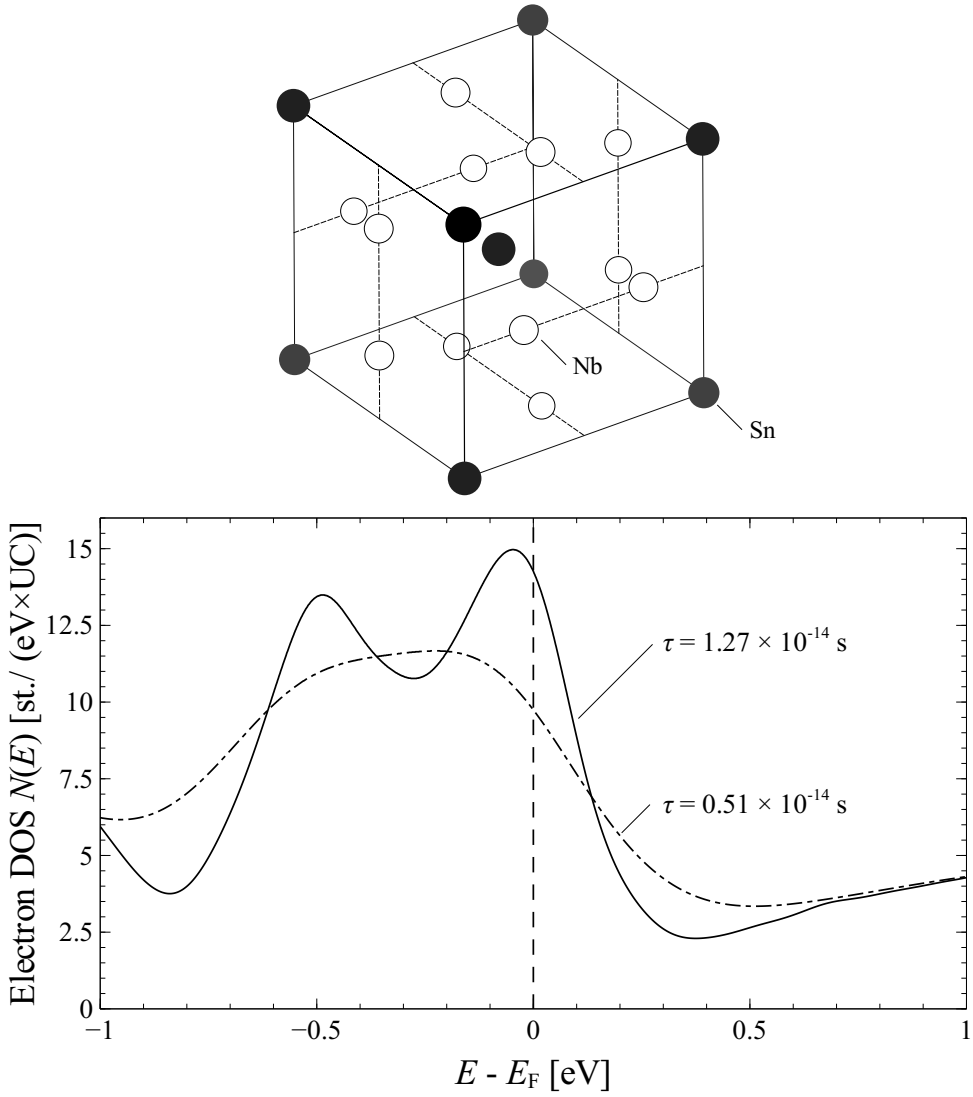

Figure 4.1: *Top: niobium and tin ions are arranged in an A15 crystal structure, after which a structural optimization is performed. Bottom: calculated electron density of states as a function of electron energy at two different mean scattering times τ.*

resistivity, uniquely determines the superconducting properties, regardless of whether the sample is stoichiometric or off-stoichiometric. The implication is that the effect of disorder on the superconducting properties of stoichiometric and off-stoichiometric Nb_3Sn is similar or identical, so that a comparison of these two systems is useful.

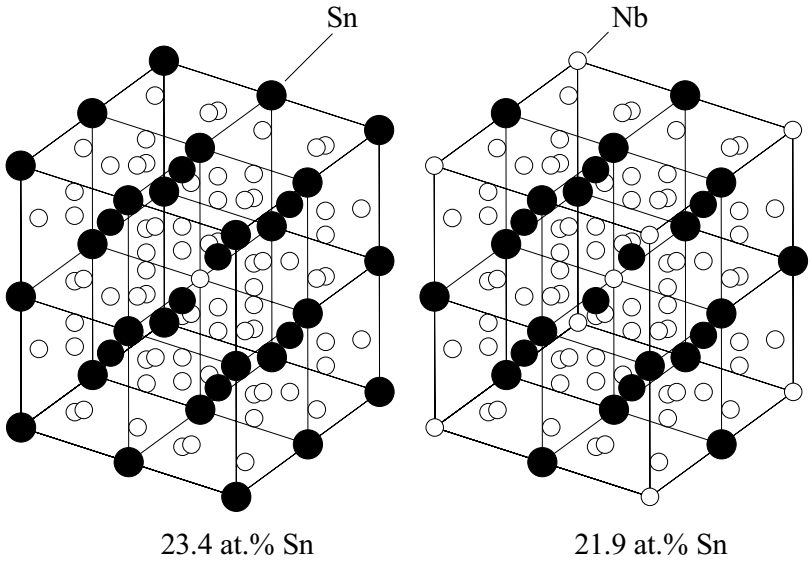

Figure 4.2: *Supercell configurations. The center Sn ion is replaced in the left configuration (23.4 at.% Sn), and both the center Sn ion and the corner Sn ions are replaced in the right configuration (21.9 at.% Sn).*

4.3.3 Electron lifetime broadening in an off-stoichiometric supercell

An attempt was made to calculate the electronic properties of two supercells containing Nb-Sn in an off-stoichiometric ratio. The supercells consists of $2 \times 2 \times 2$ unit cells for a total of 64 ions. In one case, the central tin ions are replaced by a niobium ion so that 23.4% of the ions are tin ions, while in the other case, both the center and the corner tin ion are replaced so that 21.9% of the ions are tin ions (see 4.2). The electron density of states was calculated after performing a structural optimization.

The electron density of states was calculated for both cases and compared to the stoichiometric case at two values of τ. In figure 4.3, the electron density of states of the single unit cell and the two supercells is presented at two different values of τ. In addition, a stoichiometric supercell calculation (i.e. a supercell consisting of eight single unit cells without any ion replacement in the crystal) was performed. It was determined that the results of the stoichiometric supercell and the stoichiometric single unit cell are identical in terms of the electron density of states.

The calculated result indicates that excess niobium affects the electron density of states in an additional manner besides only acting as a scattering center.

There is some uncertainty associated with this calculation. The excess niobium ions are introduced into the simulation in a perfectly periodic fashion, while in reality the distribution of niobium ions is likely either random, or clustered into regions of niobium in the vicinity of stoichiometric Nb_3Sn. As was discussed in section 2.2.4, the investigated binary bulk Nb_3Sn

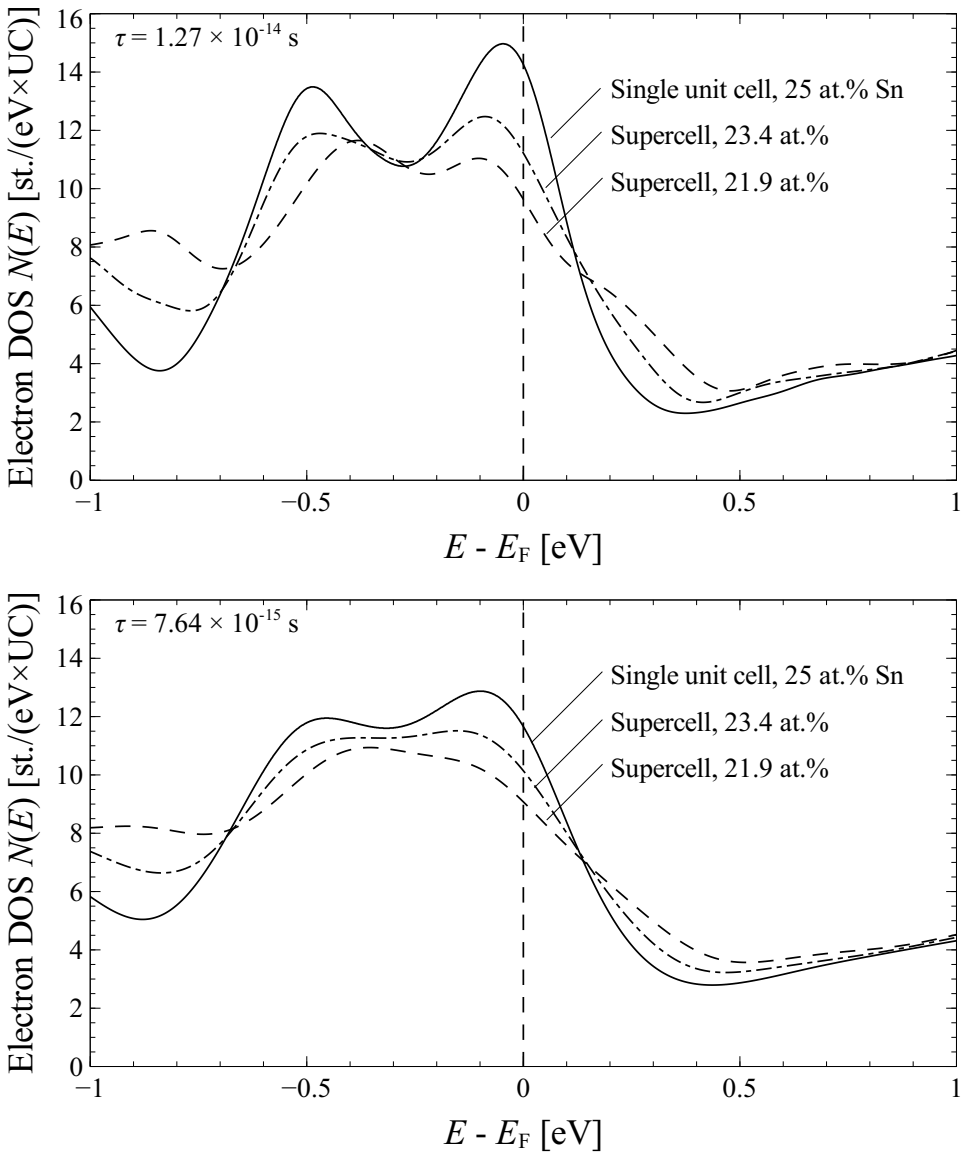

Figure 4.3: *Top: calculated electron density of states at $\tau = 1.27\times10^{-14}$ s, comparison of stoichiometric single unit cell to off-stoichiometric supercells, with 23.4 and 21.9 at.% Sn. Bottom: same as top, but with $\tau = 7.64\times10^{-15}$s.*

sample consists of regions of pure niobium and stoichiometric Nb_3Sn on a length scale of microns, while the off-stoichiometric thin films have broad T_c distributions, which implies a local variation in the niobium ion distribution on the length scale of a coherence length. As

it is not clear how the distribution of niobium ions affects the electronic properties, it is not clear to what extent these supercell configurations, in which excess niobium is introduced in a perfectly periodic fashion, are representative of off-stoichiometric Nb-Sn samples.

A larger problem is the computational effort. In comparison to the single cell calculation, the calculations take about 400 times longer to complete. For this reason, the supercell calculations are limited to electron density of states in cubic symmetry.

In theory both problems are solvable by committing significant amounts of computational power to evaluating the properties of the large supercells. However, within the constraints of this research, such an investigation was not feasible.

4.3.4 Conclusion

Three types of models are presented as candidates for the computational investigation of the effect of disorder on the microscopic properties of Nb_3Sn.

It is concluded that the free electron model is too simple to properly account for the microscopic properties of Nb_3Sn.

An electron lifetime broadening approximation is considered, in which the effect of disorder is introduced through broadening of the electronic band structure of stoichiometric Nb_3Sn. This model is useful because it was experimentally observed that the superconducting properties of Nb_3Sn are determined by disorder, regardless of whether the overall composition of the material is stoichiometric or off-stoichiometric. This model is investigated in more detail in the remainder of this chapter.

Finally, the use of the electron lifetime broadening on supercell configurations with excess niobium was considered, but it was concluded that within the resources that were available for this research, the computational cost of investigating supercells in a physically realistic manner was too high.

4.4 Martensitic transformation in Nb-Sn

The electron lifetime broadening approximation is applied to investigate the effect of disorder on Nb_3Sn. The validity of this approach was investigated by calculating the properties of Nb_3Sn and comparing these to experimental observation. In this section, the martensitic transformation of Nb_3Sn is presented.

4.4.1 Literature on the martensitic transformation

It was shown by Mailfert *et al.* [77] in an analysis of XRD data that stoichiometric binary Nb_3Sn undergoes a martensitic transformation at about 43 K. Above this temperature, the crystal structure is cubic, and below this temperature, the crystal structure is tetragonally distorted. In a similar fashion, a resistivity analysis was performed by Arko *et al.* [70], which indicated that it occurs at 51 K. An XRD analysis by Watanabe *et al.* [132] indicated that it occurs at 38 K. In a neutron scattering analysis by Axe *et al.* [159] 45 K was found. The effect of strain on the normal state resistivity was investigated by Mentink *et al.* [49], which indicated the transformation to occur at 42 ± 5 K.

Devantay *et al.* [52] and Zhou *et al.* [66] performed studies of binary Nb-Sn bulk samples

with different tin concentrations. In both investigations the normal state resistivity at T_c, the composition, and the effect of the martensitic transformation on selected X-ray diffraction peaks at room temperature and at 10 K were determined. According to Devantay, a sample with an average tin concentration of 24.4 at.% and a normal state resistivity of 19 $\mu\Omega$cm, is a mix of cubic and tetragonal Nb_3Sn at 10 K, while in a sample with a tin concentration of 23.9 at.% and a normal state resistivity of 23 $\mu\Omega$cm, no indication of tetragonal distortion was observed. In Zhou's work, tetragonal Nb_3Sn was observed in three samples with normal state resistivities below 20.9 $\mu\Omega$cm, while the material was shown to be (mostly) cubic for samples with normal state resistivities above 31.3 $\mu\Omega$cm (not including a sample with an unusually high normal state resistivity, which the author attributed to $NbSn_2$ grain boundary precipitation).

According to a study by King *et al.* [133], a martensitic transformation can be observed in material with tin concentrations as low as 22.6 at.% Sn. However, unlike Devantay and Zhou, who both used various techniques to investigate the composition and homogeneity of their samples, King derived the sample composition solely from a room temperature measurement of the lattice constant, which does not preclude the possibility of measurement anomalies due to compositional inhomogeneity and/or an unusual sample strain state.

In experiments by Goldacker *et al.* [134, 135], it was observed that the martensitic transformation in stoichiometric Nb_3Sn could be prevented through various additions, including tantalum, titanium, nickel, gallium, and hydrogen. The martensitic transformation was completely suppressed in samples with 0.6 at.% H, 2.8 at.% Ta, 1.3 at.% Ti, and 1 at.% Ni, with normal state resistivities of 37 $\mu\Omega$cm, 29 $\mu\Omega$cm, 33 $\mu\Omega$cm, and 30 $\mu\Omega$cm, respectively. The martensitic transformation did occur in a binary bulk sample following Guritanu *et al.* [36] and a sample with 0.9 at% Ga, with normal states resistivities of 13 and 23 $\mu\Omega$cm, respectively. The martensitic transformation temperature range of 20 to 50 K was observed in a sample with 1.7 at.% Ta and a normal state resistivity of 26 $\mu\Omega$cm and it was concluded that 1.7 at.% is very close to the critical tantalum concentration required to suppress the martensitic transformation.

The change in normal state resistivity with applied strain peaks at 42$\pm$5 K in a binary bulk sample [49], which was attributed to the occurrence of the martensitic transformation. At 42$\pm$5 K, the normal state resistivity of this sample is 25$\pm$3 $\mu\Omega$cm.

In summary, the literature results on samples in which the martensitic transformation is suppressed through temperature, excess niobium, and ternary additions, shows that the normal state resistivity at which the martensitic transformation is suppressed is 25$\pm$3 $\mu\Omega$cm.

4.4.2 Hypothesis and calculation details

Here the hypothesis is made that the reduction in mean scattering time with increasing scattering site density results in a stabilization of the cubic phase as well as an increase in the normal state resistivity, and that the maximum mean scattering time at which the cubic phase is stabilized corresponds to a minimum normal state resistivity ρ_n of 25$\pm$3 $\mu\Omega$cm.

The nature of the martensitic transformation in A15 superconductors was investigated in the past. It was argued by Labbé *et al.* [136] that the martensitic transformation is a Jahn-Teller effect [137]: a rearrangement of the crystal structure breaks the degeneracy of the electronic band-structure and reduces the overall energy in a manner that is sufficiently energetically

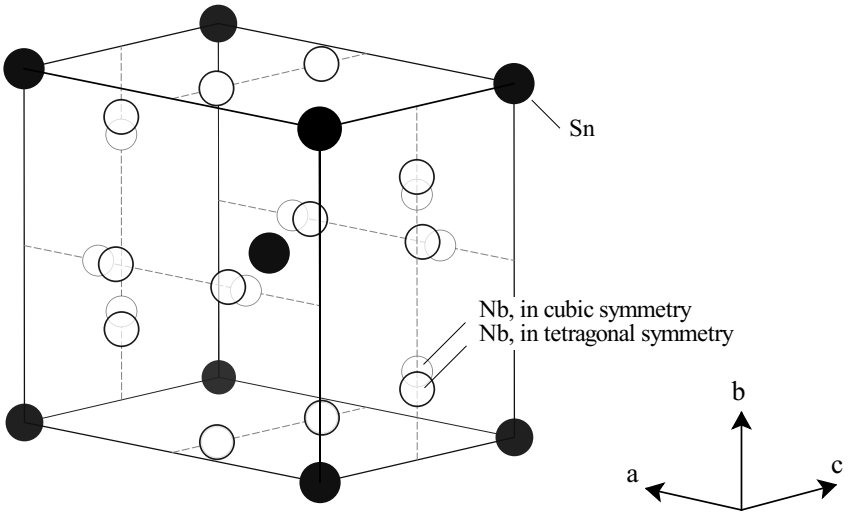

Figure 4.4: *Schematic representation of the tetragonal transformation of low-resistivity Nb_3Sn. Upon undergoing to martensitic transformation, the position of the niobium ions changes, a phenomenon that is referred to here as sublattice distortion. A quantitative study of tetragonal transformation and sublattice distortion was previously published by Sadigh et al. [138].*

favorable to overcome the cost of assuming a lower crystal symmetry.

The martensitic transformation in Nb_3Sn was also investigated from a computational perspective by Sadigh *et al.* [138] and Weber *et al.* [140]. It was shown that the tetragonal transformation of the crystal also results in sublattice distortion of the niobium chains (figure 4.4). In the two transverse directions a and b, the niobium ions move toward or away from each other. The sublattice distortion of the niobium ions was experimentally observed by Shirane *et al.* [139].

Structural optimizations are performed at various mean scattering times τ. The structural optimization involves minimizing the enthalpy of the crystal by adjusting the lattice parameters and ion positions. In order to verify that a particular ion lattice parameter and ion configuration correspond to the global optimal configuration rather than just local optimal configuration, two different starting configurations are used. Both configurations are orthorhombic with lattice parameters of 0.5318, 0.5313, and 0.5265 nm, versus 0.5318, 0.5313 and 0.5308 nm. The end results are compared and the most energetically favorable configuration is used.

For any resulting crystal symmetry that is close to a higher crystal symmetry, a calculation is also performed with this higher degree of symmetry, to verify which of the two has lower enthalphy. For instance, all orthorhombic starting configurations either converge to an optimal crystal structure that is tetragonal or nearly-tetragonal and in all cases the tetragonal

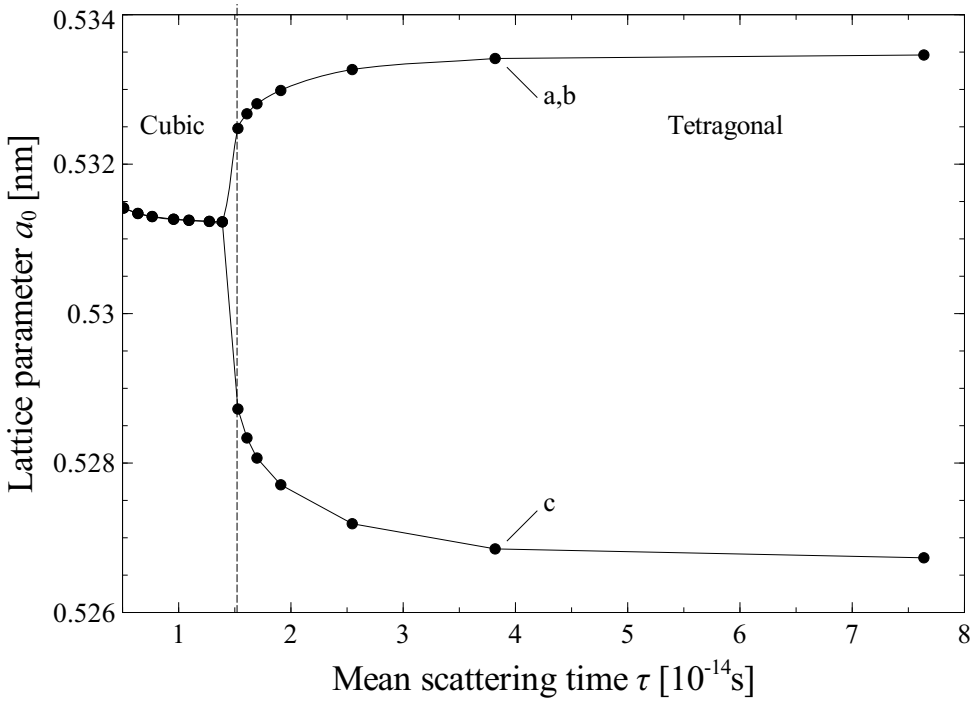

Figure 4.5: *Calculated direction dependent lattice parameter as a function of mean scattering time τ.*

configuration is energetically more favorable. Consistent with the computational investigation of Sadigh *et al.* [138], sublattice distortion of the niobium chains occurs when the crystal assumes non-cubic symmetry (figure 4.4).

The calculated result, see figure 4.5, shows that the lowest energy configuration is cubic at low τ and tetragonal at high τ. The optimal lattice parameter is 0.5313 ± 0.0001 nm for all compositions where the cubic phase is stable. Whenever the lowest energy configuration in the absence of externally applied strain is cubic, the material is referred to as preferentially cubic, and whenever the lowest energy configuration in the absence of externally applied strain is tetragonal, the material is referred to as preferentially tetragonal. This distinction is important, because it will be shown in section 5.5.4 that the behavior of preferentially cubic Nb_3Sn that is forced into tetragonal symmetry is very different from preferentially tetragonal Nb_3Sn. The transition between preferentially cubic and preferentially tetragonal crystal symmetry is not instantaneous but smooth and occurs at a critical τ_c of $(1.53 \pm 0.08) \times 10^{-14}$ s.

The regime where the lowest energy configuration is cubic in the absence of externally applied strain or stress is referred to as the preferentially cubic regime and in similar fashion the regime where the lowest energy configuration is tetragonal is referred to as the preferentially tetragonal regime.

The calculated result indicates that the *c*/*a* ratio is dependent on τ and converges to a minimum of 0.987. This is consistent with the experimentally observed *c*/*a* ratio of 0.991 by Mailfert *et al.* [77] if one considers that Mailfert's sample in all likelihood contained some disorder.

4.4.3 Normal state resistivity

To determine the resistivity of a sample with a given τ, an anisotropic Drude model is used, where the resistivity is expressed in terms of the mean scattering time, the electron density of states and the root mean square Fermi velocity, after Allen *et al.* [142]:

$$\rho_{\mathrm{n,x}} = \frac{V}{eN\left(E_{\mathrm{F}}\right) v_{\mathrm{F,x}}^2 \tau}, \tag{4.4}$$

where $\rho_{\mathrm{n,x}}$ is the normal state resistivity in direction x in [Ωm], V is the molecular volume [m^3], e the elementary charge in [C], $N(E_{\mathrm{F}})$ the electron density of states at the Fermi energy in [states $\times$ eV^{-1} $\times$ unit cell^{-1}], and $v_{\mathrm{F,x}}$ the root mean square Fermi velocity in direction x in [ms^{-1}].

This equation has commonly been applied for Nb_3Sn and other A15 superconductors, see Schachinger *et al.* [113], Mattheiss *et al.* [131], and Allen *et al.* [142]. Note that this equation is a special case of the more general Boltzmann transport equation. Instead of a k-space dependent τ and Fermi velocity, equation 4.4 uses a mean scattering time and a root mean square Fermi velocity, also see Ibach *et al.* [148]. In addition, the Boltzmann transport equation contains a correction factor to account for the direction in which electrons move before and after a scattering event, which in equation 4.4 is set equal to 1, as discussed by Grimvall [149]. According to Schachinger *et al.* [113] the use of this equation is valid when the normal state resistivity is dominated by s-wave scattering on non-magnetic impurities.

For a molecule where the lattice vectors are perpendicular to each other, the molecular volume is expressed as:

$$V = a_{\mathrm{x}} a_{\mathrm{y}} a_{\mathrm{z}}, \tag{4.5}$$

where a_{x}, a_{b}, and a_{z} are the lengths of orthogonal lattice vectors in [m].

4.4.4 Root mean square Fermi velocity

$v_{\mathrm{F,x}}$, which is the root mean square Fermi velocity in direction x, is related to the change in energy with a shift in momentum space in direction x, for every band and every point in momentum space, as expressed by Pickett *et al.* [150]:

$$\left(\hbar v_{\mathrm{F,x}}\right)^2 = \frac{\sum\limits_{k,n} \left(E_{\mathrm{x}}(k,n)^2 \delta\left(E\left(k,n\right) - E_{\mathrm{F}}\right)\right)}{\sum\limits_{k,n} \delta\left(E\left(k,n\right) - E_{\mathrm{F}}\right)}, \tag{4.6}$$

$$E_{\mathrm{x}}\left(k,n\right) = \frac{E\left(k+\Delta k_{\mathrm{x}},n\right) - E\left(k,n\right)}{\Delta k_{\mathrm{x}}}, \tag{4.7}$$

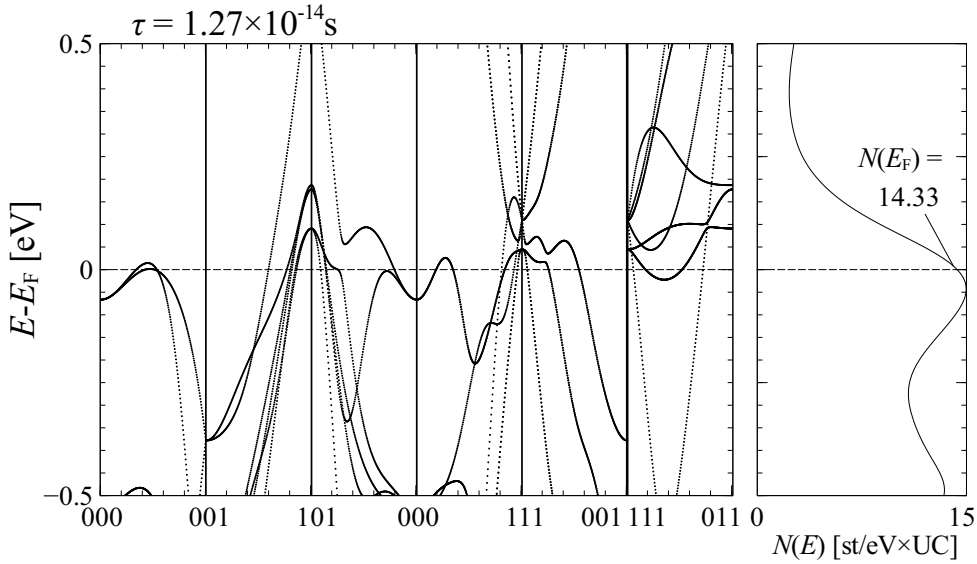

Figure 4.6: *Calculated k-space dependent electron band energy of cubic Nb_3Sn.*

$$\delta(E) = \frac{1}{2 + \exp\left(\frac{E}{\hbar\tau}\right) + \exp\left(\frac{-E}{\hbar\tau}\right)}, \tag{4.8}$$

where k indicates a momentum space coordinate in [m^{-1}], *E(k,n)* is the energy of an electron in band n and at momentum space coordinate k in [J] and $\delta(E)$ describes the Fermi-Dirac broadening term. In figure 4.6, the electronic band structure along various high-symmetry directions is presented. Both $N(E_F)$ and v_F are determined by the nature of the bands near the Fermi energy. $N(E_F)$ is determined by both the amount of bands crossed the Fermi energy and the angle at which they cross (with bands with lower $\delta E/\delta k$ contributing more than bands with higher $\delta E/\delta k$), while the Fermi velocity is determined by the angle (which bands with higher $\delta E/\delta k$ contributing more to v_F than bands with lower $\delta E/\delta k$).

Once the root mean square Fermi velocity is known in three orthogonal directions, the total effective Fermi velocity is calculated with:

$$v_F = \sqrt{(v_{F,x})^2 + (v_{F,y})^2 + (v_{F,z})^2}, \tag{4.9}$$

where directions x, y, z, are calculated along the a, b, and c planes in the crystal. In a cubic crystal with $v_{F,x} \equiv v_{F,y} \equiv v_{F,z}$, equation 4.9 is simplified to:

$$v_F = \sqrt{3} v_{F,x}. \tag{4.10}$$

4.4.5 Comparison between calculated results and experimental data

Using equation 4.4, the critical resistivity is calculated that separates the preferentially cubic and tetragonal regimes. The electron density of states and Fermi velocity are calculated for $\tau = 1.53 \pm 0.08 \times 10^{-14}$ s, resulting in an $N(E_F)$ of 15.13 $\pm$0.23 states/(eV $\times$ unit cell), a $v_{F,x}$ of (1.225$\pm$0.008) $\times 10^5$ ms^{-1}, a v_F of (2.121$\pm$0.014)$\times 10^5$ ms^{-1}, and an a_0 of 0.5312 nm. Using equation 4.4, ρ_c is calculated to be 27.0$\pm$1.4 $\mu\Omega$cm, where ρ_c is the transition point between cubic and tetragonal crystal symmetry (figure 4.4).

The experimental observations of samples in which disorder is introduced in a variety of ways indicates that the critical normal state resistivity is 25$\pm$3 $\mu\Omega$cm, which is consistent with the calculated result (section 4.4.1).

4.4.6 Discussion

The consistency of the calculation results and the experimental observations of samples where disorder was introduced in a variety of ways is a first validation that the electron lifetime broadening model a good approximation that mitigates the unrealistically large computational resources required for physically more correct supercell calculations.

The fact that low-resistivity Nb_3Sn is preferentially tetragonal presents a problem from the perspective of DFT calculations because the martensitic transformation results in a phenomenon called tweed modulation: domains are formed in which the *c*-axis is aligned along a different direction in comparison to neighboring domains throughout the Nb_3Sn sample. The resulting tweed patterns were experimentally observed in V_3Si by Goringe *et al.* [143] and Onozuka *et al.* [144]. This phenomenon has sparked a lot of scientific interest such as the computational investigation by Kartha *et al.* [145]. Goringe *et al.* [143] observed tweed pattern spacing as low at 10 nm, and speculated that even finer spacing, beyond the resolution of the TEM technique, would be present in the sample. This tweed modulation is problematic from the perspective of using single unit cell DFT calculations: an underlying assumption of DFT calculations is that the next unit cell over is identical (i.e. the crystal is periodic) which fails to incorporate the periodicity of the tweed modulation extending well beyond a single unit cell. In other words, in DFT calculations it is assumed that the *c*-axis is aligned along a single direction throughout an infinitely large single crystal, while in the case of preferentially tetragonal Nb_3Sn this assumption is incorrect. Moreover, it is not obvious to what extent this incorrect assumption affects the calculated results, which is why the choice was made to calculate the properties of preferentially cubic Nb_3Sn and to treat the properties of preferentially tetragonal Nb_3Sn as a topic that is beyond the scope of this research. An exception is made in section 4.8.7, where it calculated what the superconducting properties of low-resistivity Nb_3Sn would be if the martensitic transformation is suppressed. This is justified, because it is the tetragonal distortion that results in the formation of tweed patterns [145], which means that tweed modulation does not occur when the martensitic transformation is suppressed.

The calculated lattice parameter of 0.5313 $\pm$ 0.0001 nm for all compositions where the cubic phase is stable is somewhat higher than the experimentally observed lattice parameter of 0.5280$\pm$0.0001 nm for a slightly off-stoichiometric thin film at 45 K [77]. This discrepancy of 0.6% in the value of the lattice parameter is characteristic for the accuracy of DFT calculations.

4.4.7 Conclusion

The electron-lifetime broadening model is applied to calculate the stability of the cubic phase as a function of mean scattering time τ and the corresponding normal state resistivity ρ_n is calculated with a Drude resistivity model.

The calculated critical resistivity of 27.0±1.4 $\mu\Omega$cm, which separates the cubic from the tetragonal crystal symmetry, is consistent with experimental observations where the cubic phase is stabilized through excess niobium, ternary additions and temperature.

4.5 Microscopic properties of cubic Nb-Sn

Before considering the critical temperature and the upper critical field, an overview is given of various ab-initio calculated properties as a function of mean scattering time. These properties include various electronic properties, which are the electron density of states, the Fermi velocity, the mean free path, the normal state resistivity, and the Drude frequency, and also vibration properties, which are phonon dispersion curves and the frequency dependent phonon density of states. Various references in literature are presented to validate the calculated results.

4.5.1 Electronic properties

The mean free path is related to v_F and τ, with:

$$l_{mfp} = \tau \times v_F, \tag{4.11}$$

where l_{mfp} is the mean free path in [m]. If equations 4.4 and 4.11 are combined, the normal state resistivity can be expressed in terms of the mean free path:

$$\rho_{n,x} = \frac{V}{eN(E_F)\, v_{F,x} l_{mfp,x}}, \tag{4.12}$$

where $l_{mfp,x}$ is the directional mean free path in direction x in [m]. The Drude frequency is related to $N(E_F)$ and v_F [142], with:

$$\Omega_P = \hbar \sqrt{\frac{N_V v_F^2}{3\varepsilon_0}}, \tag{4.13}$$

where Ω_P is the Drude frequency in [eV] and ε_0 is the vacuum permittivity.

Figure 4.7 shows various electronic properties as a function of τ. Figures 4.8 and 4.9 show $N(E_F)$ and v_F as a function of normal state resistivity. Also shown are derivations of $N(E_F)$ and v_F as a function of ρ_n. Orlando *et al.* [81], Schachinger *et al.* [113], and Lim *et al.* [147] investigated the properties of stoichiometric and off-stoichiometric Nb-Sn samples with an emphasis on the ratio between ρ_n, T_c, and $\mu_0 H_{c2}(0)$, while Ghosh *et al.* [146] performed a similar analysis on stoichiometric Nb_3Sn samples that were exposed to electron irradiation. The consistency between the calculated results and the literature is quite good, with quantitative and qualitative consistency over the entire disorder range.

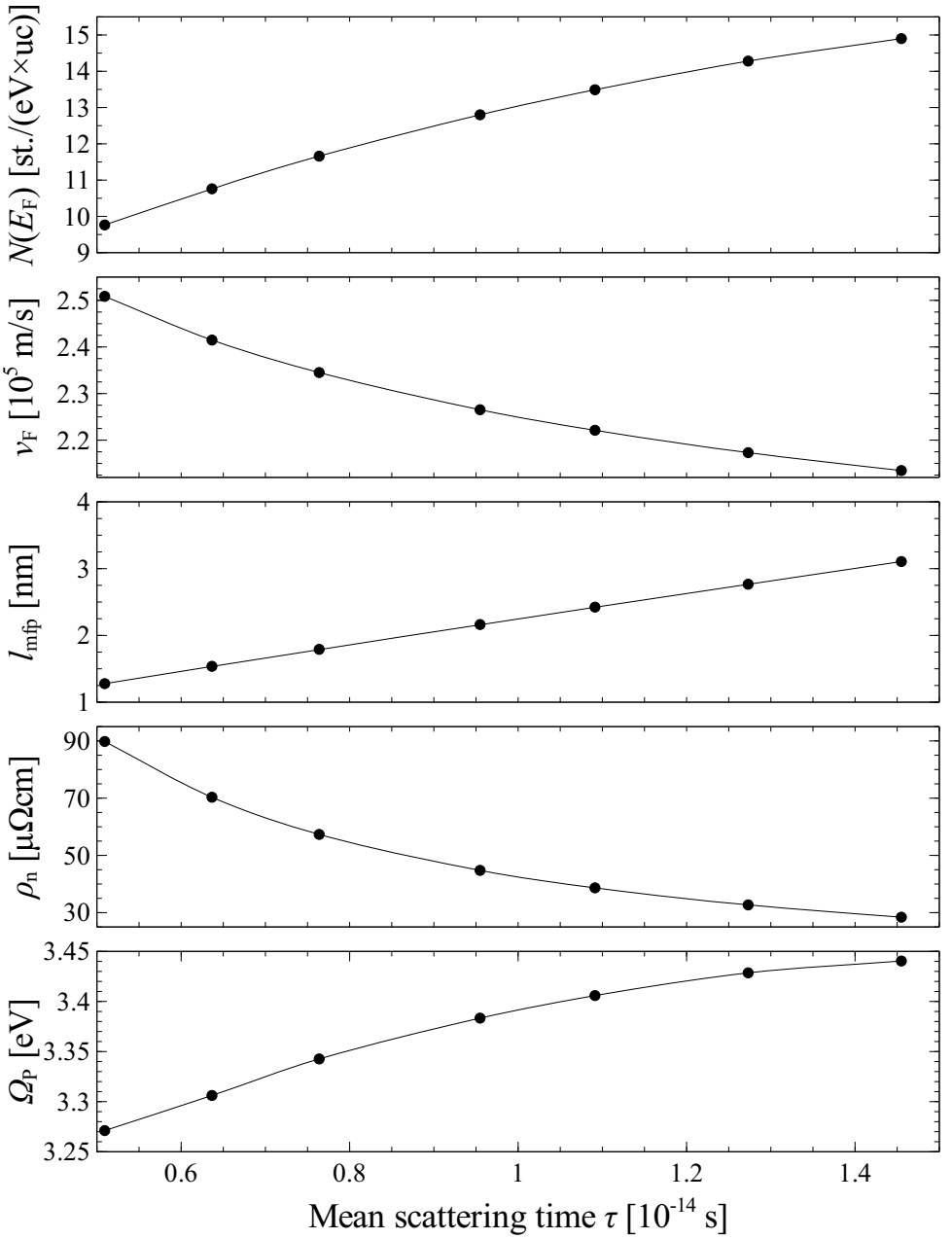

Figure 4.7: *Various calculated electronic properties as a function of the mean scattering time τ.*

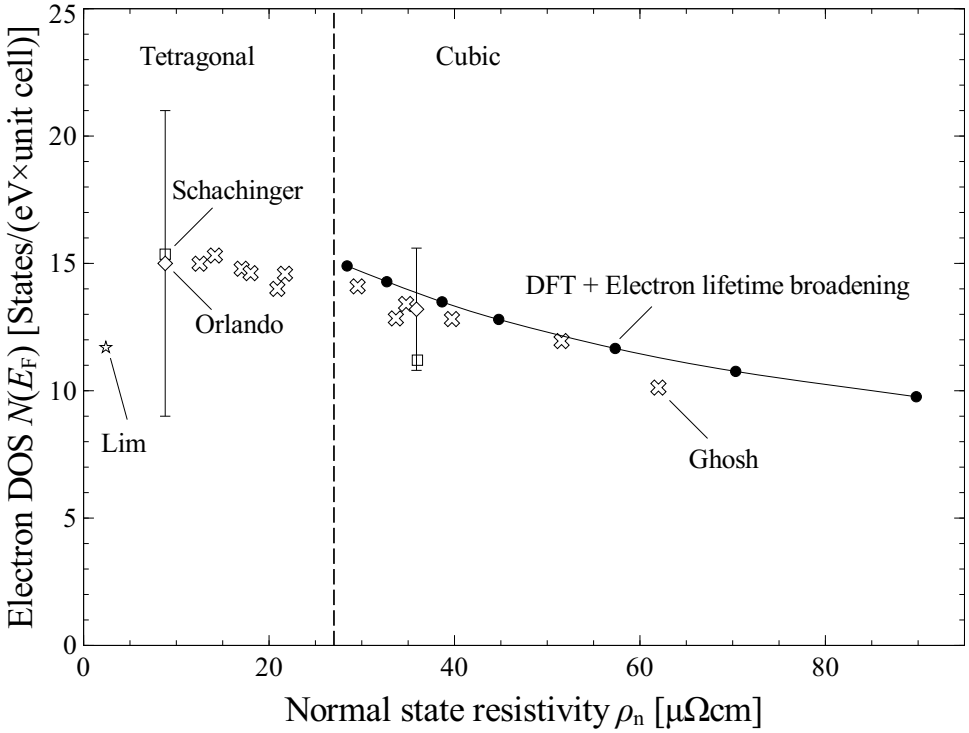

Figure 4.8: *Calculated electron density of states as a function of normal state resistivity, compared to literature results by Schachinger et al. [113], Orlando et al. [81], Lim et al. [147], and Ghosh et al. [146].*

4.5.2 Phonon dispersion curves and phonon density of states

Phonon dispersion curves and the phonon density of states were calculated at various mean scattering times and compared to experimental observations obtained through neutron scattering measurements by Axe *et al.* [156], Pintschovius *et al.* [157], and Schweiss *et al.* [158]. The comparison is shown in figures 4.10 and 4.11. As is customary, the energy equivalent of the vibrational frequency is used throughout this thesis.

The calculated phonon density of states has sharp features (i.e. very narrow frequency ranges per mode) while the experimentally observed phonon density of states is broadened. There are a number of explanations for this effect including instrument resolution, broadening due to the presence of impurities, phonon scattering due to thermally excited quasiparticles, instabilities related to the Martensitic transformation, and direct excitation by phonons of quasiparticles across the superconducting energy gap. It was shown by Axe *et al.* [159] that the observed broadening is dominated by the last effect. In order to allow for an approximate comparison between the calculated and experimentally observed phonon density of states and Eliashberg spectrum, the calculated phonon density of states is convoluted with a Gaussian function with a FWHM of 1.2 meV, which is the average phonon linewidth in stoichiometric Nb_3Sn according to [159].

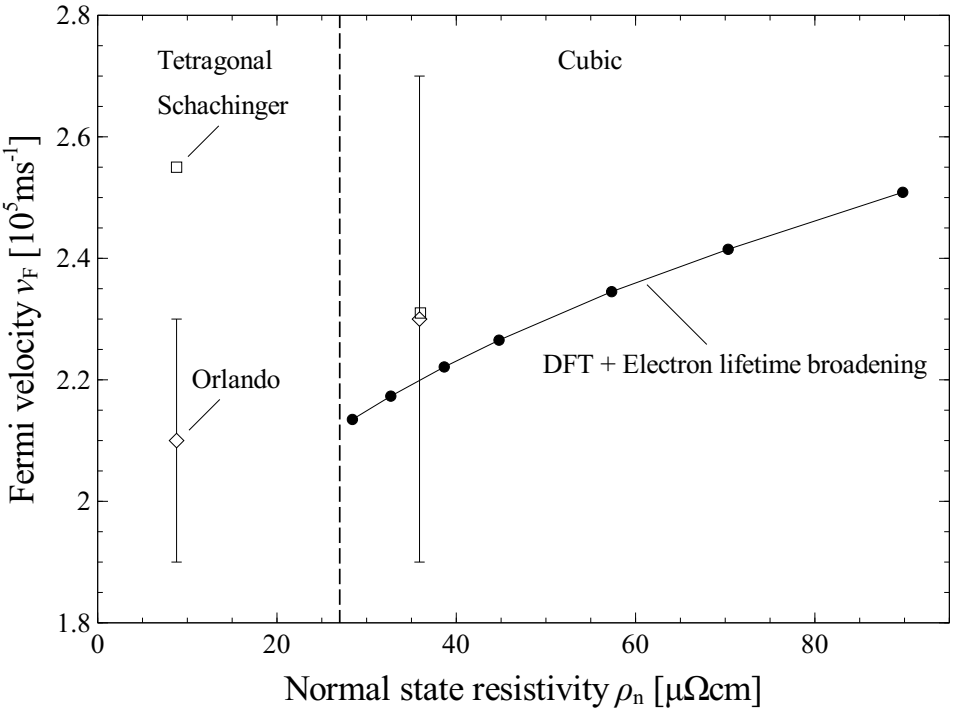

Figure 4.9: *The calculated Fermi velocity as a function of the normal state resistivity, compared to results of Orlando et al. [81], and Schachinger et al. [113].*

Note that this phenomenon does not change the parameters relevant for superconductivity, such as λ, because these are calculated through integrals over the entire phonon density of states (with an approximate width of the order of 30 meV) and small broadening features (of the order of 1 meV) do not influence the integral.

As a general statement, the phonon density of states as determined from neutron scattering measurements is not the same as the calculated phonon density of states, because it is also dependent on the neutron scattering cross-section. This distinction is expressed in the symbols used for the phonon density of states. Typically the calculated phonon density of states is denoted with F, while the phonon density of states which is measured through neutron scattering measurements is denoted with G. In the special case of Nb_3Sn, it is argued by Freeriks *et al.* [160] that $F \approx G$, because the mass of the Nb and Sn ions is of the same magnitude.

Figure 4.11 shows a comparison between calculated and measured dispersion curves. The comparison is imperfect because the measurements were performed at elevated temperatures and on low-resistivity Nb_3Sn, while the calculated result is for Nb-Sn with somewhat higher normal state resistivity at 0 K. This distinction matters to some extent, because the variation between the calculated results in figure 4.10 indicates that the phonon density of states is dependent of disorder. In the measurement data the peaks in $F(\omega)$ are found at somewhat

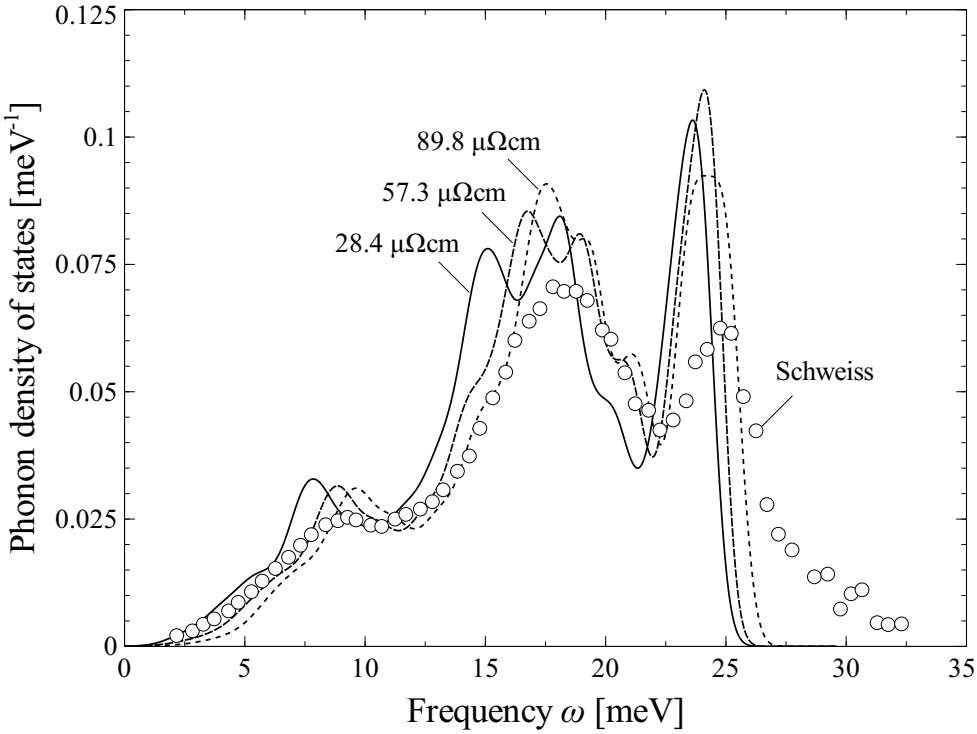

Figure 4.10: *Calculated phonon density of states as a function of vibrational frequency at various degrees of disorder, compared to experimentally determined generalized phonon density of states of low-resistivity Nb_3Sn, after Schweiss et al. [158].*

higher frequencies than in the calculated results. This could be due to the difference in disorder, because the measurement data by Schweiss *et al.* is of low ρ_n and thus preferentially tetragonal Nb_3Sn, while the calculation results are of higher ρ_n preferentially cubic Nb_3Sn. At the same time, this could also indicate a small systematic error in the calculation result.

4.6 Dependence of $\alpha^2(\omega)$ on the electronic and vibrational properties of the crystal

In this section, the dependence of the Eliashberg spectrum $\alpha^2(\omega)$ on the electronic and the vibrational properties of the material is discussed. From the Eliashberg spectrum and the dimensionless effective Coulomb repulsion term, the critical temperature can be calculated, which is discussed section 4.7.

Note that the Eliashberg spectrum can be calculated directly from ab-initio calculations, as was shown by Baroni *et al.* [126]. The validity of the calculation method was investigated by Salvetti [161, 162]. It was determined that it only produces quantitatively correct values when highly dense k- and q-point grids are utilized. An investigation of the effect of stress

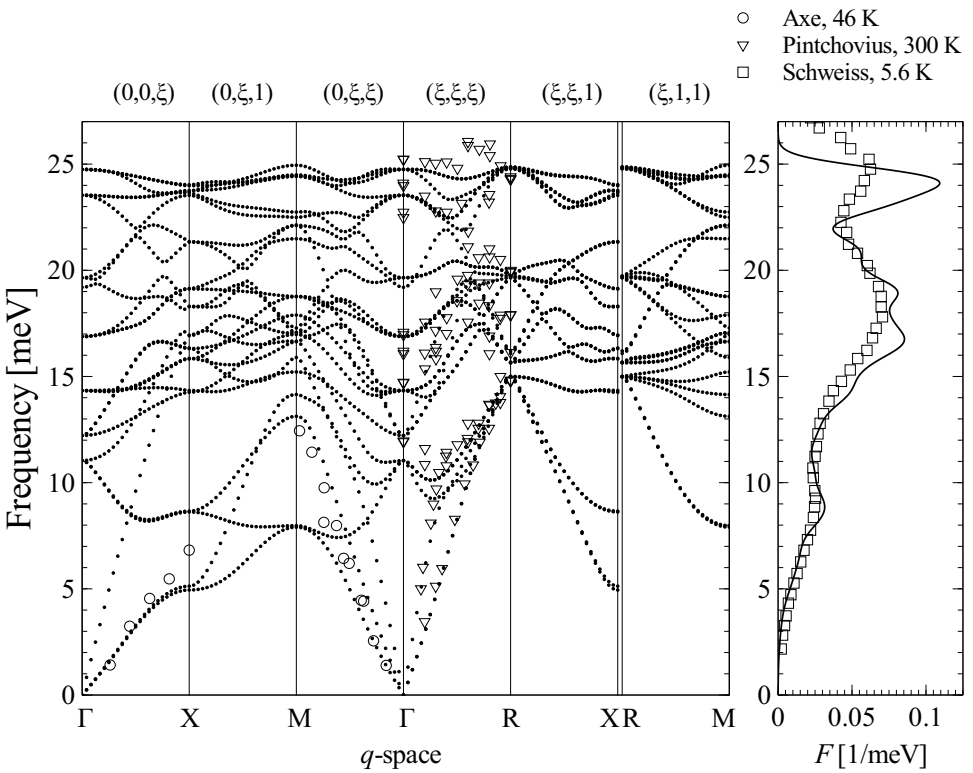

Figure 4.11: *Calculated phonon dispersion curves of cubic Nb_3Sn with ρ = 57.3 $\mu\Omega$cm, compared to literature data by Axe et al. [156], Pintschovius et al. [157], and Schweiss et al. [158]. The black symbols are calculated results and the open symbols are measurements.*

on the superconducting properties of aluminum has shown that an insufficiently dense *k*- and *q*-point grid leads to calculated results which are shown to qualitatively and quantitatively incorrect. At the same time, the computational cost of performing a sufficiently dense calculation is excessive and therefore unfeasible for a systematic study. This means that while this method might be usable in the future to directly determine the frequency dependence of $\alpha^2(\omega)$ as a function of strain and degree of disorder, the method has to be used with some caution.

In spite of this issue, the method was used to calculate the critical temperature of Nb_3Sn by Tutunce *et al.* [163] and De Marzi *et al.* [164]. However, neither author considered the influence of disorder, both authors neglected the influence of the tetragonal distortion, and both authors found that the critical temperature of *cubic* stoichiometric Nb_3Sn is 18 K. It was experimentally established by Devantay *et al.* [52] that stoichiometric Nb_3Sn with a critical temperature of 18 K is preferentially tetragonal. Without a thorough discussion on how disorder influences their calculated results, one can only conclude that the calculated results (indicating that stoichiometric Nb_3Sn is preferentially cubic with a calculated T_c of 18 K) is inconsistent with the experimental evidence (which states the stoichiometric Nb_3Sn with

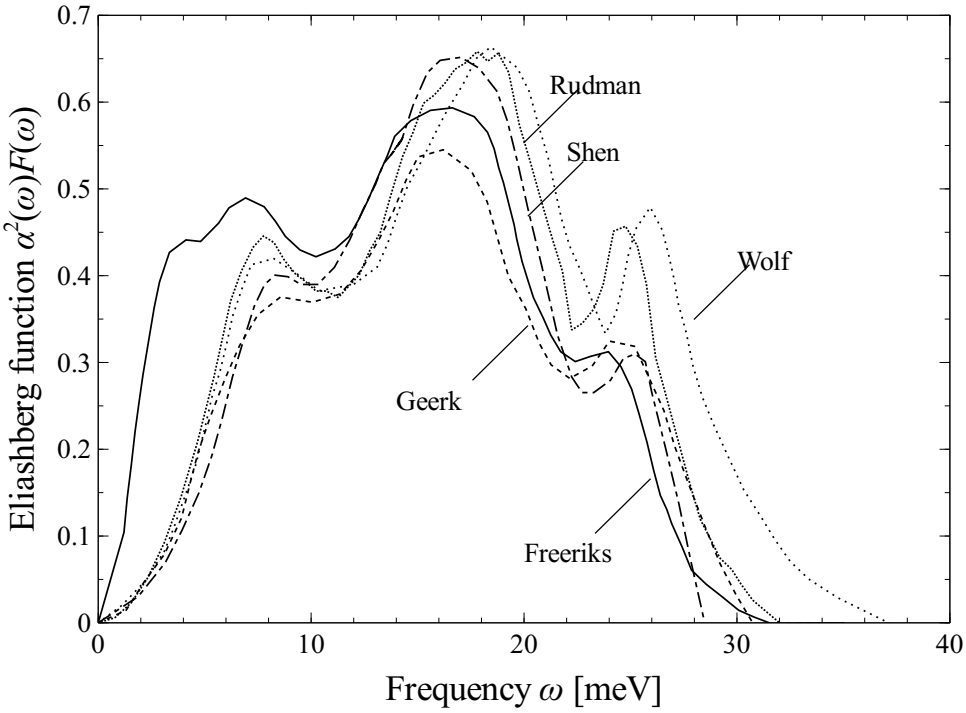

Figure 4.12: *Experimentally observed α^2F as a function of vibrational frequency of stoichiometric Nb_3Sn, after Freeriks et al. [160], Geerk et al. [166], Shen [167], Rudman et al. [168], and Wolf [169].*

a T_c of 18 K is preferentially tetragonal [41]), which could be a result of an insufficiently dense k- and q-point grid in the calculation of $\alpha^2(\omega)$.

In light of these issues, no effort was made to directly calculate $\alpha^2(\omega)$. Instead, the dependence of $\alpha^2(\omega)$ on the electronic and vibrational properties of the material was derived from experimental data as discussed in this section.

4.6.1 Derivation of α^2, simple argument

The electron-phonon coupling constant λ describes the amount of coupling between electrons and phonons and is related to an Eliashberg spectrum [14] through:

$$\lambda = 2\int \frac{\alpha^2(\omega)F(\omega)}{\omega}\delta\omega, \tag{4.14}$$

where lambda is the electron-phonon coupling constant in dimensionless units, $\alpha^2(\omega)$ is the electron-phonon coupling characteristic in [meV^{-1}], F is the phonon density of states in [meV^{-1}], and ω is the phonon frequency in [meV].

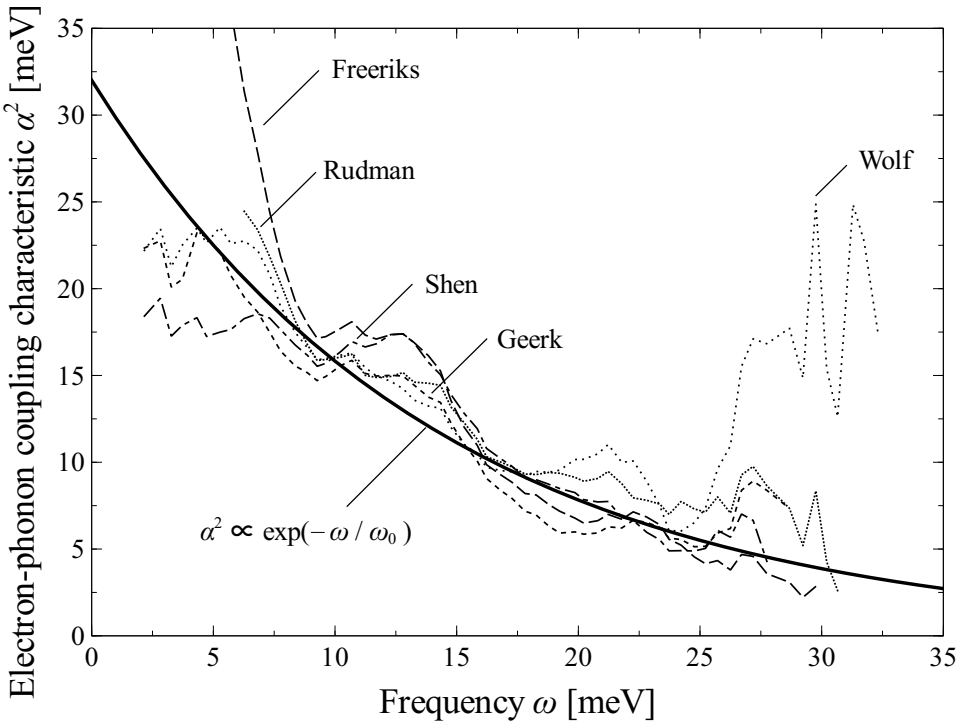

Figure 4.13: *Electron-phonon coupling characteristic α^2 as a function of vibration frequency. Empirical description compared to various experimental observations after Freeriks et al. [160], Rudman et al. [168], Shen [167], Geerk et al. [166], and Wolf [169].*

It was shown by Markiewicz [98] that the vibrational frequency dependence of Nb_3Sn can empirically be described with:

$$\alpha^2(\omega) \propto \exp(-\omega/\omega_0), \tag{4.15}$$

where ω_0 is a characteristic frequency of Nb_3Sn. In the case of intermediate coupling and in the case of a single ion species, the electron-phonon coupling constant is related to the electron density of states by McMillan and Hopfield [15, 16, 165], through:

$$\lambda = \frac{\eta}{M\langle\omega^2\rangle} = \frac{N(E_F)\langle I^2\rangle}{M\langle\omega^2\rangle}, \tag{4.16}$$

where η is the McMillan-Hopfield parameter, $< I^2 >$ is the mean squared electronic matrix element, M is the effective ion mass, and $<\omega^2>$ is the average of the squared phonon frequency in the Eliashberg spectrum.

As λ is proportional to both the amplitude of α^2 and $N(E_F)$, one could speculate that α^2 is

proportional to $N(E_F)$. Combining this with equation 4.15, one can formulate an ansatz:

$$\alpha^2_{\text{eff}}(\omega) = \alpha^2_{\text{IM,eff}} N(E_F) \exp\left(-\omega/\omega_0\right), \tag{4.17}$$

where $\alpha^2_{\text{IM,eff}}$ and ω_0 are characteristic constants. To determine the magnitude of these constants, a number of experimentally observed Eliashberg spectra of stoichiometric Nb_3Sn, after Shen [167], Geerk *et al.* [166], Freeriks *et al.* [160], Rudman *et al.* [168], and Wolf [169] as shown in figure 4.12, are divided by the experimentally observed phonon density of states by Schweiss *et al.* [158], shown in figure 4.10. This procedure is analogous to the investigation performed by Markiewicz [98]. The electron density of states of slightly disordered stoichiometric Nb_3Sn is equal to 15.36 states/(eV$\times$unit cell) according to Schachinger *et al.* [113], which is consistent with the results of Orlando *et al.* [81] and Ghosh *et al.* [146]. The optimal values of $\alpha^2_{\text{IM,eff}}$ and ω_0 are then determined to be 2.08×10^{-3} eV^2 / (states $\times$ unit cell) and 14.2 meV, respectively (figure 4.13).

4.6.2 Derivation of α^2, detailed explanation

An empirical approach was used to formulate equation 4.17, but one can also use microscopic theory to determine what α^2 is. In addition to the expression of λ, Eliashberg expressed $<\omega^2>^{0.5}$ as:

$$\left\langle \omega^2 \right\rangle = \frac{2}{\lambda} \int \alpha^2(\omega) F(\omega) \omega \delta\omega. \tag{4.18}$$

The phonon density of states is a normalized property:

$$\int_0^\infty F(\omega)\, \delta\omega \equiv 1. \tag{4.19}$$

Combining equations 4.16, 4.18, and 4.19, one can formulate a solution for α^2, which is applicable in the presence of a single ion species:

$$\alpha^2(\omega) = \frac{\left\langle I^2 \right\rangle}{2M} \frac{N(E_F)}{\omega} = \alpha^2_{\text{IM}} \frac{N(E_F)}{\omega}. \tag{4.20}$$

However, Nb_3Sn contains two ion species (niobium and tin). In a system with more than one ion, λ can be approximated as the sum of the individual contributions of the ions [158], with:

$$\lambda = \frac{\eta_1}{M_1 \langle \omega^2 \rangle_1} + \frac{\eta_2}{M_2 \langle \omega^2 \rangle_2} + \ldots \tag{4.21}$$

One can then define an effective $\alpha^2_{\text{IM,eff}}$, which is dependent on the relative contributions of the different species. A weighting function f_W is defined which accounts for the relative contributions:

$$\alpha^2_{\text{eff}}(\omega) = \frac{N(E_F) f_W(\omega)}{\omega}, \tag{4.22}$$

$$f_W(\omega) = \frac{\alpha^2_{IM,1} F_1(\omega) + \alpha^2_{IM,2} F_2(\omega) + ...}{F_{\text{total}}(\omega)} \tag{4.23}$$

where f_W is a weighting function that describes the weighted contribution of each individual ion. Through a comparison of different superconductors, Schweiss *et al.* [158] determined that the intermediate frequency range (i.e. around 14 meV) contributes more to the superconducting properties of Nb_3Sn than the low and high frequency ranges. One can thus postulate that:

$$f_W(\omega) = \alpha^2_{IM,\text{eff}} \omega \exp\left(\frac{-\omega}{\omega_0}\right), \tag{4.24}$$

which peaks at frequency ω_0. In combination with equation 4.22, one finds:

$$\alpha^2_{\text{eff}}(\omega) = \alpha^2_{IM,\text{eff}} N(E_F) \exp\left(-\omega/\omega_0\right), \tag{4.25}$$

which is the same as equation 4.17. Moreover, the equation is applicable at various levels of disorder if the variation in $\alpha^2_{IM,\text{eff}}$ and ω_0 are weakly dependent on disorder.

4.6.3 Comparison of calculated α^2F, compared to experimentally determined α^2F in disordered Nb-Sn

One can hypothesize that equation 4.17, an empirical equation that was derived from tunnel junction data of weakly disordered stoichiometric Nb_3Sn, is also applicable in strongly disordered Nb_3Sn, and thus over an entire range of disorder. In order to determine the validity of this hypothesis, the disorder dependent electron and phonon density of states are calculated, the Eliashberg spectrum is calculated using equation 4.17 and the results are compared to experimentally observed Eliashberg spectra of off-stoichiometric Nb-Sn by Rudman *et al.* [168].

The comparison is shown in figure 4.14. It is clear that the calculated and experimentally observed Eliashberg spectra are consistent, although the peaks in the experimentally observed Eliashberg spectra are at a somewhat higher vibrational frequency. In this particular case, this is likely an experimental issue. Rudman identified some persistent nonidealities in the measurement (because the characteristics of tunnel junctions are extremely sensitive to any imperfections in the junction) and was unable to determine the lower frequency range below about 8 meV.

On the right side of figure 4.14, λ and $<\omega^2>^{0.5}$ are shown, which are derived from the Eliashberg spectra through equations 4.14 and 4.18. The calculated λ is close to Rudman's result and the calculated $<\omega^2>^{0.5}$ is slightly lower than Rudman's results. Also shown are λ and $<\omega^2>^{0.5}$ derived from the various literature data of weakly disordered stoichiometric tunnel junction data (figure 4.12, table 4.1). The error bars indicate one standard deviation in the literature data (table 4.1).

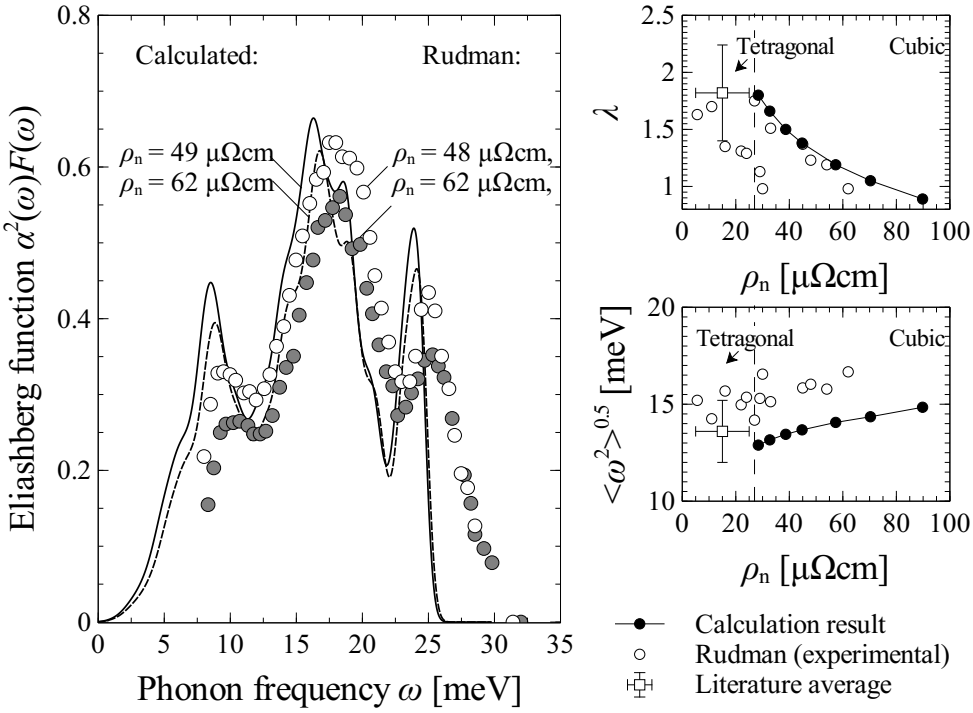

Figure 4.14: *Calculated and experimentally observed α^2F, λ, and $<\omega^2>^{0.5}$. The experimental data are reproduced from Rudman et al. [168].*

Table 4.1: *Values for λ, $<\omega^2>^{0.5}$ and μ^* of weakly disordered stoichiometric Nb_3Sn after Freeriks et al. [160], Wolf [169], Shen [167], Geerk et al. [166], and Rudman et al. [168], mean values, and standard deviations.*

	λ	$<\omega^2>^{0.5}$ [meV]	μ^*_{Kresin}	$\mu^*_{\text{Allen-Dynes}}$
Freeriks	2.55	10.9	0.17	0.17
Wolf	1.79	15.2	0.16	0.15
Shen	1.56	13.9	0.09	0.11
Geerk	1.50	13.8	0.08	0.06
Rudman	1.75	14.2	0.13	0.12
Average	1.83	13.6	0.127	0.122
Std.dev	0.42	1.6	0.042	0.044

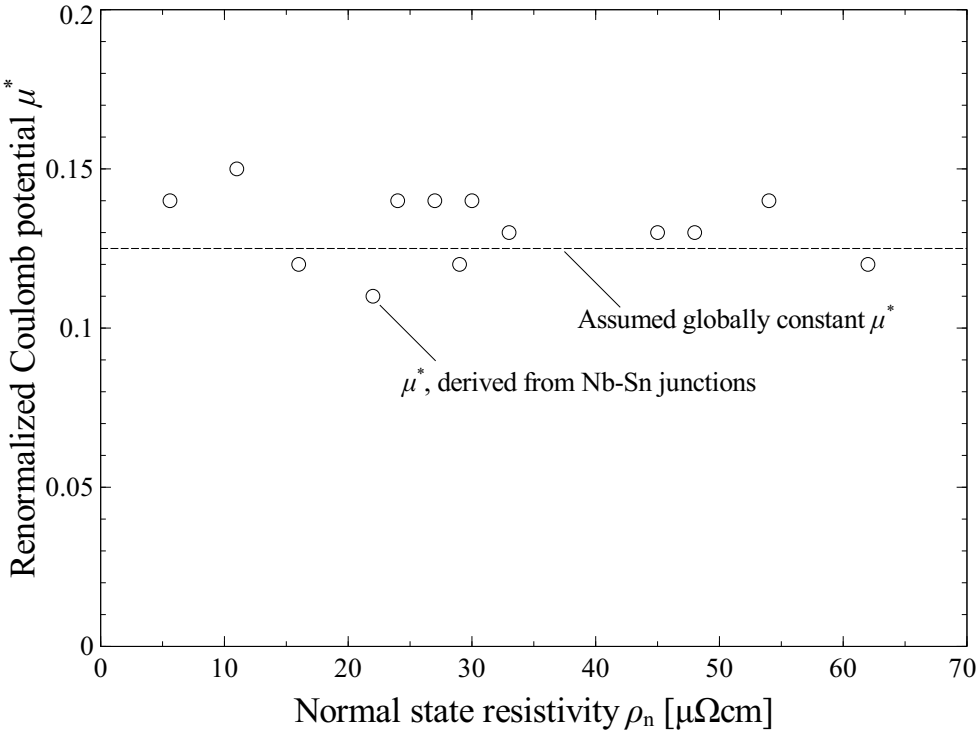

Figure 4.15: *μ^* as a function of ρ_n, derived from tunnel junction data by Rudman et al. [168], and constant μ^* approximation.*

4.7 Critical temperature

4.7.1 Kresin and Allen-Dynes critical temperature descriptions

A number of relations exist connecting the critical temperature to the electron-phonon coupling constant λ and the characteristic phonon frequencies. Here, the descriptions of Kresin [18] and Allen and Dynes [17] are used, which both have greater accuracy than original critical temperature description of McMillan [170].

Kresin's description [18, 98] relates T_c to λ, $<\omega^2>^{0.5}$, and μ^*, following:

$$t(\lambda) = 1.5\exp(-0.28\lambda), \tag{4.26}$$

$$\lambda_{\text{eff}} = \frac{\lambda - \mu^*}{1 + 2\mu^* + \lambda\mu^* t(\lambda)}, \tag{4.27}$$

$$k_B T_{c,\text{Kr}} = \frac{0.25\langle\omega^2\rangle^{0.5}}{\sqrt{\exp(2/\lambda_{\text{eff}}) - 1}}, \tag{4.28}$$

where $<\omega^2>^{0.5}$ is in [eV], T_c is in [K], t, λ_{eff}, and λ are dimensionless numbers, k_B is the Boltzmann constant in [eV/K], and μ^* is the dimensionless effective Coulomb repulsion term.

In addition to $<\omega^2>^{0.5}$, μ^*, and λ, Allen and Dynes's T_c description [17] requires additional characteristic frequencies, with:

$$\langle\omega\rangle = \frac{2}{\lambda}\int \alpha^2 F(\omega)\,\delta\omega, \tag{4.29}$$

$$\omega_{log} = \exp\left(\frac{2}{\lambda}\int \frac{\alpha^2 F(\omega)\ln(\omega)}{\omega}\delta\omega\right), \tag{4.30}$$

$$\Lambda_1 = 2.46\,(1+3.8\mu^*), \tag{4.31}$$

$$\Lambda_2 = 1.82\,(1+6.3\mu^*)\left\langle\omega^2\right\rangle^{0.5}\Big/\omega_{log}, \tag{4.32}$$

$$f_1 = \left(1+(\lambda/\Lambda_1)^{3/2}\right)^{1/3}, \tag{4.33}$$

$$f_2 = 1+\frac{\left(\left\langle\omega^2\right\rangle^{0.5}\Big/\omega_{log}-1\right)\lambda^2}{\lambda^2+\Lambda_2^2}, \tag{4.34}$$

$$k_B T_{c,AD} = \frac{f_1 f_2 \omega_{log}}{1.2}\exp\left(\frac{-1.04\,(1+\lambda)}{\lambda-\mu^*-0.62\lambda\mu^*}\right), \tag{4.35}$$

where ω_{log} and $<\omega>$ are characteristic phonon frequencies in [meV] and f_1 and f_2 are correction parameters close to unity.

The effective Coulomb repulsion term μ^* is significantly lower than the normal Coulomb repulsion term μ, due to a timing difference between the attraction and repulsion interaction. The Coulomb interaction process is retarded on a timescale of $1/\Omega_P$, where Ω_P is the plasma frequency. However, the electron-phonon attraction is retarded on a timescale $1/\Omega_D$, where Ω_D is the Debye frequency, so that the attractive force between the electrons is exerted while the repulsion force is partially screened (see Allen [165]). Because $\Omega_P \gg \Omega_D$, $\mu^* \ll 1$.

λ and the characteristic phonon frequencies are calculated from the stoichiometric tunnel junction data (figure 4.12) and μ^* is determined by setting T_c equal to 18 K and solving for μ^* using both the Kresin and the Allen-Dynes T_c equations (table 4.1). This procedure yields nearly identical values of μ^*, with 0.127 and 0.122 for the Kresin and the Allen-Dynes T_c equations, respectively. Taking the average of these values, $\mu^* = 0.125$ is found.

In an investigation of Nb-Sn samples with various compositions, Rudman *et al.* [168] found that μ^* is equal to 0.132 with a standard deviation of 0.011. No composition dependent trend was observed, which validates the use of μ^* as a global constant (figure 4.15).

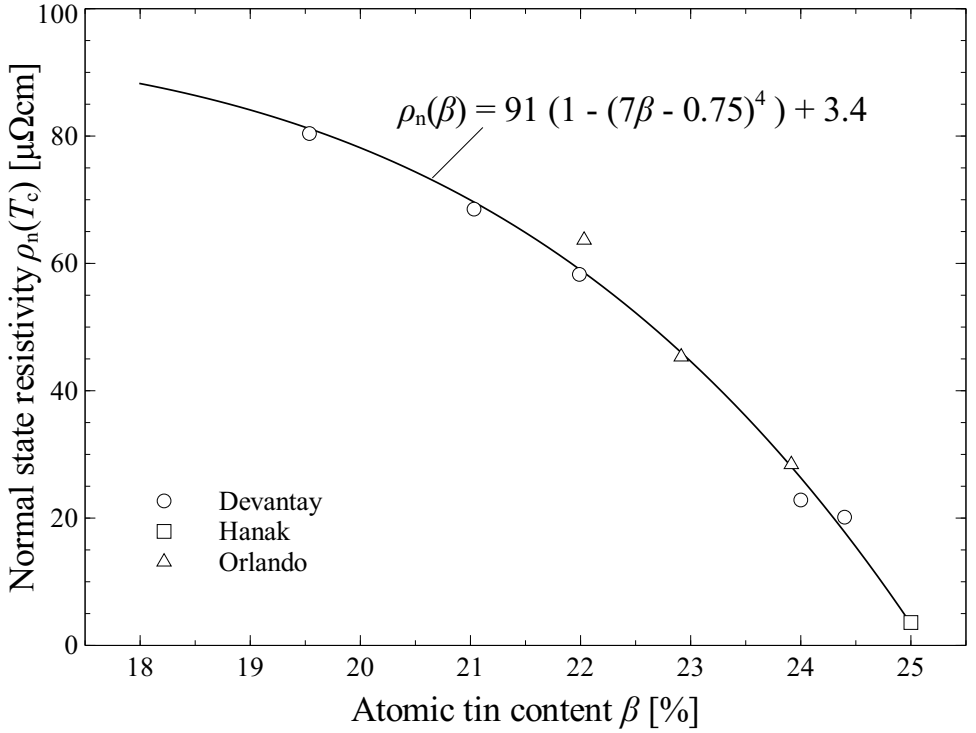

Figure 4.16: *Empirical description of the experimentally observed normal state resistivity ρ_n at T_c as a function of atomic tin content. This figure is reproduced from Godeke [41]. The experimental observations were performed by Devantay et al. [52], Hanak et al. [152], and Orlando et al. [42].*

4.7.2 Critical temperature of cubic Nb_3Sn as a function of normal state resistivity

The disorder dependent critical temperature T_c was calculated as a function of ρ_n using both the Kresin and Allen-Dynes descriptions, which are compared to experimental data. This calculation uses microscopic properties which are obtained from ab-initio calculations (section 4.5) in combination with a globally constant μ^* (figure 4.15), and an empirical description of $\alpha^2(\omega)$ (equation 4.17) which includes two global parameters $\alpha^2_{IM,eff}$ and ω_0. No further assumptions or free parameters are needed to calculate T_c as a function of ρ_n.

One issue with experimental data is that off-stoichiometric Nb-Sn is typically somewhat inhomogeneous implying a broad T_c distribution, as was discussed in section 2.4.7. The same can apply to samples in which disorder is introduced through other means. For instance, if thin film samples are irradiated then it stands to reason that more disorder (i.e. radiation damage) is introduced in side facing the irradiation source rather than in the side of the thin film facing away from the irradiation source. While in normal state resistivity measurements all the material contributes to the measurement, so that the measurement is an effective average of the sample, the superconducting properties that are determined through resistivity

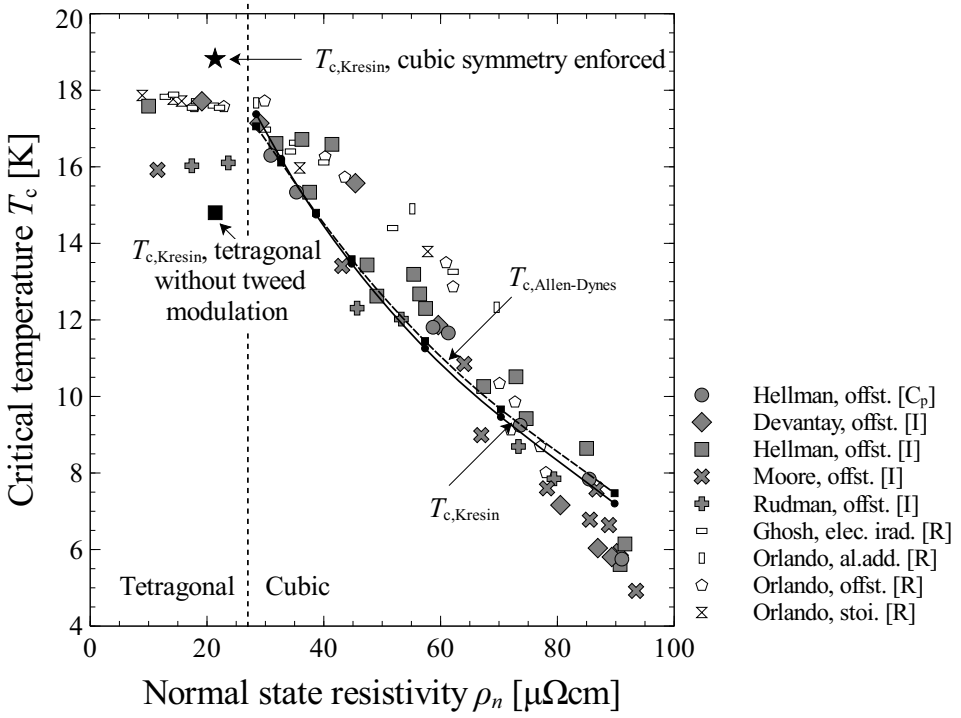

Figure 4.17: *Calculated and measured T_c as a function of normal state resistivity ρ_n. The T_c of preferentially tetragonal Nb_3Sn is approximately 18 K. The deviating literature results, indicating a T_c of about 16 K are most likely a result of a systematic error in the determination of the composition, also see Rudman et al. [43].*

measurements represent the best rather than the average properties of the sample (see section 2.4.7). Thus, the T_c and $\mu_0 H_{c2}(0)$ determined from resistivity measurements represent a different composition or degree of disorder than the normal state resistivity, unless the sample is highly homogenous.

To get around this issue, measurements are used which probe the bulk of the sample rather than the best properties of the sample, such as heat capacity measurements (the most reliable volumetric measurement type) and inductive measurements, by Hellman [51], Rudman *et al.* [82], Devantay *et al.* [52], and Moore *et al.* [13]. In these publications, the critical temperature was determined as a function of composition.

The relation between composition and normal state resistivity at T_c of binary Nb_3Sn is well understood, see Godeke *et al.* [41] (figure 4.16) and Flükiger *et al.* [188]. The relation between composition and residual resistivity can be summarized with an empirical relation, after Godeke [41]:

$$\rho_n(\beta) = 91\left(1-(7\beta-0.75)^4\right)+3.4 \text{ for } \beta \leq 25\%, \tag{4.36}$$

where β is the atomic tin fraction and ρ_n is the residual resistivity (i.e. the normal state resistivity slightly above T_c) in [$\mu\Omega$cm]. The uncertainty in this description is estimated to be about 5 $\mu\Omega$cm. These average T_c measurements are added (in grey symbols) to Orlando's original data set [42] (in open symbols) and shown in figure 4.17.

T_c is then calculated as a function of normal state resistivity using the Kresin (equation 4.28) and Allen-Dynes (equation 4.35) expressions of T_c (figure 4.17). The calculated and measured T_c as a function of normal state resistivity are closely consistent. As expected, the experimentally observed T_c from resistivity measurements (i.e. the open symbols) is in all cases the same or higher than the experimentally observed T_c which is derived from heat capacity or inductive measurements (i.e. the grey symbols). It is also interesting to note that the two expressions of T_c are closely consistent.

4.7.3 Electronic and vibrational contribution to the disorder dependence of T_c

The disorder dependence of T_c is mainly a result of the disorder dependence of $N(E_F)$, although the disorder dependence of the phonon density of states is not negligible.

The $N(E_F)$ at $\tau = 1.45\times10^{-14}$ s and 0.51×10^{-14} s is 14.90 and 9.76 states/(eV$\times$unit cell), respectively (figure 4.7), λ is 1.80 and 0.89, respectively (figure 4.14), $<\omega^2>^{0.5}$ is 12.9 and 14.8 meV, respectively (figure 4.14). With the T_c expression by Kresin (equation 4.28), critical temperatures of 17.4 and 7.2 K is found, respectively.

If the phonon density of states is fixed to the calculated value at $\tau = 1.45\times10^{-14}$ s and thus independent of disorder, then λ is 1.18, $<\omega^2>^{0.5}$ is 12.9 meV and T_c is 10.3 K at $\tau = 0.51\times10^{-14}$ s.

Thus, it is clear that the disorder dependence of T_c is mainly a result of $N(E_F)$ rather than the phonon density of states: the fraction of change in T_c that is due to a change in $N(E_F)$ is $(17.4-10.3)/(17.4-7.2) = 70\%$.

4.7.4 Critical temperature of preferentially tetragonal Nb_3Sn

In section 4.4.6 it was explained that the properties of preferentially tetragonal Nb_3Sn cannot be calculated within the single unit cell DFT approach, because the material undergoes tweed modulation.

This inconsistency can be illustrated with calculated results. At $\tau = 1.91\times10^{-14}$ s, the calculated $N(E_F)$ of a fully relaxed tetragonal unit cell is 12.9 states /(eV$\times$unit cell), the calculated v_F is 2.07×10^5 m/s, and the calculated ρ_n is 21.4 $\mu\Omega$cm. Thus, the calculated result indicates that $N(E_F)$ of preferentially tetragonal Nb_3Sn is significantly lower than preferentially cubic Nb_3Sn, which is inconsistent with literature results (figure 4.8). If the phonon density of states is assumed to be the same as at $\tau = 1.45\times10^{-14}$ s (see section 4.7.3), then T_c, calculated with Kresin's expression (equation 4.28) is 14.8 K, which deviates strongly from the experimentally observed T_c of about 18 K (figure 4.17).

In summary, the single unit cell DFT approach cannot be used to predict the microscopic properties of preferentially tetragonal Nb_3Sn.

4.7.5 Discussion

The quantitative match between the calculated and experimentally observed disorder dependent T_c is a strong indicator that the computational model used to calculate the disorder dependent T_c is accurate. This model applies three global parameters $\alpha^2_{IM,eff}$, ω_0, and μ^*. The uncertainty in $\alpha^2_{IM,eff}$, related to the uncertainty in the electron density of states of weakly disordered stoichiometric Nb_3Sn (figure 4.8) and the uncertainty in the Eliashberg spectra of weakly disordered Nb_3Sn (figure 4.13, is estimated at 5%, which implies an uncertainty in T_c of 0.9 K. The expected uncertainty in μ^* is about 0.04, leading to an uncertainty of about 2 K in T_c. The effect of uncertainty in ω_0 on T_c is small. Thus, these arguments imply that the total uncertainty in T_c is about 3 K. However, over the entire investigated range, the calculated and experimentally observed critical temperatures are consistent within the experimental scatter of about 1 K, which is why the uncertainty of T_c is estimated at 1 K.

4.7.6 Conclusion

The electron-lifetime broadening model is used to calculate the critical temperature at various degrees of disorder. An empirical description of α^2 is derived from experimental data and validated in the case of weakly and strongly disordered Nb_3Sn. The validation includes a comparison with experimentally determined values of α^2F , λ, $<\omega^2>^{0.5}$, and T_c measurements in samples with various off-stoichiometric compositions. This comparison shows that the calculated results are consistent with the experimental results, within an uncertainty of 1 K.

The consistency between the calculated results and the experimental observations indicates that the electron-lifetime broadening model in combination with DFT calculations captures most of the relevant physics that explains the variation in T_c with disorder.

4.8 Upper critical field of Nb-Sn

In the third and final comparison between calculation results and the experimental observations, the upper critical field $\mu_0 H_{c2}$ is calculated as a function of disorder and compared to the experimentally observed composition dependence of $\mu_0 H_{c2}$.

The upper critical field in phonon-mediated superconductors was thoroughly investigated in the past, resulting in a number of descriptions. After the initial success of the Ginzburg-Landau-Abrikosov-Gor'kov (GLAG) theory [7, 11, 171], various corrections were considered and developed to account for the various phenomena which affect the upper critical field. The temperature dependence of $\mu_0 H_{c2}$ was described by Maki and De Gennes [47], under the assumption of a dirty superconductor (i.e. small mean free path and high normal state resistivity), a spherical Fermi surface, a constant $N(E_F)$, and a weak-coupling interaction. Subsequent refinements were made to include various effects, such as the impurity dependence of $\mu_0 H_{c2}$ by Helfand *et al.* [172, 173], Fermi surface anisotropy by Hohenberg *et al.* [174] and Schachinger *et al.* [113], spin-orbit coupling by Werthamer *et al.* [175] Schopohl *et al.* [176] and Rieck *et al.* [177], anisotropic scattering by Schopohl *et al.* [178], Pauli paramagnetic limiting by Orlando *et al.* [81, 42] and Rieck *et al.* [177], strong coupling effects by Werthamer *et al.* [179], Masharov [180], and Schossmann *et al.* [181], p- and d-wave scattering by Rieck at al. [177] and the energy-dependence of $N(E_F)$ by Schossmann *et al.* [182]. A useful overview of these various mechanisms is provided by Rieck *et*

al. [177].

Four different approaches are used here to calculate $\mu_0 H_{c2}$. First of all, as it has previously been demonstrated by Godeke *et al.* [33, 48] that the Maki-DeGennes description accurately fits the upper critical field at various temperatures, compositions, and strains for Nb-Sn, $\mu_0 H_{c2}$ is calculated under the assumption of weak coupling, a dirty limit h^*_{c2}, without Pauli limiting, which are the underlying assumptions of the Maki-DeGennes description.

After this, a best-effort calculation is performed using first principles calculations to calculate the effect of various mechanisms on $\mu_0 H_{c2}(0)$. The calculation includes strong-coupling corrections, a variable reduced collision frequency (i.e. it considers the dirty limit and intermediate limit), Pauli limiting, and isotropic s-wave scattering.

As both T_c and $\mu_0 H_{c2}(0)$ are dependent on ρ_n, and ρ_n is dependent on temperature, the change in ρ_n between 0 and T_c affects the relation between T_c and $\mu_0 H_{c2}(0)$. The magnitude of this effect is estimated here.

Each of these approaches results in a different $\mu_0 H_{c2}(0)$ as a function of T_c, which is compared to experimental data. Finally, the relative influence of the energy dependence of the electron density states, Fermi surface anisotropy, spin-orbit coupling, and p- and d-wave scattering on $\mu_0 H_{c2}(0)$ is discussed.

4.8.1 Upper critical field without Pauli limiting $\mu_0 H^+_{c2}$

The slope of dH^+_{c2}/dT at $\mu_0 H$ = 0 T is described by GLAG theory [7, 11, 81, 131, 171], with:

$$\left.\frac{-\delta\left(\mu_0 H_{c2}\right)}{\delta T}\right|_{T_c} = \left(\frac{24\pi^2 {k_B}^2}{7\zeta(3)\hbar e}\right)\frac{\eta_{\mu_0 H_{c2}} T_c (1+\lambda)^2}{v_F^2 X(Z)}, \tag{4.37}$$

where $\delta\mu_0 H_{c2}/dT$ is in [T/K], $\zeta(3)$ is Apery's constant, k_B is in [JK^{-}1], $\hbar$ is in [Js], e is in [C], T_c is in [K], and v_F is in [ms^{-}1]. η_{Hc2} is the strong coupling correction factor for $\mu_0 H_{c2}$ [180].

Z is the reduced collision frequency [172], which is closely related to mean scattering time:

$$Z = \frac{\hbar}{2\pi k_B T_c (1+\lambda)\tau} = \frac{\hbar v_F}{2\pi k_B T_c (1+\lambda) l_{mfp}}. \tag{4.38}$$

$X(Z)$ is the Gor'kov function [131, 183], with:

$$X(Z) = \frac{\sum_{\nu=0}^{\infty} (2\nu+1)^{-2}(2\nu+1+Z)^{-1}}{\sum_{\nu=0}^{\infty} (2\nu+1)^{-3}}. \tag{4.39}$$

The upper critical field $\mu_0 H^+_{c2}$ is calculated from -$\delta(\mu_0 H_{c2}/\delta T)$ using parameter h^*_{c2}, with:

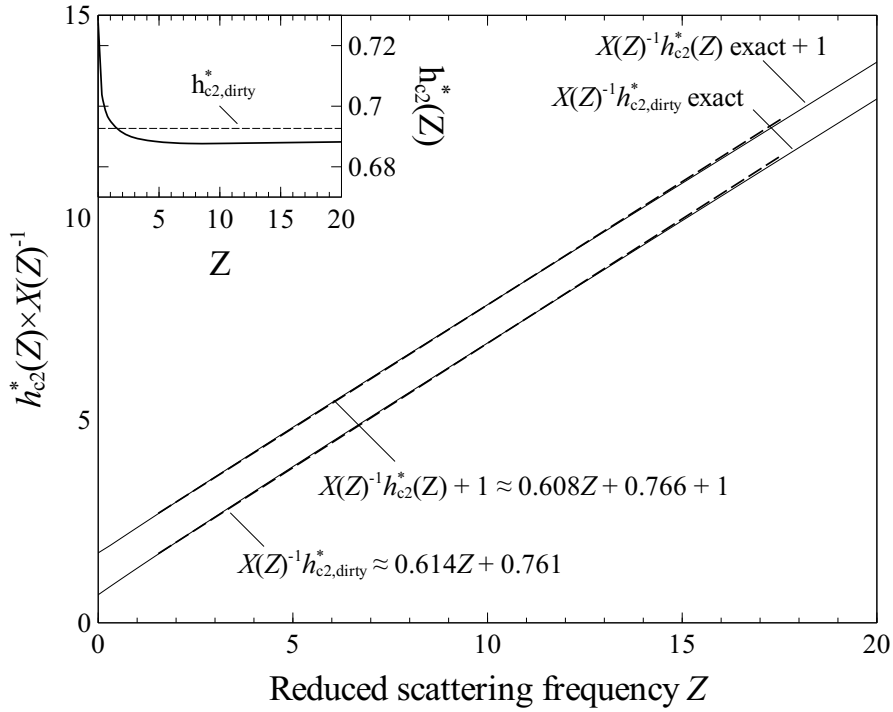

Figure 4.18: *Linearization of $h^*_{c2,dirty} \times X(Z)^{-1}$ and $h^*_{c2}(Z) \times X(Z)^{-1}$ as a function of the reduced collision frequency Z. The inset shows h^*_{c2} as a function of Z, and the dirty limit approximation of h^*_{c2}.*

$$\mu_0 H^+_{c2}(0) = h^*_{c2}(Z) \left.\frac{-\delta(\mu_0 H_{c2})}{\delta T}\right|_{T_c} T. \tag{4.40}$$

Combining equations 4.37 and 4.40, $\mu_0 H^+_{c2}$ is expressed as:

$$\mu_0 H^+_{c2}(0) = \eta_{Hc2} X(Z)^{-1} h^*_{c2}(Z) \left(\frac{24\pi^2 k_B^2}{7\zeta(3)\hbar e}\right) \frac{T_c^2 (1+\lambda)^2}{v_F^2}. \tag{4.41}$$

4.8.2 Weak-coupling approximation of $\mu_0 H_{c2}$ without Pauli limiting, with a dirty limit h^*_{c2}

As shown by Godeke *et al.* [33, 48], the Maki-DeGennes [47] calculation matches the observed temperature dependent behavior of $\mu_0 H_{c2}(T)$ in Nb_3Sn quite well. The underlying assumption is that the material is weak-coupling (i.e. η_{Hc2} = 1 [180]) without Pauli limiting in the dirty limit (i.e. $h^*_{c2,dirty}$ = 0.69267 [177]). In the inset in figure 4.18, the dirty limit approximation of $h^*_{c2,dirty}$ is compared to the variable limit h^*_{c2}.

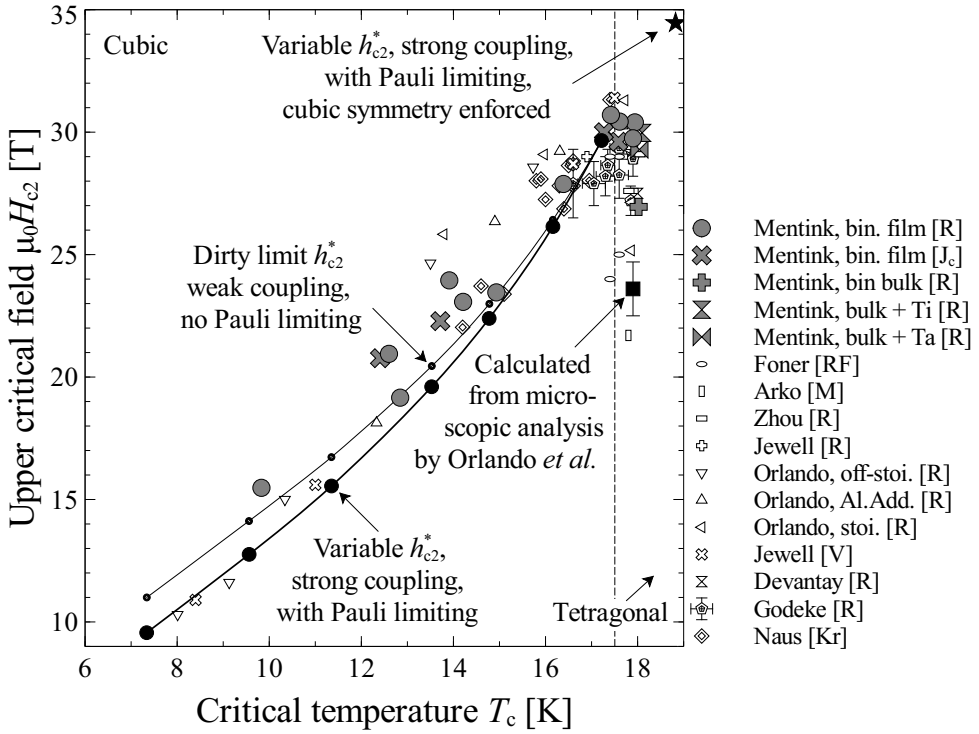

Figure 4.19: *Calculated $\mu_0 H_{c2}(0)$ as a function of T_c. The black symbols indicate calculated results, while the grey symbols indicate measurements that are part of this research and the open symbols indicate literature results, after Zhou et al. [66], Jewell et al. [68], Orlando et al. [42], Devantay et al. [52], Godeke et al. [48], Foner et al. [67], Arko et al. [70], and Naus et al. [69].*

The exact solution to the Gor'kov equation, see equation 4.39, is numerically calculated and $X(Z)^{-1}h^*_{c2,dirty}$ is linearized, as shown in figure 4.18. The appropriate range of the reduced collision frequency Z for the considered composition range is Z = 1.56 (corresponding to 27 $\mu\Omega$cm) to Z = 17.5 (corresponding to 90 $\mu\Omega$cm). In this range, linearization of $X(Z)^{-1}h^*_{c2,dirty}$ results in:

$$X(Z)^{-1}h^*_{c2,dirty} \approx 0.614Z + 0.761. \tag{4.42}$$

In the range of Z = 1.56 to 17.5, the maximum deviation between the linearized fit and the exact result is 0.7% and the average error is 0.4%. Combining equations 4.42 and 4.41 results in:

$$\mu_0 H_{c2,Maki}(0) = C_{D1}\frac{T_c^2(1+\lambda)^2}{v_F^2} + C_{D2}\frac{T_c(1+\lambda)}{v_F l_{mfp}}, \tag{4.43}$$

$$C_{D1} = \frac{0.761 \times 24\pi^2 k_B^2}{7\zeta(3)\hbar e} = 2.416 \times 10^8, \tag{4.44}$$

$$C_{D2} = \frac{0.614 \times 12\pi k_B}{7\zeta(3) e} = 2.371 \times 10^{-4}, \tag{4.45}$$

where C_{M1} is in [$Tm^2K^{-2}s^{-2}$] and C_{M2} is in [$Tm^2K^{-1}s^{-1}$], T_c is in [K], λ is dimensionless, v_F is in [ms^{-1}] and l_{mfp} is in [m]. Using the calculated T_c, λ, v_F and l_{mfp} as input, $\mu_0 H_{c2}(0)$ is calculated, see 4.19.

4.8.3 Calculation of $\mu_0 H_{c2}$ with strong coupling corrections and Pauli paramagnetic limiting in the dirty and intermediate limit

In order to improve the accuracy of the calculation of $\mu_0 H_{c2}$, several effects are included for which the macroscopic derivation is known, including strong-coupling corrections (i.e. $\eta_{Hc2} > 1$), Pauli paramagnetic limiting, and the reduced collision frequency dependence of h^*_{c2}. The strong coupling correction parameter η_{Hc2} was related to T_c and $<\omega^2>^{0.5}$ by Masharov [180]:

$$\eta_{H_{c2}} = 1 + \left(\frac{\pi k_B T_c}{\langle \omega^2 \rangle^{0.5}} \right) \left(0.6 \ln \left(\frac{\langle \omega^2 \rangle^{0.5}}{k_B T_c} \right) - 0.26 \right), \tag{4.46}$$

where $k_B T_c$ is the energy equivalent of T_c in [eV], $<\omega^2>^{0.5}$ is in [eV] and η_{Hc2} is a dimensionless parameter.

The reduced collision dependent parameter h^*_{c2} in the absence of spin-orbit coupling was described by Helfand *et al.* [173], reproduced by Rieck *et al.* [177] and shown in the inset in figure 4.18. $X(Z)^{-1} h^*_{c2}(Z)$ is linearized through:

$$X(Z)^{-1} h^*_{c2}(Z) \approx 0.608Z + 0.766, \tag{4.47}$$

which results in an average deviation of 0.4% and a maximum deviation of 0.6% in the range of Z = 1.56 to 17.5.

Combining equations 4.41 and 4.47 results in:

$$\mu_0 H^+_{c2}(0) = \eta_{Hc2} \left(C_{O1} \frac{T_c^2 (1+\lambda)^2}{v_F^2} + C_{O2} \frac{T_c (1+\lambda)}{v_F l_{mfp}} \right), \tag{4.48}$$

$$C_{O1} = \frac{0.766 \times 24\pi^2 k_B^2}{7\zeta(3)\hbar e} = 2.433 \times 10^8, \tag{4.49}$$

$$C_{O2} = \frac{0.608 \times 12\pi k_B}{7\zeta(3) e} = 2.349 \times 10^{-4}, \tag{4.50}$$

where C_{O1} is in [$Tm^2K^{-2}s^{-2}$], C_{O2} is in [$Tm^2K^{-1}s^{-1}$], T_c is in [K], λ is dimensionless, v_F is in [ms^{-1}] and l_{mfp} is in [m].

Pauli limiting describes a reduction in the free energy of the normal state relative to the superconducting state due to a difference in spin susceptibility in these two states. The reduction in energy difference results in a reduction of $\mu_0 H_{c2}$, which can be quantified through the Pauli limiting field $\mu_0 H_p$.

A description of $\mu_0 H_p$ in the absence of spin-orbit coupling is given by Orlando *et al.* [184]. Using an expression of $\mu_0 H_p$ by Clogston [185] for first-order transitions, Orlando speculated that the reduction in $\mu_0 H_{c2}$ due to Pauli paramagnetic limiting does not apply for Nb_3Sn [81]. After realizing that Clogston's expression is not applicable for Nb_3Sn, Orlando published the correct expression for $\mu_0 H_p$, as well as the relation between the upper critical field with Pauli limiting $\mu_0 H_{c2}$, the upper critical field without Pauli limiting $\mu_0 H_{c2}^+$, and the Pauli paramagnetic field $\mu_0 H_p$. After Orlando *et al.* [184], $\mu_0 H_p$ is expressed through:

$$\mu_0 H_p(0) = 1.86 T_c (1+\lambda). \tag{4.51}$$

This expression is combined with the upper critical field without Pauli limiting to find $\mu_0 H_{c2}$:

$$(\mu_0 H_{c2}(0))^{-2} = (\mu_0 H_{c2}^+(0))^{-2} + 2(\mu_0 H_p(0))^{-2}. \tag{4.52}$$

The calculated parameters T_c, λ, v_F, l_{mfp}, and $\alpha^2 F$ are used as input for $\mu_0 H_{c2}(0)$ and the result is shown in figure 4.19.

Relative to the dirty limit h_{c2}^* approximation without Pauli paramagnetic limiting and strong-coupling correction, see equation 4.43, the strong-coupling correction raises $\mu_0 H_{c2}$ by 14% at ρ_n = 28.4 $\mu\Omega$cm (with $T_c \approx 17.2$ K), and by 3% at ρ_n = 89.8 $\mu\Omega$cm (with $T_c \approx 7.3$ K). Pauli paramagnetic limiting reduces $\mu_0 H_{c2}$ by 12% at a ρ_n of 28.4 $\mu\Omega$cm and by 15% at a ρ_n of 89.8 $\mu\Omega$cm. $h_{c2}^*(Z)$ is identical to $h_{c2,dirty}^*$ at a ρ_n of 28.4 $\mu\Omega$cm and 0.6% lower at a ρ_n of 89.8 $\mu\Omega$cm .

In summary, the increase in $\mu_0 H_{c2}$ due to strong-coupling correction is mostly cancelled out by the reduction in $\mu_0 H_{c2}$ due to Pauli paramagnetic limiting over most of the composition range. However, close to the dirty limit, $\mu_0 H_{c2}$ is about 10% lower than the dirty limit h_{c2}^* approximation without Pauli paramagnetic limiting and strong coupling corrections, which is mostly due to Pauli paramagnetic limiting.

4.8.4 Temperature correction to the mean scattering time

Until now, an implicit assumption was made, which is that the normal state resistivity at the critical temperature is approximately equal to the normal state resistivity at 0 K. In other words:

$$\rho_n(T_c) \approx \rho_n(0K). \tag{4.53}$$

Experimentally, the normal state resistivity is known to scale with T^2 at low temperatures, as shown by Devantay *et al.* [52], Kaveh *et al.* [186], and Gurvich *et al.* [187]. The origin of this variation is likely related to a decrease in τ with increasing temperature due to

electron-electron scattering [186].

With increasing ρ_n, T_c is reduced. $\mu_0 H_{c2}(0)$ is a 0 K property while T_c is a property that is determined at non-zero temperature. In order to compare the calculated $\mu_0 H_{c2}(0)$ as a function of T_c to the experimentally observed T_c (in which T_c at a non-zero temperature is compared to a zero temperature $\mu_0 H_{c2}(0)$), a correction term is implemented, through:

$$\mu_0 H_{c2,corr} = \mu_0 H_{c2,calc} + \frac{\delta(\mu_0 H_{c2,calc})}{\delta \rho_n} (\rho_{n,0K} - \rho_{n,T_c}). \tag{4.54}$$

The temperature dependence of the normal state resistivity was studied in Nb-Sn samples by Gurvitch *et al.* [187]. It was shown that the temperature dependence of ρ_n varies with ρ_0, which can be summarized through a parabolic fit:

$$A(\rho_n) = 6.02\rho_{n,0K}^2 + 1.28 \times 10^{-4} \rho_{n,0K} + 8.02 \times 10^{-11}, \tag{4.55}$$

$$\rho_n(T_c) = \rho_{n,0K} + A(\rho_{n,0K}) {T_c}^2, \tag{4.56}$$

where ρ_n is in [Ωm]. The correction leads to a small increase in $\mu_0 H_{c2}(T_c)$: at $T_c \approx 16$ K, this effect raises $\mu_0 H_{c2}(0)$ by 0.9 T. At $T_c \approx 8$ K, $\mu_0 H_{c2}(0)$ is unaffected, because the difference between $\rho_n(T_c)$ and $\rho_n(0)$ becomes vanishingly small at large $\rho_n(0)$. At a T_c of about 17.5 K $\mu_0 H_{c2}(0)$ is unaffected because $\delta \mu_0 H_{c2}(0) / \delta \rho_n \approx 0$ at $\rho_n \approx 27$ $\mu\Omega$cm [42]. Thus, this effect mainly impacts $\mu_0 H_{c2}(0)$ at $T_c \approx 16$ K, which is also the critical temperature at which the calculated results (which do not take this effect into account) deviates the most from the experimentally observed $\mu_0 H_{c2}(0)$ (figure 4.19). This effect is thus considered to be relatively minor, which is why it is not included in the calculations in chapter 5.

4.8.5 Literature data on experiments

A number of results from experiments as reported in the literature are shown in figure 4.19, including measurements that were performed on bulk samples, thin films and composite wires.

The literature data consist of resistivity measurements (R), critical current density measurements (J_c), vibrating sample magnetometer measurements (V), other magnetic measurements (M) and radio frequency measurements (RF). The results by Zhou *et al.* [66], Foner *et al.* [67], Jewell *et al.* [68], Arko *et al.* [70], and Devantay *et al.* [52] are of bulk material, the results by Orlando *et al.* [42] are of thin films, and the results by Godeke *et al.* [48] and Naus [69] are of wires. Of particular interest are the resistivity measurements by Zhou *et al.* [66], Jewell *et al.* [68], and Godeke *et al.* [48], the RF measurements by Foner *et al.* [67] and the magnetic measurement by Arko *et al.* [70], which were performed in a range that extends down to temperatures close to 0 K and up to magnetic fields close to the upper critical field. In this research and in the other literature sources, after Orlando *et al.* [42], and Devantay *et al.* [52], $\mu_0 H_{c2}$ was determined through extrapolation and the uncertainty of these results is higher.

Also shown are the average superconducting properties of inhomogeneous Nb_3Sn wires, after Naus [69]. Naus used inductive measurements to determine an average T_c and an ex-

trapolated Kramer field $\mu_0 H_K$. Assuming that $\mu_0 H_K(4.2\text{ K}) \approx \mu_0 H_{c2,avg}(4.2\text{ K})$, $\mu_0 H_{c2,avg}(0)$ is determined through Maki-DeGennes extrapolation (see section 2.2.5). In spite of the sample inhomogeneity it is clear that the derived $\mu_0 H_{c2,avg}(0)$ as a function of $T_{c,avg}$ is consistent with the other literature results. The measurements by Godeke *et al.* [48] and Naus [69] illustrate the characteristic T_c of 17±1 K and $\mu_0 H_{c2}(0)$ of 28.5±1.5 T that is found in high J_c Nb_3Sn wires.

4.8.6 Other effects

Besides the effects that are implemented in the analyses presented, various other effects can influence $\mu_0 H_{c2}(0)$ as well.

In an analysis of two binary Nb-Sn samples with different compositions, Schachinger [113] argued that the upper critical field is strongly enhanced (by 30%) in the case of stoichiometric Nb_3Sn, due to Fermi surface anisotropy, and somewhat enhanced (about 5%) in the case of off-stoichiometric Nb-Sn with a T_c of 16.1 K. Indeed, in the calculations in which an isotropic Fermi surface is assumed, the resulting $\mu_0 H_{c2}(0)$ as a function of T_c dependence is somewhat below the experimentally observed $\mu_0 H_{c2}(0)$ versus T_c dependence, which gives credence to the notion that further mechanisms such as Fermi anisotropy should be considered. At the same time Schachinger did not consider various other effects that can raise $\mu_0 H_{c2}$, such as spin-orbit coupling [175] and did not include a discussion on why other effects are considered negligible, beyond the statement that these effects do not need to be included in order to achieve a good agreement between experimental data and theory.

Rieck *et al.* [177] took a different approach and constructed a model that considered the impact of various phenomena (Fermi surface anisotropy, Pauli limiting, s-, p-, and d-wave scattering, and spin-orbit coupling) where the magnitude of each phenomenon was described through a free parameter. In evaluating the same experimental data that Schachinger evaluated, Rieck determined that the experimental data was accurately described with dirty limit theory (i.e. 4.43) in the case of the off-stoichiometric sample and clean limit theory in the case of the stoichiometric sample and that fitting the free parameters only resulted in marginal improvements in the fit accuracy. Moreover, it was concluded that different combinations of free parameters resulted in equally good fit accuracy such that the appropriate magnitude of each phenomenon could not be determined with a high degree of confidence.

In summary, it is likely that additional phenomena need to be considered in order to accurately describe the upper critical field, but that it is not certain which of the above mentioned phenomena are most relevant. Further research on this topic would be beneficial, in particular if this leads to a first principle calculation of the magnitude of each of these phenomena.

As it is not clear whether additional effects such as spin-orbit coupling or Fermi surface anisotropy need to be included to accurately describe the upper critical field, the uncertainty in the calculation of $\mu_0 H_{c2}$, which takes into account a variable h^*_{c2}, strong coupling, and Pauli limiting, is estimated to be applicable for Nb_3Sn with an uncertainty of the order of 10%.

4.8.7 Effect of the tetragonal distortion on T_c and $\mu_0 H_{c2}(0)$

As is observed in figures 4.17 and 4.19, at the cubic to tetragonal crystal symmetry transition, the dependence of T_c and $\mu_0 H_{c2}(0)$ on disorder changes: T_c increases with decreasing ρ_n

in the cubic regime but is nearly independent of ρ_n in the tetragonal regime and $\mu_0 H_{c2}(0)$ increases with decreasing ρ_n in the cubic regime but decreases with decreasing ρ_n in the tetragonal regime. One could hypothesize that the transition of cubic to tetragonal crystal symmetry causes these changes in dependencies. This is a somewhat controversial issue and different authors claim different arguments.

In a study of the effect of aluminum doping on the critical temperature T_c and the lattice parameters of Nb-Sn, it was shown by Vieland *et al.* [189] that aluminum doping results in an increase in T_c as well as an inhibition of the tetragonal transformation and the authors postulate that the latter leads to the former. Consistent with this observation, it was observed by Akihama *et al.* [190] that aluminum doping raises $\mu_0 H_{c2}$ to 29 T at 4.2 K, which (through the Maki-DeGennes extrapolation) indicates that $\mu_0 H_{c2}(0)$ is 32 T, i.e. in excess of the highest $\mu_0 H_{c2}(0)$ observed in binary Nb_3Sn. The observed increase in T_c in the absence of the tetragonal transformation is consistent with an argument by Flükiger, who estimated that inhibition of the cubic-to-tetragonal transformation would increase T_c to more than 18.5 K. In similar fashion, it was argued by Devantay *et al.* and Foner *et al.* [67, 191] that it is the tetragonal transformation reduces $\mu_0 H_{c2}(0)$. Note that neither author considers the possibility of another mechanism by which to explain the variation in $\mu_0 H_{c2}(0)$, such as a lower l_{mfp} in the preferentially tetragonal Nb_3Sn.

In a more recent publication by Zhou *et al.* [66], in which 29 T is stated for the tetragonal phase, it is argued that $\mu_0 H_{c2}(0)$ is not at all suppressed by a cubic to tetragonal transition, a result that is attributed to improved homogeneity in the bulk samples that were analyzed. To address potential concerns that a presence of cubic phases could provide 29 T in a resistive measurement, the resistive results were validated by a magnetization measurement. It can, nonetheless, be argued whether the observed overlap between the resistive and magnetization measurements constitutes reliable proof of high sample homogeneity and whether accurate extrapolation of the magnetization results indeed yields the same upper critical magnetic field as a resistive measurement.

In order to determine whether the tetragonal transformation reduces T_c and $\mu_0 H_{c2}(0)$, the model was used to investigate this possibility. The model cannot be used to calculate the properties of preferentially tetragonal Nb_3Sn (as explained in section 4.7.4), but it can be used to calculate the properties of Nb_3Sn in which the cubic-to-tetragonal transformation is suppressed. At $\tau = 1.91 \times 10^{-14}$ s, the electron density of states was calculated in a calculation in with enforced cubic symmetry, and found equal to 16.1 states / eV $\times$ unit cell, while the Fermi velocity is 2.07×10^5 ms^{-1}. The associated normal state resistivity is then 21.4 $\mu\Omega$cm. The phonon density could not be evaluated, as the calculation only produces realistic results, i.e. without negative phonon frequencies, when the crystal configuration is stable. If we assume that the phonon density of states is approximately the same as at $\tau = 1.45 \times 10^{-14}$ s, a reasonable assumption as change in superconducting properties with composition is mainly a result of changes in the electron properties (section 4.7.3), then T_c is 18.8 K (figure 4.17) and $\mu_0 H_{c2}(0)$ is 34.5 T (figure 4.19).

According to Orlando *et al.* [81], in an analysis in which the influence of the tetragonal distortion is incorporated into the results, v_F, l_{mfp}, λ, T_c, and η_{Hc2} of preferentially tetragonal Nb_3Sn are $(2.1\pm0.2)\times10^5$ ms^{-1}, 10 ∓ 4 nm, 1.78, 17.9 K, and 1.17. Through equation 4.52, $\mu_0 H_{c2}(0)$ is 23.6$\pm$1.1 T, i.e. consistent with the drop in $\mu_0 H_{c2}(0)$ near $T_c \approx 18$ K (figure 4.19). This implies that equation 4.52 captures the relevant physics, a further indication that

the result that the tetragonal transformation lowers T_c and $\mu_0 H_{c2}(0)$ is valid.

In summary, the cause of the drop in $\mu_0 H_{c2}$ near stoichiometry is a controversial issue, but the calculated results and experimental evidence seems to indicate that the drop in $\mu_0 H_{c2}$ near stoichiometry is a direct result of the tetragonal transformation. Thus, a further investigation of different dopants besides titanium and tantalum could lead to further improvements of the maximum attainable upper critical field in practical superconducting wires. The experimental investigations by Vieland *et al.* [189] and Akihama *et al.* [190] suggest that aluminum might be a suitable candidate.

4.8.8 Discussion

As is seen in figure 4.19, both the $\mu_0 H_{c2}$ result that is calculated with Maki's dirty limit approximation without Pauli paramagnetic limiting and the $\mu_0 H_{c2}$ result with the strong-coupling corrected calculation with Pauli paramagnetic limiting and reduced collision frequency dependent $h^*_{c2}(Z)$ are quite close to the experimental literature data over most of the range. The largest difference between the two calculated results is found at lower T_c, i.e. closer to the dirty limit where the calculation that considers strong coupling correction and Pauli paramagnetic limiting is closer to the experimental result than the dirty limit approximation without Pauli limiting.

A variety of effects are discussed which could affect $\mu_0 H_{c2}(0)$, but it is not clear to what extent these effects affect $\mu_0 H_{c2}(0)$. In some research specific phenomena are emphasized over others without a clear explanation of why this choice is correct, while in other research a large number of phenomena are considered without a clear conclusion over the relative contribution of each of these effects. For this reason, a rather conservative error estimation of the calculation accuracy of $\mu_0 H_{c2}(0)$ is assumed in this chapter, and it is hoped that this topic will be addressed in the future.

4.8.9 Conclusion

Using the calculated input parameters T_c, λ, $<\omega^2>^{0.5}$, v_F, and l_{mfp}, $\mu_0 H_{c2}(0)$ is calculated and compared to experimental data. Two descriptions are used: a weak-coupling description with a dirty limit h^*_{c2}, without Pauli paramagnetic limiting and strong coupling corrections (which are the underlying assumptions of the Maki-DeGennes temperature dependent description of $\mu_0 H_{c2}$), and a 'best-effort' description with strong coupling correction and Pauli paramagnetic limiting which is valid in the dirty and intermediate limit. While the two descriptions predict $\mu_0 H_{c2}$ with reasonable accuracy, the 'best-effort' description is somewhat more consistent with experimental observations in disordered Nb_3Sn (with a lower T_c), which is mainly due to the inclusion of Pauli limiting in the description.

The difference between the calculated and experimentally observed $\mu_0 H_{c2}$ as a function of T_c is roughly on the same order of magnitude as the uncertainty in experimental data. However, based on the available literature, additional phenomena such as Fermi anisotropy and spin-orbit coupling might have to be considered in the description of $\mu_0 H_{c2}$. The literature on this topic does not indicate a clear consensus on how much these phenomena affect $\mu_0 H_{c2}$, so it can only be concluded that the 'best-effort' description that is formulated here might be incomplete. In light of this, the uncertainty in $\mu_0 H_{c2}$ is estimated to be of the order of 10%.

In spite of not using free parameters to calculate $\mu_0 H_{c2}$ from T_c, the calculated $\mu_0 H_{c2}$ is close to the experimental result, which is an indication that the electron lifetime broadening model in combination with DFT calculations and various microscopic relations captures most of the relevant physics that determine T_c and $\mu_0 H_{c2}(0)$.

4.9 Discussion

The various calculated results as presented in this chapter coincide with experimental results with a high degree of consistency, a strong indication that most of the relevant physics is captured in this approach. In spite of this success, some limitations can be identified.

One limitation is that this approach includes disorder but not off-stoichiometry, while the experimental observations that are presented in sections 2.4.7 and 2.4.8 are of off-stoichiometric Nb-Sn. The approach that is used here is reasonable because it was argued by Orlando *et al.* [42] that, in experimental observations in which the influence of strain is not considered, disorder determines T_c and $\mu_0 H_{c2}(0)$, regardless of whether the material is stoichiometric or off-stoichiometric. In an ideal case, DFT and DFPT calculations would be applied to off-stoichiometric Nb-Sn, which would involve using supercell configurations. Indeed, supercell configurations are discussed at the start of this chapter and calculations are performed in a limited fashion. However, it was concluded that supercell configurations are (at the present time) impractical because the computational cost of performing DFT calculations on supercells significantly exceeds the cost of performing DFT calculations on single unit cells. It is however conceivable that, with the rise of ubiquitous computing power, supercells could be evaluated in the future using the approach discussed in this chapter as a recipe.

The second limitation is the lack of evaluation of the microscopic properties of preferentially tetragonal Nb_3Sn. As was discussed in section 4.4.6, the martensitic transformation results in the formation of tweed patterns, in which the *c*-axis (figure 4.4) is aligned along different directions throughout the sample. DFT calculations on single unit cell Nb_3Sn are a poor approximation of this phenomenon, because in the single unit cell approach it is assumed that neighboring unit cells are identical, which means that the *c*-axis is aligned along the same direction throughout the sample. Because it is not understood how tweed modulation affects the microscopic properties of Nb_3Sn, emphasis is placed on the properties of preferentially cubic Nb_3Sn. In theory, a very large supercell with dimensions comparable to the spacing of the tweed modulation could be used to evaluate how tweed modulation affects the microscopic properties. In practice, such a calculation, involving hundreds or thousands of ions, is likely unrealistic for the foreseeable future.

4.10 Overall conclusion

The martensitic transformation, the critical temperature, and the upper critical field of Nb-Sn are evaluated as a function of disorder using an electron lifetime broadening model. Density functional theory software is used to evaluate the stability of the cubic phase as a function of mean scattering time. Density functional theory and density functional perturbation theory is used to calculate the disorder dependent T_c and $\mu_0 H_{c2}$.

In addition to the DFT and DFPT calculations on single unit cell stoichiometric Nb_3Sn, a

free electron model and two different supercell configurations were considered as potential models for evaluating how off-stoichiometry affects the superconducting properties of Nb_3Sn. Neither of these two approaches was utilized, because the free electron model is too simplistic to account for the properties of Nb_3Sn, while the supercell approach is impractical due to the large associated computational cost.

Using a Drude resistivity model, the normal state resistivity is calculated as a function of mean scattering time. The transition point between cubic and tetragonal crystal symmetry was determined to be $(1.53\pm0.08)\times10^{-14}$ s, which corresponds to a critical normal state resistivity of 27.0 ± 1.4 $\mu\Omega$cm. The calculated critical resistivity is shown to be consistent with the experimental results within experimental uncertainty, where normal state resistivity increases due to off-stoichiometry, additions, and temperature increase are considered.

An empirical description of α^2F is formulated and validated through comparison of calculated and experimentally observed Eliashberg spectra over a wide disorder range. Using the strong-coupling corrected Kresin and Allen-Dynes T_c equations, the normal state resistivity dependence of T_c is calculated. A comparison with literature values is provided and these calculated and experimentally determined T_c values are in good agreement.

Two descriptions are formulated to calculate the upper critical field as a function of T_c. One of the descriptions assumes a dirty limit h^*_{c2} in a weak coupled superconductor without Pauli limiting (which are also the assumptions of the Maki-DeGennes description of the temperature dependence of μ_0H_{c2}), while the other description includes strong-coupling corrections, Pauli limiting, and is valid in the dirty and intermediate limit. Based on a comparison to experimental data, both descriptions predict μ_0H_{c2} with reasonable accuracy, although the second description is somewhat more accurate in strongly disordered Nb_3Sn. This difference is mainly due to the inclusion of Pauli paramagnetic limiting.

The consistency between the calculated results and the experimental observations implies that most of the relevant physics are captured in these calculations.

Chapter 5

Computational Investigation and Experimental Observation of Strain Sensitivity

5.1 Introduction

In chapter 4, it was shown that combining microscopic theory with ab-initio density function theory and density functional perturbation theory can provide accurate calculation of various disorder dependent microscopic properties, including T_c and $\mu_0 H_{c2}$. In this chapter, the model is applied to calculate the strain dependent properties of Nb-Sn and a comparison of calculated results and experimental observations is given.

In section 5.2, the background of the model is given. Various strain dependent calculation results of microscopic properties are presented in section 5.3, including T_c and $\mu_0 H_{c2}$. The relation between sublattice distortion and the strain sensitivity of the normal state resistivity and superconducting properties of A15 Nb-Sn and bcc Nb is explored in section 5.4. And finally, in section 5.5, the model calculations are compared to experimental observations and the validity of the model is evaluated.

It is argued that strain affects the distribution of niobium ions inside the crystal, a phenomenon called sublattice distortion. It was previously shown in theoretical (Labbé *et al.* [136]), computational (Sadigh *et al.* [138]), and experimental (Shirane *et al.* [139]) analyses that sublattice distortion spontaneously occurs during the martensitic transformation (figure 4.4).

The results presented here indicate that sublattice distortion not only occurs as a result of the martensitic transformation, but also occurs when the crystal is forced into non-cubic symmetry due to externally applied strain. The sublattice distortion affects both the electronic and the vibrational properties of the crystal, and thus T_c and $\mu_0 H_{c2}$ as well.

If sublattice distortion causes strain sensitivity in A15 materials, then it follows that the strain sensitivity of bcc Nb and NbTi, which do not comprise the characteristic niobium chains as present in Nb_3Sn, is significantly lower in comparison to Nb_3Sn. The validity of this argument will be demonstrated. In addition, a partial comparison to Nb_3Al is provided, a material with a known reduced strain sensitivity in comparison to Nb_3Sn.

5.2 Computation details

5.2.1 Hypothesis

In chapter 4 it was convincingly demonstrated that the composition dependence of the superconducting properties T_c and $\mu_0 H_{c2}(0)$ can be calculated by combining an electron lifetime broadening approximation, ab-initio calculations of stoichiometric Nb_3Sn, and an empirical description of $\alpha^2 F$. The calculated and experimental results were shown to be consistent.

The hypothesis discussed here is that this model not only accurately describes the disorder dependence of the superconducting properties, but also the strain dependence of the superconducting properties.

5.2.2 Constant mean free path approximation

The mean free path is defined as the mean distance an electron can travel before it scatters. In the 0 K limit, electron scattering is dominated by scattering on defects. Other types of scattering such as electron-electron scattering and electron-phonon scattering are assumed to be minor, which in practical terms means that $\rho_n(T = 0\ \mathrm{K}) \gg \rho_n(T_c) - \rho_n(T = 0\ \mathrm{K})$. As

the mean free path l_{mfp} is determined by the distance between the scattering centers and the distance between the scattering centers is affected by strain, it follows that strain affects the mean free path.

The mean free path is expressed in three orthogonal components, with:

$$l_{\mathrm{mfp}} = \sqrt{\left(l_{\mathrm{mfp,ip,long}}\right)^2 + \left(l_{\mathrm{mfp,ip,tr}}\right)^2 + \left(l_{\mathrm{mfp,op,tr}}\right)^2}, \tag{5.1}$$

where l_{mfp} describes the mean distance that an electron travels between scattering events, and $l_{\mathrm{mfp,ip,long}}$, $l_{\mathrm{mfp,ip,tr}}$, and $l_{\mathrm{mfp,op,tr}}$ describe the in-plane longitudinal, the in-plane transverse, and the out-of-plane transverse components of the mean free path, respectively. The directions relative to the U-spring sample holder are illustrated in figure 5.2, left. With cubic symmetry, in an infinitely large crystal without an externally applied magnetic field, the magnitudes of the components are equal:

$$l_{\mathrm{mfp,ip,long}}(0) \equiv l_{\mathrm{mfp,ip,tr}}(0) \equiv l_{\mathrm{mfp,op,tr}}(0) \equiv l_{\mathrm{mfp}}(0)/\sqrt{3}. \tag{5.2}$$

The application of strain affects the three components following:

$$l_{\mathrm{mfp,ip,long}}\left(\varepsilon_{\mathrm{ip,long}}\right) = l_{\mathrm{mfp,ip,long}}(0)\left(1+\varepsilon_{\mathrm{ip,long}}\right), \tag{5.3}$$

$$l_{\mathrm{mfp,ip,tr}}\left(\varepsilon_{\mathrm{ip,tr}}\right) = l_{\mathrm{mfp,ip,tr}}(0)\left(1+\varepsilon_{\mathrm{ip,tr}}\right), \tag{5.4}$$

$$l_{\mathrm{mfp,op,tr}}\left(\varepsilon_{\mathrm{op,tr}}\right) = l_{\mathrm{mfp,op,tr}}(0)\left(1+\varepsilon_{\mathrm{op,tr}}\right). \tag{5.5}$$

An in-plane longitudinal compression of 1% (assuming a Poisson's ratio of 0.38 for Nb_3Sn [58]) leads to $\varepsilon_{\mathrm{ip,long}} = -1\%$, $\varepsilon_{\mathrm{ip,tr}} = 0.34\%$, and $\varepsilon_{\mathrm{op,tr}} = 0.40\%$ (see sections 2.4.3 and 2.4.6 for the relations between the strain components). Relative to the cubic case, equation 5.2, the in-plane compression of 1% results in an decrease in l_{mfp} of 0.08%. As this number is very small, it is deemed negligible, which means that the application of strain by the U-spring test rig does not change l_{mfp}. l_{mfp} is thus a useful measure of the degree of disorder in a sample as neither l_{mfp} nor the degree of disorder are affected by strain.

It is desirable to evaluate the strain sensitivity at a constant degree of disorder, and thus a constant l_{mfp}. However, the model uses an isotropic mean scattering τ as input and the corresponding l_{mfp} is unknown until v_{F} is calculated, so that a calculation at a fixed l_{mfp} and variable strain requires repeated iterations to determine the corresponding τ. Rather than following this computationally extensive route, the problem is better solved by assuming a value for τ, finding the corresponding l_{mfp1}, and determining the various calculated properties at a desired l_{mfp2} through:

$$X\left(l_{\mathrm{mfp2}}\right) \approx X\left(l_{\mathrm{mfp1}}\right) + \frac{\delta X\left(l_{\mathrm{mfp1}}\right)}{\delta l_{\mathrm{mfp1}}}\left(l_{\mathrm{mfp2}} - l_{\mathrm{mfp1}}\right), \tag{5.6}$$

where X refers to an arbitrary calculated parameter, such as $N(E_{\mathrm{F}})$. In all cases, the change

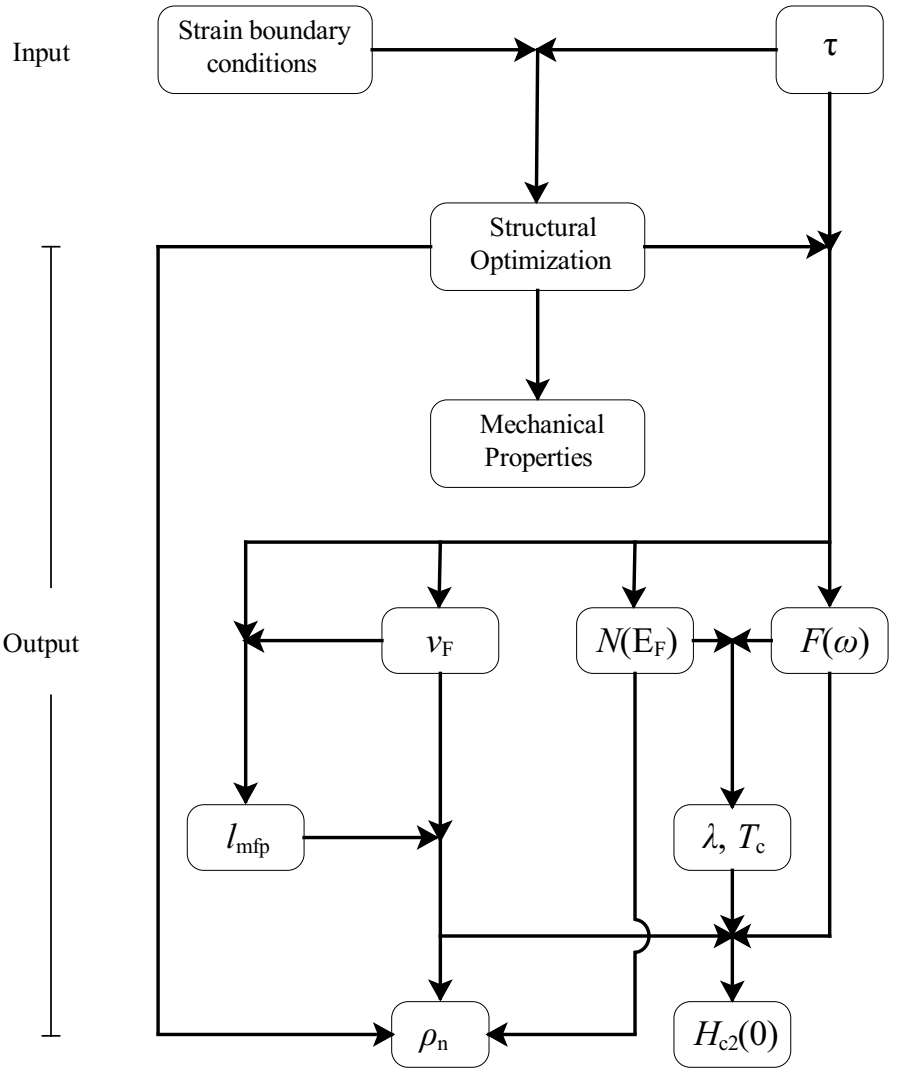

Figure 5.1: *Calculation scheme, with strain boundary conditions and mean scattering time τ as input, and structural optimization results, Fermi velocity v_F, electron density of states $N(E_F)$, phonon density of states $F(\omega)$, mean free path l_{mfp}, electron-phonon coupling constant λ, critical temperature T_c, normal state resistivity ρ_n, and upper critical field $\mu_0 H_{c2}(0)$ as output.*

in X with strain is large relative to the change in the term $(\delta X/\delta l_{mfp1})(l_{mfp2} - l_{mfp1})$ with strain, showing that linearization is justified.

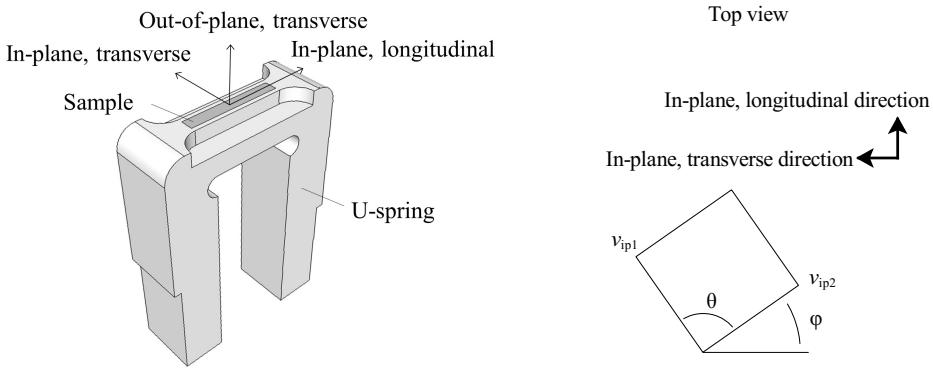

Figure 5.2: *Left: schematic of the U-spring sample holder with the in-plane longitudinal and transverse and the out-of-plane transverse directions. Right: the Nb-Sn thin films are predominately (100) oriented in the out-of-plane direction and randomly in the in-plane direction.* φ *is the in-plane rotation angle, and* θ *is the angle between the lattice vectors.*

5.2.3 Calculation scheme

Figure 5.1 shows the input and output parameters of the electron lifetime broadening model, applied for the investigation of strain sensitivity. The model takes strain boundary conditions and the isotropic mean scattering time τ as input. A structural optimization is performed for each combination of boundary conditions and τ to determine the three-dimensional lattice arrangement with the lowest enthalpy, which also provides the strain and stress state of the crystal.

Subsequently, the Fermi velocity v_F, the electron density of states $N(E_F)$, and the frequency dependent phonon density of states $F(\omega)$ are calculated, and the mean free path l_{mfp}, electron-phonon coupling constant λ, the critical temperature T_c, the normal state resistivity ρ_n, and the upper critical field $\mu_0 H_{c2}(0)$ are derived. The various expressions, introduced in chapter 4, are once again listed here.

5.2.4 Experimentally observed strain boundary conditions

The model calculates of the superconducting properties as a function of the three dimensional strain state of the Nb-Sn thin films samples which were mounted on the U-spring test rig (see figure 2.15).

Three orthogonal directions are defined, which are the in-plane longitudinal, in-plane transverse, and out-of-plane transverse directions (figure 5.2). In the calculations, it is assumed that the degree of thermal pre-compression is small (section 2.4.2) and that the in-plane transverse strain is determined by the Poisson's ratio of the sample holder (i.e. 0.342 [79], section 2.4.3). The in-plane longitudinal and transverse strains are expressed by:

$$\varepsilon_{ip,long} \approx \varepsilon_a, \tag{5.7}$$

$$\varepsilon_{\mathrm{ip,tr}} = -0.342 \times \varepsilon_{\mathrm{ip,long}}, \tag{5.8}$$

where $\varepsilon_{\mathrm{ip,long}}$, and $\varepsilon_{\mathrm{ip,tr}}$ are the in-plane longitudinal and transverse strain, and ε_{a} is the applied longitudinal strain. The thin film is free to expand in the out-of-plane direction, so that the out-of-plane stress is equal to zero:

$$\sigma_{\mathrm{op,tr}} = 0, \tag{5.9}$$

where $\sigma_{\mathrm{op,tr}}$ is the out-of-plane stress. In section 4.4.2, the lattice parameter of 0.5313 $\pm$ 0.0001 nm was found at degrees of disorder where the cubic phase is stable, so the lattice parameter a_0 is fixed to 0.5313 nm.

The Nb-Sn thin films were found to be predominantly oriented (100) in the out-of-plane direction and randomly in the in-plane direction (section 2.3.6). The orientation of the crystal relative to the in-plane longitudinal direction in the absence of applied strain is designated φ (figure 5.2, right), so that the length of the in-plane lattice vectors of the crystal and the angle between the in-plane lattice vectors are expressed with:

$$|v_{\mathrm{ip1}}| = a_0 \sqrt{\left(\left(1+\varepsilon_{\mathrm{ip,long}}\right)\cos\left(\varphi\right)\right)^2 + \left(\left(1+\varepsilon_{\mathrm{ip,tr}}\right)\sin\left(\varphi\right)\right)^2}, \tag{5.10}$$

$$|v_{\mathrm{ip2}}| = a_0 \sqrt{\left(\left(1+\varepsilon_{\mathrm{ip,long}}\right)\sin\left(\varphi\right)\right)^2 + \left(\left(1+\varepsilon_{\mathrm{ip,tr}}\right)\cos\left(\varphi\right)\right)^2}, \tag{5.11}$$

$$\theta = \cos^{-1}\left(\frac{a_0^2\left(\left(1+\varepsilon_{\mathrm{ip,long}}\right)^2 - \left(1+\varepsilon_{\mathrm{ip,tr}}\right)^2\right)\cos\left(\varphi\right)\sin\left(\varphi\right)}{a_{\mathrm{ip1}}a_{\mathrm{ip2}}}\right), \tag{5.12}$$

where $|v_{\mathrm{ip1}}|$ and $|v_{\mathrm{ip2}}|$ are the lengths of the two in-plane lattice vectors and θ is the angle between the two in-plane lattice vectors. The out-of-plane lattice vector is orthogonal to the two in-plane lattice vectors and the length of this vector is determined by using the boundary condition that the out-of-plane stress is equal to zero.

Note that there are three high-symmetry conditions. First of all, if no strain is applied then the two in-plane lattice vector lengths are equal to a_0 and θ is equal to 90°, regardless of φ.

Second, if φ = 0°, then:

$$|v_{\mathrm{ip1}}| = a_0\left(1+\varepsilon_{\mathrm{ip,long}}\right), \tag{5.13}$$

$$|v_{\mathrm{ip2}}| = a_0\left(1+\varepsilon_{\mathrm{ip,tr}}\right), \tag{5.14}$$

and θ = 90°. In this orientation, the crystal is strained along the (100) in-plane direction (figure 5.3, top). Note that the sample holder determines both the in-plane longitudinal and the transverse strains. If the Poisson's ratio of the Ti-6Al-4V sample holder were to match that of the Nb_3Sn, then (100) strain leads to a tetragonal crystal structure. However, the

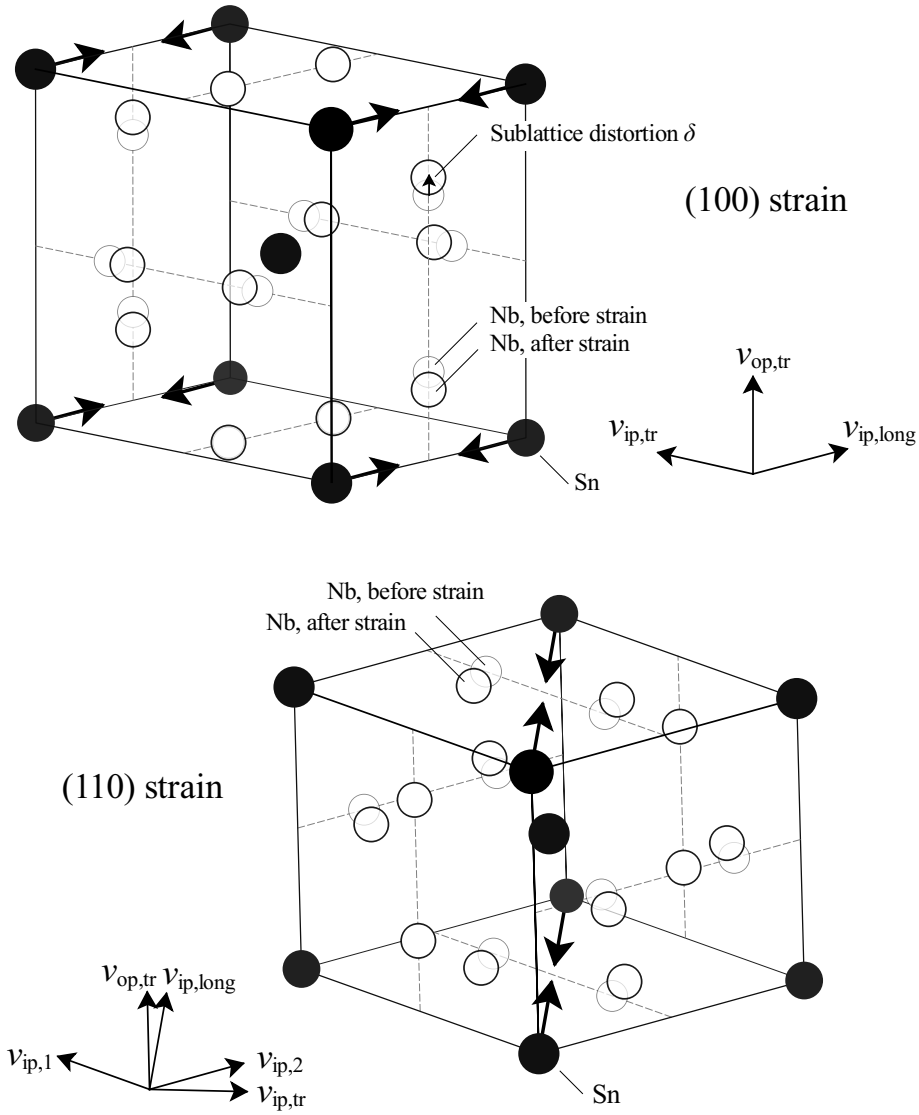

Figure 5.3: *Schematic representation of how externally applied (100) and (110) strain distorts the positions of the niobium ions inside the crystals. The fat arrows inside the crystals indicate the direction in which the crystal is compressed. The black markers represent the Sn ions. The initial positions of the Nb ions (before the crystal is strained) and the final positions of the Nb ions (after the crystal is strained) are indicated with open markers.*

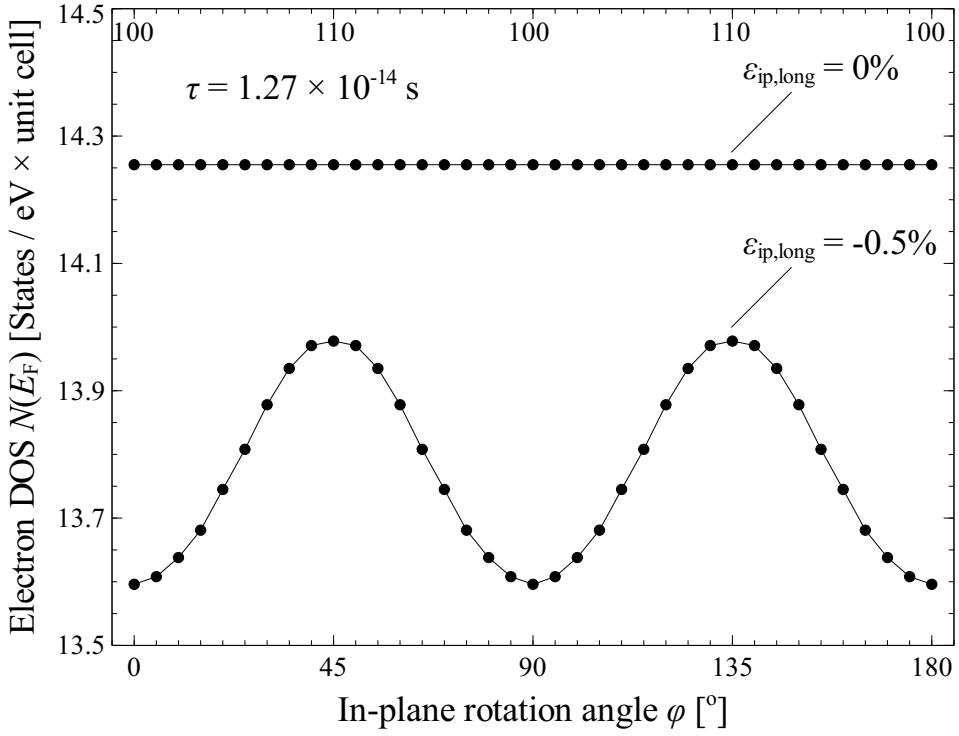

Figure 5.4: *Calculated $N(E_F)$ as a function of rotation angle φ for two strains.*

Poisson's ratio of the sample holder is 0.342 (section 2.4.3), while the Poisson's ratio of Nb_3Sn is approximately 0.38 [58], which means that (100) strain leads to an orthorhombic crystal symmetry, i.e. all three lattice parameters are different but they are orthogonal to one-another. Note that the in-plane lattice vectors are aligned along the in-plane longitudinal and transverse directions, which is why the in-plane lattice vectors are referred to as $v_{ip,long}$ and $v_{ip,tr}$ in this case.

The third high-symmetry condition is found when $\varphi = 45°$, with:

$$|v_{ip1}| = |v_{ip2}| = a_0 \sqrt{\left(1+\varepsilon_{ip,long}\right)^2 + \left(1+\varepsilon_{ip,tr}\right)^2}/\sqrt{2}, \tag{5.15}$$

$$\theta = \cos^{-1}\left(\frac{\left(\left(1+\varepsilon_{ip,long}\right)^2 - \left(1+\varepsilon_{ip,tr}\right)^2\right)}{\left(1+\varepsilon_{ip,long}\right)^2 + \left(1+\varepsilon_{ip,tr}\right)^2}\right). \tag{5.16}$$

In this orientation, the crystal is strained along the (110) in-plane direction (figure 5.3, bottom). This application of strain leads to a monoclinic crystal structure, i.e. the out-of-plane lattice vector is orthogonal to the in-plane lattice vectors, but the in-plane lattice vectors are not orthogonal to one-another, and in addition the in-plane lattice vectors are of equal length.

Table 5.1: *Quantitative description of Nb and Sn ion positions. The position of each of the eight ions in a stoichiometric unit cell is expressed relative to the vectors that span the unit cell (also see figure 5.3). The values for δ are presented in figure 5.5).*

	$v_{ip,long}$	$v_{ip,tr}$	$v_{op,tr}$
Sn_1 =	0	0	)
Sn_2 =	0.5	0.5	0.5)
Nb_1 =	0	0.5	$0.25+\delta_{op,tr}$)
Nb_2 =	0	0.5	$0.75-\delta_{op,tr}$)
Nb_3 =	$0.25+\delta_{ip,long}$	0	0.5)
Nb_4 =	$0.75-\delta_{ip,long}$	0	0.5)
Nb_5 =	0.5	$0.25+\delta_{ip,tr}$	0)
Nb_6 =	0.5	$0.75-\delta_{ip,tr}$	0)

(100) strain

	$v_{ip,1}$	$v_{ip,2}$	$v_{op,tr}$
Sn_1 =	0	0	0)
Sn_2 =	0.5	0.5	0.5)
Nb_1 =	0	0.5	0.25)
Nb_2 =	0	0.5	0.75)
Nb_3 =	$0.25+\delta_1$	$-\delta_2$	0.5)
Nb_4 =	$0.75-\delta_1$	δ_2	0.5)
Nb_5 =	$0.5+\delta_2$	$0.25-\delta_1$	0)
Nb_6 =	$0.5-\delta_2$	$0.75+\delta_1$	0)

(110) strain

5.2.5 Crystal orientation dependent strain sensitivity

The in-plane rotation of the Nb-Sn is random (figure 2.10). In order to get a qualitative impression of the angle dependence of the strain sensitivity, a simulation is performed where the relation between $N(E_F)$ and φ is investigated, with a mean scattering time τ of 1.27×10^{-14} s, and an in-plane longitudinal strain $\varepsilon_{ip,long}$ of -0.5%, compared to 0%. The calculation involves a structural optimization followed by a calculation of $N(E_F)$.

The result of the simulation is shown in figure 5.4. It is found that, compared with a $\varepsilon_{ip,long}$ of 0%, the compression of the crystal results in a reduction in $N(E_F)$. The size of reduction is dependent on φ, with the largest reduction following strain along the (100) direction and the smallest reduction for strain along the (110) direction. As (100) and (110) strain represents the extremes in terms of strain sensitivity, emphasis is placed on these two strains throughout the calculations. In both cases the lattice vector pointing in the out-of-plane direction is designated as $v_{op,tr}$.

5.3 Calculated effect of strain on the microscopic properties of disordered Nb_3Sn

The model calculation results are presented, which includes the degree of niobium ion sublattice distortion, the strain dependent electron density of states, anisotropic Fermi velocity, anisotropic normal state resistivity, strain dependent phonon dispersion curves and phonon density of states, Eliashberg spectra and derived properties, the critical temperature, and the upper critical field.

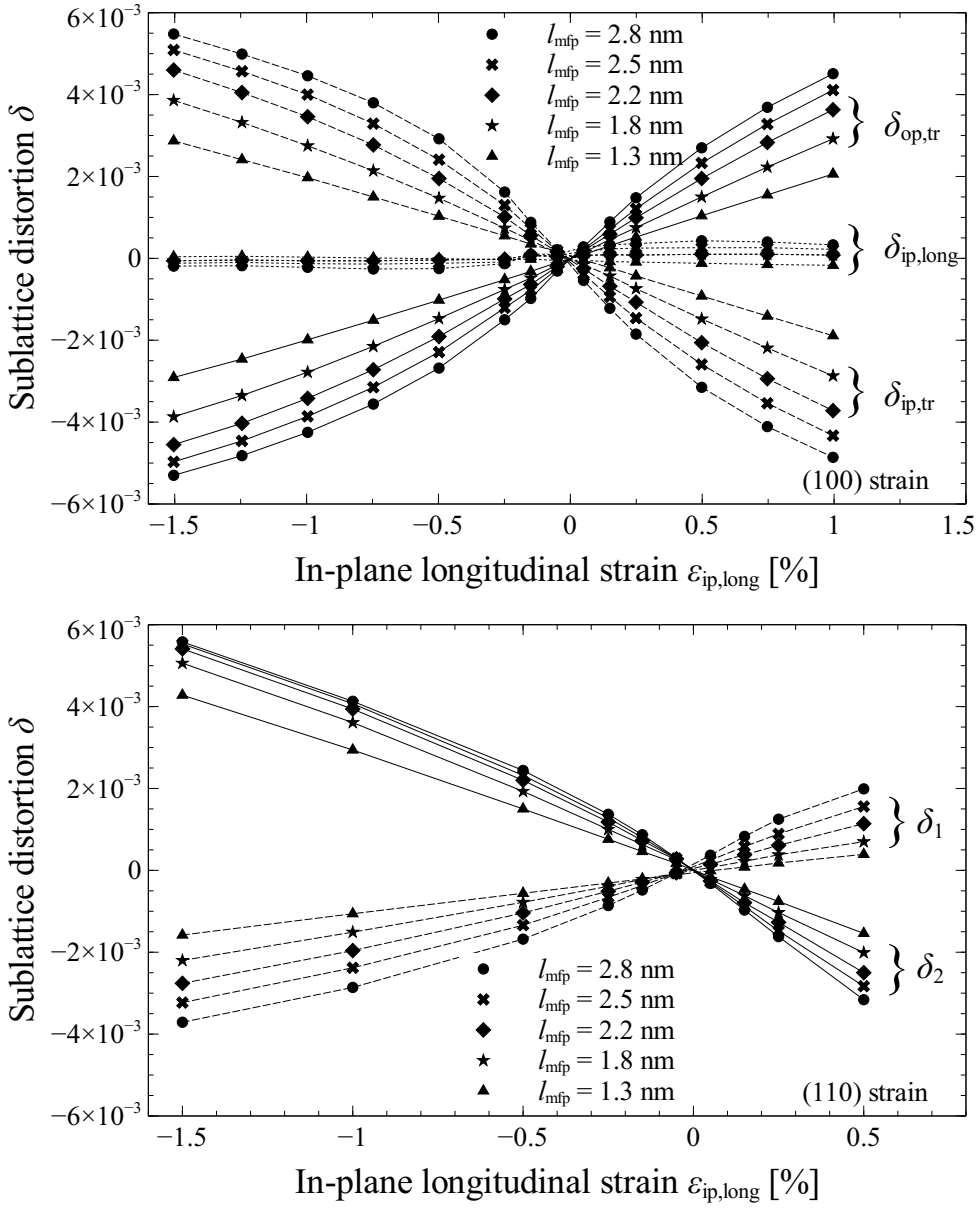

Figure 5.5: *Calculated degree of sublattice distortion as a function of in-plane longitudinal (100) and (110) strain (shown in the top and bottom figures, respectively).*

5.3.1 Niobium ion sublattice distortion

The effect of externally applied strain on the niobium ions was calculated. Structural optimizations were performed for various strains and degrees of disorder. The calculations

show that under the influence of externally applied strain, the niobium ions assume different positions inside the unit cell and the new positions are determined by the extent of disorder, the externally applied strain, and whether strain is applied along the (100) direction or the (110) direction.

Figure 5.3 illustrates how externally applied strain affects the position of the niobium ions inside the unit cell. Table 5.1 and figure 5.5 describe the sublattice distortion in quantitative terms. Figure 5.6 shows the calculated out-of-plane strain determined by setting the out-of-plane stress to 0 Pa.

Application of strain along the (100) direction results in dimerization of the niobium chains in the in-plane and out-of-plane transverse directions. Within the unit cell, the niobium ions move toward or away from each other (figure 5.3, top). The dimerization of the niobium ions along the two transverse directions is nearly identical in magnitude but opposite in sign, but the degree of dimerization along the longitudinal direction is relatively weak, as shown in figure 5.5, top. (110) strain not only results in dimerization, i.e. movement of the niobium ions along the niobium chains, but also in buckling, which means that the ions move away from the initial location of the niobium chain, which is shown in figure 5.3, bottom. The term sublattice distortion broadly indicates the movement of niobium ions, which incorporates both the dimerization and, for (110) strain, the buckling of the chains.

The degree of sublattice distortion decreases with decreasing l_{mfp}. This phenomenon can qualitatively be explained in terms of the stability of the crystal: at sufficiently large l_{mfp}, the material is preferentially tetragonal (figure 4.5) and sublattice distortion spontaneously occurs (figure 4.4). Thus, sublattice distortion is energetically favorable and no externally applied pressure is needed for sublattice distortion to occur. With decreasing l_{mfp}, the material becomes preferentially cubic. Now, sublattice distortion is energetically unfavorable, but can still be achieved by forcing the crystal structure into non-cubic symmetry through externally applied strain. With further decreases in l_{mfp} the energetic favorability of the cubic crystal symmetry relative to the tetragonal one increases, and the degree of sublattice distortion is reduced (figure 5.5).

5.3.2 Electron density of states

Figure 5.7 shows the change in electron density of states $N(E_{\mathrm{F}})$ with in-plane longitudinal strain at various mean free paths. The calculated results indicate a strong difference in the strain sensitivity of the electron density of states between (100) and (110) strain. At all compositions, the change in electron density of states is more pronounced for (100) strain than (110) strain. The degree of strain sensitivity in $N(E_{\mathrm{F}})$ decreases with decreasing l_{mfp}. As will be argued in the next section, this decrease is a result of the decrease in sublattice distortion with decreasing l_{mfp} (figure 5.5).

5.3.3 Anisotropic Fermi velocity

The Fermi velocity is affected by strain in an anisotropic manner. The root-mean-square (rms) Fermi velocity is calculated as a function of direction, in-plane longitudinal strain, and mean free path.

The calculated result indicates that the Fermi velocity is anisotropic. This anisotropy is consistent with the anisotropic nature of the sublattice distortion. For instance, as shown

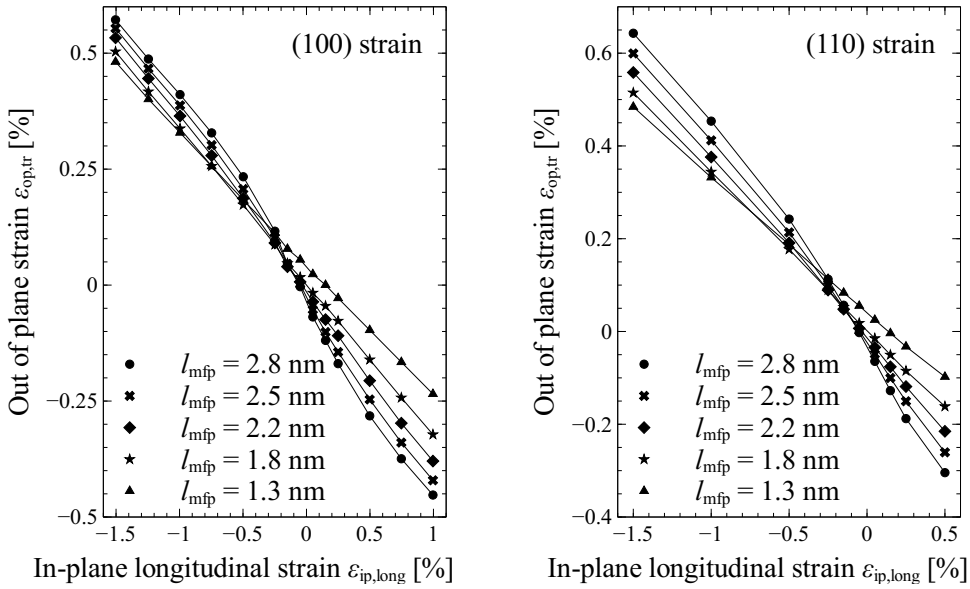

Figure 5.6: *Calculated out-of-plane strain as a function of in-plane longitudinal (100) and (110) strain (shown in the left and right figures, respectively).*

in figure 5.3, (100) strain results in a degree of sublattice distortion in the two transverse directions that is nearly identical in magnitude but opposite in sign and a degree of sublattice distortion in the in-plane longitudinal direction that is significantly smaller.

The strain sensitivity of the Fermi velocity decreases with decreasing l_{mfp}. This can also be attributed to the degree of sublattice disorder. With decreasing l_{mfp}, the degree of sublattice distortion decreases (figure 5.5).

5.3.4 Anisotropic normal state resistivity

The normal state resistivity is calculated from the crystal volume, the directional mean free path, the directional Fermi velocity and the electron density of states, with:

$$\rho_{n,x} = \frac{V}{N(E_F)\, l_{mfp,x} v_{F,x} e}. \tag{5.17}$$

If the crystal is strained, the normal state resistivity $\rho_{n,x}$ is direction dependent, i.e. compressive strain reduces the normal state resistivity along the strain direction with respect to the transverse direction. This is mainly a result of the anisotropic nature in which strain affects the Fermi velocity. A detailed comparison between the calculated and experimentally observed strain dependence of ρ_n follows in section 5.4.4.

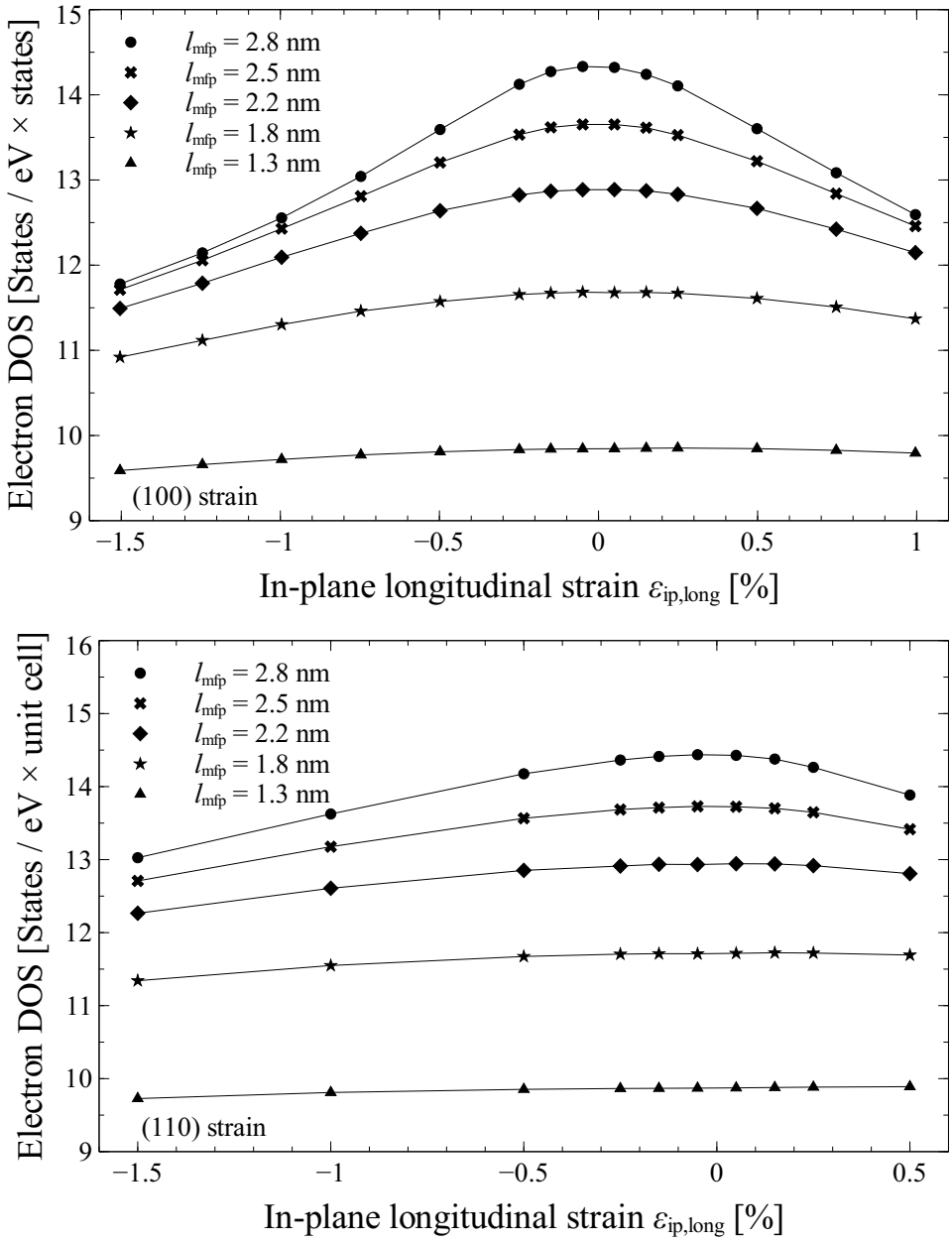

Figure 5.7: *Calculated electron density of states $N(E_F)$ as a function of in-plane longitudinal (100) and (110) strain (shown in the top and bottom figures, respectively).*

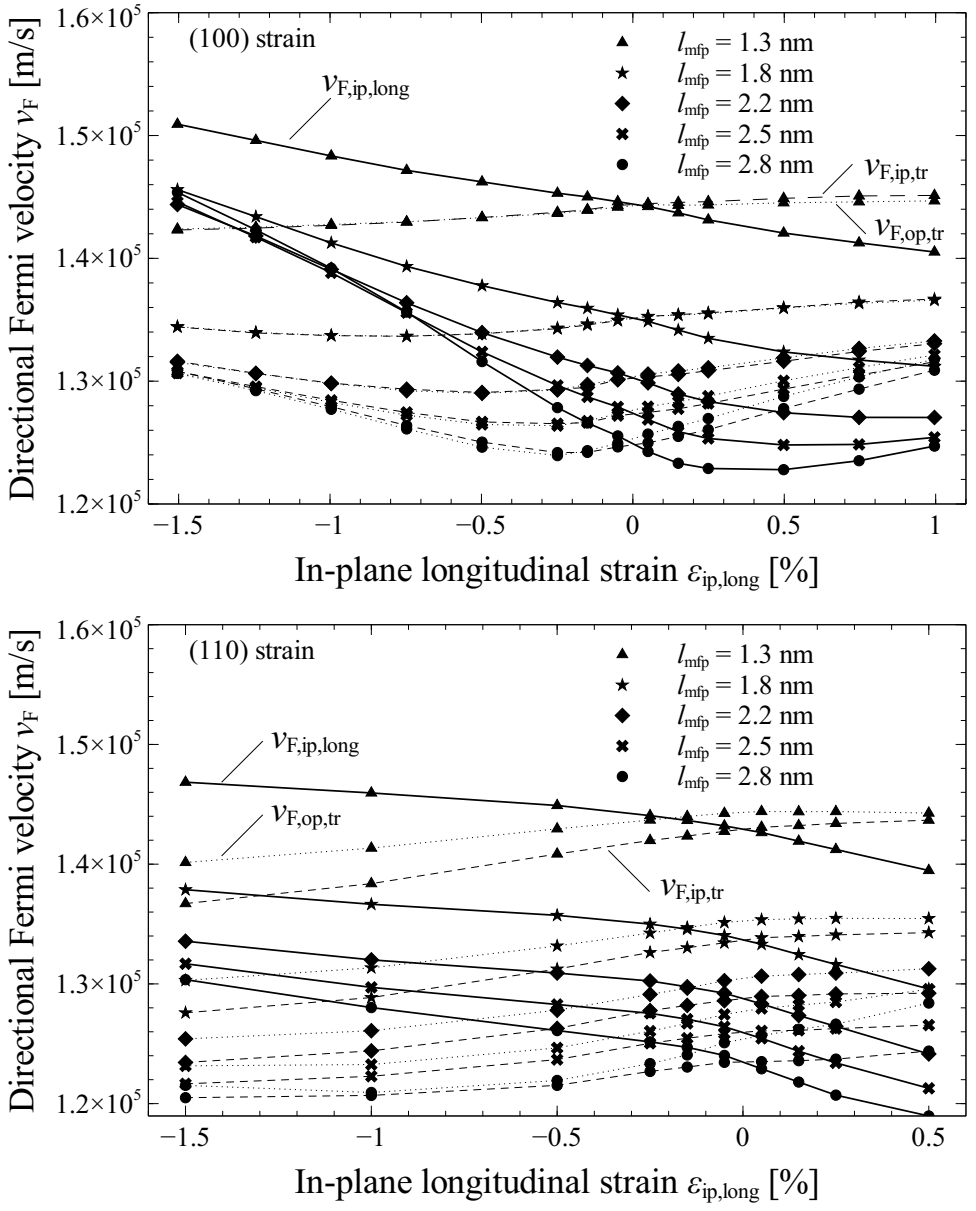

Figure 5.8: *Calculated directional Fermi velocity as a function of in-plane longitudinal strain, for various values of l_{mfp}. The solid, dashed, and dotted lines represent the in-plane longitudinal, the in-plane transverse, and the out-of-plane transverse directions respectively. The effect of (100) and (110) strain are shown in the top and bottom figures, respectively.*

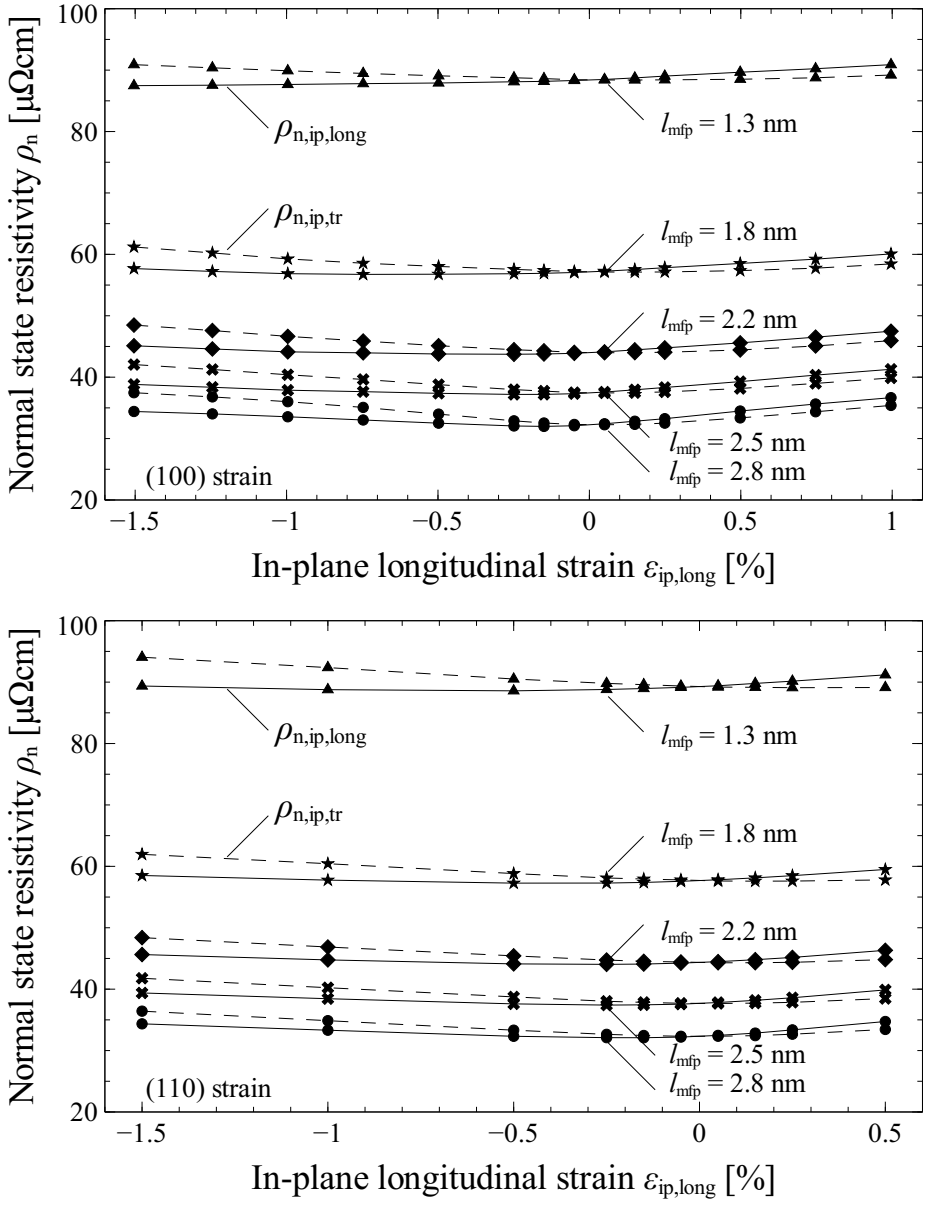

Figure 5.9: *Calculated in-plane longitudinal and transverse normal state resistivities* $\rho_{n,ip,long}$ *and* $\rho_{n,ip,tr}$ *as a function of (100) (top) and (110) (bottom) strain, at values of* l_{mfp}. *The solid and dashed lines represent the in-plane longitudinal and transverse directions, respectively.*

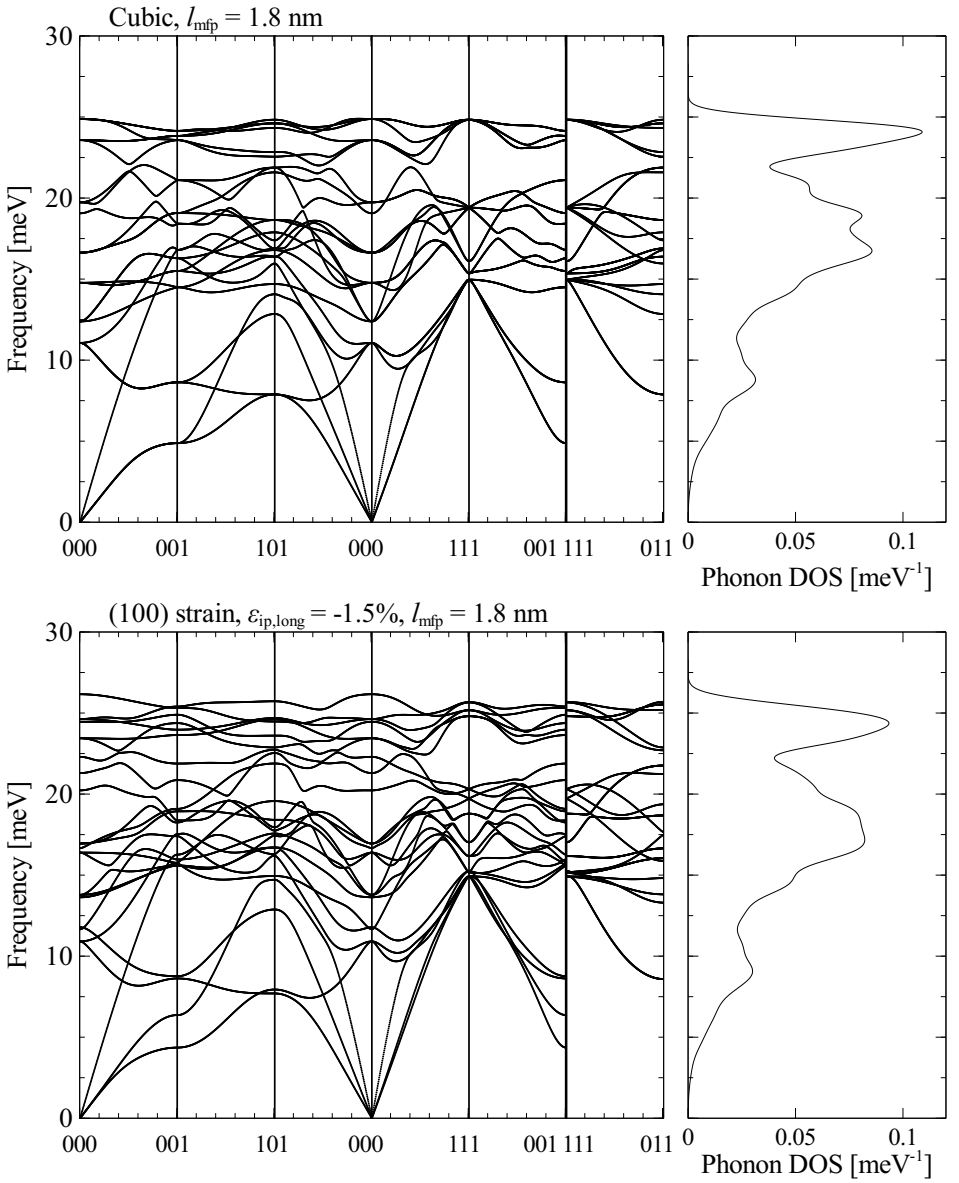

Figure 5.10: *Calculated phonon dispersion curves at l_{mfp} = 1.8 nm for cubic (top) and (100) strained (bottom) Nb_3Sn.*

5.3.5 Phonon density of states

Phonon dispersion curves were calculated as a function of strain and mean free path, which are shown in figure 5.10. In the dispersion plot splitting of vibrational modes can be ob-

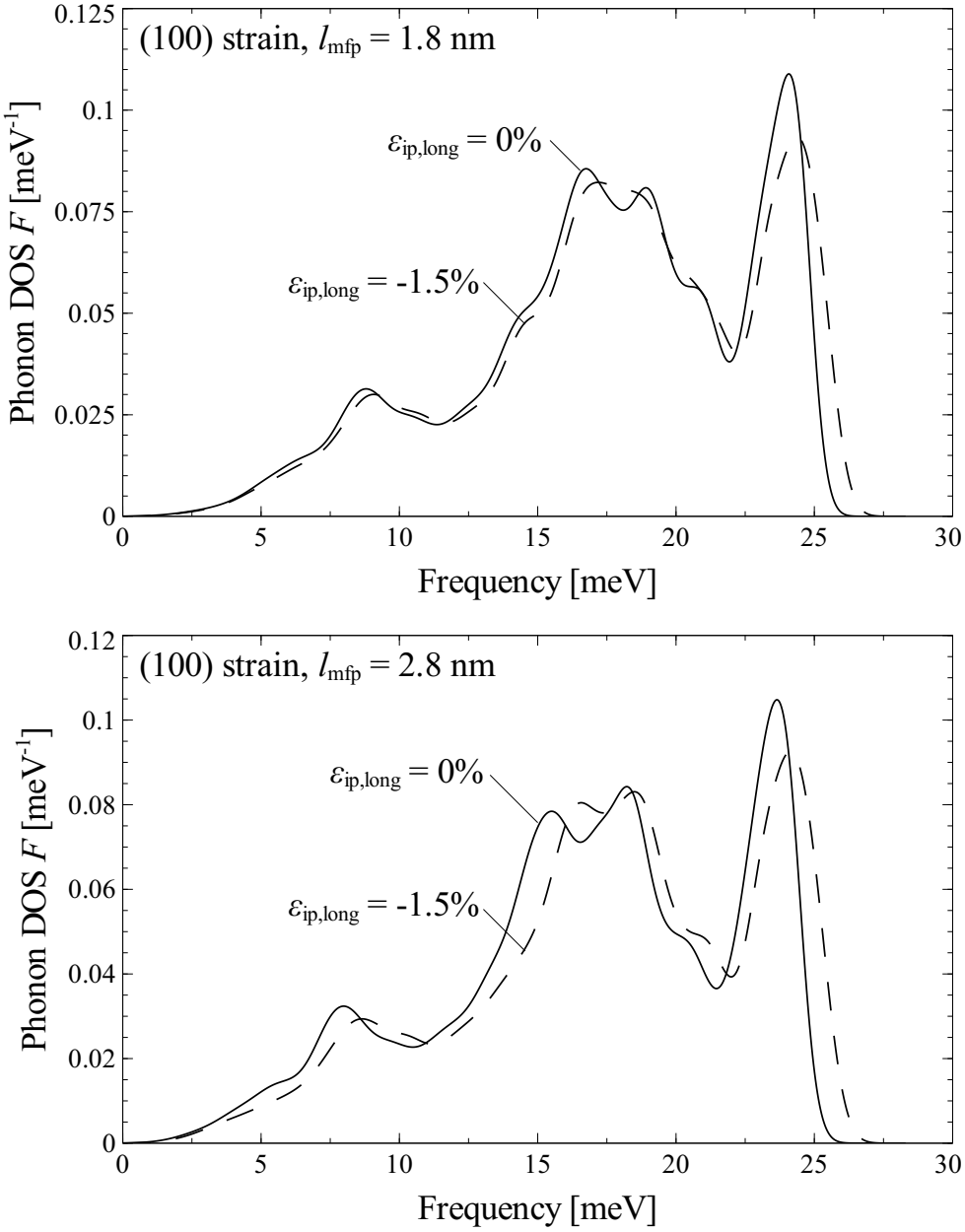

Figure 5.11: *Calculated phonon density of states as a function of frequency at two strains and l_{mfp} = 1.8 nm (top) and 2.8 nm (bottom).*

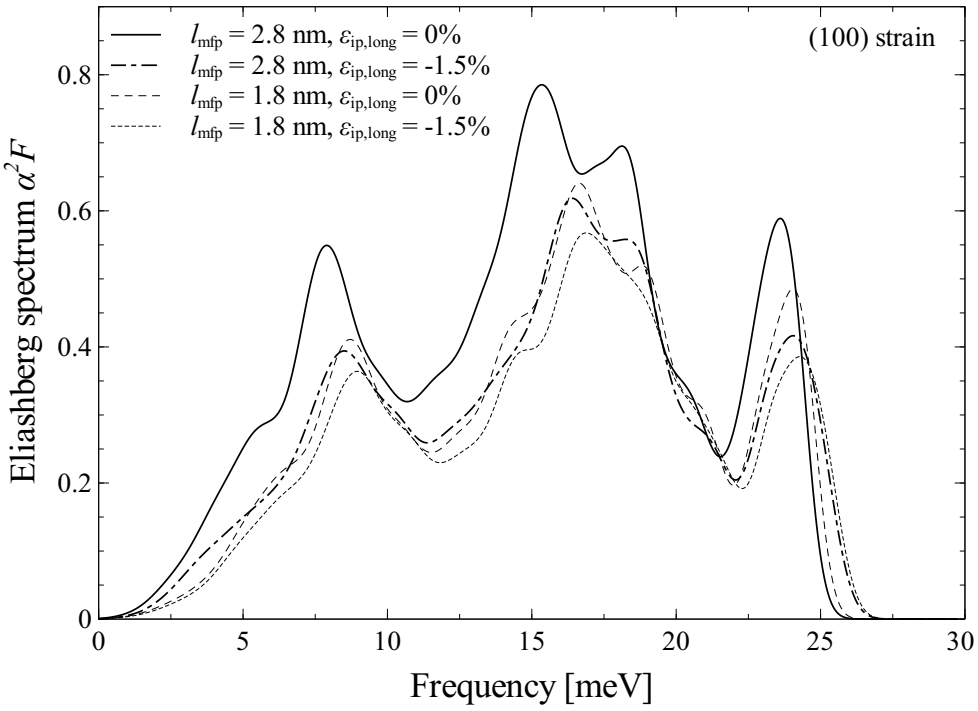

Figure 5.12: *Calculated Eliashberg spectra, α^2F as a function of frequency ω, for two mean free paths and two strains.*

served. For instance, the lowest frequency acoustic mode in the cubic crystal symmetry splits into two distinct bands at q = (001) (indicating a lattice vibration in the out-of-plane direction) when the crystal is strained. This splitting coincides with a shift towards higher vibrational frequencies, as shown in figure 5.11, in a manner that is more pronounced at a higher l_{mfp}.

5.3.6 Eliashberg spectrum, λ and $<\omega^2>^{0.5}$

As discussed in section 4.6.3, the Eliashberg spectra $\alpha^2F(\omega)$ are calculated at various mean free paths and validated through comparison to experimental tunnel junction data. Here, the Eliashberg spectra are calculated as a function of strain, and the corresponding electron phonon coupling constant λ and $<\omega^2>^{0.5}$ are determined.

These results are particularly relevant because they can be validated through comparison with experimental results. Tunnel junctions can be fabricated and strained and the Eliashberg spectra can be determined as a function of strain. An effort was made to perform this experiment [192], but within the time limits of this research, tunnel junctions of sufficient quality could not be fabricated.

The Eliashberg spectra of cubic and strained Nb_3Sn for two mean free paths are shown

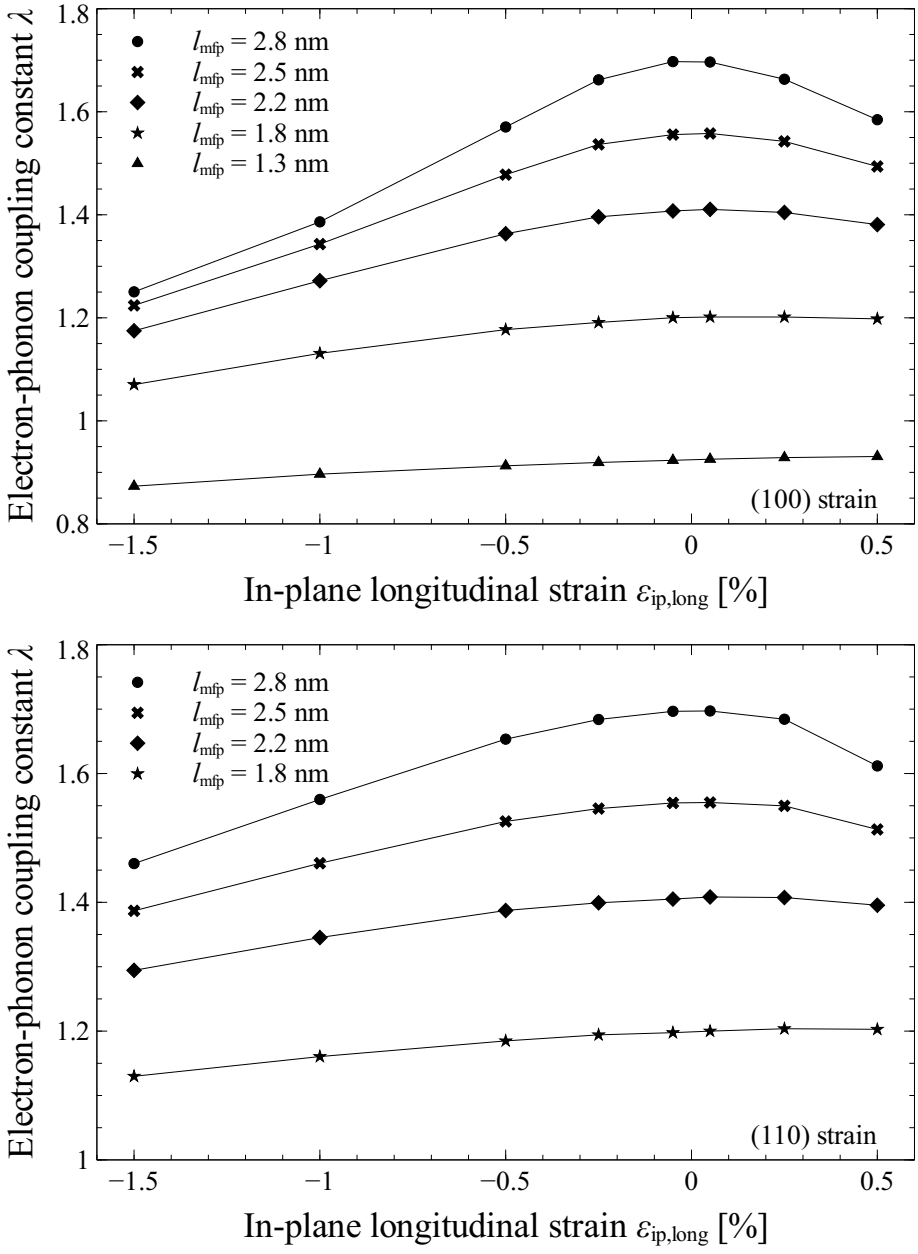

Figure 5.13: *Calculated electron-phonon coupling constant λ as a function of (100) and (110) strain (shown in the top and bottom figures), for two mean free paths.*

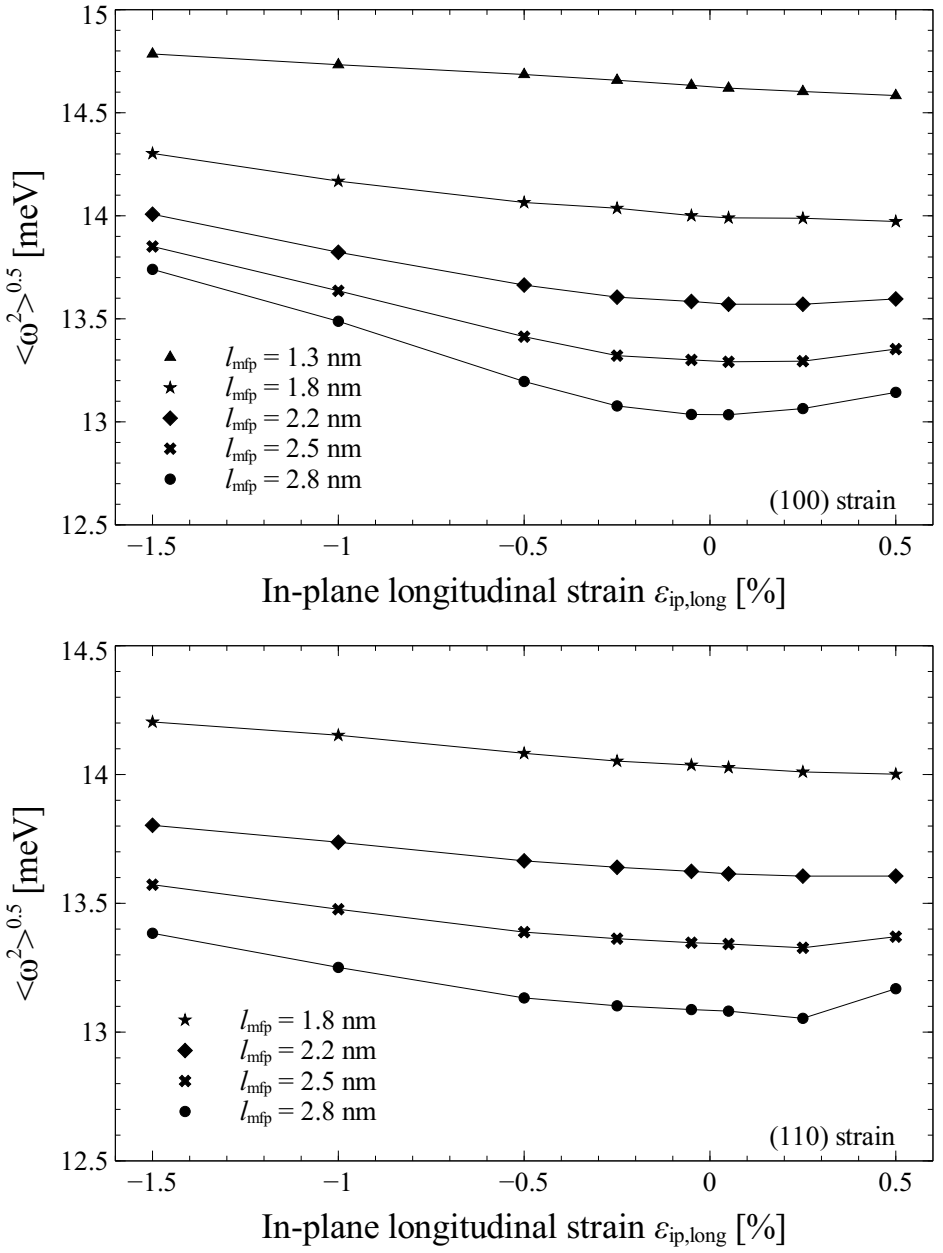

Figure 5.14: *Calculated $\langle\omega^2\rangle^{0.5}$ as a function of (100) and (110) strain (shown in the top and bottom figures), for various mean free paths.*

in figure 5.12. The calculation results point to three conclusions. Firstly, the Eliashberg spectrum shifts towards a higher frequencies under the influence of strain, due to the shift in the phonon density of states. Secondly, the overall amplitude of the Eliashberg spectrum is reduced due to a decrease in the electron density of states. Both effects are detrimental to superconductivity.

Thirdly, the effect of strain on the Eliashberg spectrum is more pronounced when the degree of disorder is lower, suggesting a larger strain sensitivity in the superconducting properties in less disordered Nb_3Sn. From the Eliashberg spectra, λ and $<\omega^2>^{0.5}$ are calculated, with:

$$\lambda = 2\int \frac{\alpha^2(\omega)F(\omega)}{\omega}\delta\omega, \tag{5.18}$$

$$\left\langle \omega^2 \right\rangle^{0.5} = \left(\frac{2}{\lambda}\int \alpha^2(\omega)F(\omega)\omega\delta\omega \right)^{0.5}. \tag{5.19}$$

In figures 5.13 and 5.14, λ and $<\omega^2>^{0.5}$ are presented as a function of strain, at various l_{mfp}. λ decreases with both compressive and tensile strain, while $<\omega^2>^{0.5}$ increases with compressive and tensile strain. The degree of strain sensitivity in both of these parameters decreases with decreasing l_{mfp}.

5.3.7 Critical temperature T_{c}

The critical temperature T_{c} was calculated using the Kresin [18], and Allen-Dynes descriptions (equations 4.28 and 4.35). Besides μ^*, Kresin's description is a function of λ and $<\omega^2>^{0.5}$, while the Allen-Dynes description also takes additional characteristic frequencies into account, which are derived from the Eliashberg spectrum.

For all investigated mean free paths and strains, the maximum absolute difference between the Kresin and Allen-Dynes descriptions is 0.38 K. Figure 5.15 shows the calculated T_{c} as a function of strain for various l_{mfp} as calculated with Kresin's description. The following conclusions can be drawn:

- The critical temperature is reduced when the crystal is forced into a non-cubic symmetry and the degree of reduction is typically in the order of several Kelvin. This reduction is a consequence of both changes in the electron and the phonon density of states.
- The critical temperature is more sensitive to (100) strain than (110) strain, because both the electron and phonon density of states are more strain sensitivity to (100) than to (110) strain.
- The strain sensitivity of T_{c} is more pronounced when l_{mfp} is larger, because both the degree of strain sensitivity in the electron and the phonon density of states increases with increasing l_{mfp}.

A detailed comparison of the calculated and experimentally observed strain dependence of T_{c} is given in section 5.5.4.

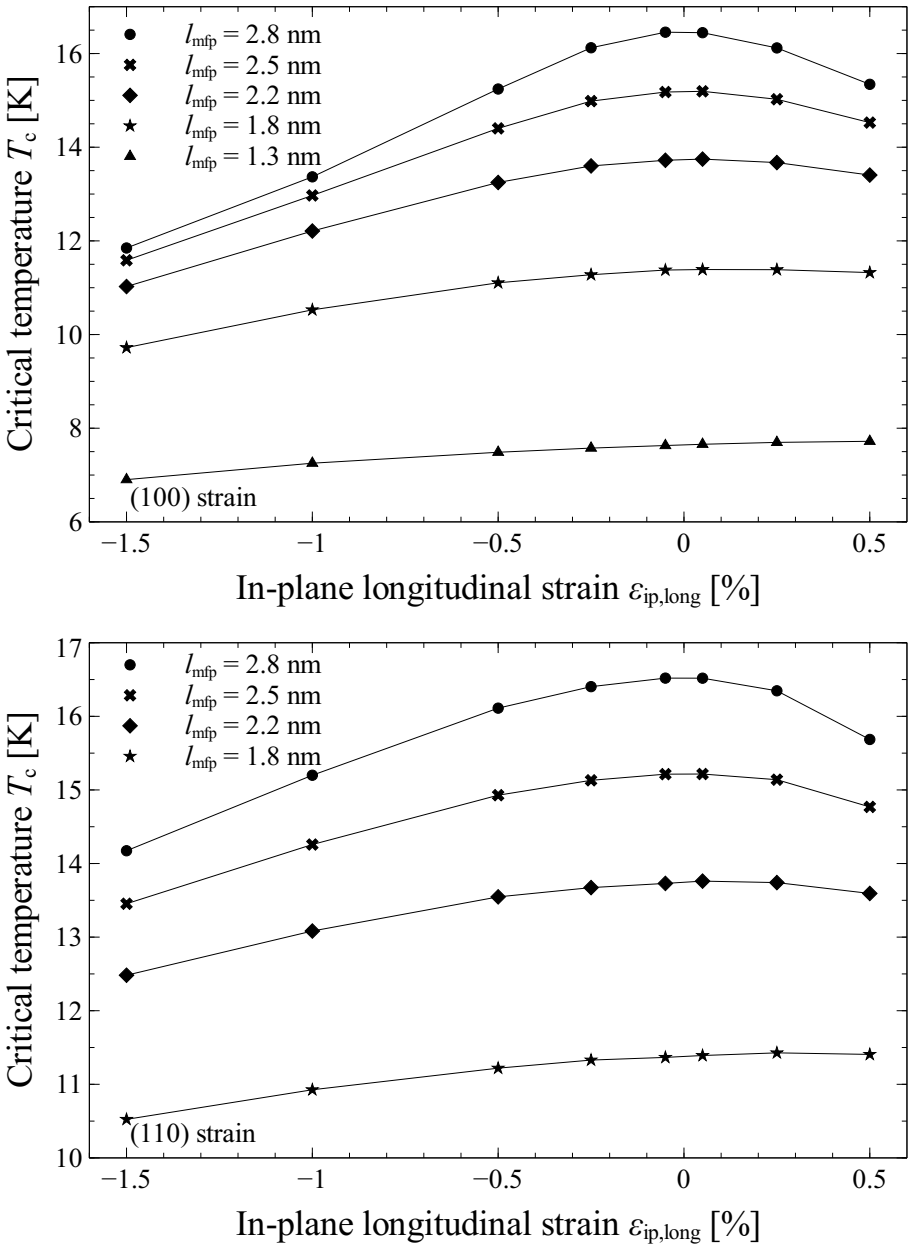

Figure 5.15: *Calculated critical temperature T_c as a function of (100) and (110) strain (top and bottom figures) for various l_{mfp}.*

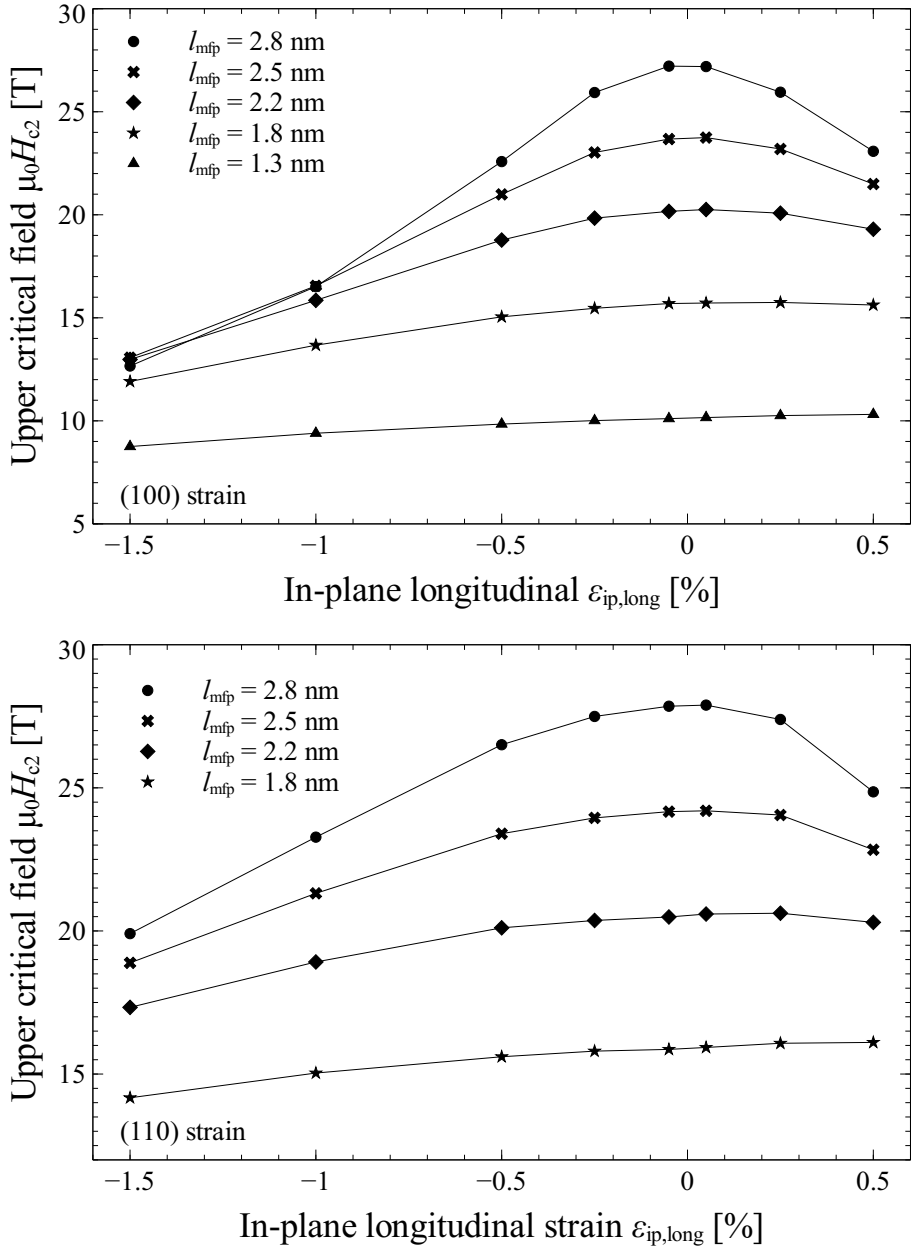

Figure 5.16: *Upper critical field $\mu_0 H_{c2}(0)$ as a function of (100) and (110) strain (top and bottom figures), for various l_{mfp}.*

5.3.8 Upper critical field $\mu_0 H_{c2}(0)$

The upper critical field at 0 K is calculated as a function of strain and mean free path. The approach used to calculate $\mu_0 H_{c2}$ is the 'best-effort' approach as discussed in section 4.8.3, which takes strong coupling corrections into consideration for a superconductor in the intermediate to dirty limit (i.e. a reduced collision frequency between 1.5 and 17.5), under the assumption of a spherical Fermi surface, without spin-orbit coupling and with Pauli paramagnetic limiting. $\mu_0 H_{c2}(0)$ is calculated following:

$$\mu_0 H_{c2}^{+}(0) = \eta_{Hc2}\left(C_{O1}\frac{T_c^2(1+\lambda)^2}{v_F^2} + C_{O2}\frac{T_c(1+\lambda)}{v_F l_{mfp}}\right), \tag{5.20}$$

$$C_{O1} = \frac{0.766 \times 24\pi^2 k_B^2}{7\zeta(3)\hbar e} = 2.433 \times 10^8, \tag{5.21}$$

$$C_{O2} = \frac{0.608 \times 12\pi k_B}{7\zeta(3) e} = 2.349 \times 10^{-4}, \tag{5.22}$$

$$\eta_{H_{c2}} = 1 + \left(\frac{\pi k_B T_c}{\langle\omega^2\rangle^{0.5}}\right)\left(0.6\ln\left(\frac{\langle\omega^2\rangle^{0.5}}{k_B T_c}\right) - 0.26\right), \tag{5.23}$$

$$\mu_0 H_p(0) = 1.86 T_c(1+\lambda), \tag{5.24}$$

$$(\mu_0 H_{c2}(0))^{-2} = (\mu_0 H_{c2}^{+}(0))^{-2} + 2(\mu_0 H_p(0))^{-2}, \tag{5.25}$$

where $\mu_0 H_{c2}^{+}$ is the upper critical field at 0 K without Pauli paramagnetic limiting in [T], $\mu_0 H_p(0)$ is the Pauli paramagnetic field at 0 K in [T], T_c is the critical temperature in [K], λ is the electron-phonon coupling constant, v_F is the rms Fermi velocity in [ms^{-1}], C_{O1} and C_{O2} are constants in [Tm^{2}K^{-2}s^{-2}] and [Tm^{2}K^{-1}s^{-1}] respectively, η_{Hc2} is the strong coupling correction factor, k_B is the Boltzmann constant in [eVK^{-1}], $<\omega^2>^{0.5}$ the characteristic phonon frequency in [eV], and $\mu_0 H_{c2}(0)$ is the upper critical field at 0 K with Pauli paramagnetic limiting in [T]. The upper critical field at various mean free paths and strains is shown in figure 5.16. The following conclusions can be drawn:

- $\mu_0 H_{c2}(0)$ is more strain sensitive at longer mean free paths and less strain sensitive at shorter mean free paths.
- $\mu_0 H_{c2}(0)$ is more strain sensitivity than T_c. This is to be expected: $\mu_0 H_{c2}(0)$ is proportional to T_c in the dirty limit but proportional to T_c^2 in the clean limit. Moreover, $\mu_0 H_{c2}(0)$ is proportional to $(1+\lambda)$ in the dirty limit and $(1+\lambda)^2$ in the clean limit. From this simple argument, it is clear that $\mu_0 H_{c2}(0)$ is expected to be more sensitive to strain than T_c, which is also consistent with experimental observations (figure 3.11).
- The upper critical field is more sensitive to (100) strain in comparison to (110) strain.

A detailed comparison of calculated and experimental results is found in section 5.5.4.

5.3.9 Conclusion

A series of calculations were performed to determine the strain dependence of the superconducting and normal state properties of Nb-Sn at various strains and degrees of disorder. The experimental boundary conditions of the U-spring were used in the model, thus allowing a comparison between calculated results and experimental observations. The following can be concluded:

- Under the influence of strain, the niobium ions are rearranged inside the crystal, a phenomenon which is referred to as sublattice distortion.
- The electron density of states is suppressed when the crystal is deformed.
- The strain dependence of v_F is dependent on the direction in which an electron travels relative to the strain direction. As a result, the strain dependence of ρ_n in the direction transverse to the strain direction is different from the strain dependence of ρ_n parallel to the strain direction, i.e. compressive strain results in a decrease of the in-plane longitudinal resistivity in comparison to the transverse resistivity.
- The vibrational modes shift towards higher frequencies when the crystal is strained.
- λ is decreased when the crystal is strained, while $<\omega^2>^{0.5}$ is increased.
- Forcing the crystal into non-cubic symmetry results in a reduction in T_c and $\mu_0 H_{c2}(0)$, a result that is in part due to a reduction in the electron density of states and a shift in the phonon density of states towards higher frequency.
- The degree of strain sensitivity of T_c and $\mu_0 H_{c2}(0)$ decreases with decreasing T_c and $\mu_0 H_{c2}(0)$.

5.4 Relation between sublattice distortion and strain sensitivity of the normal state resistivity and superconducting properties of Nb-Sn

5.4.1 Introduction

The relation between sublattice distortion, the strain dependent ρ_n and the strain dependent superconducting properties of Nb_3Sn will be discussed in more detail. The strain sensitivity of the superconducting properties, which is also observed in other A15 materials (Nb_3Au, Nb_3Al, V_3Ga, and V_3Si) by Flukiger *et al.* [193], is significantly larger than the strain sensitivity of bcc materials such as Nb and Nb-Ti (also see Ekin [109]).

An obvious difference between A15 Nb_3Sn and bcc niobium is that bcc niobium does not contain sublattices, i.e. the characteristic niobium chains present in A15 Nb_3Sn (figure 5.3). If sublattice distortion is the dominant mechanism that explains the strain sensitivity of ρ_n, T_c, and $\mu_0 H_{c2}(0)$ in Nb_3Sn, one would expect that ρ_n and the superconducting properties are only weakly affected by strain in bcc Nb.

Another difference is that unlike A15 Nb_3Sn, bcc niobium does not undergo a spontaneous cubic-to-tetragonal transformation. This is both a computational statement (i.e. the stability

of the cubic phase was evaluated and found to be consistently stable, regardless of the degree of disorder) and an experimental statement. While it was speculated that the martensitic transformation does occur in bcc Nb by Bollinger *et al.* [195], a subsequent evaluation of the temperature dependent lattice parameters by Francoual *et al.* [196] showed that this prediction is not correct.

The following questions are answered:

- Is the strain sensitivity of Nb_3Sn mainly due to the effect of strain on the electronic properties, on the vibrational properties, or on both?
- How would strain affect the properties of Nb_3Sn if the sublattice distortion would not occur?
- How does strain affect the properties of bcc Nb?
- Is sublattice distortion the origin of strain sensitivity in Nb_3Sn?
- How does the strain sensitivity of Nb_3Sn compare to that of Nb_3Al, NbTi, and Nb?

5.4.2 Strain sensitivity: electronic and vibrational properties

It was demonstrated in section 2.4.6 that the residual resistivity is affected by strain. This implies that the electronic properties are changing as a function of strain, as the residual resistivity is not related to the vibrational properties of the crystal.

It is less straightforward to determine whether the strain sensitivity of the superconducting properties is caused by changes in the electronic properties, the vibrational properties, or both. In order to determine whether the effect of strain on T_c and $\mu_0 H_{c2}$ is related to the effect of strain on the electronic properties, the vibrational properties, or both, an academic exercise is performed: what if strain affects the electronic properties but the phonon density of states is fixed?

To answer this question, a calculation is performed in which the electronic properties are calculated as a function of strain, while the phonon density of states is fixed. The result is shown in figure 5.17. A comparison is made between the 'just electronic' case, where changes in the phonon density of states are neglected and the 'electronic + phonon' case, where both cases are considered. It is clear that in the case of (100) strain at a mean free path of 2.8 nm, strain sensitivity is mainly a result of changes in the electronic properties. To quantify this, the fraction f of strain sensitivity due to changes in the electronic properties is calculated following:

$$f_{\text{electronic}} = \frac{\mu_0 H_{c2}\left(\varepsilon_{\text{ip,long}} = 0\%\right) - \mu_0 H_{c2,\text{elec}}\left(\varepsilon_{\text{ip,long}} = -1.5\%\right)}{\mu_0 H_{c2}\left(\varepsilon_{\text{ip,long}} = 0\%\right) - \mu_0 H_{c2,\text{elec+ph}}\left(\varepsilon_{\text{ip,long}} = -1.5\%\right)}, \tag{5.26}$$

where $\mu_0 H_{c2,\text{elec}}$ is the upper critical field which includes the effect of strain on the electronic but not the vibrational properties, and $\mu_0 H_{c2,\text{elec+ph}}$ includes the effect of strain on both the electronic and the vibrational properties. If only the change in electronic properties is considered then this explains 85% of the total strain sensitivity of $\mu_0 H_{c2}(0)$ and 80% of the total strain sensitivity of T_c in the case of (100) strain at l_{mfp} = 2.8 nm. With decreasing

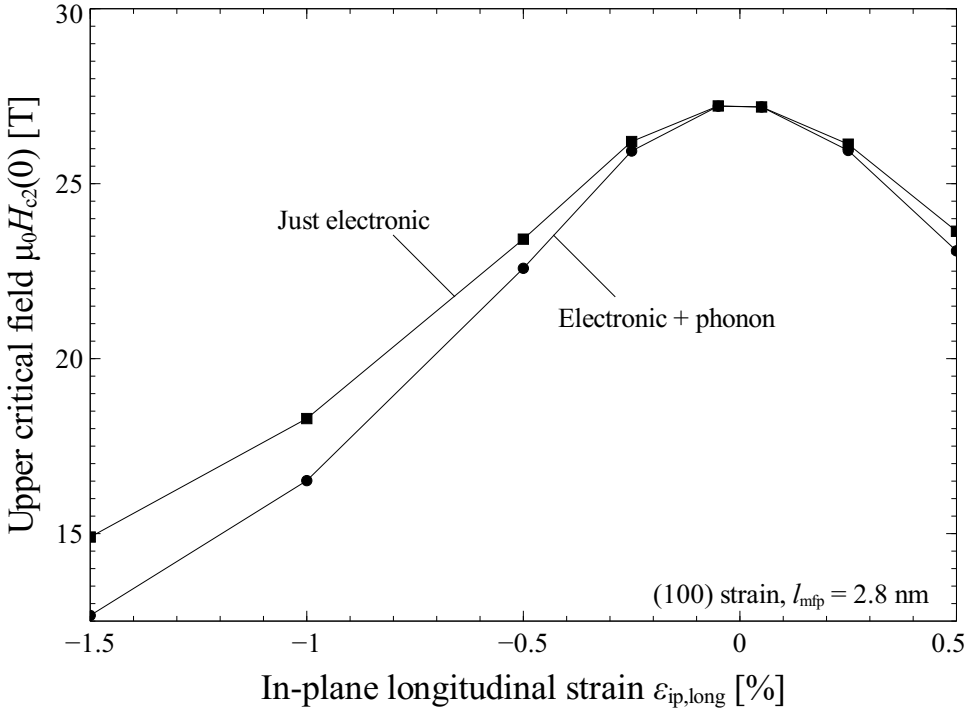

Figure 5.17: *Calculated upper critical field as a function of strain. One calculation considers only the strain sensitivity of the electronic properties, i.e. the phonon density of states is fixed, while the other is a (regular) calculation that considers both strain sensitivity of the electronic and vibrational properties.*

mean free path, the fraction of total strain sensitivity that is due to changes in the electronic properties decreases. At l_{mfp} = 1.3 nm in the case of (100) strain, the change in electronic properties with strain explains 55% of the total strain sensitivity of $\mu_0 H_{c2}(0)$ and 53% of total the strain sensitivity of T_c. Also, in the case of (110) strain at l_{mfp} = 2.8 nm, the strain sensitivity of the electronic properties explains 76% of the total strain sensitivity of $\mu_0 H_{c2}(0)$ and 77% of the total strain sensitivity of T_c.

In summary, the results indicate that changes in both the electronic and the vibrational properties of the crystal contribute to the strain sensitivity of T_c and $\mu_0 H_{c2}(0)$, but changes in the electronic properties play a larger role than changes in the vibrational properties, in particular in less disordered Nb_3Sn.

This conclusion is consistent with the investigation of a number of authors, including Lim *et al.* [147] who investigated the stress dependence of T_c, $\mu_0 H_{c2}(0)$, and ρ_n, Welch [197] who investigated the strain sensitivity of T_c relative to $\mu_0 H_{c2}$, and Cohen *et al.* [198], who constructed a simple model to account for the temperature dependent normal state resistivity and the elastic constants, which according to McEvoy [199] can explain the pressure dependence of T_c as well. It was argued by Godeke *et al.* [200] that strain affects the elec-

tron diffusion constant, which was one of the main reasons for performing experiments in which both the superconducting properties and the normal state resistivity is measured as a function of strain in this thesis.

Though the conclusion here is consistent with the observation by De Marzi *et al.* that strain sensitivity affects both the electronic and the vibrational properties, a conclusion that is also based on DFT calculations, De Marzi and our investigations are in many ways very different. For instance, they do not discuss disorder, suppress sublattice distortion after assuming that sublattice distortion is irrelevant for strain sensitivity, and their calculation indicates a degree of strain sensitivity that strongly deviates from the experimentally observed strain sensitivity.

There are a number of authors (Testardi [201], Taylor *et al.* [84], Oh *et al.* [203], Markiewicz [98]), who attribute the strain sensitivity of Nb_3Sn entirely to the strain sensitivity of the vibrational properties of the material.

The strain sensitivity of V_3Si was investigated by Testardi [201], and it was argued that the strain sensitivity is mainly related to changes in the vibrational properties of the crystal. In order to investigate the possibility that strain affects the electronic properties of the crystal, the author relies on a simple rigid band model. In using this rigid band model it is assumed that strain does not affect the band structure of the material, but simply raises of lowers the Fermi energy. One of the main insights of the research presented in this thesis is that strain affects the ion configuration and by extension the band structure in a profound way. Thus, a rigid band model is too simple to investigate the strain sensitivity of the electronic properties. The author relates the strain sensitivity of the superconducting properties to the strain induced change in the vibrational properties, after making the assumption that the change in the linear expansion term α with strain is small relative to the change in T_c. However, it is subsequently concluded that longitudinal strain does in fact affect α, so that only an upper limit due to the contribution of changes in vibrational properties could be determined. This is consistent with the analysis here: the calculated results indicate that the strain sensitivity of the phonon density of states contributes to the strain sensitivity of T_c and $\mu_0 H_{c2}(0)$, even though it is not the dominant factor.

In summary, Testardi's analysis is consistent with this research insofar as attributing the strain sensitivity of the superconducting properties in part to the strain sensitivity of the vibrational properties, but the author relies on an oversimplified rigid band model approach to argue that the strain sensitivity of the electronic properties does not play a role.

There are a number of additional investigations that attribute strain sensitivity solely to changes in the vibrational properties.

- It was argued by Taylor *et al.* [84] that the change in superconducting properties is a result of changes in the vibrational properties after assuming that the electronic properties are not affected by strain. For instance, it was assumed that the normal state resistivity is not affected by strain, which is inconsistent with experimental evidence, see section 2.4.6.
- In similar fashion, it was argued by Oh *et al.* [203] that the strain sensitivity is a result of phonon anharmonicity after making the implicit assumption that the electron density of states and Fermi velocity are independent of strain. Oh's investigation points to a 'case I' in which the change in λ is large relative to $<\omega^2>^{0.5}$, which is consistent with the notion that strain affects the electronic properties of the crystal.

Subsequently, it is speculated that this case implies that phonon anharmonicity is the dominant cause of the strain sensitivity in the superconducting properties, which is inconsistent with this research.

- Markiewicz [98] argued that strain sensitivity is a result of changes in the phonon density of states, but his analysis utilizes the experimentally observed $\delta T_c/\delta P$ dependence on the unverified assumption that this is result of changes in the vibrational properties. In addition, an implicit assumption was made that strain does not affect the electron density of states.

While these investigations are useful and instructive (in particular the work by Markiewicz), it has to be pointed out that there is a certain circular logic to these arguments: as Nb_3Sn is a phonon-mediated superconductor, one will invariably conclude that strain sensitivity must be a result of changes in the vibrational properties after making the incorrect starting assumption that changes in electronic properties do not play a part. The observation of a large degree of strain sensitivity in the residual resistivity (figure 2.20) is compelling evidence that the electronic properties are affected by strain, and therefore the strain sensitivity of the electronic properties cannot be ignored.

In summary, the present model indicates that changes in the superconducting properties as a function of strain are a result of changes in both the electronic and the vibrational properties. However, in low-resistivity cubic Nb_3Sn the strain sensitivity of the superconducting properties is mainly a result of a strain-induced change in the electronic properties.

5.4.3 Effect of sublattice distortion on the superconducting properties

As the strain sensitivity of the normal state resistivity at 0 K is entirely due to changes in the electronic properties and the strain sensitivity of T_c and $\mu_0 H_{c2}$ is mostly due to changes in the electronic properties, emphasis is placed on the effect of strain on the electronic properties. In this chapter, the concept of niobium sublattice distortion was introduced. It seems reasonable to assume that the large strain sensitivity of Nb_3Sn is a direct result of this sublattice distortion.

To determine the validity of this assumption, a calculation was performed as an academic exercise in which the sublattice distortion does not occur, i.e. $\delta \equiv 0$. The electronic band structure of cubic Nb_3Sn, strained Nb_3Sn with $\delta \equiv 0$, and strained Nb_3Sn in which sublattice distortion is allowed to occur (here denoted with $\delta \neq 0$) is shown in figure 5.18. Note that for $\delta \neq 0$, the calculated values of δ are shown in figure 5.5.

In figure 5.18, the electronic band structure is plotted along high-symmetry directions where the three-dimensional k-point coordinate indicates the relative distance to the Brillouin zone boundary along the in-plane longitudinal, in-plane transverse, and out-of-plane transverse directions, respectively. For instance, k = 000 indicates the center of the Brillouin zone, while k = 001 indicates the Brillouin zone edge. The three indices denote the in-plane longitudinal, the in-plane transverse, and the out-of-plane transverse directions, respectively.

In the cubic case and the case with $\delta \equiv 0$, a large number of electronic bands are observed near the Fermi energy. In the case of $\delta \neq 0$ these bands are spread out over a larger energy range. For instance, bands are spread out over approximately double the energy range at k = 111 in comparison to the cubic case and the case with $\delta \equiv 0$. Figure 5.19 shows $N(E_F)$

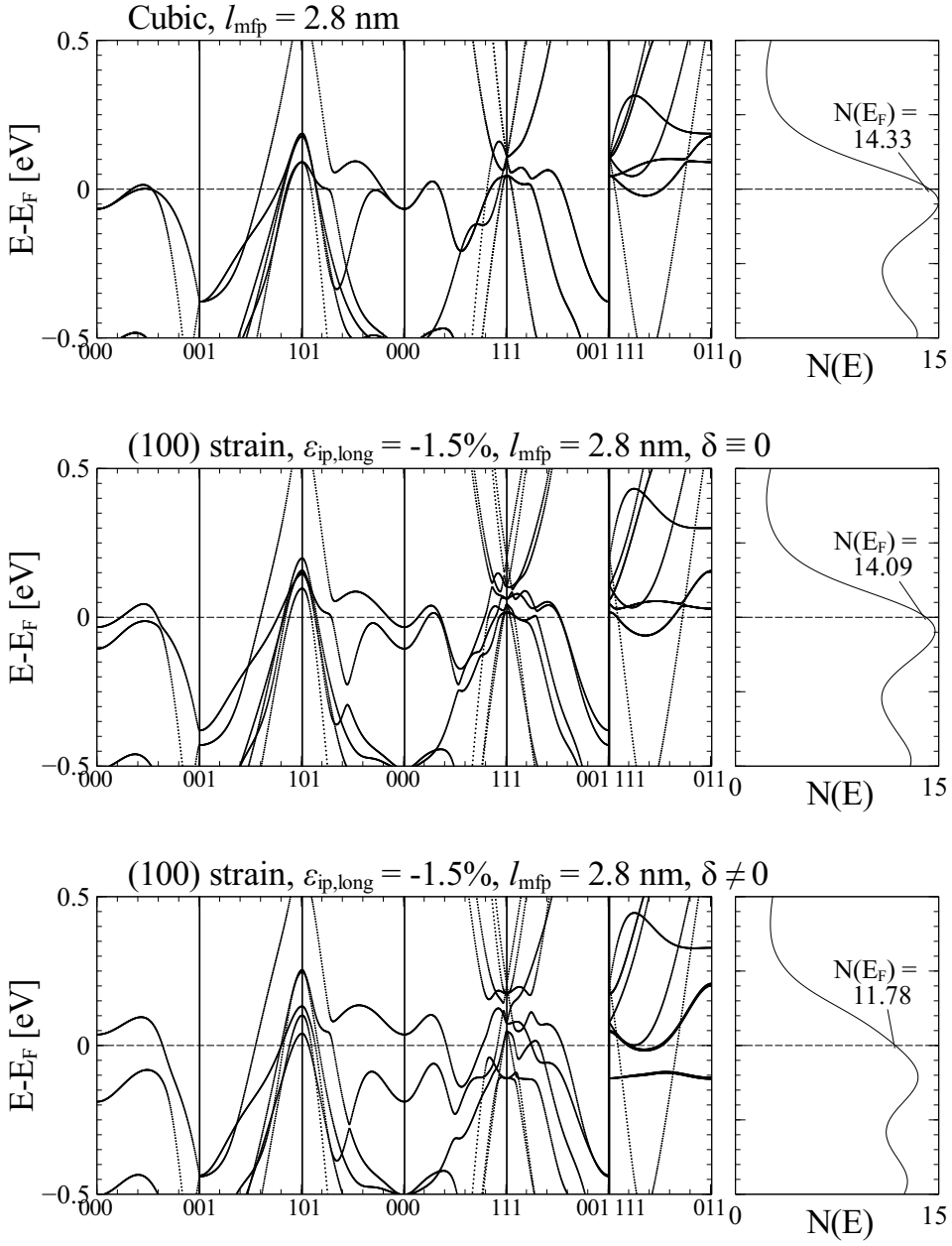

Figure 5.18: *Calculated electronic band structure of cubic (top) and (100) strained (bottom) Nb_3Sn with $\delta \equiv 0$ and $\delta \neq 0$.*

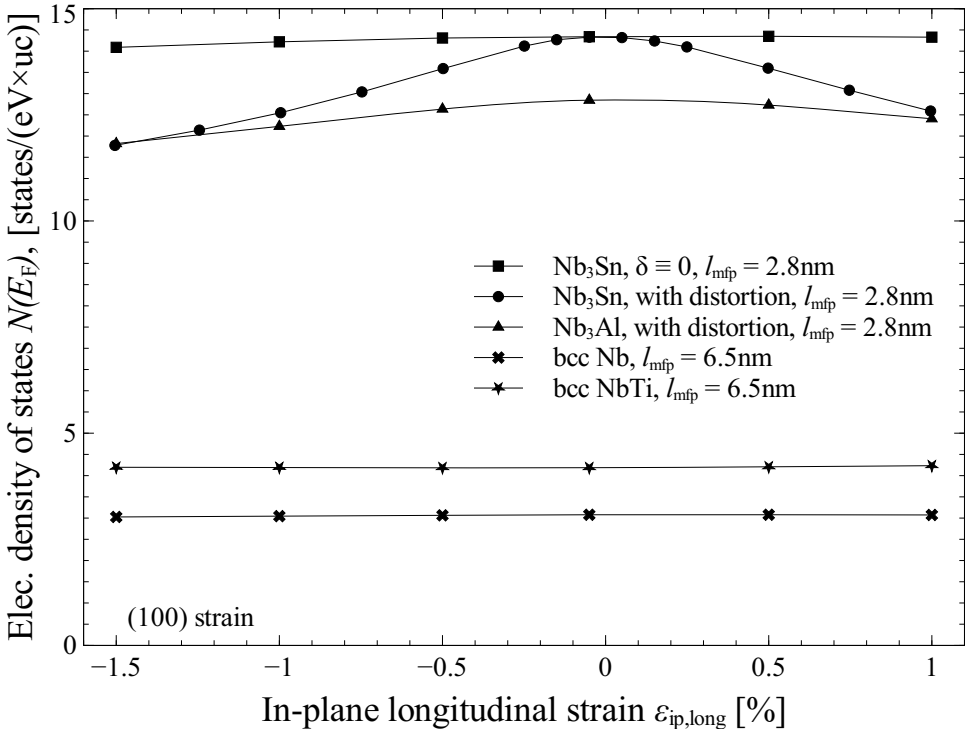

Figure 5.19: *Calculated electron density of states as a function of strain of A15 Nb_3Sn with sublattice distortion, A15 Nb_3Sn without sublattice distortion, A15 Nb_3Al with sublattice distortion, bcc Nb, and bcc NbTi.*

in the cases of $\delta \equiv 0$ and $\delta \neq 0$. Unsurprisingly, the effect of strain on $N(E_F)$ is much more pronounced in the case of $\delta \neq 0$. The electron-phonon coupling constant λ is proportional to $N(E_F)$, which means that the strain sensitivity of the superconducting properties would be dramatically reduced if the sublattice distortion could be prevented.

A more physically applicable analysis is to evaluate the effect of strain on bcc niobium. Because bcc niobium does not have the characteristic niobium chains that A15 Nb_3Sn has, sublattice distortion cannot occur. If the sublattice distortion is the main cause of the large strain sensitivity in the electron density of states, then it stands to reason that the strain sensitivity of the electron density of states is dramatically less than that of A15 Nb-Sn. Indeed, the calculated results indicate that strain only weakly affects $N(E_F)$ in bcc niobium (figure 5.19). Note that the mean free paths at which the calculations are performed differ between A15 Nb_3Sn and bcc Nb. This is done for two reasons. Firstly, the Fermi velocity of niobium is nearly three times higher in the case of bcc niobium than in A15 Nb_3Sn, so that the mean scattering time is nearly identical for the two calculations. Secondly, the mean free paths at which these calculations were performed are representative for measurements on these two sample types, so that calculated results and experimental observations can be compared. Note that in the preferentially cubic regime, the effect of strain on $N(E_F)$

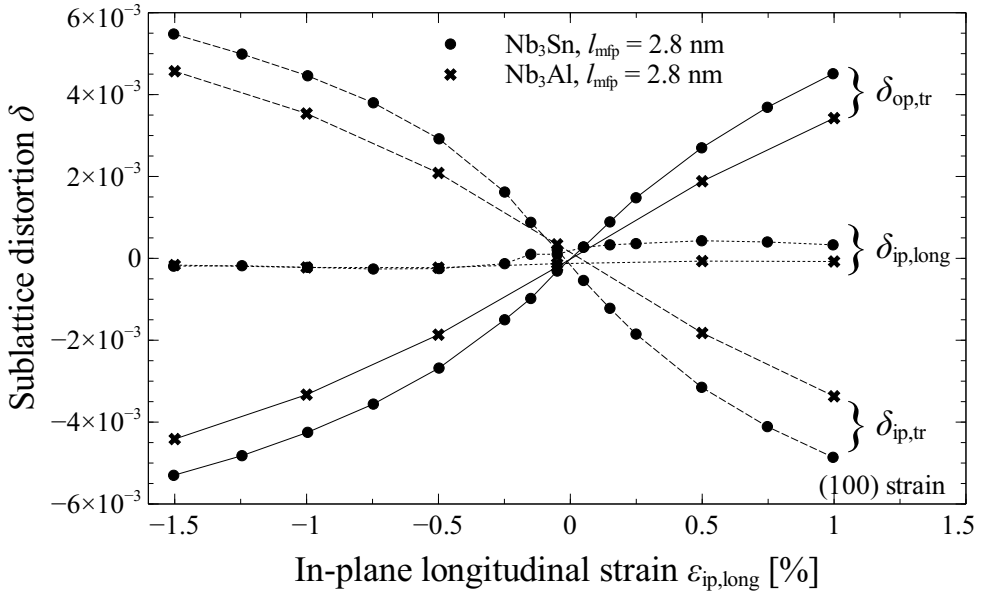

Figure 5.20: *Calculated degree of sublattice distortion as a function of longitudinal (100) strain at l_{mfp} = 2.8 nm in Nb_3Sn and Nb_3Al, also see section 5.3.1.*

increases with increasing l_{mfp}, which means that the different degree of strain sensitivity is not due to a different l_{mfp}.

In addition to Nb_3Sn and bcc niobium, calculations on Nb_3Al and bcc NbTi are performed. As with Nb_3Sn, it is found that the application of strain causes sublattice distortion in Nb_3Al. However, the effect is less pronounced in comparison to Nb_3Sn at l_{mfp} = 2.8 nm, as is shown in figure 5.20. Moreover, the effect of strain on the electronic density of states is less pronounced in comparison to Nb_3Sn (figure 5.19). At $\varepsilon_{\mathrm{ip,long}} = -1.5\%$ and l_{mfp} = 2.8 nm, $N(E_{\mathrm{F}})$ is reduced by 8% in the case of Nb_3Al, but 18% in the case of Nb_3Sn, in comparison to $\varepsilon_{\mathrm{ip,long}} = 0\%$. As the strain sensitivity of $N(E_{\mathrm{F}})$ is the main determinant of strain sensitivity of the superconducting properties of Nb_3Sn, this implies that the superconducting properties of Nb_3Al are less strain sensitivity that Nb_3Sn, which is consistent with experimental evidence by Takeuchi *et al.* [204, 205].

The effect of strain on bcc NbTi is very similar to the effect of strain of bcc Nb: sublattice distortion does not occur as a result of strain, because neither material has sublattices, i.e. the distinctive niobium chains on the faces of the A15 unit cell (figure 5.3). In both cases, the application of strain only weakly affects $N(E_{\mathrm{F}})$: in the case of bcc Nb at l_{mfp} = 6.5 nm, $N(E_{\mathrm{F}})$ is 1.7% lower at $\varepsilon_{\mathrm{ip,long}} = -1.5\%$ in comparison to $\varepsilon_{\mathrm{ip,long}} = 0\%$, while it is 0.2% higher in the case of NbTi.

In summary, it is found that sublattice distortion is the cause of the strongly strain dependent $N(E_{\mathrm{F}})$. Suppression of sublattice distortion dramatically reduces the strain sensitivity of the electron density of states. Moreover, the results indicate the degree by which strain affects

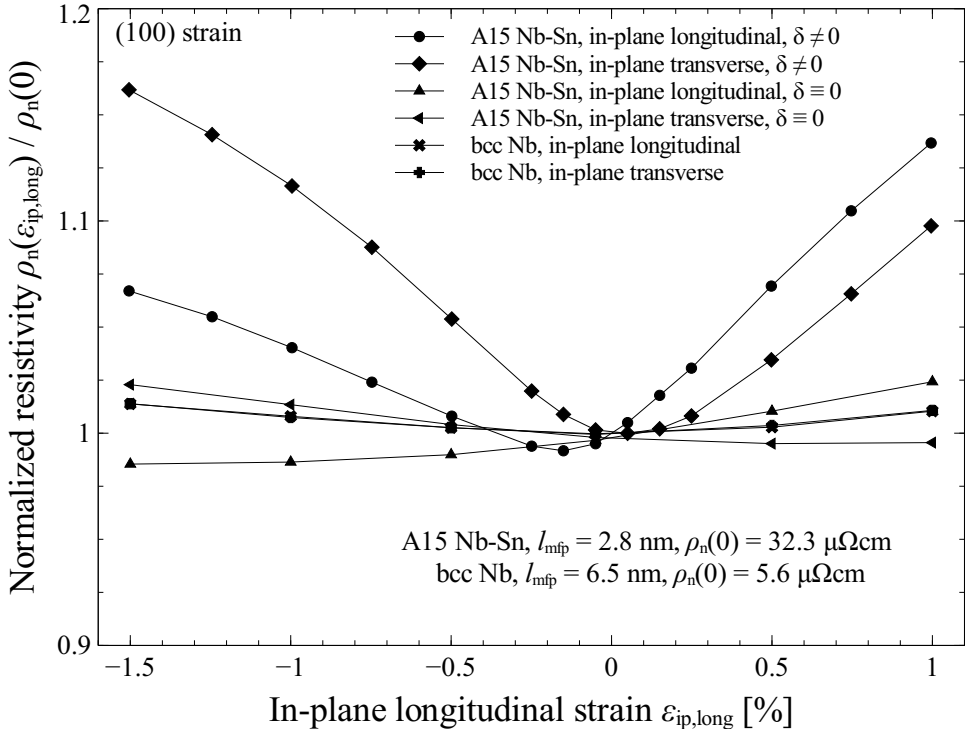

Figure 5.21: *Calculated normalized normal state resistivity as a function of* $\varepsilon_{ip,long}$.

the electronic properties of A15 Nb_3Sn and Nb_3Al is large in comparison to bcc Nb and NbTi, which can be ascribed to the absence of sublattice distortion in bcc Nb and NbTi.

5.4.4 Effect of sublattice distortion on the normal state resistivity

The calculated results indicate that the normal state resistivity, like the strain dependent superconducting properties, is affected by strain (figure 5.9).

As shown in figure 5.21, the suppression of sublattice distortion (i.e. $\delta \equiv 0$) results in a dramatic reduction in the strain sensitivity of the normal state resistivity. Furthermore, it is shown that the magnitude of the strain sensitivity of ρ_n of bcc Nb is even smaller than both Nb_3Sn cases, and that the anisotropy of the normal state resistivity is close to negligible, a result that is consistent with experimental observations (2.20). A more detailed comparison is presented in the next section.

5.4.5 Conclusion

The contribution of strain induced changes in the electronic and vibrational properties to the strain sensitivity of the normal state resistivity and the superconducting properties is discussed.

It is argued that any experimental observation of strain sensitivity in the normal state resistivity is almost entirely a result of changes in the electronic properties, because the residual resistivity dominates the low temperature resistivity in the normal state resistivity regime in which the model is applicable.

Moreover, it is argued that both changes in the electronic and the vibrational properties contribute to strain sensitivity in the superconducting properties, but that in slightly disordered Nb_3Sn, strain sensitivity is mainly a result of changes in the electronic properties.

A number of investigations reported in literature are discussed. While a number of investigations are consistent with the conclusions that are presented here, other investigations attribute the strain sensitivity of the superconducting properties entirely to the effect of strain on the vibrational properties of the crystal, after assuming that strain does not affect the electronic properties. The experimental observation that the normal state resistivity changes as a function of strain (figure 2.19) invalidates this assumption, as the vibrational properties of the crystal does not affect the residual resistivity.

The calculations indicate that the changes in the electronic properties are primarily a result of sublattice distortion. If sublattice distortion is suppressed, then the strain sensitivity of the electronic properties is dramatically reduced. Moreover, the calculation indicates that the strain sensitivity of the electron densities of states of bcc Nb and NbTi are only weakly affected by strain, which implies that strain affects the superconducting properties to a much smaller degree than in A15 Nb_3Sn. The calculation show that the strain sensitivity of Nb_3Al, another A15 material, is significantly larger than bcc Nb and NbTi, but smaller than Nb_3Sn, which is consistent with experimental evidence. The strain sensitivity of the normal state resistivities of Nb_3Sn and Nb is calculated, and the result indicates that unlike Nb_3Sn, the strain sensitivity of the normal state resistivity of Nb is close to negligible.

5.5 Comparison of calculated and experimentally observed strain sensitivity of A15 Nb-Sn and bcc Nb

5.5.1 Introduction

In section 5.4, the relation between sublattice distortion and the superconducting and normal state properties was discussed. Calculations were performed in the regime where the crystal is preferentially cubic, i.e. where the normal state resistivity exceeds 27 $\mu\Omega$cm.

A very important result is that application of strain on A15 Nb-Sn causes displacement of the niobium ions within the crystal, which is referred to as sublattice distortion. This phenomenon is identical to the sublattice distortion resulting from the martensitic transformation. The analyses, which apply to the preferentially cubic regime, show the following:

- Due to sublattice distortion in A15 Nb-Sn, the normal state resistivity at 0 K is affected by strain in an anisotropic manner. Conversely, in bcc Nb where sublattice distortion does not occur, the calculations indicate that the change in normal state resistivity is close to negligible.
- The effect of strain on the normal state resistivity at 0 K of A15 Nb-Sn is disorder dependent: at a higher normal state resistivity, both the magnitude of the strain sensitivity and the degree of anisotropy are lower.

- Like the normal state resistivity, the strain sensitivity of the superconducting properties T_c and $\mu_0 H_{c2}(0)$ of Nb-Sn is a direct result of sublattice distortion. Therefore, in bcc niobium where sublattice distortion does not occur, the magnitude of the strain sensitivity of the superconducting properties is much lower in comparison to A15 Nb-Sn.
- The degree of strain sensitivity of the superconducting properties of A15 Nb-Sn is related to the degree of disorder: in samples with more disorder and thus a higher normal state resistivity, the strain sensitivity of the superconducting properties is less severe.
- The strain sensitivity of the superconducting properties is larger when strain is applied along the (100) direction in comparison to the (110) direction.

As presented in sections 2.4.6 and 2.4.9, the superconducting properties and the normal state resistivity of Nb-Sn and Nb thin films were determined, so that the accuracy of the calculation can be validated with experimental data. In addition, measurements of commercial high J_c Nb-Sn conductors are included.

5.5.2 Normal state resistivity of Nb-Sn and Nb thin films

It was experimentally (section 2.4.6) and computationally (section 5.3.4) demonstrated that strain affects the normal state resistivity in an anisotropic manner. Here, a comparison between the experimental and computational results is given.

$\rho_n(\varepsilon)$ curves are generated by finding the optimal value of l_{mfp} at which the calculated normal state resistivity matches the measured normal state resistivity at 0%. In other words, a single free parameter l_{mfp} is used per unique sample that determines both the magnitude and the strain dependence of the normal state resistivity. The experimental observations indicate that the strain state of the Nb-Sn is $0.07 \pm 0.04\%$ after cool down (subsection 2.4.2), and in the comparison between the calculated results and the experimental observations, this slight offset is added to the experimental curve.

Figures 5.22 and 5.23 show the measured and calculated normal state resistivities in the in-plane longitudinal and transverse directions at various normal state resistivities between 32 and 92 $\mu\Omega$cm. Consistent with the calculated result, the experimental observations indicate that the degree of strain sensitivity of the normal state resistivity in the experimental strain range decreases with increasing normal state resistivity within the experimentally investigated strain regime. Of particular interest is figure 5.23, because it validates the result that the normal state resistivity of non-hydrostatically strained Nb-Sn is anisotropic: the application of compressive strain along the in-plane longitudinal direction lowers the normal state resistivity in the in-plane longitudinal direction and raises the normal state resistivity in the in-plane transverse direction.

The largest deviation between the calculated and measured normal state resistivities is observed at ρ_n = 33 $\mu\Omega$cm. This deviation is likely due to the slightly different composition of this particular sample. While all other samples only contain Nb-Sn in which the cubic phase is stable, this particular sample also contains a small fraction of preferentially tetragonal Nb_3Sn, as is evidenced by the onset of superconducting behavior at 17.7 K. As

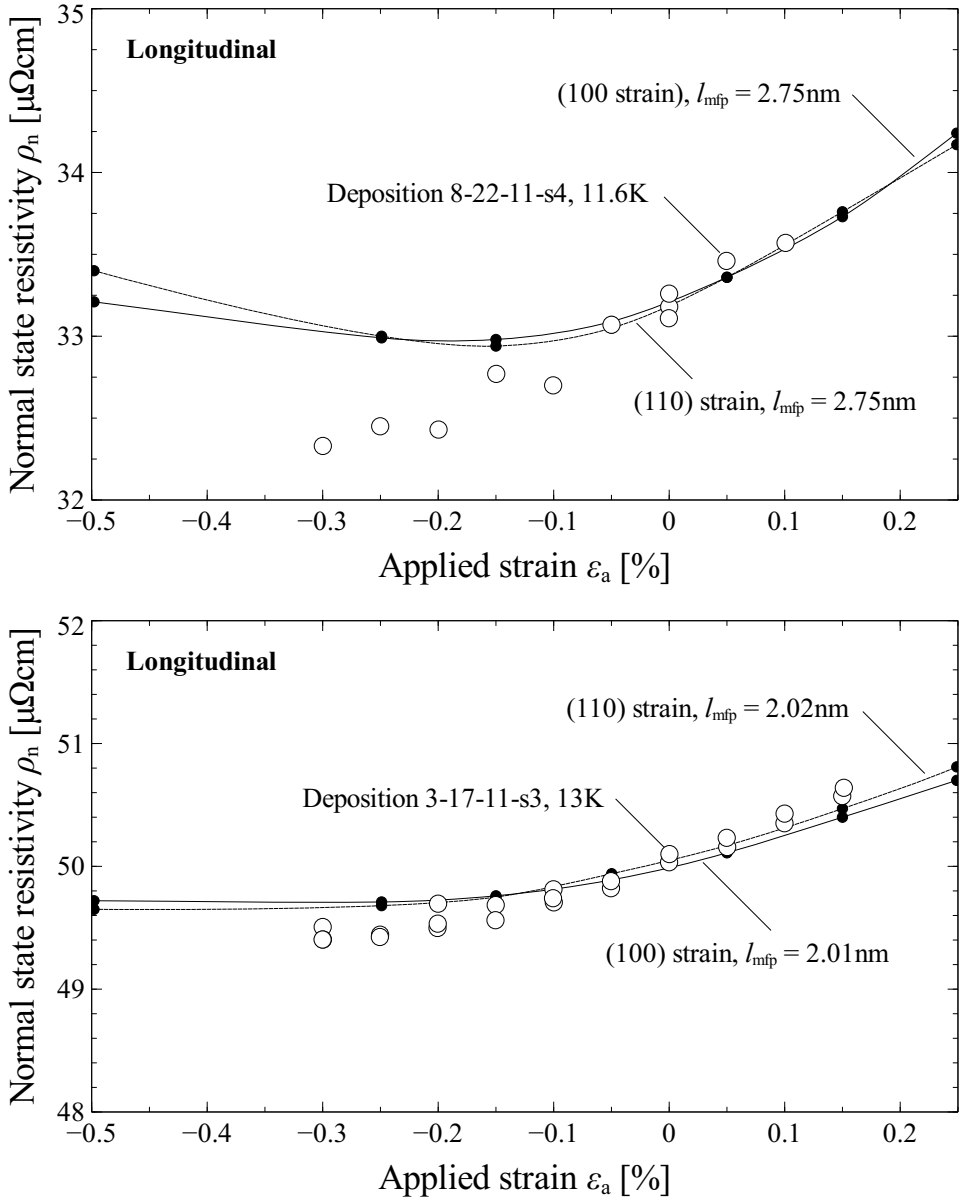

Figure 5.22: *Comparison of experimentally observed and calculated normal state resistivities as a function of applied strain along the longitudinal direction, at ρ_n = 33 (top) and 50 μΩcm (bottom). In the calculations, both (100) and (110) strain are considered.*

the model only accounts for Nb-Sn in which the cubic phase is stable, the presence of this small deviation is not surprising.

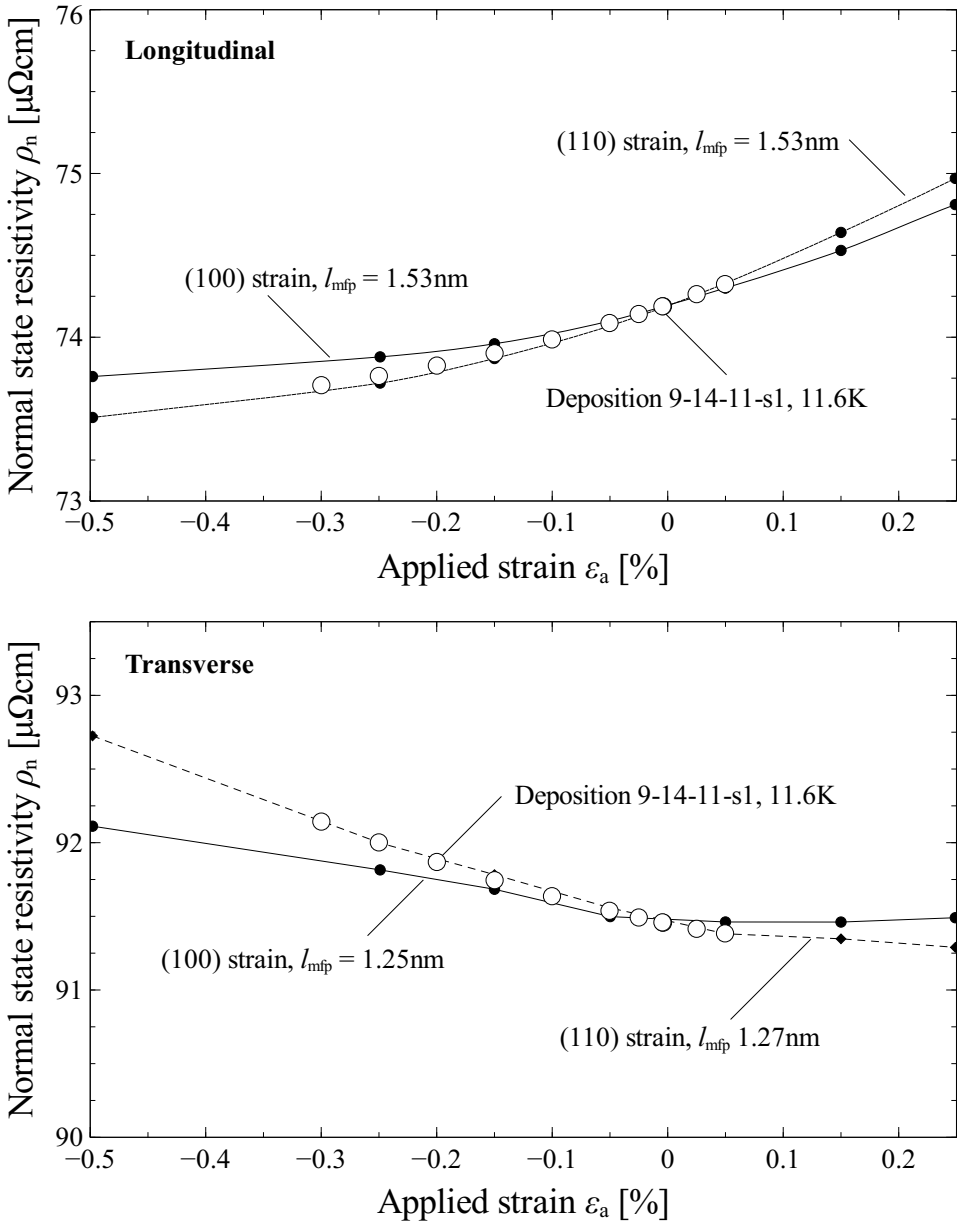

Figure 5.23: *Comparison of experimentally observed and calculated normal state resistivities as a function of applied strain along the in-plane longitudinal (top) and transverse (bottom) directions, at ρ_n = 74 (top) and 91 μΩcm (bottom). Both (100) and (110) strain are considered in the calculations.*

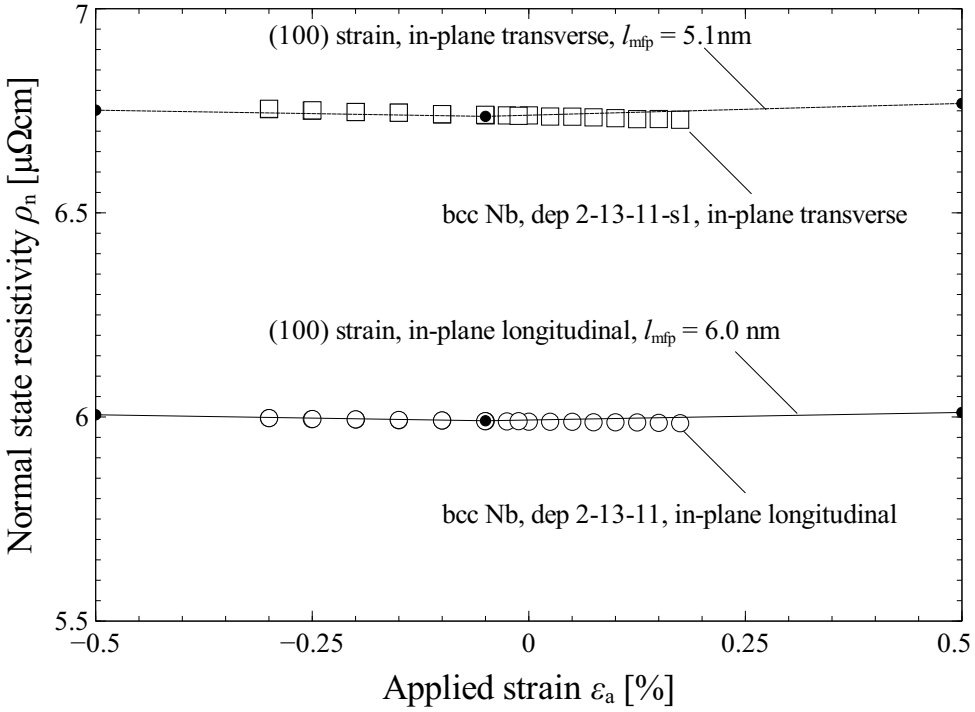

Figure 5.24: *Calculated and measured normal state resistivities of bcc Nb as a function of in-plane longitudinal strain.*

Figure 5.24 shows the calculated and measured normal state resistivities of bcc Nb. It should be noted that the calculation is a somewhat poor approximation of the Nb thin film, as the calculations assume that strain is applied along the (100) direction of the crystal, while the in-plane orientation of the bcc niobium thin film is strictly speaking unknown. Moreover, the dominant (110) out-of-plane crystal orientation indicates that other in-plane orientations are present in this film. The effect of (100) strain was calculated as this allows for a clear comparison with Nb_3Sn (figure 5.21). Even though this calculation is less representative for the bcc niobium thin film than it is for the Nb_3Sn thin films, the calculation result is correct: the application of strain on the longitudinal and transverse normal state resistivities is close to negligible.

Figure 5.25 provides an overview of the experimental data and the calculated results of the normal state resistivity. As discussed in section 2.4.6, the average strain dependence of ρ_n was determined at various temperatures and from this the average slope $\rho_n^{-1}\delta\rho_n/\delta\varepsilon_{ip,long}$ and the extrapolated $\rho_0^{-1}\delta\rho_0/\delta\varepsilon_{ip,long}$ were determined. $\rho_n(\varepsilon)$ was also calculated within a strain range of $\varepsilon_{ip,long} = -0.25$ to 0.25% and the slope was extracted. This strain range is representative of the experimentally observed strain range, after accounting for an additional small thermal pre-strain term after cool down (section 2.4.2).

The calculated slope of A15 Nb-Sn was determined over a wide resistivity range, for two dif-

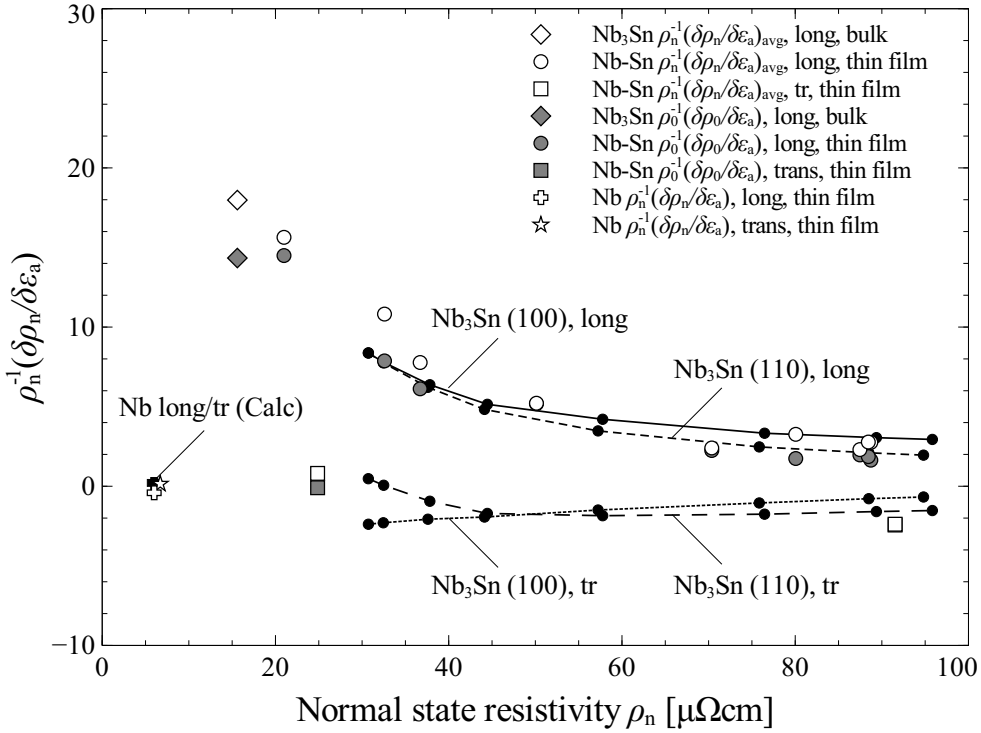

Figure 5.25: *Calculated and measured $\rho_n^{-1}\delta\rho_n/\delta\varepsilon_{ip,long}$ as a function of ρ_n of A15 Nb-Sn and bcc Nb, where ρ_n is measured and calculated parallel ('long') and perpendicular ('tr') to the longitudinal strain direction. The measurements are indicated with the open and grey symbols, while the calculated results are indicated with the lines and the black symbols.*

ferent crystal orientations and for the in-plane longitudinal and transverse directions, leading to four distinct lines. In the case of bcc niobium, however, only one crystal orientation was determined in a narrow resistivity range close to 6 $\mu\Omega$cm and the degree of strain sensitivity of the normal state resistivity in the longitudinal and transverse directions overlaps, so that the calculated result is a single point rather than a line in this case.

It is evident from figure 5.25 that the consistency between the calculated and measured strain dependence of the normal state resistivity of A15 Nb-Sn and bcc Nb is very good. This is a confirmation that the understanding of the underlying causes is correct: the application of strain strongly affects the electronic properties of A15 Nb-Sn and by extension the normal state resistivity, and only weakly affects the electronic properties and normal state resistivity of bcc niobium.

5.5.3 Superconducting properties of high-J_c Nb_3Sn conductors

A particular problem with the Nb-Sn thin films which were deposited on the R-plane sapphire substrate is that the accessible strain range is limited by the strain tolerance of the

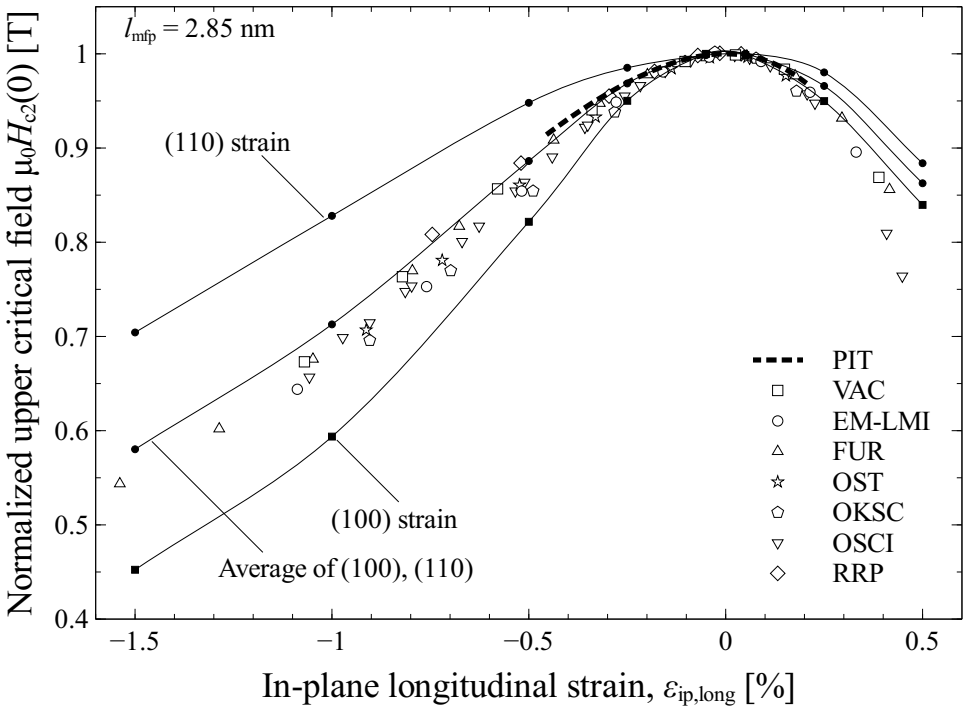

Figure 5.26: *Normalized $\mu_0 H_{c2}(0)$ as a function of strain. The experimental measurements are after Lu et al. [90, 209].*

substrate. This means that while this research was done partly for better understanding the strain behavior of Nb_3Sn conductors, the accessible strain range of the thin films is significantly smaller than that used in experiments on the Nb_3Sn wires.

An issue with high-J_c conductors is that a thorough understanding of the mechanical properties is complicated by the geometrical and compositional inhomogeneity. The conductors comprise Nb-Sn with various tin concentrations as well as voids, a copper and/or copper bronze matrix, and additional metals such as pure niobium, tantalum and titanium. Finally, the strands are twisted as well.

To understand the strain state of Nb_3Sn wires in cryogenic condition, a low temperature XRD investigation was performed by Muzzi *et al.* that allowed for the determination of the local longitudinal and transverse strains as a function of macroscopically applied tension. Two wire types were investigated: a high-J_c RRP internal-tin-type Nb_3Sn strand (OST-RRP, strand billet #8712) and an internal-tin strand (OST-I #7567). Both the longitudinal and transverse strains were determined by evaluating the lattice parameter as a function of applied strain. It was demonstrated that within the elastic regime, the externally applied strain is transferred to the local microstructure in a 1-to-1 ratio between the local longitudinal strain and the externally applied strain, while the ratio between the local transverse strain and the externally applied strain was shown to be 0.38. This observation implies that the

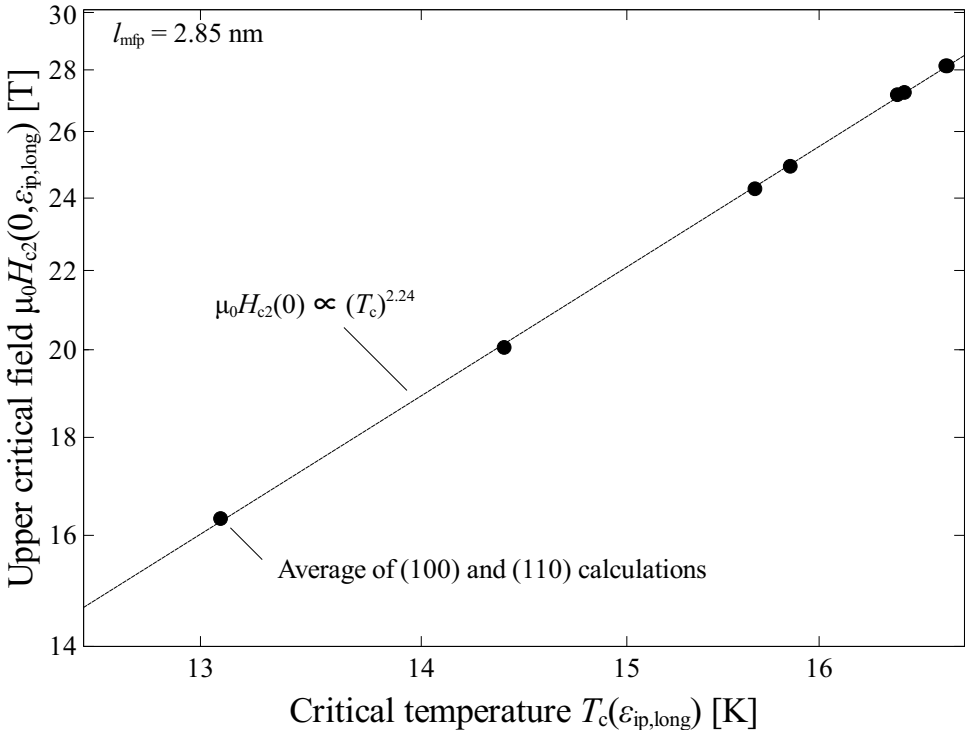

Figure 5.27: *Calculated $\mu_0 H_{c2}(\varepsilon_{ip,long})$ as a function of calculated $T_c(\varepsilon_{ip,long})$. The data points are connected with the power law approximation.*

(shallow) twist pitch of the filaments does not appreciable influence the strain state of the Nb_3Sn. Some thermal pre-strain was observed, but it was also shown that when some strain was applied to counteract the thermal pre-compression, the crystal state was cubic. Moreover, in this cubic strain state, the longitudinal and transverse lattice parameters of the two investigated un-jacketed wires are equal to 0.5277 and 0.5280 nm, very close to the strain free lattice parameter of 0.5280 nm as observed by Mailfert *et al.* above the martensitic transformation temperature of binary Nb_3Sn, which implies that the degree of hydrostatic strain is very small.

The strands investigated by Muzzi *et al.* [58] comprised a substantial amount of (100) oriented Nb_3Sn, but also other orientations such as (210), (211), (320), and (321) along the length of the wire. In contrast, it was shown by Scheuerlein *et al.* [206] that the grain orientation along the length of a powder-in-tube (PIT) conductor (B215) is preferentially (110) oriented. More recently, an investigation by Scheuerlein *et al.* [207] once again showed that the grain structures of two OST-RRP (billets #7419 and #11976) wires is mainly (100) aligned along the length of the wire, while the grain structure of a PIT wire (B215) is mainly (110) aligned.

In an analysis of the Nb-Sn composition spread in an SMI-PIT wire by Godeke [33], see figure 1.2, it was shown that the dominant composition in the fine-grain Nb_3Sn is between

23 and 24 at.% Sn. Similar work was published elsewhere by Lee *et al.* [208], which showed that the average tin content of the Nb-Sn of two RRP strands (RRP6445-2 and RRP6555) and a Modified Jelly Roll (MJR) strand (Ore110) after heat treatment is 24.0, 23.3 and 23.7 at.% Sn, respectively.

An extensive characterization of various Nb_3Sn conductors was performed which included measurements across a wide temperature range (2.35 K $\leq T \leq$ 14 K), magnetic field range (up to 28 T), and strain range (-1.6 to 0.45% strain) by Lu *et al.* [90, 209] and Taylor *et al.* [84]. The measurements were performed on a Walters spring made of Ti-6Al-4V, the same material as the sample holder on which the Nb-Sn thin films were measured. While the investigation by Muzzi *et al.* [58] showed a strong indication that the longitudinal strain is applied to the microstructure in a 1-to-1 ratio, it is not fully obvious that the transverse strain from the sample holder is transferred to the microstructure as well. In particular, the copper in the strands behaves plastically, which could relax the transverse stress state of the Nb_3Sn. However, the Poisson's ratio of the Nb_3Sn was determined as 0.38 [58], fairly close to the Poisson's ratio of the sample holder which of 0.342 [79], which means that even if the transverse strain is not fully transferred to the Nb_3Sn, the Nb_3Sn naturally assumes a transverse strain that is very close to the externally applied transverse strain.

In a recent publication on the parameterization of 112 different Nb_3Sn wires by Godeke *et al.* [210], it was determined that the typical T_c and $\mu_0 H_{c2}(0)$ of Nb_3Sn conductors is 16.7 K and 28.5 T respectively. As model input, the mean free path l_{mfp} is set to 2.85 nm, resulting in a critical temperature of 16.7 K and an upper critical field of 28.1 T. The calculated results also indicate that the normal state resistivity at this particular mean free path is 31.4 $\mu\Omega$cm. The equivalent tin concentration in binary Nb-Sn is 23.75$\pm$0.25 at.% Sn according to Godeke *et al.* [41], where an uncertainty of 5 $\mu\Omega$cm is assumed in the normal state resistivity.

The strain sensitivity of T_c and $\mu_0 H_{c2}(0)$ in the case of (100) and (110) strain is calculated using no additional free parameter besides l_{mfp} and compared to the experimentally observed strain dependence in $\mu_0 H_{c2}(0)$ of Nb_3Sn wires [90, 209] (figure 5.26). In the case of PIT strands, a parameterization was published by Lu *et al.* [209] in which $\mu_0 H_{c2}(0)$ is determined through extrapolation from lower magnetic field data, in contrast with the high field measurements of various other strands by Lu *et al.* [90], which is why the strain dependence of $\mu_0 H_{c2}(0)$ of the PIT strand is indicated with dashed lines. It is clear that the magnitude of the calculated strain sensitivity is consistent with the experimentally observed strain sensitivity in $\mu_0 H_{c2}(0)$, and that various features in the calculated results are also present in the experimental observations, such as the parabolic behavior near $\varepsilon_{ip,long} = 0\%$ and the upturn at high compressive strain.

The calculation indicates a much larger strain sensitivity from (100) strain in comparison to (110) strain. Indeed, the PIT strands, which are known to be predominantly (110) oriented, are the least strain sensitive of all the wires, but the difference is subtle. No clear experimental evidence is found that the strain sensitivity of (100) oriented Nb_3Sn is significantly larger than (110) oriented Nb_3Sn, but the larger stress sensitivity of the (100) strain orientation was demonstrated by Pulver [211] in V_3Si, another A15 superconductor: in two samples with nearly the same T_c, the sensitivity of T_c to uni-axially applied pressure in the (100) oriented V_3Si sample was roughly twice as large as the (110) oriented sample. The much smaller variation in strain sensitivity in the Nb_3Sn wires (figure 5.26) could be related to the fact that none of the wires contain a single crystal orientation (although the prevalence of

particular crystal orientations varies between the wires), so that the strain sensitivity of the critical current density depends of details such as the distribution of the crystals with various alignment in the cross-section of the filaments, the homogeneity of the crystal alignment along the length of the wire, etcetera. Further investigation of this topic would be beneficial.

The relative degree of strain sensitivity in T_c and $\mu_0 H_{c2}(0)$ is typically described using a power law, with:

$$\mu_0 H_{c2}(0,\varepsilon) \propto T_c(\varepsilon)^{\omega}, \tag{5.27}$$

where w is a free parameter with a value that is between 2 and 3 (figure 3.11) depending on the degree of disorder. This description is applied to the calculated T_c and $\mu_0 H_{c2}(0)$. Indeed, equation 5.27 is highly consistent with the calculated results, and the optimal value of w is determined to be equal to 2.24 (figure 5.27). This value is consistent with experimental observations in section 2.4.9, where it was shown that in a binary Nb-Sn thin film with a T_c of 16.4 K, the optimal value of w is 2.3±0.3. It was also shown by Taylor *et al.* [84] that the optimal value of w as determined from resistivity measurements of various Nb_3Sn conductors is 1.9±0.3 and 2.5±0.3 for a Bronze route and a modified jelly-roll (MJR) wire, respectively, while 2.2±0.1, 2.6±0.1, and 2.0±0.5 were found through scaling of J_c from a Bronze route, MJR and an Internal-tin wire respectively. According to Lu *et al.* [90], the optimal value for a group of 7 different Nb_3Sn wires is w = 2.2. However, these results are not consistent with analysis by Ekin [89], who argued that the optimal value of w is 3.0±0.1. It is clear from figure 3.11 that both Lu and Ekin might be right, but their results hold in different regimes: the optimal value of w is below 2.5 for $T_c < 17$ K, i.e. the regime where the crystal structure is preferentially cubic and close to 3 for $T_c > 17.5$ K, i.e. the regime where the crystal structure is preferentially tetragonal.

5.5.4 Superconducting properties of A15 Nb-Sn and bcc Nb thin films

The critical temperature and upper critical field of various samples were experimentally determined as a function of applied strain through resistivity measurements (section 2.4.9) and critical current density measurements (section 3.7.3). The samples include Nb-Sn bulk samples and thin films, as well as bcc Nb thin films.

A key result of the model calculations presented in this chapter is that the strain sensitivity of the superconducting properties of Nb-Sn is a direct result of the sublattice distortion that occurs in the material when it is strained. As this phenomenon does not occur in bcc Nb, it is expected that the strain sensitivity of the superconducting properties of A15 Nb-Sn is significantly higher than that of bcc Nb. The experimental observations indeed confirm this hypothesis. Figure 5.28 shows a comparison between the normalized critical temperature and upper critical field of a bcc Nb thin film and an A15 Nb-Sn thin film. The application of 0.3% compressive uni-axial strain increases T_c and $\mu_0 H_{c2}(0)$ by less than 0.5% in the case of bcc niobium, and decreases T_c and $\mu_0 H_{c2}(0)$ by 2.5% and 6.7% in the case of Nb_3Sn respectively.

Figure 5.29 shows a comparison of the calculated and experimentally observed T_c and $\mu_0 H_{c2}(0)$ as a function of strain, where the average of (100) and (110) strain is taken. The strain dependence of T_c and $\mu_0 H_{c2}(0)$ was calculated at various l_{mfp}, while the measurements were performed on binary Nb-Sn with various composition. It is clear that the

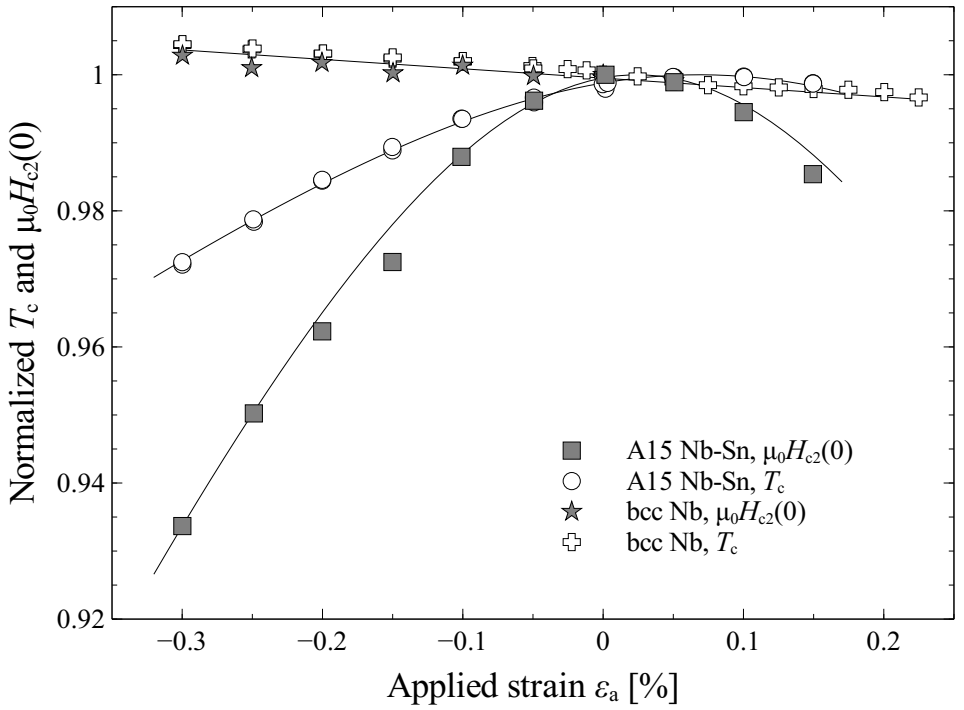

Figure 5.28: *Experimentally observed strain sensitivity in T_c and $\mu_0 H_{c2}(0)$ of a bcc Nb thin film (dep 2-12-13) and a Nb-Sn thin film (dep 3-17-11, strip 3). At ε_a = 0%, the T_c and $\mu_0 H_{c2}(0)$ of the Nb thin film are 9.27 K and 2.6 T respectively. The maximum T_c and $\mu_0 H_{c2}(0)$ of the Nb-Sn thin film are 15.8 K and 27.9 T. The grey symbols represent $\mu_0 H_{c2}(0)$ measurements and the open symbols represent T_c measurements. The lines are guides to the eye.*

measurement on deposition 3-17-11, strip 3 is quantitatively consistent with the calculated results, both in terms of T_c and $\mu_0 H_{c2}(0)$. Furthermore, consistent with the calculation, the experimentally observed strain sensitivity decreases with decreasing T_c and $\mu_0 H_{c2}(0)$ values. However, the experimentally observed strain sensitivity of the other depositions with lower critical temperatures and upper critical fields is of larger magnitude than the calculated results.

The deviatoric strain description, used for parameterizing experimental data (section 2.4.9), is once again used to parameterize the calculated results, and the deviatoric strain model parameters from experimental data and calculation results are then compared to each another (figure 5.30). It is clear that while the magnitude of the calculated strain sensitivity is consistent with experimental observations near stoichiometry (at a T_c of about 17 K and a $\mu_0 H_{c2}(0)$ of about 28 T), the calculated strain sensitivities of T_c and $\mu_0 H_{c2}$ are of lower magnitude in the off-stoichiometric limit (at a T_c of about 12 K and a $\mu_0 H_{c2}(0)$ of about 16 T). This discrepancy will be discussed further in section 5.6.

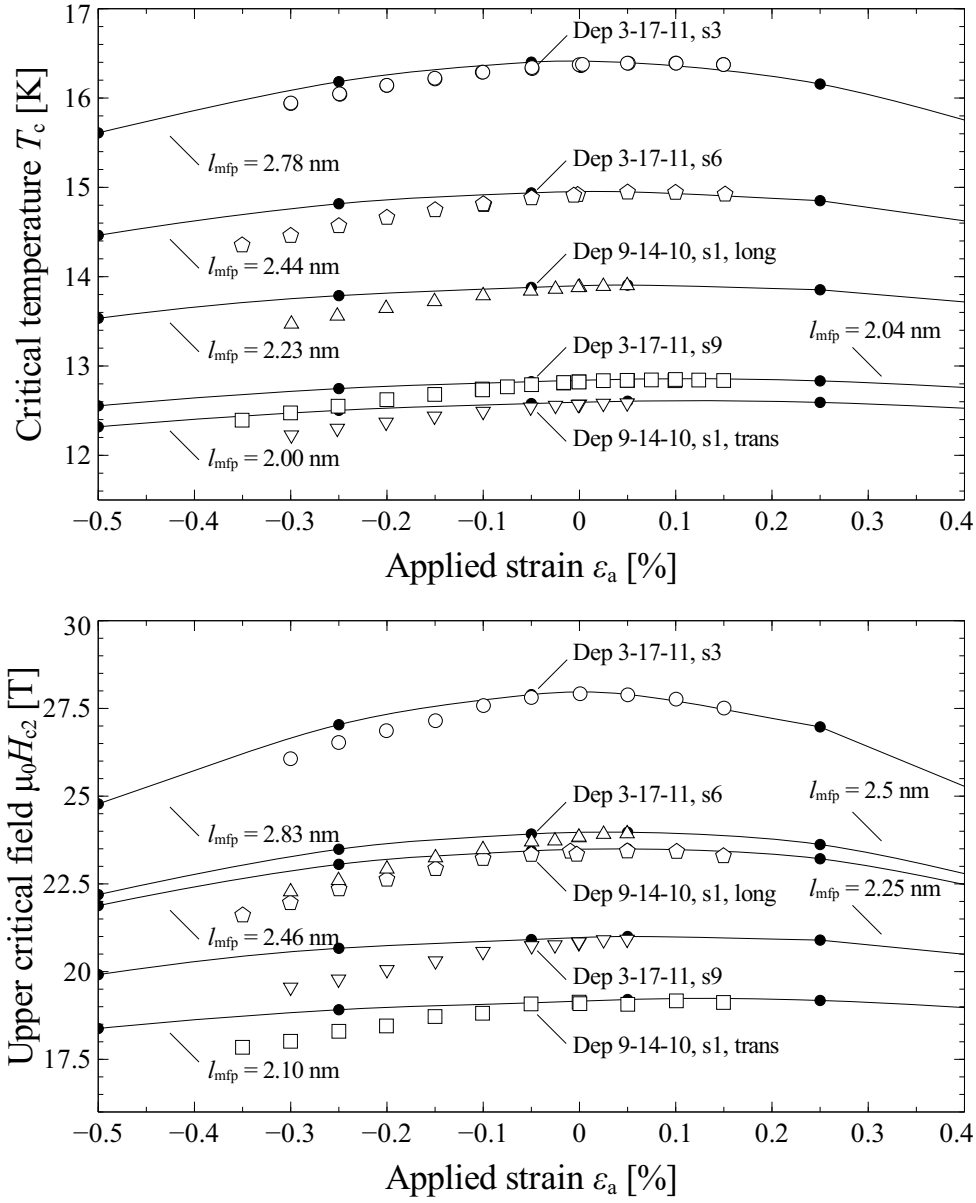

Figure 5.29: *T_c (top) and $\mu_0 H_{c2}(0)$ (bottom) as a function of strain. Comparison of experimentally determined (open markers) and calculated (black markers) results.*

The model was used to calculate the properties of the preferentially cubic regime, but not the preferentially tetragonal regime. A particular problem with preferentially tetragonal Nb_3Sn is that the manner in which externally applied strain is transferred to the microstructure is

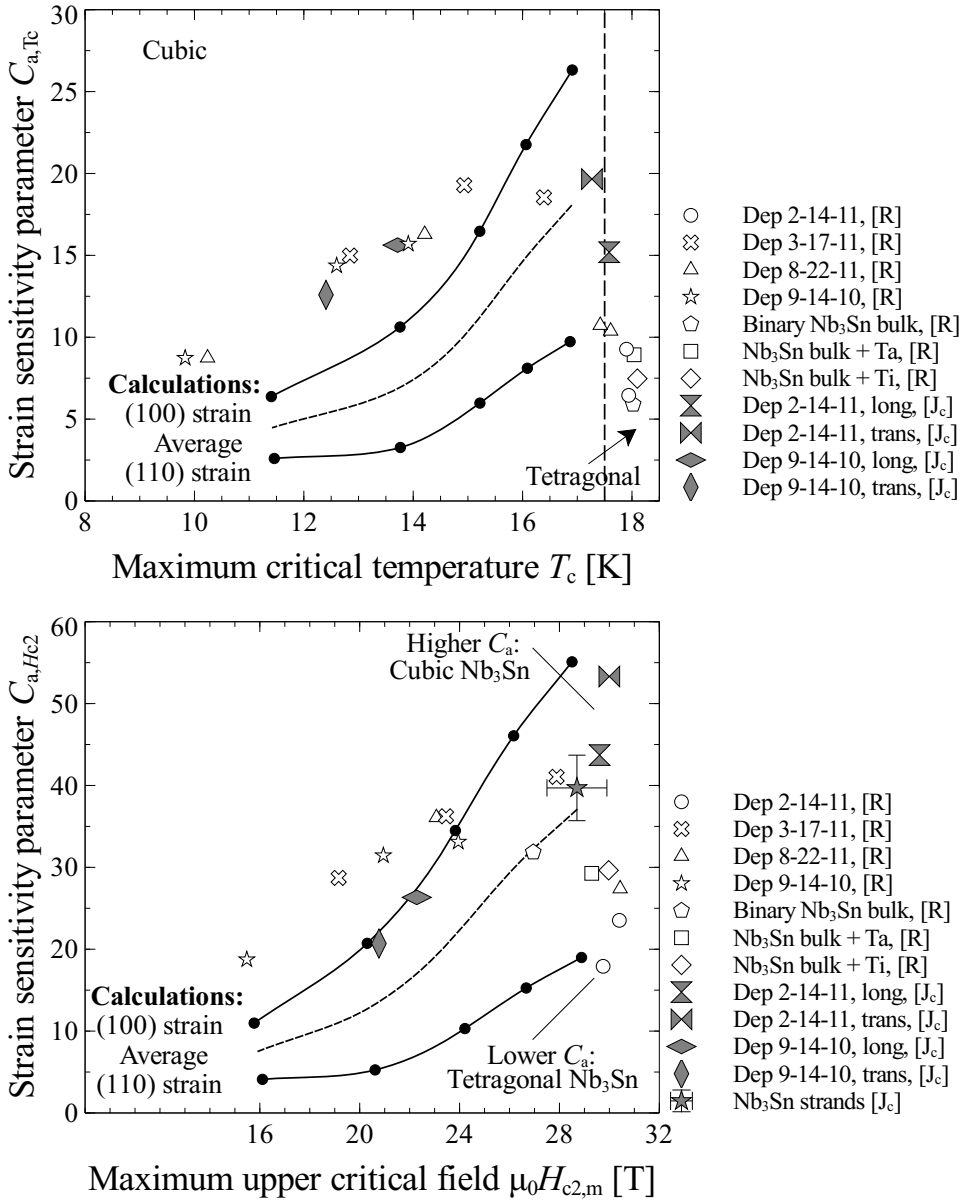

Figure 5.30: *Strain sensitivity parameters $C_{a,Tc}$ as a function of T_c (top) and $C_{a,Hc2}$ as a function of $\mu_0 H_{c2}(0)$ (bottom), determined from deviatoric strain parameterization of experimental and calculated results. The dotted line indicates the onset of the tetragonal transformation.*

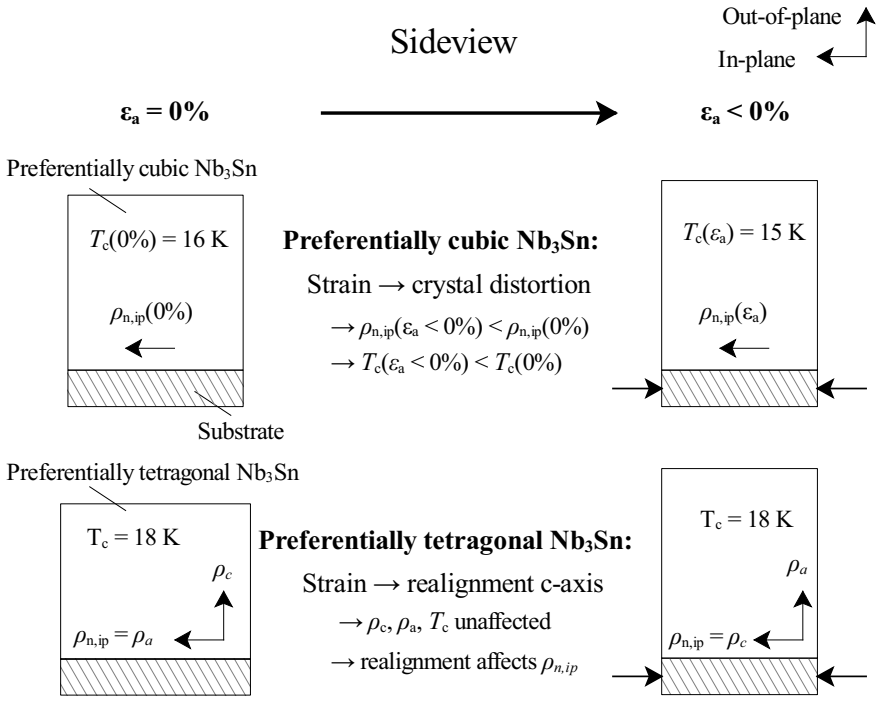

Figure 5.31: *Schematic representation of the effect of strain on preferentially cubic and preferentially tetragonal Nb_3Sn.*

very different from preferentially cubic Nb_3Sn. To paraphrase Testardi [201]: 'An applied stress may first cause (in part) domain rotation which can lead to 'macroscopic' sample strains but little or no microscopic strains'.

The martensitic transformation results in a local change in strain state, while the macroscopic strain state remains fixed, because the Nb_3Sn is fixed to a substrate. The result of these boundary conditions is a tweed pattern: the Nb_3Sn is organized in regions in which the (shorter) c-axis of the tetragonally distorted Nb_3Sn is aligned along different directions. Thus, a tweed pattern is formed, a phenomenon that is discussed by Kartha *et al.* [145].

Testardi's insight is that the manner in which strain affects preferentially cubic and tetragonal Nb_3Sn is very different: applying macroscopic strain to preferentially cubic Nb_3Sn results in a distortion of the crystal which in turn affects the microscopic properties of the material, such as T_c (figure 5.29, top), $\mu_0 H_{c2}(0)$ (figure 5.29, bottom), and $\rho_{n,ip,long}$ (figures 5.22 and 5.23). However, applying macroscopic strain to a preferentially tetragonal Nb_3Sn can result in a change in the tweed pattern rather than a distortion of the crystal. The implications of this can be illustrated with a simple two-dimensional model (figure 5.31). Applying in-plane compressive strain to a region of preferentially tetragonal Nb_3Sn in which the *c*-axis is aligned out-of-plane results in a reorientation of the *c*-axis from out-of-plane to in-plane (figure 5.31, bottom).

In this manner, the externally applied strain results in a realignment rather than a deformation of the Nb_3Sn microstructure. As the microstructure is not deformed, the microscopic properties (T_c, $\mu_0 H_{c2}(0)$, ρ_n along the *a*-axis and the *c*-axis) are not affected. However, in a resistivity measurement the current which initially flowed along the *a*-axis now flows along the *c*-axis. In a tetragonal crystal the resistivity along the *c*-axis is lower than along the *a*-axis (figure 5.9, where the *c*-axis corresponds to the longitudinal direction, and the *a*-axis corresponds to the transverse direction). Thus, the application of strain results in a reduction in the normal state resistivity measured along the in-plane direction due to the realignment of the *c*-axis in the tetragonally distorted Nb_3Sn (figure 5.31), but not a reduction in T_c and $\mu_0 H_{c2}(0)$.

This is consistent with experimental observations: the change in normal state resistivity of low-resistivity (i.e. $\rho_n < 27\ \mu\Omega$cm) and thus preferentially tetragonal (section 4.4.5) Nb_3Sn is large (figure 5.9) relative to the preferentially cubic Nb-Sn, while the strain sensitivity of T_c and $\mu_0 H_{c2}(0)$ of the preferentially tetragonal Nb_3Sn is small relative to the preferentially cubic Nb_3Sn (figure 5.30).

5.6 Discussion

A discrepancy between the calculated results and the experimental observations is the magnitude of strain sensitivity in T_c and $\mu_0 H_{c2}(0)$ in strongly disordered Nb_3Sn compared to the larger experimentally observed strain sensitivity in T_c and $\mu_0 H_{c2}(0)$ in off-stoichiometric Nb-Sn. There are four possible explanations for the discrepancy:

5.6.1 Disorder versus off-stoichiometry

The most likely explanation is that excess niobium affects the microscopic properties of Nb-Sn in a manner that is not captured by the model, and results in the observed discrepancy. This explanation is deemed the most likely because the evaluation of supercell configurations (see 4.3.3) indicates that excess niobium ions not only lower $N(E_F)$ by acting as scattering centers, but also affect the band structure directly, resulting in an additional reduction in $N(E_F)$.

As both T_c and $\mu_0 H_{c2}(0)$ are strongly dependent on $N(E_F)$, one can hypothesize that the presence of excess niobium results in an additional reduction in T_c and $\mu_0 H_{c2}(0)$, without reducing the strain sensitivity in T_c and $\mu_0 H_{c2}(0)$, which would explain the observed discrepancy. This would further imply that while disorder (as measured by ρ_n) uniquely determines T_c and $\mu_0 H_{c2}(0)$, regardless of whether the material is stoichiometric or off-stoichiometric, disorder does not uniquely determine the degree of strain sensitivity in T_c and $\mu_0 H_{c2}(0)$.

In principle, the model could be improved by evaluating the effect of strain on supercells (containing excess niobium) rather than single unit cells, and the approach that is presented in this chapter could be used as a recipe to do exactly that. However, the computational cost of this approach would far exceed the computational cost of a single unit cell approach, which is why the calculation of the effects of strain on supercells was not attempted.

Conversely, one could evaluate the effect of strain on stoichiometric Nb_3Sn in which disorder is introduced. There are a number of methods by which this can be done. For instance,

low temperature depositions of stoichiometric Nb_3Sn can be performed to achieve anti-site disorder (see Orlando *et al.* [42]), or stoichiometric Nb_3Sn thin films could be irradiated (see Ghosh *et al.* [146]). If the discrepancy is a result of the presence of excess niobium, then the strain sensitivity of these disordered Nb_3Sn samples would be much closer to the calculated result.

5.6.2 Inaccuracy in the $\alpha^2(\omega)$ expression

A second option is that the empirical description that relates α^2F to the phonon density of states breaks down in the off-stoichiometric limit. This is also a verifiable hypothesis. It is in principle possible to calculate α^2F entirely from first principles, although this comes with a number of limitations (section 4.6). Alternatively, one could attempt to strain an off-stoichiometric tunnel junction and directly determine the strain dependent α^2F using a method that was previously used by Rudman *et al.* [168]. As part of this research, such an investigation was attempted by Dollekamp [192]. However, the fabricated tunnel junctions were of insufficient quality to determine the strain dependent Eliashberg spectrum.

One might wonder if the three global constants μ^*, $\alpha^2_{\mathrm{IM,eff}}$, and ω_0 should truly be considered independent of strain. However, there are compelling reasons for why this approach is justified. First of all, the composition dependence of μ^* was investigated by Rudman *et al.* [168] (figure 4.15) and it was established that within the experimental uncertainty μ^* is constant over the entire investigated composition range. Low-resistivity Nb_3Sn is preferentially tetragonal while high-resistivity Nb_3Sn is preferentially cubic (figure 4.5). In spite of this crystal distortion, μ^* is found to be the same in the preferentially cubic and tetragonal regimes within the experimental uncertainty (figure 4.15), which implies that the strain sensitivity of μ^* is minimal. Moreover, the electron-phonon coupling constant λ is significantly larger than μ^*, which indicates that the influence of any strain dependence in μ^* on the superconducting properties is marginal.

Parameter ω_0 is introduced to take into account the relatively large contribution of the intermediate frequency range to the superconducting properties relative to the low and high frequency range in the phonon density of states (section 4.6.2, also see Schweiss *et al.* [158]). As strain affects the phonon density of states, it is not implausible that might also be ω_0 affected. However, the strain sensitivity of slightly off-stoichiometric Nb_3Sn (the most technologically relevant composition) is predominantly related to the strain dependence of the electronic properties (section 5.4.2), which implies that the contribution of any strain dependence in ω_0 to the overall strain sensitivity is minimal.

Finally, the parameter $\alpha^2_{\mathrm{IM,eff}}$ is related to the effective ion mass M and the mean squared electronic matrix element $\langle I^2 \rangle$. It is demonstrated in chapter 4 that treating this parameter as a disorder-independent constant results in a calculation result that is closely consistent with experimental observations in terms of the disorder dependence of λ, T_c and $\mu_0 H_{c2}(0)$ (figures 4.14, 4.17, and 4.19), even though both the electronic and the vibrational properties change as a function of disorder. As $\alpha^2_{\mathrm{IM,eff}}$ is not affected by the changes in the electronic and vibrational properties due to the introduction of disorder, it seems reasonable to assume that it is also not affected by changes in these properties due to strain. A second argument is that, especially in slightly off-stoichiometric Nb_3Sn, the degree of strain sensitivity in T_c and $\mu_0 H_{c2}(0)$ is qualitatively consistent and with experimental results and of the right order of magnitude, which implies that the relevant physics is captured when $\alpha^2_{\mathrm{IM,eff}}$ is taken as a

global constant.

5.6.3 Mechanical inhomogeneity due to compositional inhomogeneity

A third option is that strain inhomogeneity enhances the observed strain sensitivity in the samples: resistivity measurements probe the fraction with the highest T_c and $\mu_0 H_{c2}$ in the sample, rather than the average of the sample. If the mechanical properties vary between compositions, and the resistivity measurement only probes the properties of a particular composition, then it is possible that the strain state of the probed composition is enhanced, leading to a larger observed strain sensitivity. This problem would mainly affect the off-stoichiometric samples since the nearly-stoichiometric samples are more homogeneous (section 2.4.7). However, this argument would also imply that the degree of strain sensitivity varies with the degree of inhomogeneity, which is not observed in the experiment. In spite of being more inhomogeneous (figure 2.21, top), the observed strain sensitivity of deposition 3-17-11 is closely consistent with that of depositions 8-22-11 and 9-14-10 (figure 2.24, top), which implies that the observed discrepancy in the calculated and experimentally observed strain sensitivity cannot be attributed to mechanical inhomogeneity.

5.6.4 Averaging of the contributions of (100) and (110) strain

A fourth explanation is that the discrepancy is related to an averaging issue: it is assumed that the strain sensitivity of the Nb-Sn thin films is the average of the calculated results of (100) and (110) strain. If (100) dominates the strain dependence of T_c and $\mu_0 H_{c2}(0)$, then the observed strain sensitivity is enhanced relative to the average of (100) and (110) strain. Even if (100) strain entirely dominates the strain dependence, this still would not fully explain the difference between the calculated results and the experimental observations (figure 5.30). Therefore, this argument does not explain the observed discrepancy.

5.7 Conclusion

The model presented and validated in chapter 4 was used to determine the effect of strain and disorder on the normal state resistivity ρ_n, the critical temperature T_c, and the upper critical field $\mu_0 H_{c2}(0)$ of preferentially cubic Nb_3Sn at 0 K.

Using the strain boundary conditions of the U-spring test rig, and the crystal alignment of the Nb-Sn thin films as input for the model, various structural, electronic, and vibrational properties, as well as T_c, $\mu_0 H_{c2}(0)$, and the direction dependent ρ_n were calculated as a function of applied strain and disorder. The calculations indicate that, as in the phenomenon that occurs during the martensitic transformation, the application of strain results in a rearrangement of the niobium ions inside the crystal, which is known as sublattice distortion. An implication of this effect is that strain affects the normal state resistivity in an anisotropic manner.

Sublattice distortion affects both the electronic and the vibrational properties of the crystal, in a manner that is detrimental to superconductivity. In slightly disordered Nb_3Sn with a mean free path of 2.8 nm, approximately 80% of the strain sensitivity of T_c and $\mu_0 H_{c2}(0)$ can be explained in terms of changes in the electronic properties of the crystal, while the remaining part is caused by changes in the vibrational properties of the crystal. In highly

disordered Nb_3Sn the contribution to strain sensitivity from the electronic and vibrational properties is about equal.

In addition to Nb_3Sn, the strain dependent properties of Nb_3Al, Nb, and NbTi are investigated in a limited fashion. Bcc Nb and NbTi do not contain sublattices, i.e. the characteristic chains that are present on the faces of the A15 crystal structure, so sublattice distortion does not occur. As a result, the electron density of states of bcc Nb and NbTi is only weakly dependent on strain, which means that ρ_n, T_c, and $\mu_0 H_{c2}(0)$ are also only weakly dependent on strain. The degree of sublattice distortion is calculated to be less pronounced in Nb_3Al in comparison to Nb_3Sn, which results in a lower strain sensitivity in $N(E_F)$ in comparison to Nb_3Sn, and implies that overall the degree of strain sensitivity of the superconducting properties of Nb_3Al is smaller than in Nb_3Sn, a results that is consistent with experimental observations.

Finally, from the calculations it is found that the degree of strain sensitivity is strongly dependent on the degree of disorder, which implies that the strain sensitivity of ρ_n is lower when ρ_n is higher, that the strain sensitivity of T_c is lower when T_c is lower, and that the strain sensitivity of $\mu_0 H_{c2}(0)$ is lower when $\mu_0 H_{c2}(0)$ is lower. This in turn is related to the decreasing amount of sublattice distortion with increasing disorder.

The various calculated results are compared to experimental observations, and a high degree of consistency is demonstrated.

- Both the calculated result and the experimental observations of ρ_n indicate that the degree of strain sensitivity in ρ_n is dependent on the magnitude of ρ_n and the angle along which ρ_n is measured. The calculations and experimental observations are quantitatively consistent.

- The calculated strain dependencies of T_c and $\mu_0 H_{c2}(0)$ of slightly disordered Nb_3Sn are compared to the experimentally observed strain dependencies of Nb_3Sn wires, where the degree of disorder (through parameter l_{mfp}) in the calculation is chosen so that the magnitude of T_c and $\mu_0 H_{c2}(0)$ matches the properties of Nb_3Sn wires. The calculated strain dependencies of both T_c and $\mu_0 H_{c2}(0)$ are shown to be quantitatively consistent with the experimental observations, both for T_c and $\mu_0 H_{c2}(0)$.

- The calculated strain dependencies of T_c and $\mu_0 H_{c2}(0)$ of Nb_3Sn at various degrees of disorder are compared to composition dependent strain dependencies of T_c and $\mu_0 H_{c2}(0)$ of the Nb-Sn thin films. Consistent with the calculated results, the degree of strain sensitivity in both T_c and $\mu_0 H_{c2}(0)$ decreases with decreasing T_c and $\mu_0 H_{c2}(0)$ in the preferentially cubic regime. While the degree of strain sensitivity is closely consistent with experimental observations in slightly off-stoichiometric Nb-Sn, the calculated degree of strain sensitivity is lower than the experimentally observed strain sensitivity when the composition of the Nb-Sn is more off-stoichiometric. The accuracy of the calculations could be improved by evaluating the strain dependent properties of off-stoichiometric supercells as opposed to a single unit cell, but the evaluation of supercells would result in a dramatic increase in the amount computational resources used.

- As expected and experimentally observed, the ρ_n, T_c, and $\mu_0 H_{c2}(0)$ of bcc niobium are only weakly dependent on strain. This is a strong indication that sublattice distor-

tion, a phenomenon that occurs in the A15 crystal structure but not in the bcc crystal structure, is the underlying cause of the strain sensitivity in the normal state resistivity and superconducting properties of Nb_3Sn. This statement is validated with additional investigations of the strain sensitivities of bcc NbTi and A15 Nb_3Al.

The microscopic properties of preferentially tetragonal Nb_3Sn could not be evaluated due to tweed modulation which occurs in preferentially tetragonal Nb_3Sn (section 4.4.6). Instead, a simple model is presented to account for tweed modulation. The key insight of this model is that while the application of strain to preferentially cubic Nb_3Sn results in a distortion of the crystal, the application of strain to preferentially tetragonal Nb_3Sn result in a realignment of tetragonally distorted Nb_3Sn. Through this realignment, the degree of crystal deformation is reduced, which further implies that the degree of strain sensitivity in T_c and $\mu_0 H_{c2}(0)$ is reduced.

As the normal state resistivity of non-cubic Nb_3Sn is dependent on the angle along which the normal state resistivity is measured, the application of strain to preferentially tetragonal Nb_3Sn does still affect the measured ρ_n. Consistent with this model, the observed strain sensitivity in T_c and $\mu_0 H_{c2}(0)$ of the various investigated samples peaks at the transition between preferentially cubic and tetragonal Nb_3Sn (i.e. $T_c \approx 17.5$ K) and the degree of strain sensitivity in ρ_n continuously increases with decreasing ρ_n, regardless of the preferentially cubic to preferentially tetragonal transition at $\rho_n = 27.0 \pm 1.4$ $\mu\Omega$cm.

Commercial wires, which have an average composition of about 23.5 at.% Sn, which corresponds to the highest observed strain sensitivity of all possible compositions. As close to stoichiometric Nb-Sn is required for optimal J_c , there exist two means to mitigate the strain sensitivity of wires: firstly, by aligning the Nb_3Sn crystals in wires such that the (110) direction is parallel to the load application, and secondly by finding ways to mitigate the sublattice distortion, perhaps through alloying.

Chapter 6

Conclusion

6.1 Introduction

The main subject of this thesis is the effect of strain on the superconducting properties of the material Nb_3Sn. This phenomenon was investigated from an experimental and a computational perspective. The experimental part of the research involves determining how strain affects the superconducting properties (i.e. the critical temperature T_c, the upper critical field $\mu_0 H_{c2}(0)$, and the critical current density J_c) as well as the normal state resistivity ρ_n of A15 Nb-Sn and bcc Nb under various experimental conditions. The computational part involves constructing a model by which the effect of strain and disorder on ρ_n, T_c, and $\mu_0 H_{c2}(0)$ can be derived from ab-initio calculations. The experimental and computational sections are synergistic: a model is necessary to explain why strain influences the superconducting properties of Nb_3Sn, and validation of the model is achieved through comparison to experimental observations.

6.2 Experimental observations

6.2.1 Composition and morphology of bulk samples and thin films

The effect of strain on a variety of properties of Nb-Sn samples was determined for both bulk samples and thin films. The bulk samples were previously fabricated by mixing powders and reacting them at high pressure and temperature. The thin films were fabricated as part of this research by simultaneously sputtering niobium and tin onto heated sapphire substrates.

The compositions and morphologies of the bulk samples and thin films were investigated with a number of techniques, including scanning electron microscopy, scanning transmission electron microscopy, X-ray energy dispersive spectroscopy, X-ray diffraction, and variable temperature and magnetic field heat capacity measurements. It was concluded that the binary bulk samples and the ones with titanium and tantalum additions consist of separate areas of stoichiometric Nb_3Sn and excess niobium, while the samples with copper additions comprise both stoichiometric and off-stoichiometric Nb-Sn. Since the investigation of the relation between composition and strain sensitivity is of primary importance, the degree of inhomogeneity in the bulk samples makes them less suitable.

While not perfectly homogeneous in composition, the thin film samples are single-phased and may be prepared either stoichiometric or off-stoichiometric as desired. An extensive investigation was performed to determine their composition, morphology, and three-dimensional strain state. The Nb-Sn thin film samples are dense and polycrystalline, with grains aligned predominantly (100) in the out-of-plane orientation and random in the in-plane orientation. In addition, a niobium thin film was prepared, in which the grains are aligned in the (110) out-of-plane direction.

6.2.2 Experimental technique for observing strain sensitivity

An experimental technique was developed enabling the measurement of the normal state resistivity and various superconducting properties like T_c, $\mu_0 H_{c2}(0)$, and J_c as a function of temperature, magnetic field, as well as longitudinal and transverse strain. The so-called U-spring test rig, a tool previously developed for measuring the critical current of Nb_3Sn wires as function of temperature, magnetic field, and strain was used for this effort.

6.2.3 Experimental observation of strain sensitivity in resistivity measurements

The experiments indicate that the degree of strain sensitivity strongly depends on the composition of the material. The degree of strain sensitivity peaks at a T_c of about 17.5 K and a $\mu_0 H_{c2}(0)$ of about 29 T, which corresponds to near-stoichiometric preferentially cubic Nb_3Sn.

It was found that the degree of strain sensitivity in ρ_n depends on the magnitude of ρ_n and of the direction in which ρ_n is measured. Specifically, under the influence of strain the normal state resistivity becomes anisotropic and the degree of strain sensitivity is strongly composition dependent, with higher degrees of strain sensitivity at lower ρ_n, i.e. at compositions that are closer to stoichiometry. A variety of possible mechanisms were considered that might explain the large degree of strain sensitivity of ρ_n. It was concluded that the effect of strain on the low temperature resistivity of Nb-Sn is dominated by the effect of strain on the residual resistivity, i.e. on $\rho_n(0\ \mathrm{K})$.

In contrast to Nb-Sn, the effect of strain on ρ_n of bcc Nb is isotropic and nearly negligible, while the effect of strain on T_c and $\mu_0 H_{c2}(0)$ is weak.

6.2.4 Experimental observation of strain sensitivity in critical current density measurements

The critical current density J_c of a superconductor determines the performance of superconducting applications, such as superconducting magnets. The manner in which temperature, magnetic field, and strain affects J_c is discussed in chapter 3. This chapter mainly focuses on Nb_3Sn, but NbTi is discussed as well.

A review is given of the most commonly used descriptions of the critical current density, by which similarities and differences are highlighted. It was concluded that the various descriptions of the critical current density of Nb_3Sn are nearly identical. Furthermore, it was demonstrated that a commonly used critical current density description for Nb-Ti is nearly identical to the ones for Nb_3Sn, with the assumed temperature dependence of $\mu_0 H_{c2}(T)$ being the sole difference.

In the critical current density descriptions, the strain sensitivity in J_c is attributed to the effect of strain on T_c and $\mu_0 H_{c2}(0)$. To determine the validity of this statement, it is hypothesized that (1) the strain sensitivity of T_c and $\mu_0 H_{c2}(0)$ determined from critical current density measurements and resistivity measurements overlaps, and (2) that the effect of strain on the critical current density is independent from the direction in which current flows relative to the strain direction. Both hypotheses were shown to be correct, a strong indication that the investigation of strain sensitivity of the superconducting properties should focus on T_c and $\mu_0 H_{c2}(0)$.

6.3 Computational work

6.3.1 Microscopic origin of T_c and $\mu_0 H_{c2}(0)$

Since the strain dependence of J_c is determined solely by the strain dependence of T_c and $\mu_0 H_{c2}(0)$, a model is presented in chapter 4 for calculating T_c and $\mu_0 H_{c2}(0)$ as a function

of disorder and the results are compared to experimental observations. As the experimentally investigated samples comprise of various compositions which affects both the T_c and $\mu_0 H_{c2}(0)$ values and the degree of strain sensitivity in the superconducting properties, any model that describes the effect of strain should also consider the influence of composition. However, calculating the effect of off-stoichiometry, i.e. with excess niobium present, in ab-initio calculations is not practical due to the large computational cost of evaluating off-stoichiometric supercells.

To get around this issue, the effect of disorder on the properties of stoichiometric Nb_3Sn was evaluated. It was experimentally established that in the absense of strain, T_c and $\mu_0 H_{c2}(0)$ are determined by ρ_n, regardless of whether the Nb-Sn is stoichiometric or off-stoichiometric. Disorder is introduced into the ab-initio calculation through an electron-lifetime broadening approximation and the Eliashberg spectrum was expressed as a function of the electron and phonon density of states through an empirical approach. The validity of this approach was confirmed by calculating how disorder affects various experimentally observable properties, and comparing the calculated results to experimental observations.

- It was demonstrated that consistent with experimental observations, the crystal structure of low-resistivity Nb_3Sn is preferentially tetragonal and the crystal structure of high-resistivity Nb_3Sn is preferentially cubic. The transition between the preferentially cubic and tetragonal regimes was calculated to occur at $\rho_n = 27.0 \pm 1.4$ $\mu\Omega$cm, which is consistent with experimental observations.
- The Eliashberg spectrum was calculated at various degrees of disorder, and shown to be consistent with measured data.
- T_c was correctly calculated as a function of ρ_n.
- $\mu_0 H_{c2}(0)$ was calculated as a function of T_c and shown to be consistent with experimental observations as well.
- The calculations indicate that the martensitic transformation reduces $\mu_0 H_{c2}(0)$ and thus limits the maximum $\mu_0 H_{c2}(0)$ of Nb-Sn. While there is some controversy concerning this particular issue, it is argued that the presented result is in fact accurate.

In spite of the high degree of consistency between the calculated results and the experimental observations, the model does come with two caveats. Firstly, supercell calculations, which were performed on a limited scale, indicate that excess niobium ions not only act as scattering centers (which is captured by the electron-lifetime broadening approximation) but also influences the electronic band structure directly, further reducing the electron density of states at the Fermi energy $N(E_F)$. This means that while the consistency between the calculated and the experimental results is a strong indication that indeed disorder dominates T_c and $\mu_0 H_{c2}(0)$, regardless of whether the material is stoichiometric or off-stoichiometric, it is not clear why this statement is correct. In principle, the answer to this question can be found by supercell calculations, using the approach presented here as a recipe, but the computational cost of such an investigation is excessive, and at present unrealistic.

The second caveat is that the model can be used to calculate the microscopic properties of cubic Nb_3Sn, but that the properties of preferentially tetragonal Nb_3Sn could not be evaluated: the martensitic transformation results in the formation of a tweed pattern, in which the

shorter c-axis is oriented in different directions throughout the sample, while in the single unit cell ab-initio calculations it is assumed that the c-axis is aligned along a single direction throughout the sample. Since the manner in which tweed modulation affects the microscopic properties is unclear, the emphasis is placed on calculating the properties of cubic Nb_3Sn. In theory, this phenomenon can be evaluated with a very large supercell, but the computational cost of such an investigation is excessive, and therefore unfeasible.

6.3.2 Calculation of the effect of strain on the microscopic properties of Nb_3Sn

The model used to calculate T_c and $\mu_0 H_{c2}(0)$ as a function of disorder in chapter 4 was expanded for calculating T_c, $\mu_0 H_{c2}(0)$, and ρ_n as a function of disorder, strain, and crystal orientation as presented in chapter 5. Ab-initio calculations are highly suitable for investigating the effect of strain, because strain can be introduced into simulations by fixing selected lattice vectors, optimizing the crystal structure, and subsequently calculating the microscopic properties. This approach was used to evaluate various structural, electronic, and vibrational properties, as well as the T_c, $\mu_0 H_{c2}(0)$, and the orientation dependent ρ_n as a function of disorder, crystal orientation, and strain.

The calculations indicate that the large degree of strain sensitivity in Nb_3Sn is caused by a rearrangement of the niobium ions under the influence of non-hydrostatic strain, a phenomenon known as sublattice distortion. This phenomenon occurs in A15 materials as Nb_3Sn and Nb_3Al, but not in bcc materials like Nb and NbTi, because these materials do not exhibit the characteristic chains that are present in A15 materials, i.e. the niobium chains in Nb_3Sn and Nb_3Al. Due to this difference, the degree of strain sensitivity in ρ_n and the superconducting properties is much more pronounced in A15 materials than in bcc materials. In particular, the calculations show that the effect of strain on ρ_n in Nb_3Sn is much larger than in bcc Nb, and that strain affects ρ_n of Nb_3Sn in an anisotropic manner, i.e. ρ_n depends on the angle between the current and the direction in which strain is applied.

In addition, it was found that the degree of strain dependence of the superconducting properties of Nb_3Sn is large relative to bcc Nb. In slightly disordered, preferentially cubic Nb_3Sn the strain sensitivities of T_c and $\mu_0 H_{c2}(0)$ are mainly the result of strain induced changes in the electronic properties of the material. Strain induced changes in the vibrational properties of the material also contribute to the strain sensitivities of the superconducting properties, but the degree by which this affects T_c and $\mu_0 H_{c2}(0)$ is relatively weak. This outcome is consistent with some authors' findings, but in contrast to various other references reporting that the strain sensitivities of T_c and $\mu_0 H_{c2}(0)$ is mostly or entirely due to strain induced changes in the vibrational properties. However, most of the references are based on the a-priori assumption that strain does not affect the electronic properties of the material, an assumption that is inconsistent with the experimental observation and well confirmed fact that the low temperature normal state resistivity is strongly influenced by strain.

The model is used to determine how the degree of disorder, strain, and the crystal orientation relative to the strain orientation affects T_c and $\mu_0 H_{c2}(0)$, as well as the anisotropic ρ_n. Beyond three well-established global parameters discussed in chapter 4, no free parameters are necessary except for the mean free path l_{mfp} which determines the magnitude of ρ_n, T_c, and $\mu_0 H_{c2}(0)$, as well as the degree of strain sensitivity in ρ_n, T_c, and $\mu_0 H_{c2}(0)$.

The calculated results are compared to experimental observations, yielding a high degree of consistency.

- The calculated orientation dependent ρ_n is compared to experimental observations at various degrees of disorder. In quantitative agreement with the calculations, the experimental data on of Nb-Sn with various compositions indicate that the magnitude of strain sensitivity in ρ_n depends on the magnitude of ρ_n and on whether strain is applied parallel or perpendicular to the resistivity measurement.

- The model was used to calculate the strain sensitivity of T_c and $\mu_0 H_{c2}(0)$ of Nb_3Sn wires yielding quantitatively correct results for both of these properties.

- The magnitudes of the strain sensitivity in T_c and $\mu_0 H_{c2}(0)$ were calculated as a function of disorder and compared to the measured strain sensitivity of T_c and $\mu_0 H_{c2}(0)$ in Nb-Sn with various compositions. The results are consistent in the preferentially cubic regime near the stoichiometric composition. Furthermore, the prediction that the degree of strain sensitivity decreases with decreasing T_c and $\mu_0 H_{c2}(0)$ is qualitatively consistent with experimental observations. However, the value of the calculated strain sensitivities of T_c and $\mu_0 H_{c2}(0)$ is low in comparison to the experimentally observed magnitude in off-stoichiometric Nb-Sn. A likely explanation for this discrepancy is that the presence of excess niobium is affecting the superconducting properties in a manner that is not fully captured by the model. In other words, even though disorder, as measured by ρ_n, seems to be the main determinant for T_c and $\mu_0 H_{c2}(0)$ regardless of the composition of the sample, the composition influences the degree of strain sensitivity in a way that is not fully covered in a single unit cell approach.

- Consistent with the calculated result, the degree of strain sensitivity in ρ_n, T_c, and $\mu_0 H_{c2}(0)$ of bcc Nb is weak in comparison to Nb-Sn, which supports the main conclusion that sublattice distortion, a phenomenon that does not occur in bcc niobium, causes the large strain sensitivity in Nb_3Sn. In addition, the calculation indicates that the degree of sublattice distortion and the strain sensitivity of Nb_3Al is lower than that of Nb_3Sn, which is consistent with experimental evidence.

Due to the occurrence of tweed modulation in preferentially tetragonal Nb_3Sn, the ab-initio calculations were not used to calculate the strain sensitivity this structure. Instead, a simple model was presented. The main insight of this model is that unlike preferentially cubic Nb_3Sn, in which the application of strain results in a distortion of the crystal structure, the application of strain to preferentially tetragonal Nb_3Sn results, in part, in a realignment of the crystal structure. Through this realignment, the degree of distortion in the crystal structure is reduced, which subsequently results in a lower degree of strain sensitivity in T_c and $\mu_0 H_{c2}(0)$. Since ρ_n of non-cubic Nb_3Sn depends on the alignment of the crystal, this realignment does result in a change in the measured ρ_n. This model explains the seemingly contradictory observation that the degree of strain sensitivity in T_c and $\mu_0 H_{c2}(0)$ peaks in samples which are slightly off-stoichiometric and preferentially cubic, but that the degree of strain sensitivity in ρ_n continues to increase with decreasing ρ_n, well into the preferentially tetragonal regime.

6.4 Recommendations for further research

For this thesis, calculations were performed on disordered stoichiometric unit cells. The advantage of this approach is that the use of supercells is avoided, which, at present, would require an unrealistic computation time. However, as more and more processing power becomes available over the years, one could consider to undertake calculations on supercells using the approach that is outlined in this research as a recipe.

- The effect of disorder on the superconducting properties in stoichiometric and off-stoichiometric unit cells can be investigated. This can also be applied to strain sensitivity, to see if the way in which off-stoichiometry affects the strain sensitivity of the superconducting properties is different from the way it does in stoichiometric Nb_3Sn affects the superconducting properties. Such research could improve the accuracy of the model presented here in the case of off-stoichiometric Nb-Sn.
- Instead of investigating off-stoichiometry (i.e. excess niobium), with such calculations one can also investigate the influence of various additions. Perhaps strain sensitivity in the superconducting properties can be suppressed through the introduction of a particular addition, and this addition may be found through supercell calculations.

A more straightforward line of inquiry is to see how strain affects the properties of other (A15) materials, an investigation with both an experimental and a theoretical component. Here, other superconductors than Nb_3Sn were investigated in a limited fashion. The investigation can be extended towards a more systematic study. An interesting result is that for Nb_3Al the calculations show less strain sensitivity than for Nb_3Sn. Understanding the causes of this difference could lead to new insights on how to mitigate strain sensitivity in Nb_3Sn.

Finally, it is interesting to investigate experimentally how the crystal orientation of Nb_3Sn wires influences the strain sensitivity of the superconducting properties. The calculations indicate that the strain sensitivity vary between crystal orientations, and indeed there is some experimental indication that this is correct. This may imply that the strain sensitivity of Nb_3Sn wires may potentially be reduced by carefully tuning the crystal orientation inside the filaments.

References

[1] B. T. Matthias, T. H. Geballe, S. Geller, and E. Corenzwit, *Phys. Rev.* **95**, 1435-1435 (1954).
[2] G. F. Hardy and J. K. Hulm, *Phys. Rev.* **89**, 884 (1953).
[3] J. P. Charlesworth, I. Macphail, and P. E. Madsen, *J. Mat. Sci.* **5**, 580 (1970).
[4] H.K. Onnes, *Roy. Neth. Ac. Arts Sci. Proc.* **13**, 1274 (1911).
[5] W. Meissner and R. Ochsenfeld, *Naturwissenschaften* **21**, 787 (1933).
[6] F. London and H. London, *Proc. Roy. Soc.* **A149**, 866 (1935).
[7] V. L. Ginzburg, and L. D. Landau, *Zh. Eksp. Teor. Fiz.* **20**, 1064 (1950).
[8] H. Fröhlich, *Phys. Rev.* **79**, 845 (1950).
[9] E. Maxwell, *Phys. Rev.* **78**, 477 (1950).
[10] A. B. Pippard, *Proc. Roy. Soc.* **A216**, 547 (1953).
[11] A. A. Abrikosov, *Zh. Eksp. Teor. Fiz.* **32**, 1442 (1957).
[12] J. Bardeen, L. N. Cooper, and J.R. Schrieffer, *Phys. Rev.* **108**, 1175 (1957).
[13] D. F. Moore, R. B. Zubeck, and J. M. Rowell, *Phys. Rev.* **20B**, 2721 (1979).
[14] G. M. Eliashberg, *Zh. Eksp. Teor. Fiz.* **38**, 966 (1960).
[15] W. L. McMillan, *Phys. Rev.* **167**, 331 (1968).
[16] J. J. Hopfield, *Phys. Rev.* **186**, 443 (1969).
[17] P. B. Allen, and R. C. Dynes, *Phys. Rev.* **12B**, 905 (1975).
[18] V. Z. Kresin, *Phys. Lett.* **A122**, 434 (1987).
[19] L. P. Gorkov, *Zh. Eksp. Teor. Fiz.* **36**, 1918 (1959).
[20] B. D. Josephson, *Phys. Lett.* **1**, 251 (1962).
[21] P. W. Anderson, and J. M. Rowell, *Phys. Rev. Lett.* **10**, 230 (1963).
[22] J. G. Bednorz, and K. A. Müller, *Z. Physik* **B64**, 189 (1986).
[23] C. W. Chu, L. Gao, F. Chen, Z. J. Huang, R. L. Meng, and Y. Y. Xue, *Nature* **365**, 323 (1993).
[24] J. Nagamatsu, N. Nakagawa, T. Muranaka, Y. Zenitani, and J. Akimitsu, *Nature* **410**, 63 (2001).
[25] Y. Kamihara, H. Haramatsu, M. Hiran, R. Kawamura, H. Yanagi, T. Kamiya, and H. Hosono, *J. Am. Chem. Soc.* **128**, 10012 (2006).
[26] A. Godeke, A. den Ouden, A. Nijhuis, and H.H.J. ten Kate, *Cryogenics* **48**, 308 (2008).
[27] R. M. Scanlan, D. R. Dietderich, H. C. Higley, K. R. Marken, L. R. Motowidlo, R. S. Sokolowski, and T. Hasegawa, *IEEE Trans. Appl. Supercond.* **9**, 130 (1999).
[28] D. R. Dietderich, R. M. Scanlan, T. Hasegawa, Y. Aoki, R. S. Sokolowski, and L. R. Motowidlo, *IEEE Trans. Appl. Supercond.* **11**, 3577 (2001).
[29] A. Godeke, D. Cheng, D. R. Dietderich, P. Ferracin, S. O. Prestemon, G. Sabbi, and R. M. Scanlan, *IEEE Trans. Appl. supercond.* **17**, 1149 (2007).
[30] A. Godeke, P. Acosta, D. Cheng, D. R. Dietderich, M. G. T. Mentink, S. O. Prestemon, G. L. Sabbi, M. Meinesz, S. Hong, Y. Huang, H. Miao, and J. Parrell, *Supercond. Sci. Techn.* **23**, 034022 (2010).
[31] W. Goldacker, R. Nast, G. Kotzyba, S. I. Schlachter, A. Frank, B. Ringsdorf, C. Schmidt, and P. Komarek, *J. Phys. Conf.* **43**, 901 (2006).
[32] D. C. van der Laan, P. D. Noyes, G. E. Miller, H. W. Weijers, and G. P. Willering, *Supercond. Sci. Techn.* **26**, 045005 (2013).
[33] A. Godeke, *Performance boundaries in Nb_3Sn superconductors*, PhD thesis, University of Twente (2005).

[34] M. Suenaga, D. O. Welch, R. L. Sabatini, O. F. Kammerer, and S. Okuda, *J. Appl. Phys.* **59**, 840 (1986).
[35] W. Goldacker, S. I. Schlachter, A. Jung, H. Fillinger, A. Godeke, and M. G. T. Mentink, *Presented at Int. Cryog. Mat. Conf.*, Tucson, Az, USA (2009).
[36] V. Guritanu, W. Goldacker, F. Bouquet, Y. Wang, R. Lortz, G. Goll, and A. Junod, *Phys. Rev.* **70B**, 184526 (2004).
[37] M. Marz, G. Goll, W. Goldacker, and R. Lortz, *Phys. Rev.* **82B**, 024507 (2010).
[38] Y. Wang, C. Senatore, V. Abacherli, D. Uglietti, and R. Flukiger, *Supercond. Sci. Techn.* **19**, 263266 (2006).
[39] M. G. T. Mentink, A. Anders, M. M. J. Dhallé, D. R. Dietderich, A. Godeke, W. Goldacker, F. Hellman, H. H. J. ten Kate, D. Putnam, J. L. Slack, M. D. Sumption, and M. A. Susner, *IEEE Trans. Appl. Supercond.* **21**, 2550 (2011).
[40] R. Flükiger, *Atomic ordering, phase stability and superconductivity in bulk and filamentary A15 type compounds*, Postdoctoral thesis, University of Geneva (1987).
[41] A. Godeke, *Supercond. Sci. Techn.* **19**, R68 (2006).
[42] T. P. Orlando and M. R. Beasley, *Phys. Rev. Lett.* **46**, 1598 (1981).
[43] D. A. Rudman, F. Hellman, R. H. Hammond, and M. R. Beasley, *J. Appl. Phys.* **55**, 3544 (1984).
[44] M. G. T. Mentink, M. M. J. Dhallé, D. R. Dietderich, A. Godeke, W. Goldacker, F. Hellman, H. H. J. ten Kate, M. D. Sumption, M. A. Susner, *Phys. Proc.* **36**, 491 (2012).
[45] M. G. T. Mentink, J. E. Bonevich, M. M. J. Dhallé, D. R. Dietderich, A. Godeke, F. Hellman, H. H. J. ten Kate, *IEEE Trans. Appl. Supercond.* **23**, 7100505 (2013).
[46] C. Senatore, and R. Flükiger, *Appl. Phys. Lett.* **102**, 012601 (2013).
[47] P. G. De Gennes, *Superconductivity of Metals And Alloys*, W. A. Benjamin, New York City (1966), Addison-Wesley, Reading (1989).
[48] A. Godeke, M. C. Jewell, C. M. Fischer, A. A. Squitieri, P. J. Lee, and D. C. Larbalestier, *J. Appl. Phys.* **97**, 093909 (2005).
[49] M. G. T. Mentink, M. M. J. Dhallé, D. R. Dietderich, A. Godeke, W. Goldacker, F. Hellman, and H. H. J. ten Kate, *AIP Conf. Proc.* **1435**, 225 (2012).
[50] F. Hellman and T. Geballe, *Phys. Rev.* **36B**, 107 (2005).
[51] F. Hellman, *Specific heat and non-equilibrium aspects of vapor deposition growth of A15 superconductors*, PhD thesis, Stanford University (1985).
[52] H. Devantay, J. L. Jorda, M. Decroux, and J. Muller, *J. Mat. Sc.* **16**, 2145 (1981).
[53] L. J. Vieland, *RCA Rev.* **25**, 366 (1964).
[54] M. M. M. Bilek, R. N. Tarrant, D. R. McKenzie, S. H. N. Lim, and D. G. McCulloch, *IEEE Trans. Pl. Sci.* **31**, 939 (2003).
[55] M. M. M. Bilek and D. R. McKenzie, *Surf. Coat. Techn.* **200**, 4345 (2006).
[56] D. R. McKenzie and M. M. M. Bilek, *Thin Solid Films* **382**, 280 (2001).
[57] B. Ten Haken, A. Godeke, and H. H. J. ten Kate, *Adv. Cryog. Eng.* **42**, 1463 (1997)
[58] L. Muzzi, V. Corate, A. della Corte, G. De Marzi, T. Spina, J. Daniels, M. Di Michiel, F. Buta, G. Mondonico, B. Seeber, R. Flükiger, and C. Senatore, *Supercond. Sci. Techn.* **25**, 054006 (2012).
[59] K. Watanabe, H. Oguro, K. Minegishi, S. Awaji, and G. Nishijima, *IEEE Trans. Appl. Supercond.* **20**, 1420 (2010).
[60] W. M. Yim and R. J. Paff, *J. Appl. Phys.* **45**, 1456 (1974).
[61] J. W. Edwards, R. Speiser, and H. L. Johnston, *J. Appl. Phys.* **22**, 424 (1951).

[62] C. R. Tottle, *J. Inst. Met.* **85**, 375 (1957).
[63] H. W. Schadler, L. M. Osika, G. P. Salvo, and V. J. DeCarlo, *Trans. Met. Soc. Aime* **230**, 1074 (1964).
[64] R. L. Barns, *J. Appl. Phys.* **39**, 4044 (1968).
[65] ESPI Metals, *http://www.espimetals.com/index.php/technical-data/170-niobium*.
[66] J. Zhou, Y. Jo, Z. H. Sung, H. Zhou, P. J. Lee, and D. C. Larbalestier, *Appl. Phys. Lett.* **99**, 122507 (2011).
[67] S. Foner and E. J. McNiff Jr., *Sol. St. Comm.* **39**, 959 (1981).
[68] M. C. Jewell, A. Godeke, P. J. Lee and D. C. Larbalestier, *Adv. Cryo. Eng.* **711**, 474 (2004).
[69] M. Naus, *Optimization of Internal-Sn Nb_3Sn Composites*, PhD thesis, University of Wisconsin - Madison (2002).
[70] A. J. Arko, D. H. Lowndes, F. A. Muller, L. W. Roeland, J. Wolfrat, A. T. van Kessel, H. W. Myron, F. M. Mueller, and G. W. Webb, *Phys. Rev. Lett.* **40**, 1590 (1978).
[71] B. ten Haken, A. Godeke, and H. H. J. ten Kate, *J. Appl. Phys.* **85**, 3247 (1999).
[72] B. ten Haken, *Strain effects on the critical properties of high-field superconductors*, PhD thesis, University of Twente (1994).
[73] R. Bijman, *Effects of strain on the superconducting properties of various Niobium-Tin compounds*, Internship report, University of Twente (2005).
[74] M. G. T. Mentink, *Strain dependency of Nb_3Sn bulk samples*, M. S. thesis, University of Twente (2009).
[75] B. L. Brandt, D. W. Liu, L. G. Rubin, *Rev. Sci. Instr.* **70**, 104 (1999).
[76] Vishay Precision Group, *http://www.vishaypg.com/docs/11013/bond610.pdf*.
[77] R. Mailfert, B. W. Batterman, and J. J. Hanak, *Phys. Lett.* **24A**, 315 (1967).
[78] Battelle Columbus Labs Ohio metals and ceramics information center, *Handbook on Materials for Superconducting Machinery*, Metals and Ceramic Information Center, Battelle (1974).
[79] Aerospace Specification Metals inc, *http://asm.matweb.com/search/SpecificMaterial.asp?bassnum=MTP641*
[80] E. D. Marquardt, J. P. Le, and R. Radebaugh, *Presented at Proc. 11th Intern. Cryoc. Conf.*, Keystone, Co, USA (2000).
[81] T. P. Orlando, E. J. McNiff Jr., S. Foner, and M. R. Beasley, *Phys. Rev.* **19B**, 4545 (1979).
[82] D. A. Rudman, F. Hellman, R. H. Hammond, and M. R. Beasley, *J. Appl. Phys.* **55**, 3544 (1984).
[83] J. W. Ekin, *Cryog.* **20**, 611 (1980).
[84] D. M. J. Taylor and D. P. Hampshire, *Supercond. Sci. Techn.* **18**, 241 (2005).
[85] E. S. Rosenblum, S. H. Autler, K. H. Gooen, *Rev. Mod. Phys.* **36**, 77 (1964).
[86] A. Godeke, G. Ambrosio, G. Chlachidze, D. R. Dietderich, H. Felice, A. K. Ghosh, M. Marchevsky, M. G. T. Mentink, S. O. Prestemon, and G. L. Sabbi, *Superc. Sci. and Techn.* **26**, 095015 (2013).
[87] International Thermonuclear Experimental Reactor, *http://www.iter.org/*.
[88] The office of High Energy Physics, U.S. Department of Energy, *http://science.energy.gov/hep/*.
[89] J. Ekin, *Supercond. Sci. and Techn.* **23**, 083001 (2010).
[90] X. F. Lu, D. M. J. Taylor, and D. Hampshire, *Supercond. Sci. Techn.* **21**, 105016 (2008).

[91] L. Bottura, *IEEE Trans. Appl. Supercond.* **10**, 1054 (2000).
[92] L. Bottura and B. Bordini, *IEEE Trans. Appl. Supercond.* **19**, 1521 (2009).
[93] M. Tinkham, *Introduction to Superconductivity*, 2nd ed., McGraw-Hill, New York (1996).
[94] J. D. Livingston and H. W. Schadler, *Progr. Mater. Sci.* **12**, 183 (1964).
[95] E. J. Kramer, *Philosophical Magazine* **15**, 1189 (1967).
[96] L. D. Cooley, C. M. Fischer, P. J. Lee, and D. C. Larbalestier, *J. Appl. Phys.* **96**, 2122 (2004).
[97] W. D. Markiewicz, *Cryogenics* **46**, 846 (2006).
[98] W. D. Markiewicz, *Cryogenics* **44**, 767 (2004).
[99] B. Bordini, P. Alknes, L. Bottura, L. Rossi, and D. Valentinis, *Supercond. Sci. Techn.* **26**, 075014 (2013).
[100] M. M. J. Dhallé, *Handbook of Superconducting Materials*, Institute of Physics Publishing, Bristol (2003)
[101] B. ten Haken, A. Godeke, and H. H. J. ten Kate, *IEEE Trans. Appl. Supercond.* **5**, 1909 (1995).
[102] B. ten Haken, A. Godeke, and H. H. J. ten Kate, *J. Appl. Phys.* **85**, 3247 (1999)
[103] A. Godeke, B. ten Haken, H. H. J. ten Kate, and D. C. Larbalestier, *Supercond. Sci. Techn.* **19**, R100 (2006).
[104] M. G. T. Mentink, *Critical surface parameterization of high J_c RRP Nb_3Sn strand*, Internship report, University of Twente / Lawrence Berkeley National Laboratory (2008).
[105] A. Godeke, M. G. T. Mentink, D. R. Dietderich, and A. den Ouden, *IEEE Trans. Appl. Supercond.* **19**, 2610 (2009).
[106] D. Arbelaez, A. Godeke, and S. O. Prestemon, *Supercond. Sci. Techn.* **22**, 025005 (2009).
[107] A. Godeke, M. M. J. Dhallé, A. Morelli, L. Stobbelaar, H. van Weeren, H. J. N. van Eck, W. Abbas, A. Nijhuis, A. den Ouden, and B. ten Haken, *Rev. Sci. Instrum.* **75**, 5112 (2004).
[108] C. R. Walters, I. M. Davidson, and G. E. Tuck, *Cryogenics* **26**, 406 (1986).
[109] J. W. Ekin, *IEEE Trans. Magn.* **17**, 658 661 (1981).
[110] J. W. Ekin, *Adv. Cryog. Eng.* **30**, 823 (1984).
[111] M. S. Lubell, *IEEE Trans. Magn.* **19**, 754 (1983).
[112] M. A. Green, *IEEE Trans. Magn.* **25**, 2119 (1989).
[113] E. Schachinger and M. Prohammer, *Phys. C.* **156**, 701 (1988).
[114] H. J. Muller, *The upper critical field of niobium-titanium*, PhD thesis, University of Wisconsin - Madision (1989).
[115] A. Godeke and D. R. Dietderich, *preprint*.
[116] D. R. Dietderich, M. Kelman, J. R. Litty, and R. M. Scanlan, *Adv. Cryo. Eng.* **44**, 951 (1998)
[117] A. W. West and D. C. Larbalestier, *IEEE Trans. Magn.* **19**, 548 (1983).
[118] J. W. Ekin, *IEEE Trans. Magn.* **23**, 1634 1637 (1987).
[119] C. M. Fischer, *Investigation of the relationships between superconducting properties and Nb_3Sn reaction conditions in Powder-in-Tube Nb_3Sn conductors*, M. S. thesis, University of Wisconsin Madison (2002).
[120] L. H. Thomas, *Proc. Cambridge Phil. Soc.* **23**, 542 (1927).
[121] E. Fermi, *Rend. Accad. Naz. Lincei* **6**, 602 (1927).

[122] P. Hohenberg, W. Kohn, *Phys. Rev.* **136**, B864 (1964).
[123] J. C. Cuevas, *Presented at the Institute of Advanced Studies*, Jerusalem, Israel (2012).
[124] W. Kohn and L. J. Sham, *Phys. Rev.* **140**, A1133 (1965).
[125] S. Baroni, P. Giannozzi, and A. Testa, *Phys. Rev. Lett.* **58**, 1861 (1987).
[126] S. Baroni, S. de Gironcoli, A. Dal Corso, and P. Giannozzi, *Rev. Mod. Phys.* **73**, 515 (2001).
[127] P. Giannozzi, S. Baroni, N. Bonini, M. Calandra, R. Car, C. Cavazzoni, D. Ceresoli, G. L. Chiarotti, M. Cococcioni, I. Dabo, A. Dal Corso, S. de Gironcoli, S. Fabris, G. Fratesi, R. Gebauer, U. Gerstmann, C. Gougoussis, A. Kokalj, M. Lazzeri, L. Martin-Samos, N. Marzari, F. Mauri, R. Mazzarello, S. Paolini, A. Pasquarello, L. Paulatto, C. Sbraccia, S. Scandolo, G. Sclauzero, A. P. Seitsonen, A. Smogunov, P. Umari, and R. M. Wentzcovitch, *J. Phys. Condens. Matter.* **21**, 395502 (2009).
[128] H. Hellman, *J. Chem. Phys.* **3**, 61 (1935).
[129] J. P. Perdew, J. A. Chevary, S. H. VOsko, K. A. Jackson, M. R. Pederson, D. J. Singh, and C. Fiolhais, *Phys. Rev.* **46B**, 6671 (1992).
[130] L. R. Testardi, and L. F. Mattheiss, *Phys. Rev. Lett.* **41**, 1612 (1978).
[131] L. F. Mattheiss, and L. R. Testardi, *Phys. Rev.* **20B**, 2196 (1979).
[132] Y. Watanabe, N. Toyota, T. Inoue, H. Komatsu, and H. Iwasaki, *Jap. J. Appl. Phys.* **27**, 2218 (1988).
[133] H. W. King and D. W. Penfold, *Adv. Cryo. Eng. Mat.* **28**, 371 (1982).
[134] W. Goldacker and R. Flukiger, *Physica* **135B**, 359 (1985).
[135] R. Flükiger, C. Senatore, M. Cesaretti, F. Buta, D. Uglietti, and B. Seeber, *Supercond. Sci. Techn.* **21**, 054015 (2008).
[136] J. Labbé and J. Friedel, *J. de Phys.* **27**, 303 (1966).
[137] H. Jahn and E. Teller, *Proc. Roy. Soc.* **161**, 220 (1937).
[138] B. Sadigh and V. Ozolins, *Phys. Rev.* **57B**, 2793 (1998).
[139] G. Shirane and J. D. Axe, *Phys. Rev.* **4B**, 2957 (1971).
[140] W. Weber and L. F. Mattheiss, *Phys. Rev.* **25B**, 2270 (1982).
[141] Y. Fujii, J. B. Hasting, M. Kaplan, and G. Shirane, *Phys. Rev.* **25B**, 364 (1982).
[142] P. B. Allen, W. E. Pickett, K. M. Ho, and M. L. Cohen, *Phys. Rev. Lett.* **40**, 1532 (1978).
[143] M. J. Goringe and U. Valdre, *Proc. Roy. Soc.* **A295**, 192 (1966).
[144] T. Onozuka, N. Ohnishi, and M. Hirabayashi, *Met. Trans. A* **19A**, 797 (1988).
[145] S. Kartha, J. A. Krumhansl, J. P. Sethna, and L. K. Wickham, *Phys. Rev.* **52B**, 803 (1995).
[146] A. K. Ghosh, M. Gurvich, H. Wiesmann, and Myron Strongin, *Phys. Rev.*, **18B**, 6116 (1978).
[147] K. C. Lim, J. D. Thompson, and G. W. Webb, *Phys. Rev.* **27B**, 2781 (1983).
[148] H. Ibach and H. Lüth, *Solid-state physics: An introduction to Principles of Materials Science*, 3rd edition, Springer-Verlag, Berlin Heidelberg (2003).
[149] G. Grimvall, *The electron-phonon interaction in metals*, 16th edition, North-Holland publishing company, Amsterdam (1981).
[150] W. E. Pickett and P. B. Allen, *Sol. St. Comm.* **12**, 677 (1973).
[151] R. Flükiger, H. Küpfer, J. L. Jorda, and J. Muller, *IEEE Trans. Magn.* **23**, 980 (1987).
[152] J. J. Hanak, K. Strater, and G. W. Cullen, *RCA Rev.* **25**, 342 (1964).
[153] M. Gurvitch, *Phys. Rev.* **24B**, 7404 (1981).
[154] A. F. Ioffe and A. R. Regel, *Prog. Semicond.* **4**, 237 (1960).

[155] M. F. Mott, *Metal Insulator Transitions*, 2nd edition, Taylor and Francis, London (1990).
[156] J. D. Axe and G. Shirane, *Phys. Rev.* **28B**, 4829 (1965)
[157] L. Pintschovius, H. Takei and N. Toyota, *Phys. Rev. Lett.* **54**, 1260 (1985).
[158] B. P. Schweiss, B. Renker, E. Schneider, and W. Reichardt, *Superconductivity in d- and f-band metals*, Plenum Press, New York (1976).
[159] J. D. Axe and G. Shirane, *Phys. Rev.*. **8B**, 1965 (1973).
[160] J. K. Freericks, A. Y. Liu, and A. Quandt, *Phys. Rev.* **64B**, 224510 (2002).
[161] M. F. Salvetti, *Hyperelastic Continuum Modeling of Cubic Crystals based on First-Principles Calculations*, PhD thesis, Massachusetts Institute of Technology (2010).
[162] M. F. Salvetti, M. Calandra, N. Bonini, J. Minervini, D. M. Parks, N. Marzari, *Presented at APS Mar. Meet.*, Portland, OR, USA (2010)
[163] H. M. Tütünce , G. P. Srivastava, S. Bagci, and S. Duman, *Phys. Rev.*. **74B**, 212506 (2006).
[164] G. De Marzi, L. Morici, L. Muzzi, and A. della Corte, *J. Phys. Cond. Matt.* **10**, 25 (2012).
[165] P. B. Allen, *Handbook of superconductivity*, 1st edition, Academic Press, Waltham, (1999).
[166] J. Geerk, U. Kaufmann, W. Bangert, and H. Rietschel, *Phys. Rev.* **33B**, 1621 (1986).
[167] L. Y. L. Shen, *Phys. Rev. Lett.* **29**, 1082 (1972).
[168] D. A. Rudman and M. R. Beasley, *Phys. Rev.* **30B**, 2590 (1984).
[169] E. L. Wolf, *Rep. Prog. Phys.* **41**, 1439 (1978).
[170] W. L. McMillan, *Phys. Rev.* **167**, 331 (1968).
[171] L. P. Gor'kov, *Sov. Phys. JETP* **36**, 1364 (1959).
[172] E. Helfand and N. R. Werthamer, *Phys. Rev. Lett.* **13**, 686 (1964).
[173] E. Helfand and N. R. Werthamer, *Phys. Rev.* **147**, 288 (1966).
[174] P. C. Hohenberg and N. R. Werthamer, *Phys. Rev.* **153**, 493 (1967).
[175] N. R. Werthamer, E. Helfand, and P. C. Hohenberg, *Phys. Rev.* **147**, 295 (1966).
[176] N. Schopohl and K. Scharnberg, *Physica* **107B**, 293 (1981).
[177] C. T. Rieck, K. Scharnberg, and N Schopohl, *J. Low Temp. Phys.* **84**, 381 (1991).
[178] N. Schopohl and K. Scharnberg, *Physica* **135B**, 482 (1985).
[179] N. R. Werthamer and W. L. McMillan, *Phys. Rev.* **158**, 415 (1967).
[180] N. F. Masharov, *Fiz. Tverd. Tela.* **16**, 2343 (1974).
[181] M. Schossmann and E. Schachinger, *Phys. Rev.* **33B**, 6123 (1986).
[182] M. Schossmann and E. Schachinger, *Phys. Rev.* **30B**, 1349 (1984).
[183] N. R. Werthamer, *Superconductivity I*, 1st ed., Marcel Dekker inc., New York (1969).
[184] T. P. Orlando, M. R. Beasley, *Phys. Rev. Lett.* **46**, 1598 (1981).
[185] A. M. Clogston, *Phys. Rev. Lett.* **9**, 266 (1962).
[186] M. Kaveh and N. Wiser, *Adv. Phys.* **33**, 257 (1984).
[187] M. Gurvitch, A. K. Ghosh, H. Lutz, and M. Strongin, *Phys. Rev.* **22B**, 128 (1980).
[188] R. Flükiger, *Handbook of superconducting materials*, 1st ed., IOP publishing ltd., Bristol (2003).
[189] L. J. Vieland and A. W. Wicklund, *Phys. Lett.* **34A**, 43 (1971).
[190] R. Akihama, K. Yasukochi, and T. Ogasawara, *IEEE Trans. Magn.* **13**, 803 (1977).
[191] S. Foner and E. J. McNiff, Jr., *Phys. Lett.* **58A**, 318 (1976)

[192] E. Dollekamp, *Obtaining the Eliashberg spectrum from Nb_3Sn tunnel junctions*, Internship report, University of Twente / Lawrence Berkeley National Laboratory (2012).
[193] R. Flükiger, R. Isernhagen, W. Goldacker and W. Specking, *Adv. Cryo. Eng.* 30, 851 (1984).
[194] J. W. Ekin, *Adv. Cryo. Eng.* **30**, 823 (1985).
[195] R. K. Bollinger, B. D. White, J. J. Neumeier, H. R. Z. Sandin, Y. Suzuki, C. A. M. dos Santos, R. Avci, A. Migliori, and J. B. Betts, *Phys. Rev. Lett.* **107**, 075503 (2011).
[196] S. Francoual, M. von Zimmerman, J. Neumeier, R. Bollingen, and H. Sandim, *DESY annual report* (2012).
[197] D. O. Welch, *M. S. thesis*, Brookhaven National Laboratory (1981).
[198] R. W. Cohen, G. D. Cody, and J. J. Halloran, *Phys. Rev. Lett.* **19**, 840 (1967).
[199] J. P. McEvoy, *Physica* **55**, 540 (1971).
[200] A. Godeke, M. C. Jewell, A. A. Golubov, B. ten Haken, and D. C. Larbalestier, *Supercond. Sci. and Techn.* **16**, 1019 (2003).
[201] L. R. Testardi, *Phys. Rev.* **3B**, 95 (1971).
[202] L. Qiao, L. Yang, and X. Zheng, *J. Appl. Phys.* **114**, 033905 (2013).
[203] S. Oh and K. Kim, *J. Appl. Phys.* **99**, 033909 (2006).
[204] T. Takeuchi, Y. Iijima, K. Inoue, and H. Wade, *Appl. Phys. Lett.* 71, 122 (1997)
[205] T. Takeuchi, *Supercond. Sci. Techn.* 13, R101 (2000)
[206] C. Scheuerlein, U. Stuhr, and L. Thilly, *Appl. Phys. Lett.* **91**, 042503 (2007).
[207] C. Scheuerlein, G. Arnau, P. Alknes, N. Jimenez, B. Bordini, A. Ballarino, M. Di Michiel, L. Thilly, T. Besara, and T. Siegrist, *to be published in Supercond. Sci. and Techn.*.
[208] P. J. Lee and D. C. Larbalestier, *IEEE Trans. Appl. Supercond.* **15**, 3474 (2005).
[209] X. F. Lu and D. P. Hampshire, *Supercond. Sci. and Techn.* **23**, 025002 (2010).
[210] A. Godeke, G. Chlachidze, D. R. Dietderich, A. K. Ghost, M. Marchevsky, M. G. T. Mentink and G. L. Sabbi, *Supercond. Sci. and Techn.* **26**, 095015 (2013).
[211] M. Pulver, *Z. Physik* **257**, 261 (1972).

Summary

Summary

The superconducting properties of Nb_3Sn are strongly affected by strain. This phenomenon is not just of interest from a fundamental perspective, but is also relevant for the performance of high magnetic field Nb_3Sn superconducting magnets, since the strain sensitivity of Nb_3Sn conductors may influence the performance of the magnet in a detrimental way.

The critical current density and resistivity of Nb-Sn bulk samples and thin films were measured as a function of temperature and applied magnetic field as well as longitudinal and transverse strain. From the critical current density and resistivity measurements, the strain dependent critical temperature T_c and upper critical field $\mu_0 H_{c2}(0)$ were determined. In addition to the strain sensitivity of these superconducting properties, it is also observed that strain affects the normal state resistivity ρ_n in an anisotropic manner: the strain dependence of ρ_n varies with the angle between the current and the applied strain.

A detailed study of previously developed critical current scaling relations was performed, and differences as well as similarities are discussed. The critical current density was measured as a function of temperature, magnetic field, longitudinal strain, and transverse strain in both stoichiometric and off-stoichiometric binary thin films. It is shown how, consistent with literature results, the strain sensitivity of the critical current density is dominated by the strain sensitivity of T_c and $\mu_0 H_{c2}(0)$.

It is observed that the degree of strain sensitivity in T_c and $\mu_0 H_{c2}(0)$ varies with composition. Thus, to understand the strain sensitivity, the composition dependence of T_c and $\mu_0 H_{c2}(0)$ needs to be understood as well. However, performing ab-initio calculations on off-stoichiometric compositions requires the evaluation of large supercells, which is at present not feasible due to the associated high computational load. Instead, the effect of disorder of T_c and $\mu_0 H_{c2}(0)$ is investigated computationally, which is validated by the experimental statement that T_c and $\mu_0 H_{c2}(0)$ is strongly dependent of ρ_n, regardless of composition. This approach is combined with an empirical description of the electron-phonon coupling characteristic $\alpha^2(\omega)$ and it was demonstrated that these calculations accurately capture the relation between ρ_n and the Martensitic transformation, the ρ_n dependent Eliashberg spectrum, T_c as a function of ρ_n and finally $\mu_0 H_{c2}(0)$ as a function of T_c.

The same approach is then applied to calculate the effect of strain on various microscopic properties, including ρ_n, T_c, and $\mu_0 H_{c2}(0)$. The main insight obtained from the ab-initio calculations is that the application of strain results in a distortion of the niobium chains within the A15 crystal structure, which is referred to as sublattice distortion. Due to sublattice distortion, both the electronic and the vibrational properties of Nb_3Sn are affected in a manner that is detrimental for superconductivity. In the nearly stoichiometric and preferentially cubic Nb_3Sn that dominates the superconducting properties of Nb_3Sn wires, the strain sensitivity of T_c and $\mu_0 H_{c2}(0)$ is mainly a result of changes in the electronic properties of the material, although the contribution of the vibrational properties is not negligible.

The validity of the calculated results is determined through a comparison with experimental observations:

- The strain dependent anisotropic ρ_n behavior is calculated and shown to be quantitatively consistent with experimental observations.
- The strain dependence of T_c and $\mu_0 H_{c2}(0)$ in Nb_3Sn wires is calculated and is shown to be quantitatively consistent with experimental results.
- The strain dependence of T_c and $\mu_0 H_{c2}(0)$ in Nb-Sn thin films is calculated, and once more the calculated results are quantitatively consistent with the experimental observations of preferentially cubic Nb_3Sn close to the stoichiometric composition.
- Consistent with the experimental observation that the strain sensitivity of T_c and $\mu_0 H_{c2}(0)$ decreases with off-stoichiometry, the calculations indicate that the degree of strain sensitivity in T_c and $\mu_0 H_{c2}(0)$ decreases with increasing disorder. However, the assumption that off-stoichiometry is simply a type of disorder is likely too simplistic: the magnitude of the experimentally observed strain dependence in T_c and $\mu_0 H_{c2}(0)$ of strongly off-stoichiometric Nb-Sn exceeds the calculated strain value. Consistent with this discrepancy, it was determined in a limited investigation of off-stoichiometric supercells that excess niobium does not just act as scattering centers but also affects the electron density of states directly. This implies that the accuracy of the calculations may be improved by evaluating the properties of supercells instead of single unit cells.
- The calculated results indicate that the strain dependence of ρ_n, T_c, and $\mu_0 H_{c2}(0)$ of bcc niobium, in which sublattice distortion does not occur, is much weaker than of A15 Nb_3Sn, and this is found to be consistent with experimental observations. In addition, the calculations indicate that Nb_3Al is less strain sensitive than Nb_3Sn due to a lower degree of sublattice distortion, which is also consistent with experimental evidence.

To summarize, the calculations and the experimental observations are for the most part consistent. This is a strong indication that the main insight of the calculations, that the large strain sensitivity in Nb_3Sn is a direct result of sublattice distortion, is correct.

Samenvatting (Summary in Dutch)

Samenvatting

De supergeleidende eigenschappen van Nb_3Sn zijn erg gevoelig voor rek. Dit is niet alleen van fundamenteel belang, maar ook relevant voor de prestatie van hoog-magneetveld supergeleidende Nb_3Sn magneten, omdat de rektoestand van het Nb_3Sn het gedrag van de magneet beïnvloedt.

De kritieke stroomdichtheid en resistiviteit van Nb-Sn bulk en dunne film proefstukken zijn gemeten als functie van temperatuur, magneetveld en longitudinale en transversale rek. Van deze metingen zijn de rekafhankelijke kritieke temperatuur T_c en het bovenste kritieke magneetveld $\mu_0 H_{c2}(0)$ bepaald. Naast de rekgevoeligheid van de supergeleidende eigenschappen beïnvloedt rek ook de resistiviteit in de normale toestand ρ_n op een anisotrope manier: De rekafhankelijkheid van ρ_n hangt af van de hoek tussen de stroom en de aangebrachte rek.

Verscheidende schalingsrelaties van de kritieke stroom van Nb_3Sn worden beschouwd en de overeenkomsten en verschillen tussen deze schalingsrelaties worden besproken. De kritieke stroom van stoichiometrische en off-stoichiometrische binaire dunne films is gemeten als functie van temperatuur, magneetveld, longitudinale rek, en transversale rek. In overeenstemming met de literatuur volgt dat de rekgevoeligheid van de kritieke stroom van Nb_3Sn voornamelijk het resultaat is van de rekgevoeligheid van T_c en $\mu_0 H_{c2}(0)$.

Uit de analyse volgt dat de rekgevoeligheid van T_c en $\mu_0 H_{c2}(0)$ van het materiaal samenstelling afhankelijk is. Daarom is het nodig om deze afhankelijkheid van T_c en $\mu_0 H_{c2}(0)$ te berekenen om de rekgevoeligheid van Nb_3Sn te begrijpen. Maar, ab-initio berekeningen van off-stoichiometrische samenstellingen vereisen de berekening van grote supercellen, iets dat op dit moment niet realistisch is vanwege de omvang van deze berekeningen. In plaats daarvan zijn T_c en $\mu_0 H_{c2}(0)$ berekend als een functie van de wanorde, omdat het experimenteel aangetoond is dat T_c en $\mu_0 H_{c2}(0)$ sterk afhankelijk zijn van de resistiviteit en dat de samenstelling daarbij een ondergeschikte rol heeft. Dit is gecombineerd met een empirische beschrijving van de electron-phonon koppeling. Het is aangetoond dat deze berekeningen met grote nauwkeurigheid de martensitische transformatie, T_c en $\mu_0 H_{c2}(0)$ als functie van ρ_n beschrijven.

Dezelfde methode is vervolgens toegepast om de rekafhankelijkheid van verscheidene microscopische eigenschappen te berekenen, inclusief ρ_n, T_c en $\mu_0 H_{c2}(0)$. Het belangrijkste resultaat dat volgt uit de ab-initio berekeningen is dat rek de niobium ketens in de A15 kristal structuur verstoort, iets dat 'subrooster vervorming' genoemd wordt. Als gevolg van dit effect veranderen zowel de elektronische als de trillingseigenschappen op een wijze die nadelig is voor de supergeleidende eigenschappen van Nb_3Sn. In bijna-stoichiometrisch, kubisch Nb_3Sn die de kritieke stroom van Nb_3Sn draden bepaald is de rekgevoeligheid van de supergeleidende eigenschappen met name een gevolg van de rekgevoeligheid van de elektronische eigenschappen, alhoewel de bijdrage van de rekgevoeligheid van de trillingseigenschappen niet verwaarloosbaar is.

De nauwkeurigheid van de berekeningen is gevalideerd door middel van een vergelijk met experimentele observaties:

- Het is aangetoond dat de berekende rekafhankelijke ρ_n quantitatief consistent is met

experimentele observaties.

- De rekgevoeligheid van T_c en $\mu_0 H_{c2}(0)$ van Nb_3Sn draden is berekend en de resultaten zijn kwantitatief consistent met experimentele observaties.
- De rekgevoeligheid van T_c en $\mu_0 H_{c2}(0)$ van bijna-stoichiometrisch kubische Nb_3Sn dunne films is berekend en de uitkomst is kwantitatief consistent met de metingen.
- Consistent met de metingen laten de berekeningen zien dat de mate van rekgevoeligheid afneemt naarmate de mate van wanorde toeneemt. Maar de aanname dat off-stoichiometrie simpelweg een soort wanorde is, is naar alle waarschijnlijkheid te simplistisch. De mate van rekgevoeligheid in T_c en $\mu_0 H_{c2}(0)$ van de off-stoichiometrische dunne films die experimenteel waargenomen is, is hoger dan de berekende waardes. Consistent met dit resultaat is het aangetoond in een beperkte beschouwing van off-stoichiometrische supercellen dat het extra niobium niet alleen als verstrooiingscentra fungeert, maar daarnaast ook de elektronische eigenschappen rechtstreeks beïnvloedt. Dit betekent dat de nauwkeurigheid van de berekeningen verbeterd kan worden door de eigenschappen van supercellen te berekenen.
- Zowel de berekeningen als de experimentele observaties laten zien dat de rekgevoeligheid van ρ_n, T_c en $\mu_0 H_{c2}(0)$ van bcc niobium, dat niet het karakteristieke subrooster van Nb_3Sn bevat, veel minder sterk is dan in Nb_3Sn. Daarnaast laten zowel de berekeningen als experimentele resultaten zien dat de rekgevoeligheid van Nb_3Al een stuk lager is dan die van Nb_3Sn, wat gerelateerd is aan de lagere mate van subroostervervorming.

Samenvattend, de berekeningen en experimentele resultaten zijn voor het grootste deel consistent. Dit is een sterke indicatie dat rekgevoeligheid in Nb_3Sn inderdaad een direct gevolg is van subroostervervorming.

Peer Reviewed Publications

Peer Reviewed Publications

1. M. G. T. Mentink, J. E. Bonevich, M. M. J. Dhallé, D. R. Dietderich, A. Godeke, F. Hellman, H. H. J. ten Kate, *Superconductivity in Nb-Sn Thin Films of Stoichiometric and Off-Stoichiometric Compositions*, IEEE trans. Appl. Supercond. **23**, 7100505 (2013)

2. M. G. T. Mentink, M. M. J. Dhallé, D. R. Dietderich, A. Godeke, W. Goldacker, F. Hellman, H. H. J. ten Kate, M. D. Sumption, M. A. Susner, *The Effect of Ta and Ti Additions on the Strain Sensitivity of Bulk Niobium-Tin*, Phys. Proc. **36**, 491 - 496 (2012)

3. M. G. T. Mentink, A. Anders, M.M.J. Dhallé, D.R. Dietderich, A. Godeke, W. Goldacker, F. Hellman, H.H.J. ten Kate, D. Putnam, J.L. Slack, M.D. Sumption, M. A. Susner, *Analysis of bulk and thin film model samples for investigating the strain sensitivity of Niobium-Tin*, IEEE Trans. Appl. Supercond. **21**, 2550-2553 (2011)

4. M. G. T. Mentink, M. M. J. Dhallé, D. R. Dietderich, A. Godeke, W. Goldacker, F. Hellman, H. H. J. Ten Kate, *Towards analysis of the electron density of states of Nb_3Sn as a function of strain*, AIP Conf. Proc. **1435**, 225-232 (2011)

5. T. Salmi. D. Arbelaez, S. Caspi, H. Felice, M. G. T. Mentink, S. Prestemon, A. Stenvall, and H. H. J. ten Kate, *A Novel Computer Code for Modeling Quench Protection Heaters in High-Field Nb3Sn Accelerator Magnets*, Accepted for IEEE trans. Appl. Supercond. (2014)

6. A. Godeke, G. Chlachidze, D. R. Dietderich, A. K. Ghosh, M. Marchevsky, M. G. T. Mentink, G. L. Sabbi, *A review of conductor performance for the LARP High-Gradient Quadrupole Magnets*, Supercond. Sci. And Techn. **26**, 095015 (2013)

7. A. Godeke, D. W. Cheng, D. R. Dietderich, M. G. T. Mentink, S. O. Prestemon, G. L. Sabbi, *Heat treatment optimizations for Wind-and-React Bi-2212 racetrack coils*, Phys. Proc. **36**, 812 - 817 (2012)

8. A. Godeke, P. Bish, D. R. Dietderich, C. S. Gorham, A. R. Hafalia, H. C. Higley, N. L. Liggins, M. G. T. Mentink, G.L. Sabbi, *Novel Methods for the Measurement of the Critical Current of Superconducting Wires*, AIP Conf. Proc. **1435**, 209-216 (2011)

9. H. Wu, H. Pan, M. A. Green, D. R. Dietderich, T. E. Gartner, H. C. Higley, M. G. T. Mentink, D. G. Tam, F. Y, Xu, F. Trillaud, X. K. Liu, L. Wang, S. X. Zheng, *The Resistance and Strength of Soft Solder Splices Between Conductors in MICE Coils*, Appl. Supercond. **21**, 1738-1741 (2011)

10. A. Godeke, P. Acosta, D. Cheng, D. R. Dietderich, M. G. T. Mentink, S. O. Prestemon, G. L. Sabbi, M. Meinesz, S. Hong, Y. Huang, H. Miao, J. Parrell, *Wind-and-React Bi-2212 coil development for accelerator magnets*, Supercond. Sci. and Techn. **23**, 034022 (2010).

11. A. Godeke, D. R. Dietderich, M. G. T. Mentink, A. Den Ouden, *Characterization of High Current RRP Wires as a Function of Magnetic Field, Temperature and Strain*, IEEE Trans. Appl. Supercond. **19**, 2610-2614 (2009)